UNIVERSITÉ DE STRASBOURG

ÉCOLE DOCTORALE DES SCIENCES CHIMIQUES

ICPEES – UMR 7515

THÈSE présentée par :

Vincent GAUTIER

soutenue le : **10 Décembre 2024**

pour obtenir le grade de : **Docteur de l'université de Strasbourg**

Discipline/ Spécialité : Chimie / Génie Chimique

Membrane reactors for methanol synthesis: from material science to process simulations

THÈSE dirigée par :

Pr. ROGER Anne-Cécile	Professeure, ICPEES – UMR 7515
Dr. CHAISE Albin	Docteur, CEA Grenoble

RAPPORTEURS :

Pr. GALLUCCI Fausto	Professeur, Eindhoven University of Technology
Dr. JULCOUR Carine	Docteure, LGC – UMR 5503

AUTRES MEMBRES DU JURY :

Pr. FONGARLAND Pascal	Professeur, CP2M – UMR 5128
Dr. VANDEGEHUCHTE Bart	Docteur, TotalEnergies

INVITÉS :

Dr. HERTZ Audrey	Docteure, CEA Marcoule

Remerciements - acknowledgement

Ces travaux de thèse ont été réalisés entre trois laboratoires : le LPSD (Laboratoire de Procédés Supercritiques et de Décontamination) du CEA Marcoule, l'équipe ECED (Energie et Carburants pour un Environnement Durable) de l'ICPEES (Université de Strasbourg) et enfin le LRP (Laboratoire des Réacteurs et Procédés) du CEA Grenoble. Je souhaite remercier chaque laboratoire pour leurs accueils chaleureux et leurs soutiens cruciaux qui me permettent, aujourd'hui, de présenter ces travaux de thèse. Merci aux responsables de ces différents laboratoires : Marine PEYROT (CEA Grenoble), Olivier LEMAIRE (CEA Grenoble), Laurent BEDEL (CEA Grenoble) et Alexandre CARELLA (CEA Marcoule) pour avoir su mettre en place un environnement propice au bon déroulement de cette thèse.

Je remercie mon encadrement : Anne-Cécile ROGER (ICPEES), Albin CHAISE (CEA Grenoble) et Audrey HERTZ (CEA Marcoule), pour tous leurs conseils et leurs soutiens durant ces trois années. Merci d'avoir consacré autant de temps à me conseiller, m'écouter, m'encourager et m'aider à naviguer entre ces trois laboratoires aux cultures très variées. Nos échanges m'ont permis de me développer tout autant sur le plan professionnel que personnel.

Je souhaite également remercier tous les étudiants qui ont collaboré avec moi durant ces travaux : François BIHL, Clément HOCINE, Robin MOCHEL, Tobias BOUDON et Loan AVEDIKIAN. J'ai pris énormément de plaisir à travailler avec vous, à savourer les succès comme partager les échecs. Je vous souhaite le meilleur pour vos carrières professionnelles.

Je souhaite remercier tout le personnel qui m'a aidé sur le plan technique durant ces travaux de thèse: Pierre VENDITTI, Alexandre GAILLARD, Pascal ANTONUCCI, Fabien FRANCES, Anne-Clémence AUN, Christophe SUTTER, Michel JOUVE, Benoît SOMMACAL et Julien CIGNA.

Je remercie également tous les ingénieurs/chercheurs pour toutes les conversations et tous vos conseils enrichissants : Antoine LEYDIER, Jeremy MASCARADE, Sebastien THOMAS, Ksénia PARKHOMENKO, Luc BERTIER, Vincent LACROIX, Sandra BEGHI et Alban CHAPPAZ.

I would also like to thank all the members of this thesis jury: Fausto GALLUCCI, Carine JULCOUR, Pascal FONGARLAND and Bart VANDEGEHUCHTE. Thank you for agreeing to be part of this jury and taking the time to review my work.

Je remercie aussi tous les amis que j'ai pu rencontrer ou retrouver dans chaque ville où j'ai travaillé. À Avignon, je remercie Lucas CHATRE, Simon VERRIER, Gabriel PORAS, Martin WIESKOTTEN, Lorianne GINOT et Mathieu CAPPON pour tous les bons moments et les jeudis soirs aux sommets de la gastronomie. À Strasbourg, je remercie Morvan GUILLON et François BIHL pour les moments moins sérieux au labo et les batailles dans les dunes. À Grenoble, je remercie Titouan FABIANI, Maïté MICHAUD, Guillaume LHERMET et Alexis FERRÉ pour tous les bons moments en soirées et le week-end.

Merci aux membres de ma famille pour votre soutien durant ces trois années et de m'avoir encouragé et motivé depuis le début de mes études jusqu'à présent mon doctorat.

Et enfin, un grand merci à toi, Jeanne, pour avoir partagé ma vie durant ces trois années, malgré la distance. Ton soutien indéfectible, ton écoute et ta présence dans les moments difficiles ont rendu ces trois années soutenables et m'ont grandement aidé dans la poursuite de ces travaux.

Table of contents

List of figures

Figure **Page**

List of tables

Table **Page**

Chapter I

General Introduction

The climate change crisis is driven by greenhouse gases (GHGs) emissions from fossil fuel consumption. To combat this threat, the gradual phasing out of fossil hydrocarbons is essential. As the demand for fossil raw materials continues to rise, finding ecological substitutes has become a critical global priority.

CO_2 is the primary GHG responsible for global warming. Establishing a circular economy around CO_2 offers a potential solution for limiting its accumulation in the atmosphere. This approach, known as carbon capture, utilization, and storage (CCUS), involves capturing anthropogenic CO_2 and either storing it or converting it into valuable products (Figure I.1).

The conversion of CO_2 into valuable products is part of the Power-to-X concept. This term refers to the conversion of surplus electrical energy (mainly during periods when intermittent renewable electricity production exceeds demand) so that it can be stored and redirected to other uses. These uses encompass, among others, chemical synthesis (Power-To-Chemicals) or synthetic fuel production (Power-to-Gas, Power-To-Liquid, Power-To-Fuel or "e-fuel").

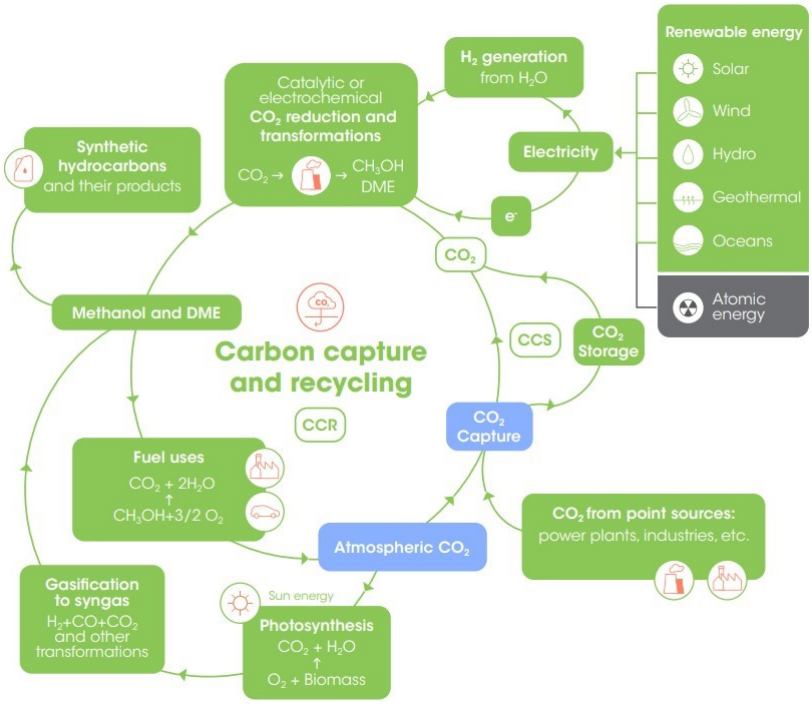

Figure I.1: Anthropogenic carbon cycle for a circular economy [23]

In the Power-To-X concept, the conversion of CO_2 is achieved through a catalytic reaction between CO_2 and hydrogen, produced by electrolysis of water powered by excess low-carbon electrical energy. Depending on the process used, a variety of high-energy compounds can be synthesized:

- **Methanation** (Power-To-CH_4 or Power-To-Gas): producing methane as a substitute of natural gas.
- **Fischer-Tropsch synthesis (FTS)** (Power-To-FTS): using synthesis gas (mixture of CO_2, CO, H_2) to produce paraffins and olefins (for the manufacture of fuels, polymers and other petrochemical products).
- **Methanol synthesis** (Power-To-MeOH): performed using synthesis gas or CO_2 and H_2 to create methanol (manufacture of fuels, solvents, polymers, etc.).

This PhD research focuses on methanol synthesis through the Power-To-MeOH concept. The following sections will address current methods of methanol synthesis from fossil carbon sources, along with the challenges and potential solutions associated with transitioning to captured CO_2 as a feedstock.

I.1 The challenges of carbon-neutral methanol production

In Section I.1.1, the current applications of methanol and outlooks arising from its production from renewable resources are examined, highlighting future perspectives on its sustainable role.

Section I.1.2 reviews conventional methanol production processes, which rely on CO-rich reaction mixtures produced from fossil-based feedstocks. This section also addresses the challenges of transitioning to more sustainable carbon-based feedstocks, which typically yield reaction mixtures with lower CO content and higher CO_2 content.

Finally, Section I.1.2 explores strategies for converting CO_2-rich reaction mixtures into methanol, introducing the membrane reactor as the solution investigated in this PhD research.

I.1.1 Methanol: current applications and outlooks

Methanol is often described as a very versatile compound. Indeed, methanol is the source of many chemicals (formaldehyde, MTBE, acetic acid, polymers, etc.) and has a wide range of applications. For example, methanol is used in the manufacture of plastics, solvents, paints, cosmetics, fuels, etc. (Figure I.2). In 2023, close to 110 million tonnes of methanol were produced worldwide [21] with most of it in Asia [2]. Moreover, methanol demand and production are growing. In 2030, global production capacity is estimated at 300 million tonnes, almost double that observed in 2020 [3].

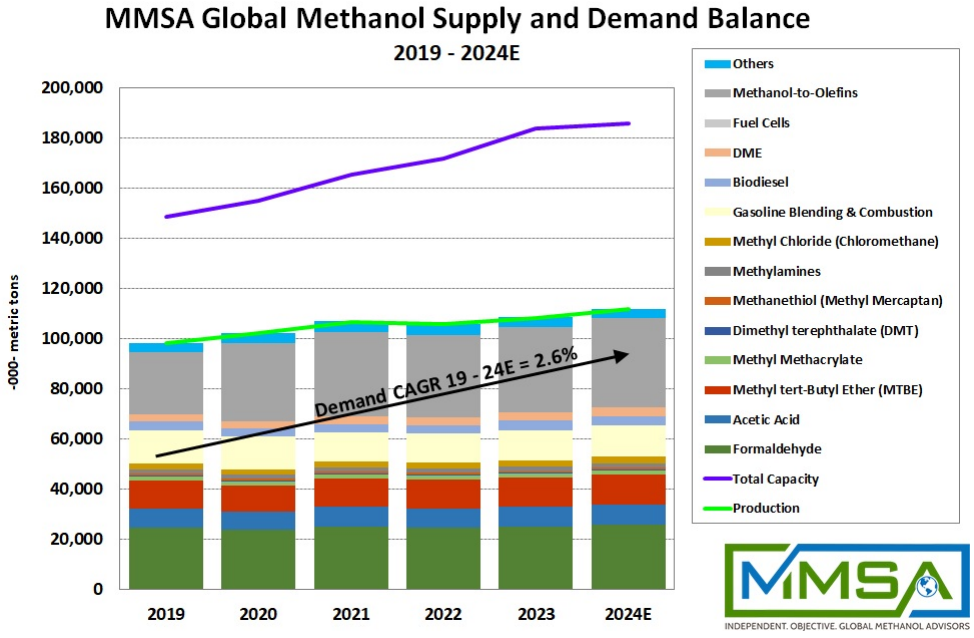

Figure I.2: Global methanol supply and demand. Data: MMSA [21].

Methanol is also an environmentally friendly energy vector when synthesized from sequestered carbon and hydrogen produced by water electrolysis powered by low-carbon energy. Methanol thus belongs to the "e-fuel" class, comprising "carbon-neutral" synthetic fuels (including e-fuels derived from FTS). In this context, the term "e-methanol" is used. This compound can substitute fossil fuels in many applications. Liquid at room temperature and atmospheric pressure, methanol is compatible with conventional hydrocarbon transport systems (pipelines, tankers,

etc.) [24] and can be used as an environmentally friendly fuel in combustion engines. However, with its high-octane number and low energy density, methanol as such is hardly compatible with use in aviation [14] or in diesel engines [24]. It can, however, be combined with additives or dehydrated to dimethyl ether (DME) as a substitute for diesel fuel. It can also be transformed into a mixture of hydrocarbons (as a substitute for gasoline) using the Methanol-to-Gasoline (MTG) process with acid catalysts [24].

Heavy transports, whether by air or sea, are under increasing pressure to reduce their CO_2 emissions. However, these modes of transportation are often incompatible with electrification, and are therefore forced to use liquid fuels. They could therefore benefit greatly from these "carbon-neutral" fuels. For example, at European Union level, new laws could oblige airlines to integrate up to 50% synthetic fuels (such as those derived from methanol) into their aircraft by 2050 [7]. The marine sector is also considering using synthetic fuels, especially e-methanol. In particular, Danish shipping giant Maersk plans to buy half of the methanol produced by the future e-methanol plant in Kasso, Denmark, once construction is completed in 2023 [28]. The plant is billed as the first large-scale e-methanol synthesis facility [28].

Currently, with a global annual capacity of 6 000 tons (approximately 0.005% of global methanol production) and only three demonstrator-scaled operational plants, e-methanol production remains very marginal [21]. The first e-methanol plant began operations in 2012 in Reykjavik, Iceland. The subsequent plants commenced operations more recently, with facilities opening in Lanzhou, China, and Punta Arenas, Chile, in 2020 and 2022, respectively, indicating a growing industrial interest in e-methanol. Several additional e-methanol plants with much higher capacities are either under construction (mainly in China) or in the planning stages and are expected to become operational in the coming years (Figure I.3).

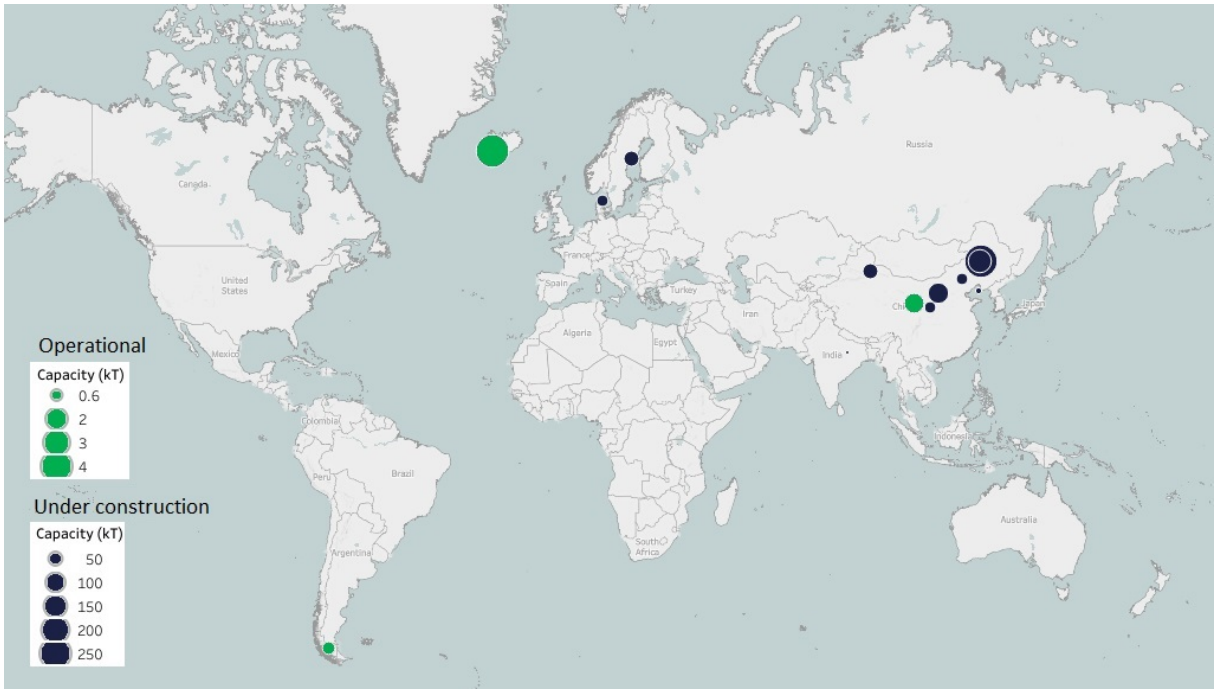

Figure I.3: E-methanol production plants throughout the world [21].

I.1.2 Current industrial methanol production: processes and thermodynamics

Despite the ecological advantages of e-methanol, current methanol production still relies primarily on fossil feedstocks, with natural gas being the main source. An analysis of current methanol synthesis processes provides an insight into the challenges and technical constraints, such as reaction equilibria, operating conditions, reagent compositions, among others, involved in methanol synthesis. The limitations of these processes illustrate the challenges of shifting away from fossil feedstocks to synthesize methanol.

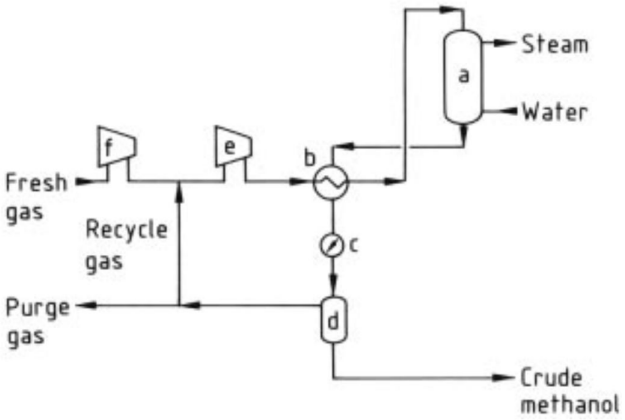

Figure I.4: Simplified diagram of a conventional methanol synthesis process (distillation step excluded): (a) reactor, (b) heat exchanger, (c) cooler, (d) separation, (e) recycle compressor, (f) feed compressor [24].

Current industrial production of methanol is carried out in 3 stages [5]:

1. Production of synthesis gas (syngas) (H_2, CO and CO_2) by steam reforming of fossil feedstock.
2. Conversion of syngas to methanol in a catalytic reactor (Figure I.4).
3. Separation of reaction products by distillation.

After syngas production, this gas mixture reacts in a catalytic reactor described by two balanced reactions: the hydrogenation of CO_2 into methanol (Eq. I.1) and the water-gas shift (WGS) reaction (Eq. I.3).

$$CO_2 + 3\,H_2 \rightleftharpoons CH_3OH + H_2O \qquad \Delta_r H^\circ_{298K} = -49.8\,\mathrm{kJ \cdot mol^{-1}} \tag{I.1}$$

$$CO + 2\,H_2 \rightleftharpoons CH_3OH \qquad \Delta_r H^\circ_{298K} = -90{,}8\,\mathrm{kJ \cdot mol^{-1}} \tag{I.2}$$

$$CO + H_2O \rightleftharpoons CO_2 + H_2 \qquad \Delta_r H^\circ_{298K} = -41{,}0\,\mathrm{kJ \cdot mol^{-1}} \tag{I.3}$$

Gas phase methanol synthesis reactions are exothermic and therefore favored at low temperatures (Eqs. I.1 and I.2). Additionally, decreasing the number of moles during the reaction

leads to improved conversion under high pressure conditions.

The WGS reaction is also exothermic, but with no change in mole number during the reaction. This reaction is therefore favored at low temperatures and remains independent of pressure conditions. In the conventional process, the CO reacts with water through the WGS reaction to produce additional CO_2 and H_2 reactants. Thus, in addition to removing water, which shifts the thermodynamic equilibrium of the CO_2 hydrogenation reaction according to Le Chatelier's principle and protects the water-sensitive copper-zinc-alumina catalysts, the additional production of reactants further drives methanol production [2, 22].

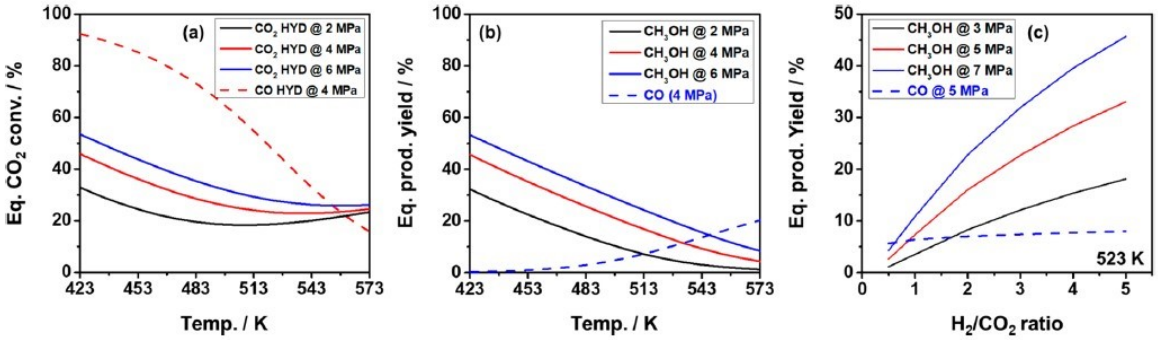

Figure I.5: (a) CO_2/CO conversion at equilibrium, (b) methanol yield as a function of temperature and pressure (H_2/CO_2=3), (c) methanol yield as a function of the H_2/CO_2 ratio [16].

Despite favorable reaction equilibria around 200°C (Figure I.5a), current methanol synthesis processes operate at temperatures above 250°C to reach sufficient reaction kinetics. However, the temperatures imposed are always kept below 300°C to ensure thermodynamically favorable conditions for methanol formation (Figure I.5b). Furthermore, the pressure must remain as low as possible to limit the economic cost of reactants compression, but sufficient enough to achieve suitable yields (Figure I.5) [2]. Advancements in catalysis have progressively increased catalyst activity, enabling processes to operate under milder conditions (Figure I.6). An example of a modern methanol synthesis process is Air Liquide's MegaMethanol process, operating at 250-260°C and 50-60 atm [2, 12].

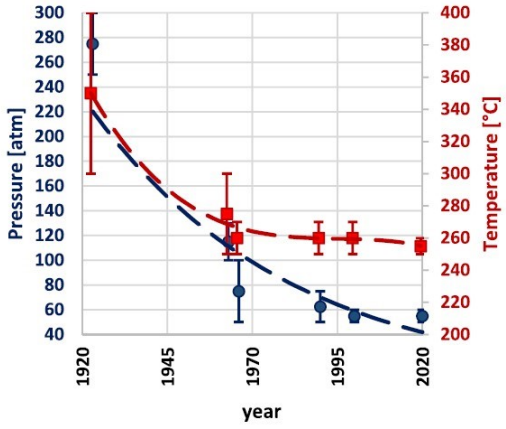

Figure I.6: Trends in operating conditions used in industrial process reactors for methanol synthesis [2].

The synthesis gas used as a reagent for methanol synthesis is mainly produced through the steam reforming of natural gas (or methane steam reforming). This highly endothermic reaction accounts for a large proportion of the process's energy consumption [18]. Other raw materials (oil, coal, biomass, etc.) may nevertheless be used, depending on various economic or environmental criteria [24, 5]. The composition of the syngas, influenced by the feedstock used, plays an important role in the efficiency of the process. Manufacturers use two factors to qualify the composition of this gas: the stoichiometric ratio (S) (Eq. I.4), the carbon oxides ratio (COR or CO_2/CO_x) (Eq. I.5) [2].

$$S = \frac{x_{H_2} - x_{CO_2}}{x_{CO_2} + x_{CO}} \tag{I.4}$$

$$COR = \frac{x_{CO_2}}{x_{CO} + x_{CO_2}} \tag{I.5}$$

A S ratio slightly above 2 (generally targeted industrially) indicates an excess of hydrogen over stoichiometric conditions and is optimal for maintaining high selectivities for most of the catalysts used [24, 5]. The reforming of methane results in a synthesis gas with an S ratio of 2.8 to 3, enabling either the excess hydrogen to be used for other applications (e.g. ammonia synthesis), or the addition of CO_2 to approach an S ratio close to 2 [24, 5].

$$CO_2 + H_2 \rightleftharpoons CO + H_2O \qquad \Delta_r H^\circ_{298K} = 41{,}0\,\mathrm{kJ \cdot mol^{-1}} \tag{I.6}$$

Industrial methanol synthesis processes also operate with a COR factor generally below 0.6 [22] in order to limit the CO_2 content of the gas mixture [2]. With increasing CO_2 content, the equilibrium of the WGS reaction is exceeded and the reverse reaction takes place. In this case, the reverse water-gas shift (RWGS) reaction (Eq. I.6) becomes a parasitic reaction, consuming the reactants (CO_2 and H_2) to form carbon monoxide and water. The presence of water at high temperatures degrades the catalyst, mainly through sintering of the active particles [16, 27, 8], as well as hindering equilibrium conversions and reaction kinetics [2].

I.1.3 New CO_2 synthesis processes: Focus on membrane catalytic reactors

I.1.3.1 Sustainable sources of carbonaceous reagents for methanol production

With the aim of moving away from fossil feedstocks for methanol production, alternative sources of CO_2 are being explored. There are three main ways of producing CO_2: gasification or steam reforming of carbonaceous materials, capture from CO_2-rich sources (flue gas or industrial waste) and direct capture of atmospheric CO_2.

For the first route (also called pre-combustion), the carbonaceous feedstock in solid form is transformed through gasification (Eq. I.7), and in gaseous or liquid through steam reforming (Eq. I.8). These processes take place at high temperatures and high pressures to produce synthesis gas [11]. This route encompasses the production of syngas by steam-reforming fossil feedstock, used for current methanol production. However, in order to move towards a sustainable source of carbonaceous reactants, it is preferable to substitute the fossil feedstock with biomass to produce syngas. Although, the use of biomass typically yields syngas with lower CO contents

and therefore more challenging to convert into methanol [9].

$$C_nH_m + \frac{n}{2} O_2 \longrightarrow \frac{m}{2} H_2 + nCO \tag{I.7}$$

$$C_nH_m + \frac{n}{2} H_2O \longrightarrow \frac{m+n}{2} H_2 + nCO \tag{I.8}$$

The second method for sustainable CO_2 production derives from sources where CO_2-rich sources, such as flue gases from coal and gas-fired power plants (also known as CO_2 from post-combustion), as well as CO_2-rich emissions from cement and steelworks [20]. Here, CO_2 is generally captured by absorption using aqueous amine solutions [11, 20]. This method has the advantage of being easily adaptable to existing infrastructures [11]. However, to be applied to current methanol synthesis processes, part of the CO_2 must be converted into CO, and hydrogen must be supplied from an external source.

Finally, direct capture of atmospheric CO_2 involves recovering the CO_2 present in the air. The technologies used to capture atmospheric CO_2 are absorption by a solution (hydroxide, amine, amino acid) or adsorption on a solid support (such as activated carbons) [11, 20]. Thanks to this technique, CO_2 can be removed from the atmosphere to mitigate the effects of global warming. However, the concentration of CO_2 in the atmosphere is very low (around 400 ppm) and so these plants have to treat a significant amount of air to capture the CO_2. This results in energy consumption around 4 times higher than that of CO_2 captured after post-combustion [11, 20]. The recovered gas also contains no CO, and no dihydrogen for methanol synthesis.

I.1.3.2 Suitable processes for CO_2-rich feed streams

Current industrial methanol synthesis processes are unsuitable for handling these types of CO_2-rich feeds for the reasons outlined above. Indeed, working with such CO_2-rich feeds greatly complicates the process, as large quantities of water are generated in the reactor. The water generated limits reactant conversion and prematurely degrades the catalyst. To circumvent these problems, several technical solutions currently being studied are described here.

At the process level, two broad solutions are available for methanol synthesis (Figure I.7). The first consists in a two-stage process with RWGS followed by methanol synthesis from syngas (CAMERE process) [26]. The second one does the direct conversion of CO_2 in one step.

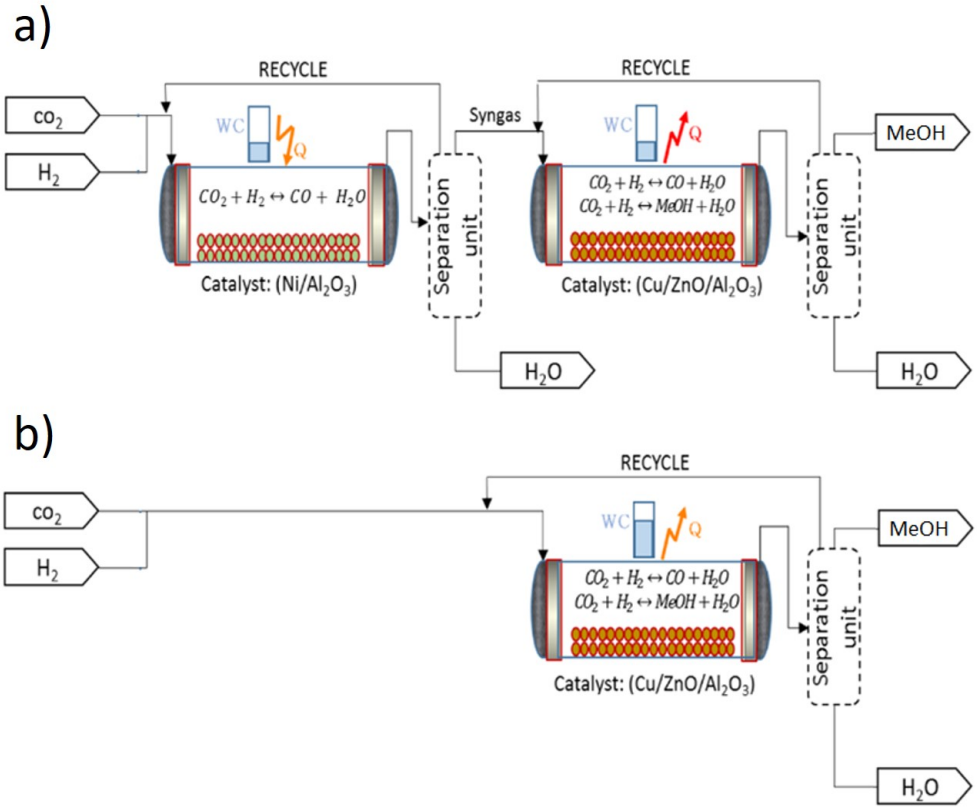

Figure I.7: Processes for CO_2 hydrogenation to methanol. a) indirect methanol synthesis (CAMERE process), b) direct methanol synthesis. Adapted from [13].

These different strategies imply different technological choices. Conventional fixed-bed catalytic reactors perform better in the indirect CAMERE route as the water generated is removed by the WGS reaction [20, 13]. The direct pathway makes it possible to eliminate the endothermic syngas generation step through the RWGS reaction at the expense of aggravated constraints with regard to the water generated in the reactors [13]. Nevertheless, innovative reactors that can separate water from the reaction mixture aim to improve the direct route:

1. Membrane reactors, described in detail below,
2. Three-phase reactors condensing methanol and water during reaction [4],
3. Reactors using sorbents to capture water [17].

In the context of e-methanol synthesis, none of the innovative reactors described above have yet to see commercial applications, as they have only been discussed in academic literature. Consequently, no commercial processes utilizing these technologies currently exist, and their economic and environmental viability at the process scale remains an active area of research [25, 10, 1].

I.1.3.3 Principle of the catalytic membrane reactor and application to the synthesis of methanol from CO_2

Membrane catalytic reactors are reactors equipped with one or more membranes that (1) allow the separation of at least one of the reaction products to shift the thermodynamic equilibrium of a reaction (extracting function) to improve the conversion and selectivity of the reaction [6], (2) to control the addition of a reagent to limit side reactions and improve the selectivity of the reaction (distributing function). For methanol synthesis, the membrane reactor will enable a chemical reaction to be carried out while simultaneously separating compounds from the reaction mixture. This type of technology is therefore in line with the philosophy of process intensification, by combining two unitary operations in a single step. In the case of the catalytic hydrogenation of CO_2 to methanol, the membrane's extractant function will be of great interest in removing water from the reaction medium in order to shift the reaction equilibrium (Le Chatelier principle). As a result, conversion to CO_2 and yields of methanol can be improved with this technology. Moreover, the life of the water-sensitive catalyst can potentially be extended with the membrane reactor.

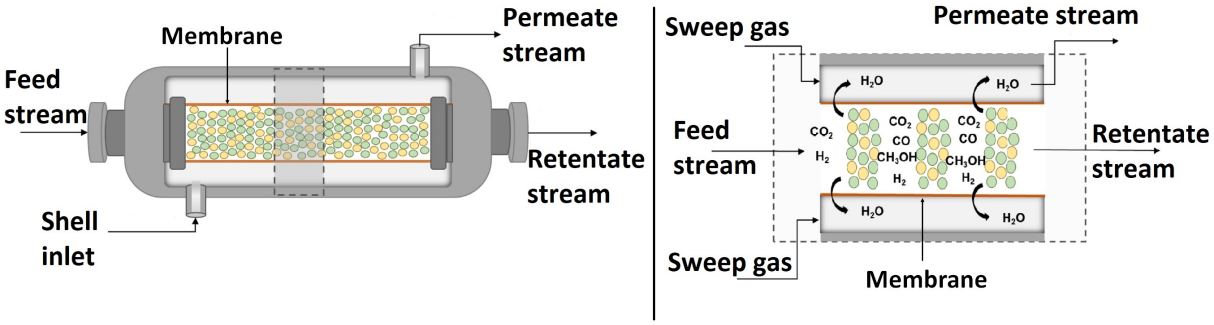

Figure I.8: Example of a membrane reactor applied to methanol synthesis. Adapted from [15].

In the example shown on Figure I.8 of a catalytic membrane reactor applied to methanol synthesis, the reactor comprises two coaxial tubes. The inner tube, inside which a fixed bed of catalyst is deposited, corresponds to the membrane. The outer tube is the reactor shell. A sweep gas (inert or reagent-laden) circulates between the two tubes, to remove the extracted compound that has passed through the membrane. The choice of membrane material depends on the process conditions (induced by the choice of catalyst and reaction) and the nature/size of the molecules to be extracted.

I.2 Research Objectives

Methanol synthesis reactions are currently carried out under harsh conditions (250°C-300°C, $>$ 20 bar), in order to ensure sufficient activity of usual copper-based catalysts. However, the separation of gases (H_2O, CO_2, CO, H_2, MeOH) at these conditions is a technical challenge regarding membrane development [19]. Thus, the design of a catalytic membrane reactor suitable for methanol synthesis must converge research: towards a high-performance membrane at high temperatures ($>$ 250°C) and towards catalysts active at low temperatures ($<$ 250°C).

Additionally, as aforementioned in Section I.1.3.2, no commercial process built around a

membrane reactor for methanol synthesis yet exists. A significant challenge in scaling this technology is the gap between materials science research and process simulation studies. Consequently, available literature on membrane separation performances often lacks comprehensive data, requiring extrapolation beyond experimental ranges for reactor simulations at reaction conditions [15].

Thus, this PhD work aims to investigate the potential of membrane reactors compared to conventional fixed-bed reactors for methanol synthesis from CO_2 by bridging gaps between each field. To do so, a comprehensive approach that links material development, catalyst design, and process-scale analysis is proposed.

Therefore, in Chapter II, preparation methods to produce high quality zeolite membrane that can selectively separate water at high temperatures will be investigated. The most effective synthesized membranes will undergo extensive testing to establish permeation laws under reaction conditions, enabling accurate modeling of membrane behavior.

In Chapter III, potential catalysts active in low-temperature methanol synthesis, where membrane efficiency is highest, will be investigated. Additionally, alternative synthesis routes enabling catalyst synthesis directly on the membrane will be explored to assess potential synergies between the catalyst and membrane.

Chapter IV will compare membrane reactors to conventional fixed-bed reactors at the process scale through process optimization. By minimizing an energy cost function, this chapter aims to quantify the maximum benefits of membrane reactors over conventional ones and to determine optimal operating conditions for both reactor types.

Glossary (Chapter I)

Acronyms

CAMERE CArbon dioxide hydrogenation to **ME**thanol via **RE**verse water gas shift reaction

CCUS Carbon Capture, Utilization, and Storage

COR Carbon Oxides Ratio (or CO_2/CO_x)

DME Dimethyl ether

FTS Fischer-Tropsch synthesis

GHG Greenhouse Gas

MMSA Methanol Market Services Asia

MTBE Methyl Tert-Butyl Ether

MTG Methanol-to-Gasoline

RWGS Reverse Water-Gas Shift reaction

WGS Water-Gas Shift reaction

Roman letters

S Stoichiometric ratio for methanol synthesis

x_i Molar fraction of species i (-)

References

[1] Akhil Arora et al. "Optimal Methanol Production via Sorption-Enhanced Reaction Process". In: *Industrial & Engineering Chemistry Research* 57.42 (Oct. 24, 2018). Publisher: American Chemical Society, pp. 14143–14161. ISSN: 0888-5885. DOI: 10.1021/acs.iecr.8b02543.

[2] Filippo Bisotti et al. "Century of Technology Trends in Methanol Synthesis: Any Need for Kinetics Refitting?" en. In: *Industrial & Engineering Chemistry Research* 60.44 (Nov. 10, 2021), pp. 16032–16053. ISSN: 0888-5885, 1520-5045. DOI: 10.1021/acs.iecr.1c02877.

[3] Trinath Biswal et al. "Conversion of carbon dioxide to methanol: A comprehensive review". en. In: *Chemosphere* 298 (July 2022), p. 134299. ISSN: 00456535. DOI: 10.1016/j.chemosphere.2022.134299.

[4] M.J. Bos and D.W.F. Brilman. "A novel condensation reactor for efficient CO_2 to methanol conversion for storage of renewable electric energy". en. In: *Chemical Engineering Journal* 278 (Oct. 2015), pp. 527–532. ISSN: 13858947. DOI: 10.1016/j.cej.2014.10.059.

[5] Giulia Bozzano and Flavio Manenti. "Efficient methanol synthesis: Perspectives, technologies and optimization strategies". en. In: *Progress in Energy and Combustion Science* 56 (Sept. 2016), pp. 71–105. ISSN: 03601285. DOI: 10.1016/j.pecs.2016.06.001.

[6] J Caro. "Basic Aspects of Membrane Reactors". en. In: ().

[7] *European Parliament backs higher green jet fuel targets to decarbonise aviation.* 2022. [Online; accessed 2024-08-05]. URL: https://www.euractiv.com/section/aviation/news/european-parliament-backs-higher-green-jet-fuel-targets-to-decarbonise-aviation/.

[8] Shanshan Dang et al. "A review of research progress on heterogeneous catalysts for methanol synthesis from carbon dioxide hydrogenation". en. In: *Catalysis Today* 330 (June 2019), pp. 61–75. ISSN: 09205861. DOI: 10.1016/j.cattod.2018.04.021.

[9] Marcello De Falco and Mauro Capocelli. "Direct Synthesis of Methanol and Dimethyl Ether From a CO_2-Rich Feedstock: Thermodynamic Analysis and Selective Membrane Application". en. In: *Methanol*. DOI: 10.1016/B978-0-444-63903-5.00005-4. Elsevier, 2018, pp. 113–128. ISBN: 978-0-444-63903-5.

[10] Vincent Dieterich et al. "Performance Requirements of Membrane Reactors for the Application in Renewable Methanol Synthesis: A Techno-Economic Assessment". In: *Advanced Sustainable Systems* 6.12 (Dec. 2022), p. 2200254. ISSN: 2366-7486, 2366-7486. DOI: 10.1002/adsu.202200254.

[11] Aseem Dubey and Akhilesh Arora. "Advancements in carbon capture technologies: A review". en. In: *Journal of Cleaner Production* 373 (Nov. 2022), p. 133932. ISSN: 09596526. DOI: 10.1016/j.jclepro.2022.133932.

[12] Jürgen Haid and Ulrich Koss. "Lurgi's Mega-Methanol technology opens the door for a new era in down-stream applications". en. In: *Studies in Surface Science and Catalysis*. Vol. 136. DOI: 10.1016/S0167-2991(01)80336-0. Elsevier, 2001, pp. 399–404. ISBN: 978-0-444-50544-6.

[13] Homa Hamedi and Torsten Brinkmann. "Valorization of CO_2 to DME using a membrane reactor: A theoretical comparative assessment from the equipment to flowsheet level". en. In: *Chemical Engineering Journal Advances* 10 (May 2022), p. 100249. ISSN: 26668211. DOI: 10.1016/j.ceja.2022.100249.

[14] *Chevron - Alternative Jet Fuels*. 2006. [Online; accessed 2024-08-05]. URL: https://skybrary.aero/sites/default/files/bookshelf/2479.pdf.

[15] Igor G.I. Iwakiri, Carlos V. Miguel, and Luis M. Madeira. "Modeling and simulation of a steam-selective membrane reactor for power-to-methanol". en. In: *Computers & Chemical Engineering* 156 (Jan. 2022), p. 107555. ISSN: 00981354. DOI: 10.1016/j.compchemeng.2021.107555.

[16] Xiao Jiang et al. "Recent Advances in Carbon Dioxide Hydrogenation to Methanol via Heterogeneous Catalysis". en. In: *Chemical Reviews* (Feb. 12, 2020), acs.chemrev.9b00723. ISSN: 0009-2665, 1520-6890. DOI: 10.1021/acs.chemrev.9b00723.

[17] Jasper van Kampen et al. "Steam separation enhanced reactions: Review and outlook". en. In: *Chemical Engineering Journal* 374 (Oct. 2019), pp. 1286–1303. ISSN: 13858947. DOI: 10.1016/j.cej.2019.06.031.

[18] Avishai Lerner et al. "Life cycle analysis (LCA) of low emission methanol and di-methyl ether (DME) derived from natural gas". en. In: *Fuel* 220 (May 2018), pp. 871–878. ISSN: 00162361. DOI: 10.1016/j.fuel.2018.02.066.

[19] Zhan Li et al. "High Temperature Water Permeable Membrane Reactors for CO_2 Utilization". en. In: *Chemical Engineering Journal* 420 (Sept. 2021), p. 129834. ISSN: 13858947. DOI: 10.1016/j.cej.2021.129834.

[20] Siphesihle Mbatha et al. "Power-to-methanol process: a review of electrolysis, methanol catalysts, kinetics, reactor designs and modelling, process integration, optimisation, and techno-economics". en. In: *Sustainable Energy & Fuels* 5.14 (2021), pp. 3490–3569. ISSN: 2398-4902. DOI: 10.1039/D1SE00635E.

[21] *Methanol Institute*. [Online; accessed 2024-08-05]. URL: https://www.methanol.org/.

[22] Florian Nestler et al. "Methanol Synthesis - Industrial Challenges within a Changing Raw Material Landscape". en. In: *Chemie Ingenieur Technik* 90.10 (Oct. 2018), pp. 1409–1418. ISSN: 0009286X. DOI: 10.1002/cite.201800026.

[23] George A. Olah, Alain Goeppert, and G. K. Surya Prakash. *Beyond Oil and Gas: The Methanol Economy, 3rd Edition*. Wiley-VCH Verlag GmbH & Co. KGaA. 2018. ISBN: 978-3-527-80567-9.

[24] Jörg Ott et al. "Methanol". en. In: *Ullmann's Encyclopedia of Industrial Chemistry*. DOI: 10.1002/14356007.a16_465.pub3. Weinheim, Germany: Wiley-VCH Verlag GmbH & Co. KGaA, Oct. 15, 2012. ISBN: 978-3-527-30673-2.

[25] Serena Poto et al. “Techno-economic assessment of the one-step CO_2 conversion to dimethyl ether in a membrane-assisted process”. In: *Journal of CO_2 Utilization* 69 (Mar. 2023), p. 102419. ISSN: 22129820. DOI: 10.1016/j.jcou.2023.102419.

[26] Fereshteh Samimi, Dornaz Karimipourfard, and Mohammad Reza Rahimpour. “Green methanol synthesis process from carbon dioxide via reverse water gas shift reaction in a membrane reactor”. en. In: *Chemical Engineering Research and Design* 140 (Dec. 2018), pp. 44–67. ISSN: 02638762. DOI: 10.1016/j.cherd.2018.10.001.

[27] Poonam Sharma et al. “Recent advances in hydrogenation of CO_2 into hydrocarbons *via* methanol intermediate over heterogeneous catalysts”. en. In: *Catalysis Science & Technology* 11.5 (2021), pp. 1665–1697. ISSN: 2044-4753, 2044-4761. DOI: 10.1039/D0CY01913E.

[28] *We’re Gonna Need a Greener Boat*. [Online; accessed 2024-08-05]. URL: https://time.com/6189877/maritime-shipping-green-energy/.

Chapter II

Membranes for high temperature water separation from $H_2/CO_2/CO/MeOH$

The separation of gases (H_2O, H_2, CO_2, ...) at methanol synthesis reaction conditions (200-300°C; 20-50 bar) is not trivial. This chapter starts with a literature review on the membrane materials able to selectively separate water from gases during methanol synthesis (Section II.1). Next, the recent developments in the synthesis of defect-free LTA and SOD zeolites are explored to develop synthesis methods (Section II.2). Finally, permeation studies under methanol synthesis reaction conditions are carried out to assess the presence of defects in the synthesized membrane and to gather comprehensive data on its performance, for more accurate membrane-assisted process simulations. (Section II.3).

II.1 Membrane materials to separate water from a high-temperature gas-mixture

This section explores materials capable of selectively separating water from the reaction mixture under these synthesis conditions. This section will then focus on zeolite-based mineral membranes, which appear to be best suited to solve this problem. The effect of the zeolite nature (structure/pore size, composition/hydrophilicity) will be discussed, before a brief look at the associated membrane synthesis methodologies. LTA and SOD membranes, more commonly described in the literature for the applications targeted in this paper, in particular for methanol synthesis, will finally be described in more detail.

II.1.1 Membranes for gas permeation / dehydration

Gas permeation is the separation of gases through a membrane. The principle and operation of membrane separation in the context of gas permeation will therefore first be described in this section.

II.1.1.1 Membranes: definition, porosity and performance criteria

II.1.1.1.a Definition

A membrane can be generally defined as a thin barrier, allowing the selective passage of substances between two media. The zone where the fluid retained by the membrane circulates is

called the "retentate", and the zone where the fluid that has passed through the membrane circulates is called the "permeate" (Figure II.1). Separation takes place under the action of a driving force, which, in the case of gas permeation, is a partial pressure gradient across the membrane [19]. The characteristics of a membrane (defined in more detail below) are related to: its porosity, selectivity, permeability and stability.

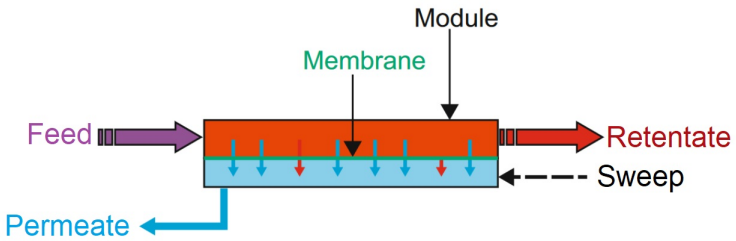

Figure II.1: Diagram illustrating crossflow filtration through a membrane. Translated from [19].

II.1.1.1.b Porosity scale

The porosity scale of a membrane is defined by the International Union of Pure and Applied Chemistry (IUPAC) classification according to the pore size of the medium. Microporosity corresponds to pore sizes of less than 2 nm, mesopore size is between 2 and 50 nm and macroporosity is defined for pore sizes greater than 50 nm [48, 16]. Some membranes, such as polymer membranes, have no pores. These membranes are called "dense".

In the case of methanol synthesis, the aim is to separate molecules in a gas (which kinetics diameters are around 2 to 5 Å (TableII.1)). Thus, the appropriate porosity scale is of the order of the size of the molecules present in the reaction mixture, i.e. of the order of the Angstrom (noted Å, equivalent to 0.1 nm). Therefore, membranes suitable for this operation must be either microporous or dense.

Table II.1: Comparisons between the pore size of the studied zeolites and the kinetic diameter of the molecules present during the synthesis of methanol from CO_2 [41, 58, 75].

Maximum zeolite pore size (Å)							Kinetic diameters (Å)				
SOD	CHA	LTA (NaA)	MFI	MOR	T	FAU	H_2O	H_2	CO_2	CO	MeOH
2.7	3.7	4.1	5.5	6.5	6.6	7.5	2.65	2.89	3.30	3.76	3.8

II.1.1.1.c Membrane performance criteria

The performance of a membrane is characterized by three criteria: (1) the permeance, corresponding to the membrane's ability to allow a certain quantity of matter to pass through it; (2) the selectivity, corresponding to the membrane's ability to separate two species contained in a mixture; and (3) the stability, corresponding to the invariability over time of the other two criteria under the imposed operating conditions.

The permeance (expressed in $mol.Pa^{-1}.m^{-2}.s^{-1}$), noted as Π_i is defined by the molar flux of the species across the membrane according to its surface area and the difference in partial

pressure of the species between the two sides of the membrane (Eq. II.1). The permeance can be normalized by the membrane thickness, to obtain the permeability (noted G_i and expressed in mol.m^{-1}.Pa^{-1}.s^{-1}) [63].

$$\Pi_i = \frac{F}{S\Delta P_i} \quad ; \quad G_i = \frac{\Pi_i}{e} \tag{II.1}$$

Membrane selectivity can be expressed in two ways (Eq. II.2). The permselectivity, noted as α_{AB}, corresponds to the ratio of the permeances of two species, A and B. The separation factor, noted α^*_{AB}, is defined according to the molar fractions of the two species A and B in the feed and in the permeate. The respective values of permselectivity and separation factor can differ whether the gas permeation experiment was done with a single gas or a gaseous mixture. For example, during gas permeation studies with mixtures, preferential adsorption of a molecule can block the pore access to another and thus lead to a discrepancy with experiments conducted with a single gas [6, 17].

$$\alpha_{AB} = \frac{\Pi_A}{\Pi_B} \; ; \; \alpha^*_{AB} = \frac{(x_A/x_B)_{Permeate}}{(x_A/x_B)_{Feed}} \tag{II.2}$$

No single parameter is conventionally used to qualify membrane stability. Measurements of prolonged membrane operation at operating conditions provide information on this characteristic.

II.1.1.1.d Gas transport mechanisms in microporous membranes

The way in which molecules are transported depends on the porosity of the membrane. In this subsection, the various transport and separation mechanisms in gas permeation membranes are represented in Figure II.2.

If the diameter of the pores is greater than the mean free path (the average distance a molecule travels before colliding with another) of the gaseous molecules present in the medium, transport takes place through viscous flow [19]. This convective mode of transport is non-selective and, at the molecular scale, collisions between molecules are predominant [19].

If the diameter of the pores is smaller than the mean free path of the molecules but greater than their kinetic diameters, transport takes place mainly by Knudsen diffusion [19, 30]. In this mode of transport, molecules move according to successive collisions with the pore walls. The selectivity of two gases in this mode of transport is proportional to the square root of the molar mass ratio and therefore generally remains low [63, 19].

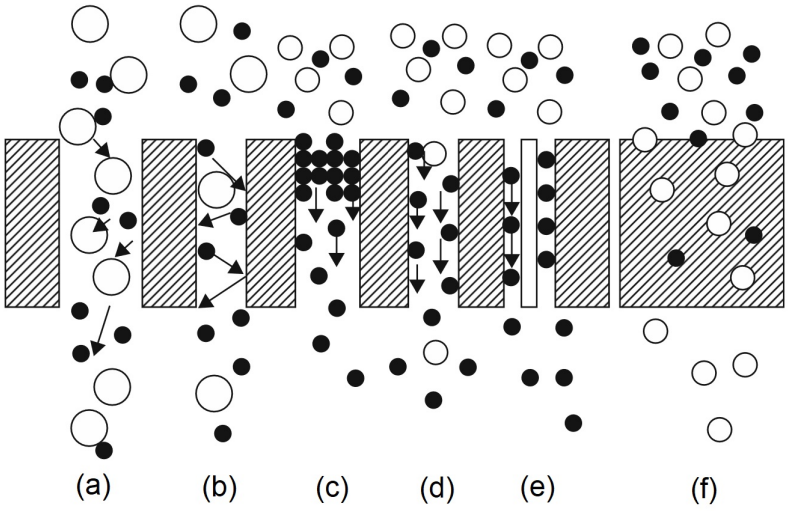

Figure II.2: The different scales of transport in the membrane in gas permeation. a) viscous flow, b) Knudsen diffusion, c) capillary condensation, d) configurational diffusion, e) molecular sieving, f) solution-diffusion. Adapted and translated from [19].

When the pore size is of the same order of magnitude as the diameter of the molecules to be separated, the mode of transport through the membrane is that of configurational diffusion [16]. In this mechanism, the molecules adsorb onto the membrane pore wall, and diffuse along it [16, 14]. Separation according to this mechanism is guided by the difference between the diffusion kinetics of each molecule in the pore (resulting from different affinities between the molecules, the nature of the pore wall and the size of the molecule (lighter molecules diffuse faster)) [6, 16, 14].

Transport of a molecule through micropores can be denied due to molecular sieving. In this case, the larger kinetic diameter of a molecule induces a steric hindrance too large for it to diffuse in the smaller micropore [6, 16, 14].

Capillary condensation is another phenomenon that can happen if proper conditions are united. These conditions depend on the vapor pressure, the saturated vapor pressure, the pore diameter, the surface tension and the temperature all linked through the Kelvin equation (Eq. II.3). This phenomenon can have a significant impact on the overall permeability of the membrane [19]. However, the significance of this mechanism decreases with rising temperatures (Eq. II.3).

$$\ln\left(\frac{P_i}{P^{sat}}\right) = \frac{2\sigma_i v_i^l}{r_p RT} \tag{II.3}$$

In a dense membrane, the mode of transport is called "solution-diffusion". Through dense membranes, gases dissolve in the solid phase of the membrane and are then transported by diffusion [63]. This mode of transport is driven by a chemical potential difference on either side of the membrane [63]. The selectivity of these membranes derives from the solubility of the gas in the membrane and its diffusion rate within the material [63].

II.1.1.2 Membranes for water gas permeation: choice of material

During the hydrogenation of CO_2 to methanol, the membrane must separate the water from the other reactants and products (H_2, CO_2, CO, MeOH) at the reaction conditions. Dense polymer membranes and microporous inorganic membranes (either amorphous ceramics (TiO_2, SiO_2, Al_2O_3 or SiO_2/Al_2O_3), or zeolites) have been studied for this purpose [32, 56, 3].

The first membrane reactor studied for methanol synthesis by Struis *et al.* [62] used a dense Nafion polymer membrane. Since then, polymer membranes have been discarded for methanol synthesis, due to performance degrading too quickly between 50 and 200°C (permeances H_2O varying from $4{\cdot}10^{-7}$ to $4{\cdot}10^{-8}$ mol.Pa^{-1}.m^{-2}.s^{-1} ; separation factor H_2O/H_2 varying from 150 to 18) [3, 62].

Since then, the use of mineral membranes in membrane reactors has dominated the literature for this application. These membranes need to be very thin, ideally with a thickness of less than ten micrometers. As pore sizes are small (less than 1 nm), permeances are reduced. Reducing the thickness of these membranes improves the flow through the filtering media. So, to provide mechanical strength to these thin films, they need to be deposited on a macroporous support, thicker but with larger pore sizes so as not to slow down the flow.

Among inorganic porous membranes, amorphous aluminosilicate membranes have demonstrated very modest selectivities in methanol synthesis (Permselectivities $H_2O/H_2 < 10$) [32, 56, 3]. Moreover, degradation of these materials has been observed above 150°C [56, 3]. Microporous silica membranes have been widely investigated for gas permeation [16]. However, their sensitivity towards steam leading to pore closure [16] makes them an unlikely candidate for methanol synthesis. Thus, zeolite (cristaline aluminosilicate) membranes appear to be the most suitable for separating water in methanol synthesis. Indeed, they outperform other materials in terms of permeance and selectivity at reaction conditions. Recent literature reports zeolite membranes with H_2O/H_2 separation factors of the order of 100 and permeances of around 10^{-7} mol.Pa^{-1}.m^{-2}.s^{-1} (Table II.2). Zeolite membranes have been selected for their high performance and will be described in greater detail in the following sub-section.

II.1.2 Focus on zeolite membranes

This sub-section focuses on zeolite membranes. First, the chemical and physical characteristics of zeolites will be described. Next, the mechanisms of gas transport and separation within these materials will be discussed. Finally, state-of-the-art synthesis techniques for producing high-quality zeolite membranes will be reviewed.

II.1.2.1 Definition and characteristics of zeolites

Zeolites are hydrated aluminosilicates (presence of adsorbed water molecules in their structure), microporous and crystalline. Due to their structure, zeolites have properties in adsorption, ion exchange, catalysis and molecular separation (sieving), among others.

The solid lattice of zeolites, with the chemical formula $M_xAl_xSiO_{1-x}O_2 \cdot yH_2O$ (with x between 0 and 1), is made up of TO_4 tetrahedra (with T = Al, Si, or other) connected by the oxygen atoms present on the tetrahedron vertices. In reality, the value of x in the chemical

formula cannot exceed 0.5, and the minimum Si/Al ratio is 1. According to Löwenstein's rule, it is impossible to link two AlO_4 tetrahedra [46]. On the other hand, in the solid lattice, each "T" cation is associated with two oxygen anions O_2. For Si^{4+}, the charges of the cations and anions cancel each other out, and the tetrahedron is electrically neutral. For Al^{3+}, the charges are not balanced, and the tetrahedron carries an overall negative charge. To ensure an electrically neutral zeolite structure, the charge defect is compensated by the presence of other cations generally localized in the zeolite micropores (so-called charge-compensating or exchangeable cations) [50].

The structures formed by the aluminosilicate solid network are various. In fact, there are currently 255 different types of structure (a figure that is constantly changing). The nomenclature of these structures, consisting of three letters, is given by the International Zeolite Association (IZA) and is not necessarily based on the crystalline or chemical form of the structure. A structure may, for example, bear the name of the company that patented it, or of the natural rock in which the structure was observed. Of all the possible structures, the most notable are LTA, Chabazite (CHA), Mordenite (MOR), FAU and Mobil Five (MFI).

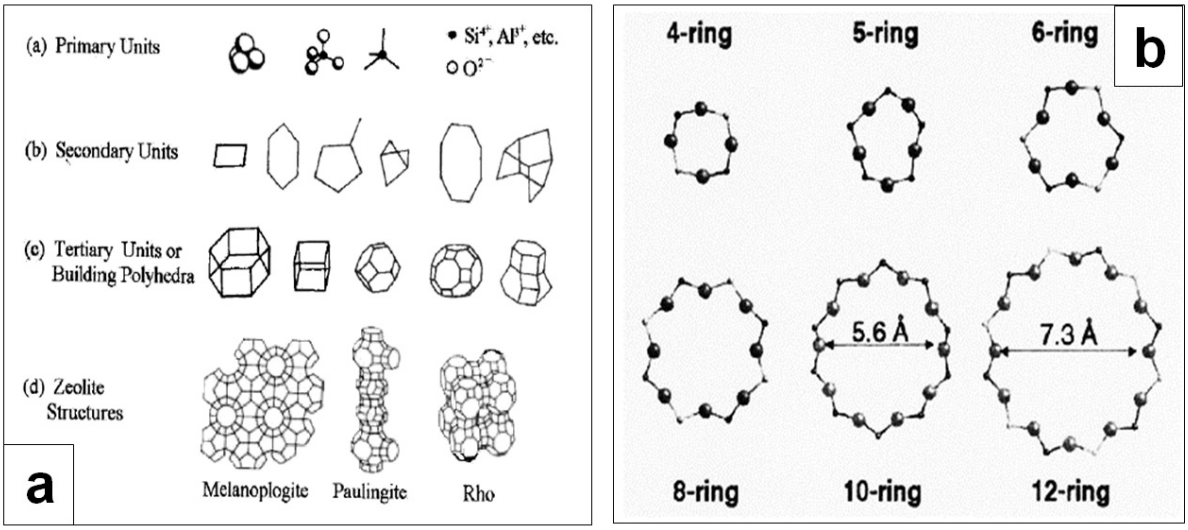

Figure II.3: Classification scheme (a) of the different scales of zeolite structures and (b) of the different ring sizes according to the number of involved TO_4 tetrahedra [50].

Going into more detail, zeolite networks are made up of finer building units, classified according to different scales (Figure II.3a):

1. Primary Building Units (PBUs) correspond to the TO_4 tetrahedron.
2. Secondary Building Units (SBUs) are assemblies of PBUs in simple geometric shapes (Figure II.3 a: the vertices represent a Si, Al or other metal cation; the edges represent a chain of T-O-T atoms).
3. CBUs are the result of connections between SBUs.
4. The last scale corresponds to the three-dimensional structures formed by the assemblies of CBUs and forming the microporous solid network.

The properties of zeolites mainly derive from their crystalline structure induced by the assembly of the building units, through their chemical composition and the size of the micropores formed. Indeed, pore size is directly related to the bonds between CBUs and therefore to the size of the rings that will form. The size of a ring is defined by the number of tetrahedrons making it up. A ring comprising n tetrahedra is called an "n-ring" (Figure II.3 b: the rings shown are circular, but deformed rings can be obtained, as in MFI zeolites). Rings can also join to form complex polyhedra such as cages and prisms [50]. These cages are defined as polyhedra whose rings constitute access windows (the size of molecules that can diffuse into the structure is defined by the size of these windows). In this way, these cages can enclose ions or molecules large enough to prevent them from escaping.

II.1.2.2 Zeolite membranes for gas permeation

The zeolites most commonly used in gas permeation membrane separation processes have pore diameters of the order of 0.5 nm. The main transport mechanisms within zeolite membranes are configurational diffusion and molecular sieving.

II.1.2.2.a Separation by molecular sieving

The molecular sieving mechanism only works if the molecules to be separated have distinct kinetic diameters, some larger than the pore diameter (molecules end up in the retentate stream) and others smaller (molecules pass through the membrane and end up in the permeate stream). For each application, the kinetic diameters of the molecules to be separated are compared with the pore sizes of the zeolites. In the case of methanol synthesis, the water molecule (Ø = 2.65 Å) has to be separated from the rest of the reaction mixture (H_2, CO_2, CO, MeOH) whose molecule sizes, although slightly larger, are very close to that of water (Table II.1). Between LTA and SOD zeolites, only the SOD structure has a pore size fine enough to allow only the water molecule to pass through. Nevertheless, the small pore size of SOD zeolite (very close to the size of water molecules) results in low permeances and therefore limited water flux through the membrane [41].

II.1.2.2.b Separation guided by diffusion and adsorption of molecules in pores

Molecular sieving is not the only mechanism for separating zeolites. Surface diffusion, based on the zeolite's affinity for certain molecules, also plays an important role. This mechanism relies on interactions between molecules and pore walls, generating different diffusion velocities for each molecule [6], [17]. In addition, the adsorption of molecules to the zeolite can influence this mechanism. A molecule adsorbed preferentially on the zeolite wall can block access to adsorption for other molecules [6, 8]. For example, in the case of a hydrophilic membrane, the affinity between zeolite and water can lead to the filling of pores with water molecules, thus blocking access to hydrogen or CO_2 [32]. In this way, zeolites can still separate molecules despite their pore sizes, which are sometimes larger than the sizes of the molecules to be separated. These mechanisms are influenced by the composition of the material, its hydrophilicity/phobicity (Si/Al ratio and nature of the charge-compensating cation), the polarity of the molecule and also by temperature. Thus, water permeance through a hydrophilic zeolite membrane generally

increases with temperature, while the separation mechanism becomes less and less selective due to the exothermic nature of molecule adsorption to the zeolite material [41, 20].

To illustrate this effect, Sawamura *et al.* [58] observed, by exchanging the H^+ ions of an H-ZSM-5 zeolite with Na^+ cations, an increase in the H_2O/H_2 permselectivity from 1 to 6 at 250°C, due to the increased hydrophilicity of their zeolite membrane and thus its ability to adsorb water molecules. On the other hand, Li *et al.* [36] provided evidence of the influence of Na^+ cations on the hydrophilicity of LTA zeolites by Density Functional Theory (DFT). The presence of Na^+ ions generates a higher potential barrier for apolar molecules than for polar molecules. The Si/Al ratio of a zeolite influences the quantity of these charge-compensating cations in the zeolite and therefore its membrane hydrophilicity. Indeed, by increasing the quantity of Al^{3+} ions in the structure, the quantity of cations is also increased to ensure the electrical neutrality of the structure. To improve the hydrophilicity of a zeolite, it is therefore preferable to use an alumina-rich zeolite that can accommodate as many hydrophilic cations as possible. This is why the hydrophilicity of a zeolite is inversely proportional to its Si/Al ratio [41, 57] (Figure II.4).

However, increasing the Si/Al ratio reduces the hydrothermal stability of the zeolite membrane. Indeed, hydrophilic zeolites tend to deal with dealumination (loss of Al^{3+} ions) in the presence of large amounts of water at high temperatures [41, 42]. For example, the study by Li *et al.* [39] shows degradation of a LTA membrane after 4 h for a solution composed of 50 wt.% of water from 70°C, while the study by Liu *et al.* [42] shows stability of their LTA membrane for a gas also composed of 50 wt.% of water at 250°C. The hypothesis of Liu *et al.* [42] is that the liquid state of water in the study by Li *et al.* [39] causes membrane erosion. Long term stability of zeolite membrane under membrane reactor conditions (>200°C, >20 bar) are nevertheless often absent from the literature.

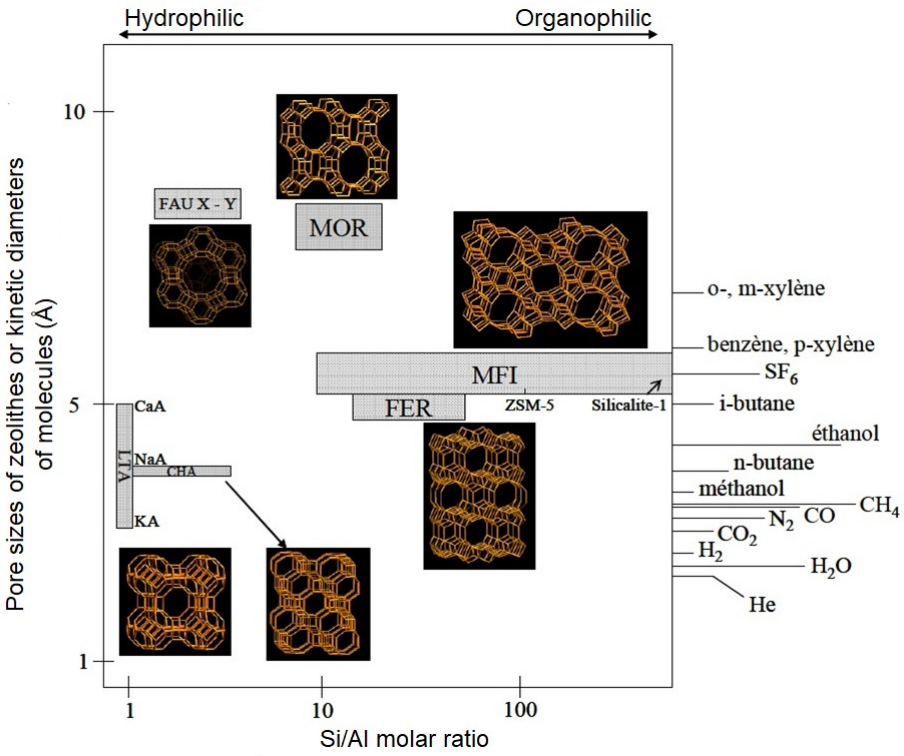

Figure II.4: Si/Al ratio and comparison between pore diameters and common molecule diameters for different zeolite structures [57].

II.1.2.2.c Influence of inter-crystal defects

Molecule transport by surface diffusion takes place in the micro-channels of zeolite structures. However, the thin film of zeolite forming the membrane is rarely perfect (presence of defects between crystals due, for example, to crystal misalignment). The inter-crystal meso/macro-pores formed during synthesis, thus generate a space where molecules can circulate more freely than in the zeolite micropores, with higher permeance but at the expense of membrane selectivity [6]. In these inter-crystal pores and during gas permeation, molecules are transported by Knudsen diffusion (Figure II.5). Thus, a membrane is considered to be of high quality if no inter-crystal defects are observed.

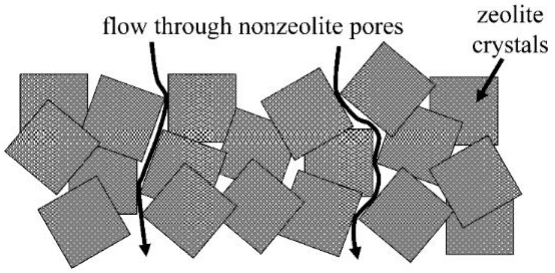

Figure II.5: Intercrystalline holes in a zeolite membrane [6].

II.1.2.3 Main synthesis routes for zeolite membranes

The synthesis of zeolite membranes is mainly based on hydrothermal chemical reactions (carried out in a closed autoclave or reaction vessel at autogenous pressure, in an aqueous environment). The zeolite membrane is then deposited on a porous support from a solution (or gel) generally composed of water, a source of silica, a source of aluminum, a mineralizing agent (often NaOH) and sometimes organic additives ("Template" or Structure Directing Agent (SDA)) [6]. The nature and pre-treatment of the supports, the synthesis operating conditions (heating methods, temperature, times, gel composition, nature of the precursors) will influence the nucleation/growth of the zeolite films and their crystallization in a defined structure to obtain membranes of varying quality (thickness, defects, pore size, etc.).

II.1.2.3.a Choice of materials

To synthesize zeolites, the choice of available precursors is vast. Common silica sources include colloidal silica (e.g. LUDOX), fumed silica (e.g. Aerosil) and tetraethyl orthosilicate (TEOS). Common sources of aluminum are sodium aluminate, aluminum isopropoxide and aluminum hydroxide. Each type of precursor reacts differently under hydrothermal conditions [49]. Furthermore, the operating conditions (concentration, temperature and duration) must be systematically adapted to obtain a precise zeolite structure, a specific crystal morphology and, above all, an adequate membrane quality. Moreover, the substrate has a major influence on zeolite membrane synthesis [13]. There is a wealth of literature on the synthesis of zeolite powders and membranes, with each team and each study highlighting specific operating conditions. Numerous reviews on the subject continue to be published, providing a picture of the effects of different parameters on the characteristics of synthesized zeolites [14, 8, 13, 72, 40, 7, 5, 18, 47, 65, 67].

The synthesis of the zeolite layer is also impacted by the nature of the support used. Indeed, one of the key parameters in zeolite membrane synthesis is the adhesion of the zeolite crystals to the support. Support materials with a greater affinity for zeolites will be better suited to synthesis methods. Alumina is the most common support for membrane zeolite. The adhesion of zeolite to these supports is very good, because the chemical composition of these supports is close to that of zeolite [10, 45]. However, these supports are expensive to produce, accounting for around 70% of the membrane's final cost [9]. A great deal of research is currently underway to reduce the cost of these ceramic supports. The use of macroporous alumina tubes [37, 69, 68] (pores greater than 1 µm) and the manufacture of supports from natural clay are part of this approach [10]. Alternative supports have been evaluated in the literature such as sintered stainless steel [45, 44, 25, 26, 22], mullite and silica.

II.1.2.3.b Hydrothermal synthesis by primary or secondary growth

Conventional synthesis takes place in a hermetically sealed Teflon-coated hydrothermal reaction vessel, where the support is brought into contact with an alumino-silicate gel. The heating of the solution within the hydrothermal reaction vessel is an important parameter for controlling membrane synthesis. Conventional industrial reactors use a double jacket to deliver heat to

the reaction mixture. In this method, heat is diffused from the wall to the core of the reaction mixture with a certain inertia. An alternative is to use microwaves to (1) heat the solution more efficiently and thus considerably reduce synthesis times, (2) achieve volumetric heating to avoid diffusion phenomena, (3) selectively heat the reagents, due to the unequal interaction of microwaves with the different reagents [38].

Two routes can be distinguished for conventional hydrothermal synthesis: the *in-situ* route (primary growth) and the *ex-situ* route (secondary growth) (Figure II.6).

For the *in-situ* route, zeolite nuclei are formed directly on the support in the reaction vessel, and the crystals (the membrane) grow from these nuclei. Nucleation/growth is achieved in a single step, so *in-situ* hydrothermal synthesis is fairly straightforward to implement. However, controlling membrane growth is complicated because it is highly sensitive to operating conditions [41]. In addition, this method often suffers from reproducibility problems, due to the nucleation of germs and their simultaneous growth on the membrane, which are highly dependent on the microscopic and chemical qualities of the support [40, 1]. The best results for defect-free membrane synthesis using this method are obtained after treating the support with a functional group such as APTES. The chemical ligand then provides anchor points on the support for the zeolite nuclei [29]. Another strategy is to synthesize a thin layer of homogeneous porous ceramic (such as TiO_2) on rough substrates or substrates with low chemical affinity for zeolites, in order to promote attachment of zeolite nuclei [57, 40].

For the *ex-situ* route, nucleation is decoupled from growth. Zeolite seeds are first synthesized and then used to seed a support. Growth of the crystals, and hence of the membrane, takes place in a second stage, during hydrothermal synthesis. This is currently the most commonly used method for synthesizing zeolite membranes. This method avoids the difficult control of the nucleation stage to only focus on membrane growth during hydrothermal synthesis [57, 40, 1]. The result is generally high-quality zeolite membranes with improved reproducibility. The main difficulty lies in ensuring the correct distribution of seeds on the support, so as not to create defects in the membrane during the growth stage.

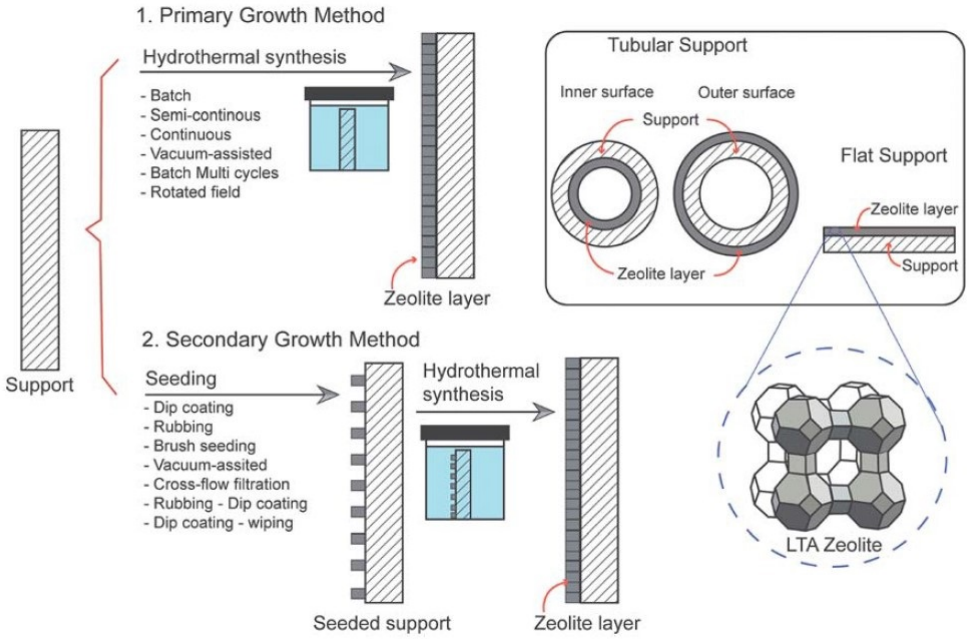

Figure II.6: Hydrothermal synthesis applied to LTA zeolite [72].

Different methods, detailed in Figure II.6 have been implemented to deposit zeolite seeds on a membrane support. Most of these methods are based on manual deposition. They do not allow deposition inside small-diameter tubular supports, and are not reproducible enough for industrial synthesis purposes [40]. Dip-coating (dipping the support in a germ suspension) or cross-flow filtration (filtration under flow of a germ suspension) currently appear to be the most suitable methods. Alongside the development of new seed deposition methods, the use of nano-sized seed has also improved the quality of synthesized membranes [36, 72, 2]. Indeed, nanometric sizes (around 100 nm) enable a more homogeneous distribution of seeds on the support. In order to exploit macroporous supports, Li *et al.* [37] suggested using larger seeds, followed by finer seeds to promote homogeneous membrane growth.

However, the synthesis of these nanometric seeds is complicated and requires fine control of powder synthesis conditions. They can also be obtained by fine grinding of micronsized zeolite particles down to nanometric size [72]. In addition, the poor adhesion of the seeds to the support can subsequently lead to major defects in the membrane. Li *et al.* [36] anneal their substrate at 200°C after dip-coating in order to chemically bond the LTA seeds to the substrate. According to their study, this annealing step is responsible for the low presence of defects in their membrane. Chen *et al.* [11] and Li *et al.* [37] preheat the seed suspension at different temperatures according to the seed size to improve control of seed deposition on the support (seed layer thickness and coverage).

II.1.3 Zeolite membranes for methanol synthesis

Zeolite membranes were initially used for solvent dehydration by pervaporation (a membrane process with a liquid retentate and a gaseous permeate). However, the mild conditions in pervaporation (<100°C) make the selectivity of zeolite membranes less sensitive to the presence

of defects [6]. Thus, new protocols for synthesizing high-quality zeolite membranes tested above 200°C had to be developed in order to obtain high-performance zeolite membranes in a membrane reactor for methanol synthesis (the aim is to separate the water generated at high temperature (>200°C)). The zeolite membrane must therefore have good hydrophilicity (characterized by a low Si/Al ratio) and must not degrade during operation. To expand the range of zeolite membranes discussed in this section, membranes tested for DME synthesis, which operate under conditions similar to methanol synthesis, are also included in this literature review. Several types of zeolite have been used in methanol synthesis: LTA, SOD, Zeolite Socony Mobil-5 (ZSM-5), MOR, Linde type T (T) and CHA (Table II.2).

LTA membranes largely dominate the literature for methanol and DME synthesis and to date, only defect-free LTA membranes have shown concrete evidence in intensifying this reaction [41]. Numerous experimental examples of LTA zeolite membranes tested at reaction conditions (>200°C, >20 bar) are available in the literature (Table II.2). This structure shows high selectivities thanks to its excellent hydrophilicity (linked to its Si/Al ratio of 1) and high water permeances thanks to its moderate pore size (4.1Å for NaA). In addition, LTA zeolite was the first structure to be commercialized as a membrane and thus benefits from a very extensive bibliographic background [72]. Primary growth synthesis techniques [74] and secondary growth [36, 59] are available for the manufacture of high-performance LTA membranes.

Some examples of SOD membranes applied to methanol and DME synthesis can be found in the literature [34, 70]. These membranes have a finer pore size than LTA zeolite (2.7Å), enabling them to act as molecular sieves between water and the rest of the molecules, whereas molecules are separated mainly by surface diffusion in the case of LTA zeolite. In this sense, the selectivities of SOD membranes are theoretically higher than those of LTA membranes. However, the finer pore size induces lower permeances than for LTA membranes [41]. Despite this, the SOD membranes shown in Table II.2 still fail to match the selectivities of LTA membranes.

In their study, Raso *et al.* [55] compared MOR, T and CHA membranes with an LTA membrane for the separation of $H_2O/H_2/CO_2$ mixtures above 200°C. Their conclusions exclude MOR membranes because of their insufficient selectivity at reaction conditions (separation factors H_2O/H_2 <1) and T membranes because of their instability above 200°C (separation factor H_2/N_2 divided by around 200 after testing at 215°C). The selectivities of CHA membranes are also lower than those of LTA membranes (maximum H_2O/CO_2 separation factor of 3). Finally, Raso *et al.* [55] conclude that the LTA membrane largely outperforms MOR, T and CHA membranes for separating $H_2O/H_2/CO_2$ mixtures above 200°C. Among the various zeolite membranes reported in the literature, LTA and SOD zeolites are selected for their performances in terms of permeance and selective water separation above 200°C. The following sub-sections detail each type of zeolite with their specific features, structure and the synthesis techniques applied to these membranes.

Table II.2: Zeolite membranes tested above 200°C for water separation in methanol/DME synthesis.

Zeolite	**Support**	**Synthesis route**	**Thickness (µm)**	**Permeance H_2O ($mol.Pa^{-1}.m^{-2}.s^{-1}$)**	**Permselectivities (*separation factor)**			**Ref.**	**Date**
					H_2O/H_2	**H_2O/CO_2**	**H_2O/MeOH**		
LTA	α -Al_2O_3	*In-situ*	-	$\sim 10^{-7}$	-	-	-	[21]	2004
LTA	α-Al_2O_3	*In-situ*	3.5	-	-	-	-	[70]	2015
LTA	TiO_2 on stainless steel	*In-situ*	20	-	-	-	[22-5]* (at [150-250]°C)	[20]	2015
LTA	α-Al_2O_3	*Ex-situ*	-	[4-9] $\cdot 10^{-7}$ (at [200-260]°C)	[200-5]* (at [200-260]°C)	[700-15]* (at [200-260]°C)	-	[55, 23]	2018-2021
LTA	α-Al_2O_3	*Ex-situ*	2.9	$2.97 \cdot 10^{-7}$ (at 240°C)	0.18* (at 240°C)	-	-	[35]	2018
LTA	α-Al_2O_3	*Ex-situ*	3-4	[2.3-1.4] $\cdot 10^{-7}$ (at [200-250]°C)	>92 (at [200-250]°C)	>209 (at [200-250]°C)	>31 (at [200-250]°C)	[36]	2020
LTA (Si-rich)	α-Al_2O_3	*Ex-situ*	-	$1.5 \cdot 10^{-6}$ (at 200°C)	-	-	2000 (at 200°C)	[42, 59]	2021
LTA	α-Al_2O_3	*In-situ*	6	$1.1 \cdot 10^{-7}$ (at 260°C)	34.1 (at 260°C)	55.4 (at 260°C)	258.1 (at 260°C)	[74]	2021
LTA	α-Al_2O_3	*Ex-situ*	4	$4.8 \cdot 10^{-7}$ (at 260°C)	>10,000 (at 200°C)	>10,000 (at 200°C)	>300 (at 200°C)	[15]	2022
LTA	α-Al_2O_3	*Ex-situ*	4.36	$[8.6\text{-}5.5] \cdot 10^{-7}$ (at [200-300]°C)	[110,000-220,000] (at [200-300]°C)	[200,000-440,000] (at [200-300]°C)	[265-334] (at [200-300]°C)	[61]	2023
SOD	α-Al_2O_3	*In-Situ*	-	$6.59 \cdot 10^{-8}$ (at 200°C)	4.6* (at 200°C)	22.6* (at 200°C)	233* (at 200°C)	[70, 71]	2015
SOD	ZrO_2/TiO_2	*Ex-situ*	-	$1 \cdot 10^{-7}$ (at 200°C)	[2.8-1.4] (at [200-250]°C)	[11.7-4.8] (at [200-250]°C)	-	[34]	2017
ZSM-5	α-Al_2O_3	*Ex-situ*	2	$2.8 \cdot 10^{-7}$ (at 250°C)	22 (at 250°C)	-	-	[58]	2008
MOR	α-Al_2O_3	*Ex-situ*	1	-	0.7* (at 200°C)	2* (at 190°C)	-	[55]	2018
T	-	-	-	-	[11-2] (at [200-230]°C)	[11-5] (at [200-230]°C)	-	[55]	2018
CHA	α-Al_2O_3	*Ex-situ*	-	-	-	3 (at 210°C)	-	[55]	2018

II.1.3.1 LTA (Linde Type A)

II.1.3.1.a Structure and features

Linde Type A (LTA) zeolite (Figure II.7a) is characterized by the chemical formula $|Na_{12}(H_2O)_{27}|[Al_{12}Si_{12}O_{48}]_8$ corresponding to its hydrated form (the most common). In this form, LTA zeolite is called NaA, but the sodium ion may be substituted by another ion such as lithium (LiA), calcium (CaA) or potassium (KA) [31]. The three CBUs making up LTA zeolite are d4r, α-cage and β-cage (Figure II.7b). Charge-compensating cations are found in the α-cage and β-cage, they can exchange/diffuse through the pore network structured by the 8-rings of the β-cage. The size of these pores depends on the nature of the charge-compensating cation contained in the zeolite (3.0 Å for KA; 4.1 Å for NaA; 5.0 Å for CaA) [31]. Some examples in the literature name the different LTAs according to their pore size and not according to the cation hosted. Thus, zeolite KA is called 3A, zeolite NaA is called 4A and zeolite CaA is called 5A [31].

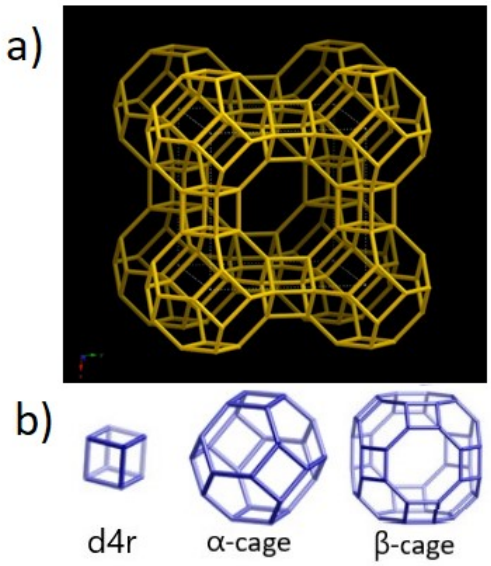

Figure II.7: a) Structure of LTA zeolite. b) CBUs making up the LTA structure [43].

II.1.3.1.b Synthesis techniques

The literature on the synthesis of high-quality LTA membranes is relatively extensive, and reliable synthesis methods are described for both primary and secondary growth.

LTA membrane synthesis conditions are generally mild, with hydrothermal synthesis temperatures generally around 60-80°C (Table II.3). The molar composition of the commonly used synthesis gel is 1 Al_2O_3 : 5 SiO_2 : 50 Na_2O : 1000 H_2O (Table II.3). For the synthesis of LTA membranes, conventional hydrothermal synthesis takes around 24 h (Table II.3), whereas microwave-assisted hydrothermal syntheses are much shorter, with reaction times of only a few tens of minutes [68, 4, 24, 73]. However, no microwave-synthesized LTA membranes tested for gas permeation of water vapor above 200°C have been found in the literature.

Table II.3: Synthesis conditions for LTA membranes tested for water gas permeation above 200°C. *APTES-treated supports.

Method	**Molar composition of the gel (Al_2O_3 : SiO_2 : Na_2O : H_2O)**	**Ageing duration of the synthesis solution**	**Synthesis duration**	**Synthesis temperature**	**Number of syntheses**	**Refs.**
*In-Situ**	1:5:50:1000	1 night	24 h	60°C	1	[70]
In-Situ	1:5:50:1000	-	20h	50°C	2-3	[20]
Ex-Situ	0.5:1:1:75	-	4 h	100°C	1	[55, 23]
Ex-Situ	1:2:3:200	-	24 h	70°C	1	[35]
Ex-Situ	1:5:50:1000	6 h	5 h	80°C	1	[36]
Ex-Situ	0.21:1:0.27:38	6 h	72 h	120°C	1	[42]
*In-Situ**	1:5:50:1000	-	24 h	60°C	1	[74]
Ex-Situ	1:5:50:1000	-	24 h	60°C	1	[15]

To synthesize LTA membranes by primary growth, the use of supports functionalized by a chemical ligand (such as APTES) is commonplace. Indeed, without a chemical ligand, the membranes present numerous inter-crystalline defects unfavorable to molecular separation selectivity. Thus, Huang's team was able to synthesize various LTA membranes with few defects with their protocol using APTES [29].

Progress on LTA membrane synthesis techniques by secondary growth has been made on the support seeding step. Li *et al.* [36] attribute the high quality of their membrane to the use of LTA nano-seeds and the use of annealing at 200°C after dip-coating, in order to chemically bond the seeds to the ceramic support.

Liu *et al.* [42, 59] have taken advantage of recent advances in the synthesis of silica-rich LTA zeolite [12] to produce a membrane combining hydrophilicity and hydrothermal stability. The seeding protocol uses rub-coating (deposition of LTA seeds on the support by friction) with silica-rich LTA seeds (synthesized according to the protocol of Conato *et al.* [12]). What differentiates the method of Liu *et al.* [42] from the rest of the literature, is the high synthesis temperature of 120°C, the very long synthesis time of 72 h and the molar composition of their gel of 0.21 Al_2O_3 : SiO_2 : 0.27 Na_2O : 38 H_2O (much more concentrated with few Na_2O than the conventional gel composition of 1 Al_2O_3 : 5 SiO_2 : 50 Na_2O : 1000 H_2O).

II.1.3.2 SOD (Sodalite)

II.1.3.2.a Structure and features

Unlike the LTA structure, the Sodalite (SOD) structure (Figure II.8) consists solely of α-cages. This structure has a very small pore size of 2.7 Å corresponding to the 6-rings of the α-cages. This structure is therefore the only one capable of acting as a molecular sieve between water and the other molecules in the reaction mixture. Nevertheless, the presence of defects and non-zeolitic pores in SOD membranes synthesized in the literature do not make them perfectly impermeable to other molecules larger than 2.7 Å [8, 2, 70]. SOD zeolites are also marked by their hydrophilicity, with a Si/Al ratio of between 1 and 3. In addition, SOD zeolites show better hydrothermal stability than the LTA structure, thanks to its higher Si/Al ratio as well

as its greater structural density [70].

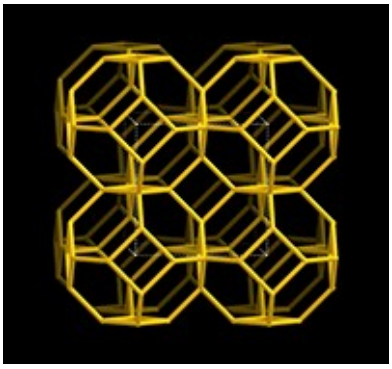

Figure II.8: Structure of SOD zeolite [60].

II.1.3.2.b Synthesis techniques

The synthesis conditions for SOD membranes are harsher than for LTA membranes, with temperatures generally in excess of 120°C. However, the composition of the synthesis gel remains similar to that used for LTA membrane synthesis (1 Al_2O_3 : 5 SiO_2 : 50 Na_2O : 1000 H_2O).

Table II.4: Synthesis conditions of SOD membranes tested for water gas permeation above 200°C (*Except van Niekerk *et al.* [51]).

Method	**Molar composition of the gel (Al_2O_3 : SiO_2 : Na_2O : H_2O)**	**Ageing duration of the gel**	**Synthesis duration**	**Synthesis temperature**	**Number of syntheses**	**Refs.**
In-Situ	1:5:50:1005	1 night	24 h	120°C	2	[70, 71]
Ex-Situ	1:5:50:1005	-	3.5 h	140°C	3	[34]
In-Situ	1:5:50:450 (Synthesis 1) 1:5:50:500 (Synthesis 2)	6h (Synthesis 1) 4h (Synthesis 2)	6h (Synthesis 1) 5h (Synthesis 2)	90°C	2	[51]

Wang *et al.* [71] explored *in-situ* SOD membrane synthesis for water separation for methanol synthesis. In their protocol, two consecutive syntheses at 120°C and for 24 h were applied to obtain a homogeneous layer of SOD zeolite. Their study illustrates the difficulty of synthesizing a homogeneous layer of SOD on a support after only one *in-situ* synthesis.

The *ex-situ* route was explored by Lafleur *et al.* [34]. Germs are deposited on the support using the "pore-plugging" method, which consists in plugging the pores of the support with SOD germs by applying a pressure gradient across the support. Using this technique, the authors succeeded in creating a homogeneous layer of seeds inside the support. Next, three hydrothermal syntheses at 140°C for 3.5 h (inspired by the protocol of Khajavi *et al.* [33]) were used to grow the seeds in the SOD membrane.

To extend the list of protocols shown in Table II.4 the protocol of van Niekerk *et al.* [51] whose membranes have not been tested above 200°C, is presented here. A particular feature of this protocol is that it achieves membrane deposition at a lower temperature (90°C) by carrying

out two consecutive hydrothermal syntheses with a synthesis gel twice as concentrated as in the other protocols. The authors note that the high concentration of the synthesis gel enables selective synthesis of the SOD [51].

II.1.4 Conclusion

Among the materials studied for water separation in a membrane reactor for methanol and DME synthesis, microporous zeolite membranes appear to be the most suitable for this purpose. Indeed, the performance of these materials in terms of selectivity at reaction conditions (>200°C) far exceeds that of dense polymer membranes and other microporous materials.

In this section, two types of zeolite were selected: LTA and SOD. These structures are characterized by their low Si/Al ratio, which is responsible for their hydrophilicity. In addition, differences in structure and chemical composition between these zeolites impact membrane performance. Zeolites with smaller pores (such as SOD zeolites) are theoretically more selective than zeolites with larger pores (such as LTA zeolites). However, the very fine pores of SOD zeolites are accompanied by a lower permeance trade-off than for LTA zeolites. In addition, membrane selectivity between polar and apolar molecules is strongly influenced by the zeolite's Si/Al ratio. This explains the excellent separation performance of LTA membranes for H_2O/CO_2 and H_2O/H_2 mixtures. On the other hand, although a Si/Al ratio close to 1 is targeted to obtain the most selective membrane possible, a low Si/Al ratio exposes the membrane to hydrothermal degradation. Thus, membranes richer in silica, such as SOD membranes, will potentially be more stable than LTA membranes at higher water contents and temperatures.

LTA membranes are the most extensively studied for their application to the hydrogenation of CO_2 to methanol. Very few studies report on SOD membranes tested for water separation above 200°C. Thus, comparisons between SOD membranes and LTA membranes are difficult. Further studies on the performance of SOD membranes at reaction conditions are needed in order to make relevant comparisons on these different structures.

Finally, the cost of manufacturing zeolite membranes is currently a major obstacle to their democratization. Given that most of the economic and environmental impact is linked to the manufacture of the support, research into new supports that are more competitive in these respects could make zeolite membranes more viable.

II.2 Development of preparation methods for high-quality zeolite membranes

In this section, preparation methods for thin defect-free membranes will be developed from the recent advances in the field. First, synthesis conditions and parameters will be studied on short 1 cm long membrane samples (Section II.2.2). Then, selected membrane preparation protocols will be scaled-up to 5 cm long supports for gas permeation trials (Section II.2.3). All of the experiments presented in this section were conducted at CEA Marcoule's LPSD (Laboratoire de Procédés Super-critiques et de Décontamination) under the supervision of Dr. Audrey Hertz.

II.2.1 Materials and methods

II.2.1.1 Membrane support

II.2.1.1.a Materials

Porous α-Al_2O_3 tubes (inner diameter: 6 mm, outer diameter: 10 mm, Pall Corporation) were used as membrane supports. The structure of the supports contained three layers: a thick layer on the outer wall of the tube made from coarse particles (pore diameter = 12 µm), an intermediate layer (pore diameter = 0.8 µm) and a thin layer on the inner wall of the tube, on which the zeolite membranes are synthesized upon (pore diameter = 200 nm) (Figure II.9). The supports were cut to be 1 cm long in Sections II.2.2 and 5 cm in Section II.2.3. Flat dense alumina plates (1 mm thick, 7x7 mm wide, Final Advanced Materials) were also used as support for zeolite deposit, for XRD analysis.

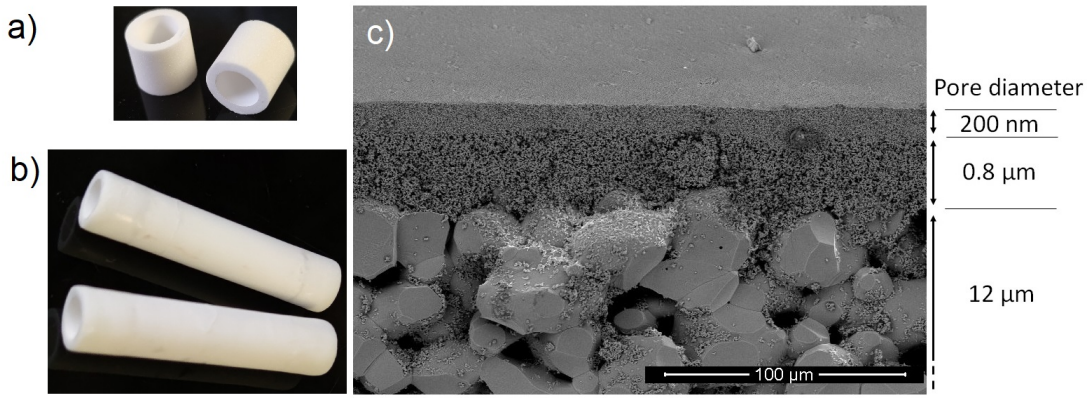

Figure II.9: a) 1 cm long alumina tubular support. b) 5 cm long alumina tubular support, c) SEM micrographs of the side cut of the bare tubular alumina support employed in this study.

II.2.1.1.b Sealing procedure

The 5 cm long zeolite membranes, prepared for gas permeation, had 1 cm of both ends of their supports sealed using a clear glaze (Duncan Envizion IN1001). The extremities of the support were dipped in the liquid glaze and left to dry at ambient temperature until the glaze hardened. This procedure was repeated twice more to get sufficient glaze coverage on the support. Afterwards, the supports were placed in an oven under air and the following program was employed

to set the following temperatures: ambient temperature to 900°C (1°C/min), 900°C held for 20 min, 900°C to ambient temperature (5°C/min).

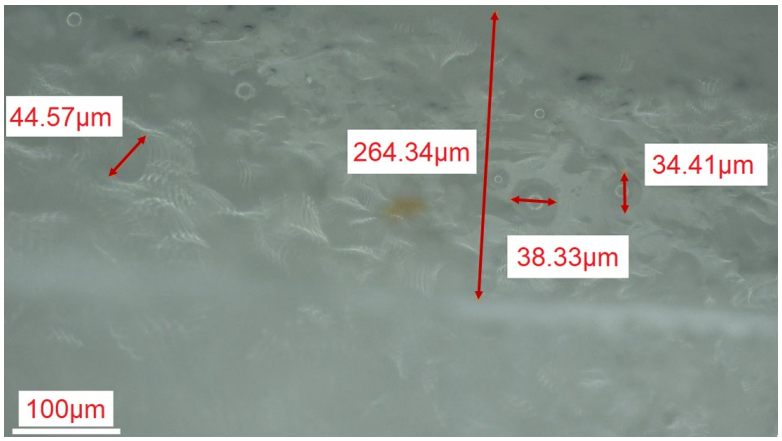

Figure II.10: Photograph of a side cut of a glazed support taken on an optical microscope.

While this glazing procedure produced bubbles inside the glaze layer, their diameters being at maximum 50 µm should not create pinholes on the 200 to 300 µm thick glaze layer (Figure II.10).

II.2.1.1.c Support treatment

Prior to any support treatment, the tubular supports were washed in ethanol under ultrasounds for 5 minutes and then dried at 80°C overnight.

APTES treatment for primary growth For the primary growth protocols, the supports were treated with 3-aminopropyltriethoxysilane (APTES, 99%, Sigma-Aldrich) according to a procedure inspired by A.Huang's team [28, 29, 74, 75].

For the Sections II.2.2.1.c and II.2.2.1.b, the supports were immersed in an APTES solution in toluene with a concentration of 50 g/L. Then the solution with the supports was heated to reflux (110°C) under air. The supports were subsequently dried at 80°C overnight. Finally, the supports were washed with ethanol in a Soxlhet extractor for 24 h then dried again at 80°C overnight.

Dip-Coating for secondary growth The supports were seeded by dip-coating with the as-synthesized sub-micronic LTA seeds with a procedure inspired by Li *et al.* [36]. A slurry of LTA seeds with a concentration of 1 wt.% in deionized water was sonicated for 30 minutes in order to uniformly disperse the seeds. The tubular supports were slowly immersed in the slurry for 20 seconds before drying at 80°C for at least 3 hours. The procedure was repeated three times for the short 1 cm long LTA membranes and only twice for the 5 cm long LTA membranes. Afterwards, the supports were placed overnight in an oven at 200°C.

II.2.1.2 Hydrothermal synthesis

II.2.1.2.a Chemicals

To produce the various synthesis gels, the following chemicals were used as received: fumed silica (SiO_2, Sigma-Aldrich) as Si source; sodium aluminate ($NaAlO_2$, Al_2O_3: 50-56 wt.%, VWR Chemicals) as Al source; sodium hydroxide (NaOH, >98%, Sigma-Aldrich). Deionized water was homemade.

II.2.1.2.b Reaction vessels

Stainless steel reaction vessels (Parr) were employed, incorporating a Teflon cup for hydrothermal synthesis. The Teflon cup has a volume of 125 mL, with internal dimensions characterized by an inside diameter of 44.5 mm and an inside depth of 82.6 mm.

For the preparation of the 5 cm long membranes (Section II.2.3), custom Teflon holders were crafted to hold the support vertically. The two Teflon holders crafted were 6 cm tall and 4 cm wide in diameter and had four 5 cm deep holes which are 1.1 cm wide in diameter (Figure II.11a). The Teflon holders were later cut to be around 4.5 cm tall to accommodate more synthesis gel inside the hydrothermal vessel (Figure II.11b). Dimensions between the two Teflon holders varied slightly as both holders were hand-crafted.

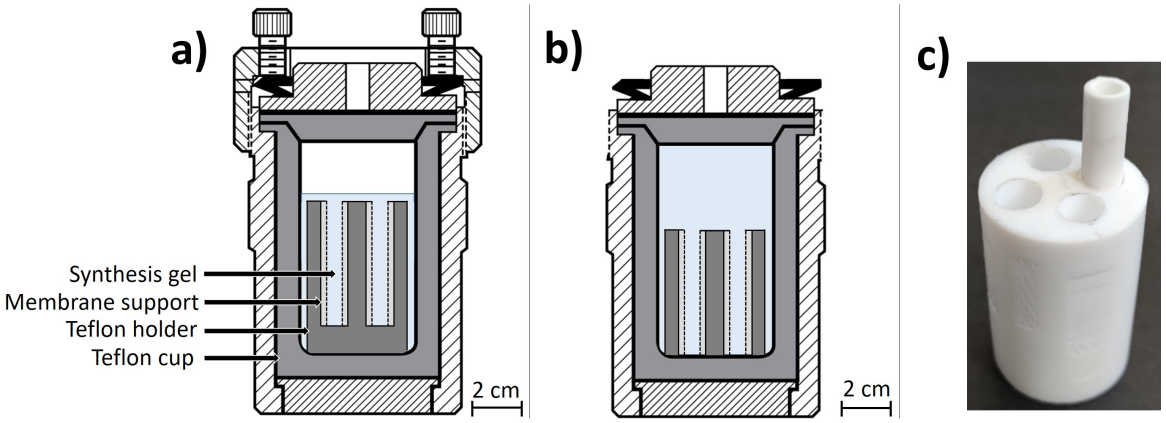

Figure II.11: Up to scale layout of the hydrothermal vessel employed for the 5 cm long membrane preparations: (a) configuration with low quantities of synthesis gel, (b) configuration with high quantities of synthesis gel. (c) Photograph of one of the custom-made Teflon holders with a bare support half-way inserted.

II.2.1.2.c LTA seeds preparation

Sub-micronic sized LTA seeds were synthesized for the preparation of LTA membranes through hydrothermal synthesis. The following procedure was followed to produce around 5 g of LTA seeds. A sodium aluminate solution (5.75 g $NaAlO_2$ in 35 mL of deionized water) and a sodium hydroxide solution (2.65 g of NaOH in 26.25 g of deionized water) were simultaneously poured in a Teflon cup. 2 g of fumed silica were then added before closing the reaction vessel. The reaction vessel was heated in an oven at 40°C for 20 h and then at 120°C for 2 h. The obtained product was filtered and washed with 1 L of deionized water and finally dried at 80°C overnight.

The resulting LTA seeds ranged from 200 to 400 nm in size.

II.2.1.2.d LTA membrane preparation

A synthesis gel was prepared by mixing a sodium aluminate solution with a silica and sodium hydroxide solution. The resulting solution was then aged under stirring at ambient temperature for 20 h.

For the hydrothermal synthesis of the short 1 cm long LTA membranes, the outer wall of the supports was sealed with Teflon tape. Then, the supports were placed in the Teflon cup and held vertically. The synthesis gel was poured inside the Teflon cup and the reaction vessel was sealed and placed inside an oven at a set temperature for a set amount of time.

For the hydrothermal syntheses of the 5 cm long LTA membranes for gas permeation, the outer wall of the seeded supports was sealed with Teflon tape and put inside the custom-made Teflon holder. Then, the supports inside the Teflon holder were placed in Teflon cup. The synthesis gel was then poured until all the membranes were submerged (Figure II.11a) and the hydrothermal vessel was sealed. For the syntheses with higher amounts of synthesis gel, the cut Teflon holder was used and the Teflon cup was completely filled. In this latter case, the hydrothermal vessel remained unsealed for safety concerns (Figure II.11b). The amount of synthesis the introduced gel varied according to the number of membranes being synthesized and which Teflon holder was employed.

After the hydrothermal synthesis, the membranes were thoroughly rinsed with deionized water and then sonicated in deionized water for 5 minutes to remove the unreacted gel for better observations on the microscope. Finally, the LTA membranes were dried at 80°C overnight and the SOD membranes were dried at room temperature until the weight of the membranes were stable.

Table II.5 summarizes all the synthesis conditions involved for LTA membrane preparation in each section.

Table II.5: Reaction conditions for LTA membrane preparation in each section.

Section	**Method**	**Molar composition of the gel (Al_2O_3 : SiO_2 : Na_2O : H_2O)**	**Ageing duration of the synthesis solution**	**Synthesis duration**	**Synthesis temperature**
II.2.2.1.a	Both	1:5:50:1000	20 h	24 h	60°C
II.2.2.1.b	Both	1:5:50:1000	2 h/20 h	24 h	60°C
II.2.2.1.c	*In-situ*	1:5:50:1000	20 h	24 h/30 h/48 h	60°C/80°C
II.2.3.1	*Ex-situ*	1:5:50:1000	20 h	24 h	60°C

II.2.1.2.e SOD membrane preparation

The preparation of SOD membranes involved either one or two consecutive hydrothermal syntheses. For a hydrothermal synthesis, a synthesis gel was prepared by mixing a sodium aluminate solution with a silica and sodium hydroxide solution and aged for 20 hours prior to the hydrothermal synthesis. Afterwards, the outer wall of the seeded supports was sealed with Teflon

tape and put inside the Teflon cup. The synthesis gel was then poured in the reaction vessel and then placed in an oven at the desired reaction conditions.

After the hydrothermal synthesis, the membranes were thoroughly rinsed with deionized water and then sonicated in deionized water for 5 minutes to remove the unreacted gel for better observations on the microscope. Finally, the membranes were dried at room temperature until the masses of the membrane were stable.

For the hydrothermal syntheses of the 5 cm long SOD membranes for gas permeation, the supports were put inside the shorter 4.5 cm long version of the custom-made Teflon holder. Then, the supports inside the Teflon holder were placed in a Teflon cup and the synthesis gel was poured until the Teflon cup was completely filled (see Figure II.11b).

Table II.6 summarizes all the synthesis conditions involved in each section.

Table II.6: Reaction conditions for SOD membrane preparation in each section.

Section	**Molar composition of the gel (Al_2O_3 : SiO_2 : Na_2O : H_2O) (Synthesis 1)**	**Molar composition of the gel (Al_2O_3 : SiO_2 : Na_2O : H_2O) (Synthesis 2)**	**Ageing duration of the synthesis solution**	**Synthesis duration**	**Synthesis temperature**
II.2.2.2	1:5:50:500	-	20 h	24 h	60°C
II.2.2.2	1:5:50:450	1:5:50:500	20 h	6 h (1st) / 8 h (2nd)	90°C
II.2.2.2	1:5:50:1000	-	20 h	24 h	120°C
II.2.2.2	1:5:50:1000	-	20 h	3 h 30	140°C
II.2.3.2	1:5:50:450	1:5:50:500	20 h	6 h (1st) / 8 h (2nd)	90°C

II.2.1.3 Membrane characterization

II.2.1.3.a Crystalline structure

Crystalline structure of the zeolite powders and membranes were analyzed by XRD. Diffractograms were used to identify the synthesized zeolite structure and assess any side phases present in the sample.

The diffractograms were produced at CEA Marcoule's LFCM (Laboratoire de Formulation et Caractérisation des Matériaux minéraux) under the supervision of Pascal Antonucci, using a Panalytical X'Pert MPD Pro instrument. The X-ray source employed was a copper anode ($\lambda K\alpha 1 = 1.5406$ Å) operating at 60 kV and 40 mA, with an X'Celerator detector in Bragg-Brentano geometry.

Zeolite membranes deposited on flat dense alumina plates were fixed on a stainless steel support with an adhesive paste for the XRD analysis.

II.2.1.3.b Micrography

A SEM was used to qualitatively assess defects on the synthesized membranes and to measure the size of zeolite crystals and membrane thicknesses.

SEM characterizations were carried out with a beam voltage set between 10 KV and 20 KV on a Tungsten Scanning Electron Microscope (FEI - INSPECT S50), available at CEA Marcoule's LFCM/LPSD laboratories under the supervision of David Rudloff and Dr. Audrey Hertz. Non-

conductive samples are placed on an analysis pad covered with a self-adhesive carbon pad. A thin layer of platinum (a few Å) is then sputtered on to ensure electron conduction and avoid charge effects.

II.2.1.3.c Ninhydrine assay

A ninhydrine assay was conducted to identify the presence of APTES on the support after the functionalization step. Ninhydrine is a chemical agent that reacts with primary amine groups to produce a distinctive purple compound (Equation II.4). If the APTES functionalization is successful, the ninhydrine reagent will react with the amine groups of the aminosilane bound to the support, producing a purple shade on the wall of the support.

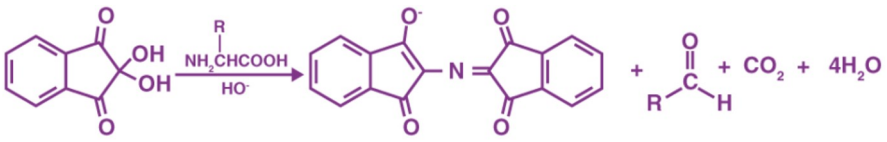

(II.4)

To conduct this assay, supports were dipped in a 2% solution of ninhydrine ($C_9H_6O_4$, Merck) in ethanol. Afterwards, the samples were left still under air while awaiting the change in color.

II.2.1.3.d Rheology

The viscosity of synthesis gels was measured using a TA Instrument DHR-1 rheometer to investigate on reactant diffusion within the static hydrothermal synthesis conditions.

II.2.2 Investigating hydrothermal synthesis parameters for LTA and SOD membrane preparation

The aim of this subsection is to develop and adapt preparation methods for the synthesis of high-quality LTA and SOD membranes. To reach this goal, primary growth and secondary growth preparation methods (inspired by the recent advances in the literature) are evaluated on small membrane samples (1 cm long). A study of the main parameters of each step of the membrane preparation is presented to understand the key factors for achieving defect-free LTA and SOD membranes.

II.2.2.1 LTA membrane preparation

II.2.2.1.a Effects of the support treatment

Two methods for support treatment were tried. The first method is a APTES functionalization method inspired by Huang *et al.* [28, 29, 74, 75], which goal is to generate an anchor point for the zeolite crystal during their nucleation step. The second one is seeding the support by dip-coating it in a slurry of nano-sized LTA crystal. This second method aims to decouple the nucleation step from the hydrothermal synthesis by depositing LTA seeds directly on the support.

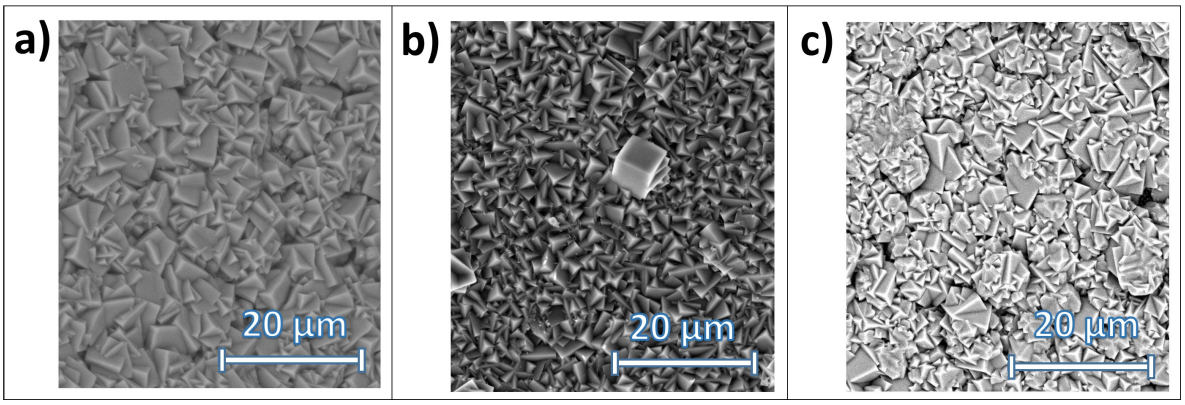

Figure II.12: SEM micrographs of LTA membranes prepared through primary and secondary growth with various support treatments: (a) APTES treated support, (b) dip-coated support, (c) untreated support.

SEM micrographs of the support after hydrothermal synthesis are featured on Figure II.12. The dip-coated support displays a denser layer of LTA zeolite compared to the untreated support while the APTES-treated support displays negligible density gains compared to the untreated support. The dip-coated support exhibits smaller but more intertwined crystals, which correspond to the growth of the deposited LTA seeds (Figure II.12). The APTES-treated and the untreated support both features slightly bigger crystals more distant to one another and some defects are visible on the corresponding micrographs.

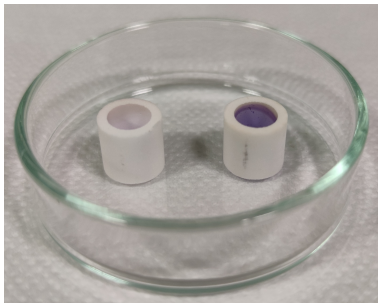

Figure II.13: Photograph of supports after the ninhydrine assay. Left: untreated support, right: APTES-treated support.

To explore the effectiveness of the APTES treatment, a ninhydrine assay was conducted to qualitatively assess whether the APTES functionalization was successful or not. In Figure II.13, the support treated with APTES exhibits a higher intensity of purple coloration than the untreated support. These photographs indicate that at least some APTES are being fixed on the support during the functionalization step. Various attempts were undertaken by changing the APTES solution concentration within the range of 0.13 to 67 g/L, adjust the functionalization duration from 1.5 to 72 hours, conduct the functionalization step under N_2, and omit the washing step in the Soxhlet extractor. Nevertheless, all these attempts yielded similar unenhanced membrane density after hydrothermal synthesis compared to the untreated support.

According to Noack *et al.* [54], the shortcomings of primary growth protocols on untreated supports originate from the high aluminum content of LTA crystals, resulting in a negatively charged surface on the crystals. Moreover, Huang *et al.* [28] showed that at synthesis pH,

the surface of the Al_2O_3 support is also negatively charged. During hydrothermal synthesis, negative charges repel zeolite crystals from each other and from the support, resulting in the formation of defects. The role of APTES is to mitigate the negative charge of the support which would reduce the repulsive forces between the support and the zeolite crystals [28]. However, this effect could not be reproduced in the experiments performed here.

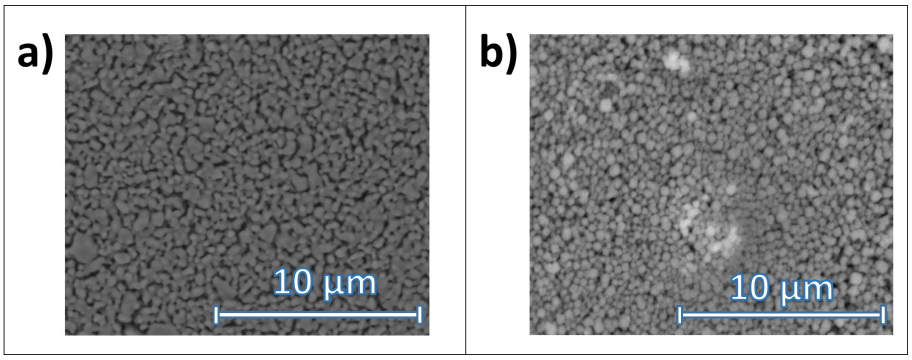

Figure II.14: SEM micrographs of a (a) bare alumina support, (b) support seeded with LTA seeds.

Seeding of the support is effective in producing a well-intergrown LTA membrane after hydrothermal synthesis. The success of this method lies in the high density of nanosized LTA seeds deposited onto the support (Figure II.14). Furthermore, by not requiring the nucleation step during hydrothermal synthesis, a well-intergrown LTA membrane can be achieved under conditions in which the same outcome cannot be reproducible for primary growth methods even with support treatment. These results are consistent with trends in the literature where secondary growth protocols have become more popular due to being less prone to the formation of defects [72]. Nevertheless, secondary growth protocols are more complex and require extra steps, involving synthesizing the seeds separately and seeding the support material.

II.2.2.1.b Effect of ageing duration of the synthesis gel

The study of ageing duration of the synthesis gel was done on LTA membranes grown with primary and secondary growth protocols.

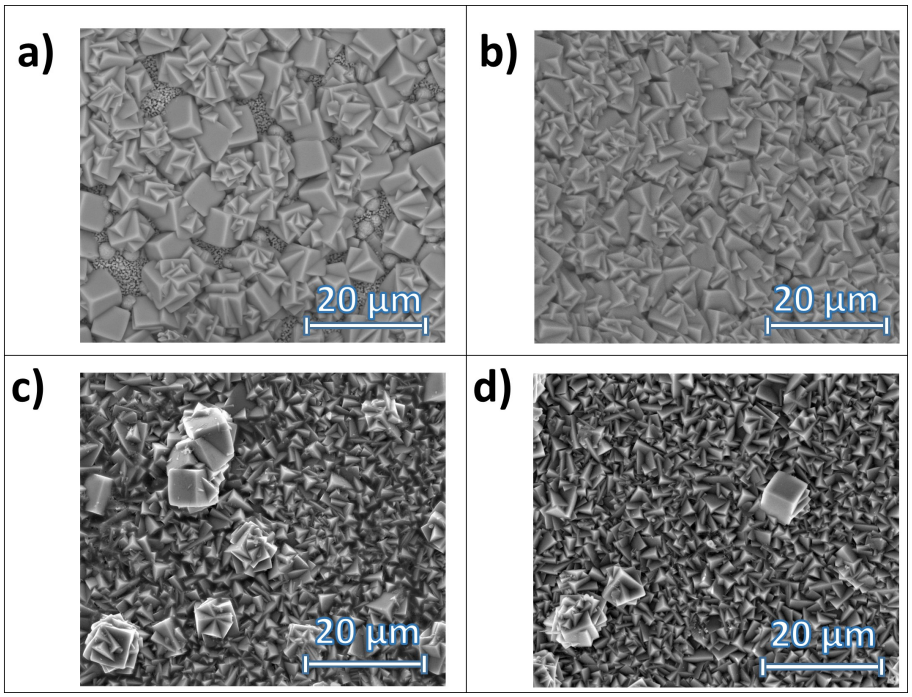

Figure II.15: SEM micrographs of LTA membrane prepared through primary and secondary growth with synthesis gel aged with various durations: (a) primary growth - 2 h, (b) primary growth - 20 h, (c) secondary growth - 2 h, (d) secondary growth - 20 h.

On the SEM micrographs featured on Figure II.15, increasing the ageing duration of the synthesis gel leads to denser LTA deposits for the primary growth protocol, covering previously bare support surfaces. In contrast, ageing duration of the synthesis gel seems to make minimal to negligible differences on the density of the LTA deposit for the secondary growth protocol.

In primary growth, the nucleation and the growth of zeolites crystals on the support happen simultaneously during the hydrothermal synthesis. Conversely, in secondary growth, the nucleation step is decoupled from the growth step. Prolonged ageing of the synthesis gel produces additional zeolite nuclei within the gel before hydrothermal synthesis and thus partly alleviates the nucleation step for the primary growth protocol. The secondary growth protocol does not experience this benefit, as its nucleation step is manually achieved prior to the hydrothermal synthesis.

II.2.2.1.c Effects of the temperature and duration of the hydrothermal synthesis

The diffractograms featured on Figure II.16 display the formation of side phases aside LTA. Small rays belonging to the FAU phase are visible after a hydrothermal synthesis at 60°C for 24 h. The same rays appear bigger in comparison to the LTA ones after a synthesis at a temperature of 80°C for 24 h. This observation is corroborated with the SEM micrographs exhibited on Figure II.17, on which the main crystal visible at 60°C are cubic ones, identifiable to the LTA phase. At 80°C, the cubic LTA crystals are less prominent and octahedral shaped crystals, identifiable as FAU, become much more noticeable while some shard-like crystals, identifiable as SOD, become visible.

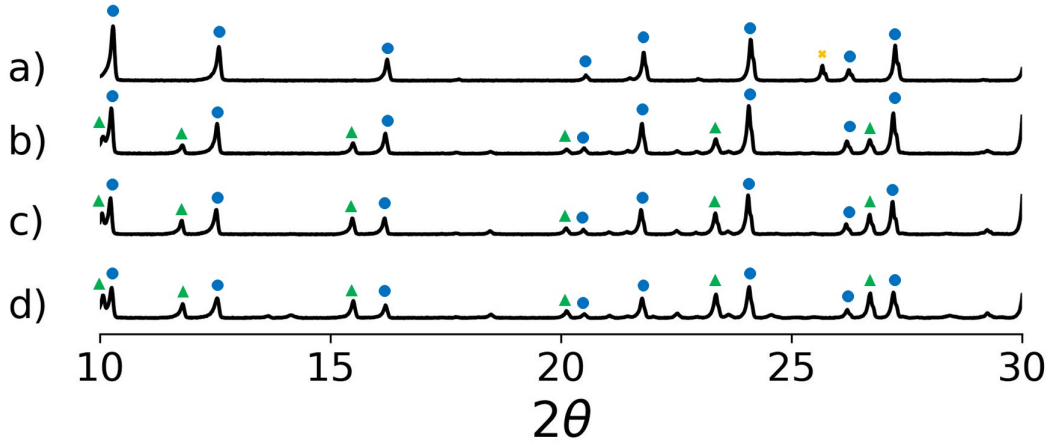

Figure II.16: XRD diffractograms of LTA membranes prepared through hydrothermal synthesis with the following conditions: (a) 60°C - 24 h, (b) 60°C - 30 h, (c) 60°C - 48 h, (d) 80°C - 24 h. ● LTA, ▲ FAU, × alumina support.

Synthesis duration is also detrimental to the LTA phases. As seen on the diffractograms on Figure II.16, LTA rays are the most distinguishable after 24 h of hydrothermal synthesis and some smaller rays belonging mainly to the FAU phase are visible. These smaller rays are increasing with longer synthesis duration. The same observation can be made on the SEM micrograph (Figure II.17). After 24 h of synthesis, the main crystals observable are the cubic crystals of the LTA phase. Moreover, the octahedral shaped FAU crystals are more noticeable as the synthesis duration is increased.

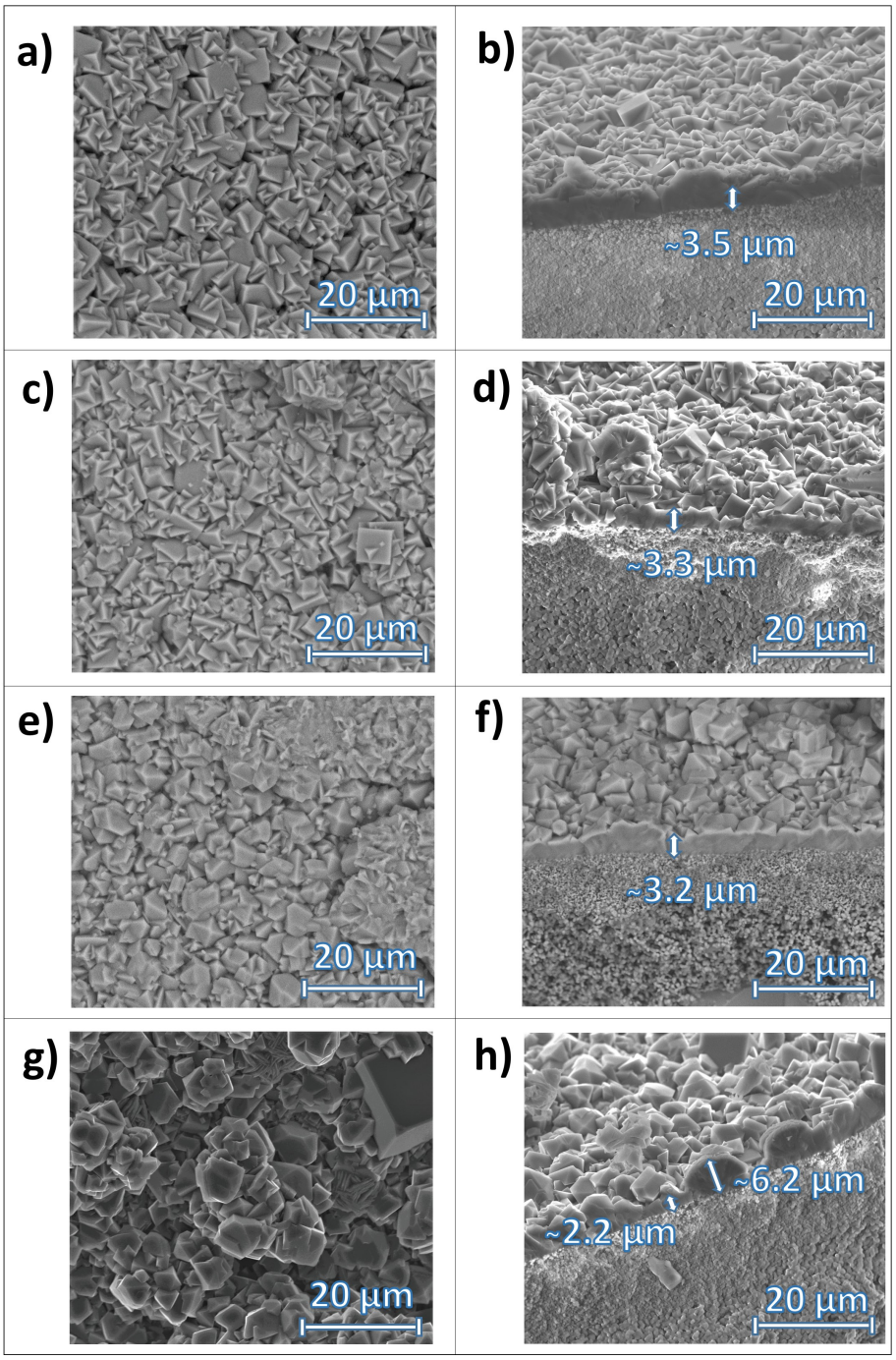

Figure II.17: SEM micrographs of LTA membranes prepared through hydrothermal synthesis with the following conditions: (a,b) 60°C - 24 h, (c,d) 60°C - 30 h, (e,f) 60°C - 48 h, (g,h) 80°C - 24 h.

All synthesis conditions yielded membrane that were around 3 to 4 µm thick with the presence of defects (Figure II.17b,d,f,h). Thus, no relationship was found concerning the thickness of LTA membranes relative to the synthesis temperature and duration.

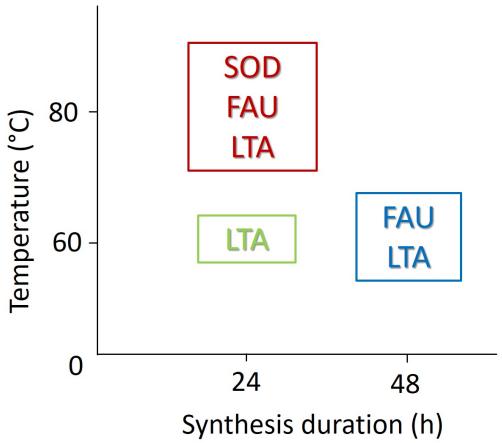

Figure II.18: Zeolite phase distribution for LTA membrane preparation through hydrothermal synthesis ranging from 60 to 80°C and from 24 to 48 h.

These observations on the study of the temperature and duration of the hydrothermal synthesis (Figure II.18) match the ones found by Arepalli *et al.* [2] in their study on the synthesis of H-SOD powders, in which they used similar gel composition albeit at higher temperature and shorter duration. LTA being the main phase at low temperatures and synthesis durations suggest that this phase is kinetically favorable over FAU and SOD zeolites in fresh synthesis gel. However, the LTA phase seems to be thermodynamically unstable and transforms into either FAU or SOD.

II.2.2.2 SOD membrane preparation

Higher synthesis temperatures were tried with the aim of synthesizing a defect free SOD membrane.

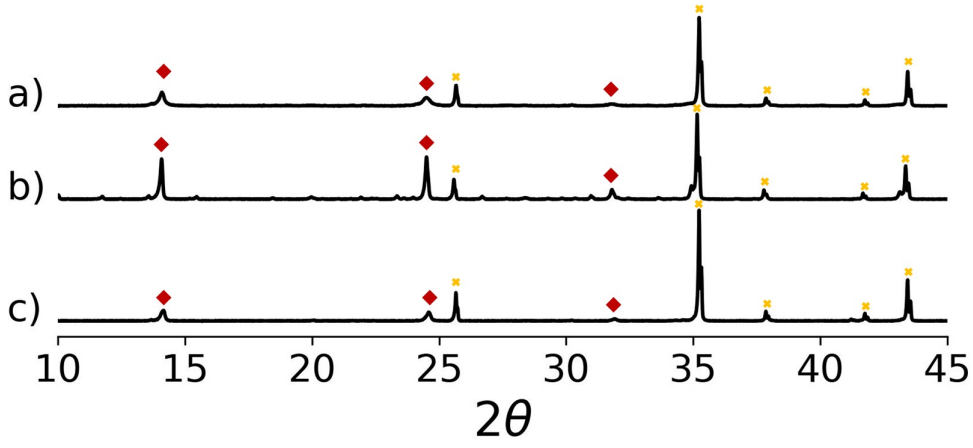

Figure II.19: XRD diffractograms of SOD membranes prepared through hydrothermal synthesis with the following conditions: (a) two successive hydrothermal syntheses (90°C - 6 h then 90°C - 8 h), (b) 120°C - 24 h, (c) 140°C - 3 h 30 min. ♦ SOD, × alumina support.

The most significant rays featured on Figure II.19 belong to the SOD phase and the Al_2O_3 plate. Thus, higher synthesis temperatures increase the selectivity of the growth of SOD crystal

even though some big LTA crystal remains observable on the SEM micrographs (Figure II.20c). However, unlike LTA crystals which tend to homogeneously cover the surface of the support, the shard like SOD crystals form spherical shapes that leave significant uncovered surface on the support (Figure II.20a,c). Crystal growth kinetics are greatly accelerated at higher temperatures, producing much bigger and more intertwined crystals even with much shorter synthesis duration (Figure II.20d). Conversely, the high temperature conditions produced undesirably thick membranes which would likely hinder permeation performances (Table II.21).

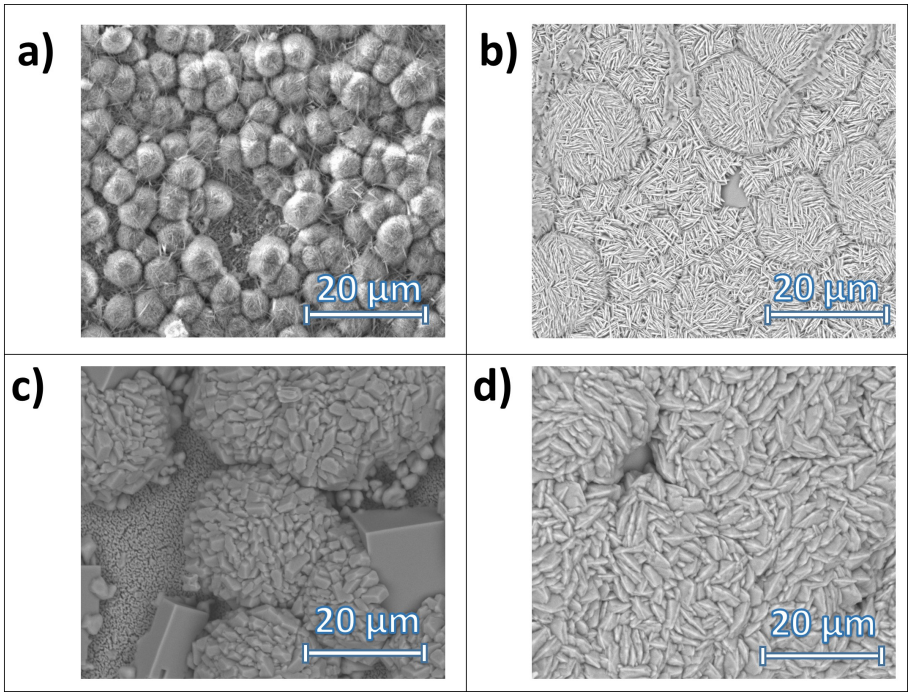

Figure II.20: SEM micrographs of SOD membranes prepared through hydrothermal synthesis with the following conditions: (a) 60°C - 24 h, (b) two successive hydrothermal syntheses (90°C - 6 h then 90°C - 8 h), (c) 120°C - 24 h, (d) 140°C - 3 h 30 min.

By increasing the gel concentration to 1 Al_2O_3 : 5 SiO_2 : 50 Na_2O : 500 H_2O, it was found by serendipity that SOD shard like crystals can selectively grow at temperatures as low as 60°C (Figure II.20a). The modified composition of the gel either plays a role in what phase is kinetically favorable or accelerates kinetics for the phase transition from LTA to SOD. However, as aforementioned, the SOD crystals still agglomerate in spherical shapes leaving significant gaps of uncovered support (Figure II.20a).

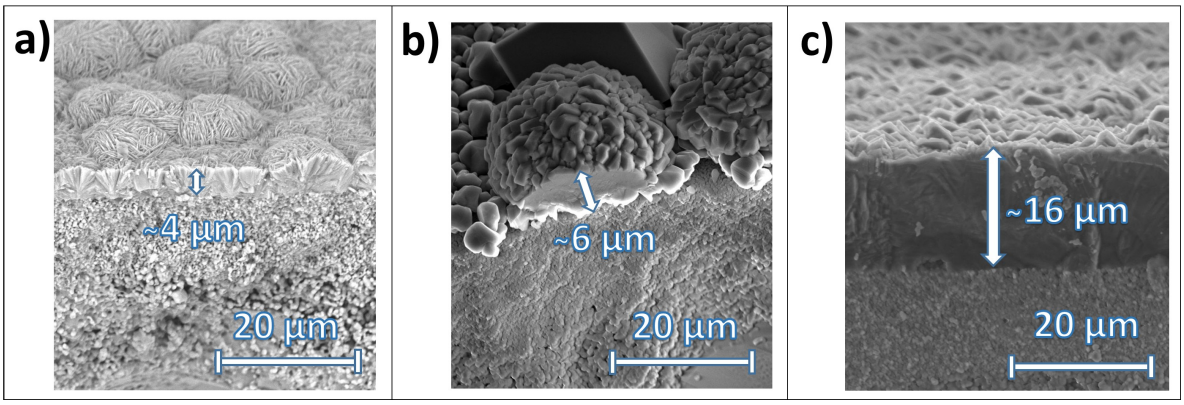

Figure II.21: SEM micrographs of the side cut of SOD membranes prepared through hydrothermal synthesis with the following conditions: (a) two successive hydrothermal syntheses (90°C - 6 h then 90°C - 8 h), (b) 120°C - 24 h, (c) 140°C - 3 h 30 min.

In an attempt to fill in the gaps between crystals, a protocol with two successive hydrothermal syntheses inspired by Van Niekerk *et al.* [51] was implemented.

After the first synthesis, the surface of the support is sparsely populated with agglomerates of SOD crystals (Figure II.22a). However, the second successive synthesis yields a dense layer of SOD zeolite and no defects have been seen on the SEM micrographs (Figure II.22b). As mentioned by Van Niekerk *et al.* [51], this two consecutive hydrothermal syntheses protocol can be analog to a secondary growth method, where the first synthesis would seed the support of SOD crystals while the second one would grow the SOD crystals to form the membrane. Moreover, even after two successive hydrothermal syntheses, the low temperature syntheses yield thin SOD membranes with thicknesses around 4 µm (Table II.21a).

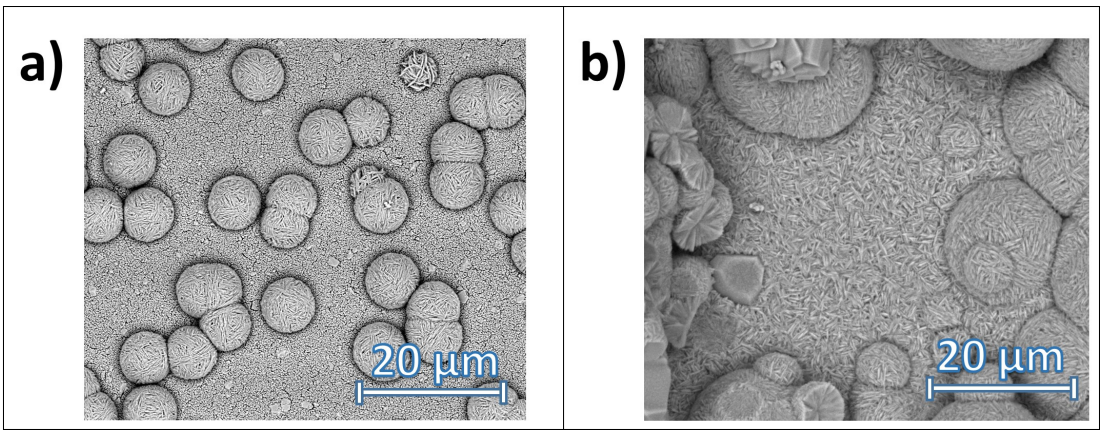

Figure II.22: SEM micrographs of SOD membranes prepared through two successive hydrothermal syntheses: (a) after the first synthesis (90°C - 6 h), (b) after the second synthesis (90°C - 8 h).

II.2.2.3 Thermal stability of LTA and SOD membranes

After a drying step at 80°C of LTA and SOD membranes, it was observed that SOD membranes were prone to crack while LTA membranes remained unchanged (Figure II.23b,c). However, fracture of the SOD membrane can be prevented by drying the membrane at room temperature

(Figure II.23a). These observations sparked this study of the thermal stability of LTA and SOD membrane at methanol synthesis reaction temperature ranging from 200°C to 300°C.

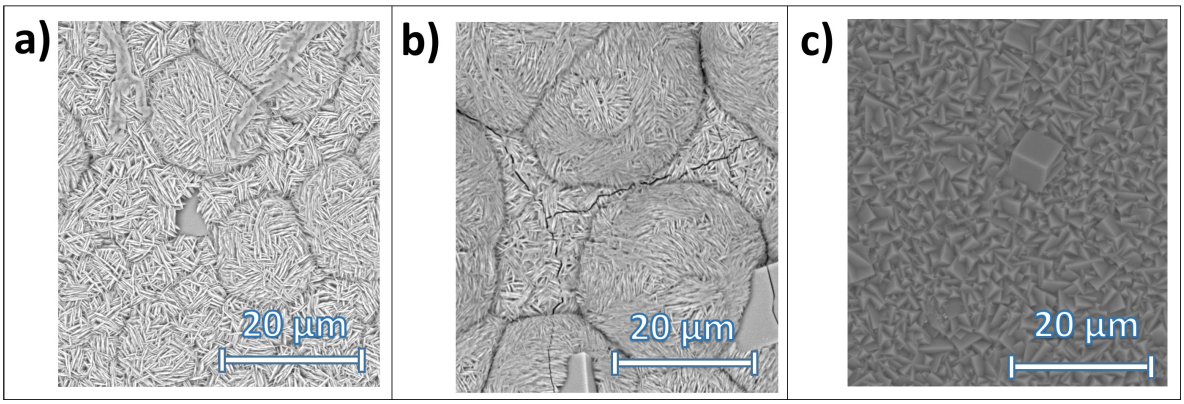

Figure II.23: SEM micrographs SOD and LTA membrane after drying at (a) room temperature (SOD), (b) 80°C (SOD), (c) 80°C (LTA).

To further investigate the thermal stability of LTA and SOD membranes, samples were placed in an oven under air and heated 200°C for 24 h. The heating rate was set to 1°C/min and the cooling rate was set to 5°C/min. On the SEM micrographs featured on Figure II.24a,b, it can be seen that both LTA and SOD display no crack after being exposed to 200°C. Thus, during the previous drying step at 80°C, thermal shock, due to rapidly exposing the membrane to ambient temperature (after taking them out of the oven), is likely responsible for the crack formation in the SOD samples.

To investigate the limits of the thermal stability of both LTA and SOD samples, the temperature was further increased to 300°C and the heating rate to 5°C/min. Cooling rate remained unchanged at 5°C/min. While the LTA sample is able to withstand the harsher temperature, the SOD sample displays wide and pronounced fractures (Figure II.24c,d). These observations insist on the superior thermal stability of LTA membranes compared to SOD membranes.

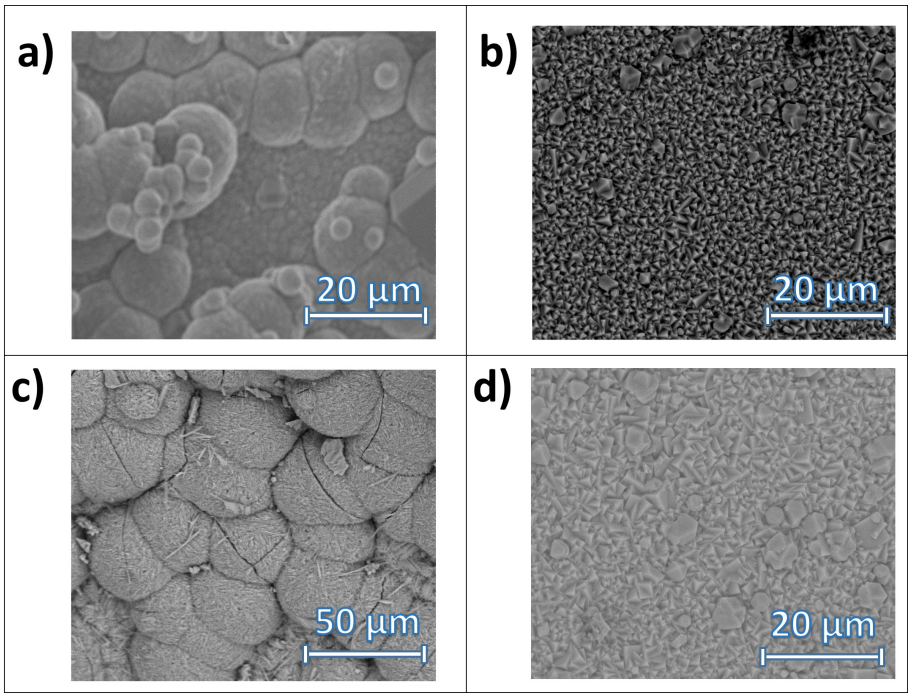

Figure II.24: SEM micrographs of SOD and LTA membranes after a thermal stress test. (a) SOD: 200°C (at 1°C/min), (b) LTA: 200°C (at 1°C/min), (c) SOD: 300°C (at 5°C/min), (d) LTA: 300°C (at 5°C/min).

Wang *et al.* have described SOD zeolites as having a higher thermal stability than LTA zeolite owing to their higher structural density [71, 70]. However, in our experiments, SOD membranes were shown to be more sensitive to temperature changes compared to LTA membranes. This discrepancy may be attributed to the dry conditions of our experiments that would lead to the dehydration of the SOD zeolite. The SOD structure being stabilized through hydrogen bonds between the adsorbed water and its framework oxygen atoms [71, 64], the rapid removal of this structural water could have hypothetically caused the formation of cracks in our samples.

II.2.3 Scale-up of membrane preparation methods

The previous section examined several crucial parameters for preparing LTA and SOD membranes through hydrothermal synthesis. However, this study was conducted on short 1 cm long samples whereas longer membranes are required for the permeation studies. This section utilizes the parameters that produced the highest quality and thinnest zeolite membranes to perform a small scale-up of the LTA and SOD membrane preparation method. The objective is to achieve comparable outcomes for 5 cm long supports as those observed for 1 cm long supports.

II.2.3.1 Long LTA membrane preparation

The first attempt for synthesizing 5 cm long LTA membranes was conducted with the optimum synthesis parameters studied the Section II.2.2.1. For this first attempt, synthesis gel was poured until all membranes and the Teflon holder were completely submerged (as shown on Figure II.11a).

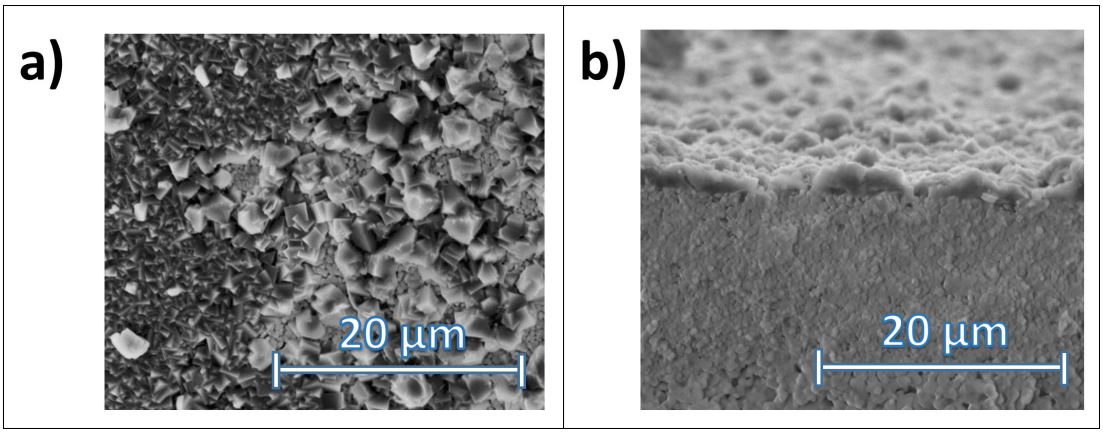

Figure II.25: SEM micrographs of the first attempt in synthesizing 5 cm long LTA membranes: (a) top view, (b) side view.

SEM micrographs of the surface of the membrane reveal a deposit of small LTA zeolite crystals with the presence of wide uncovered support surfaces (Figure II.25a). The size of the crystals are smaller than was obtained on the small 1 cm long supports (Figure II.25a). Furthermore, the membrane is thinner, with an approximate thickness around 1 to 2 µm (Figure II.25b). Based on these images, it can be assumed that the membrane's growth was constrained by either an insufficient presence or restricted accessibility of the reactants to the support surface.

Increasing the concentration of the synthesis gel could elucidate whether the membrane's growth was limited by a deficiency of reactant inside the hydrothermal vessel. However, as seen in Section II.2.2.1.c, increasing the synthesis gel concentration leads to the formation of SOD membrane. As such, the amount of synthesis gel inside the hydrothermal vessel will rather be studied. To study whether the membrane's growth was constrained due to low diffusivity of the reactants towards the support surface, a mixing of the synthesis gel during hydrothermal synthesis will be attempted.

II.2.3.1.a Study on reactant deficiency during hydrothermal synthesis

To study whether the membrane's growth in the initial trial was limited by a lack of reactants inside the hydrothermal vessel, the quantity of synthesis gel was increased. To do so, the Teflon holder was cut shorter and the hydrothermal vessel was filled completely as described on Figure II.11b.

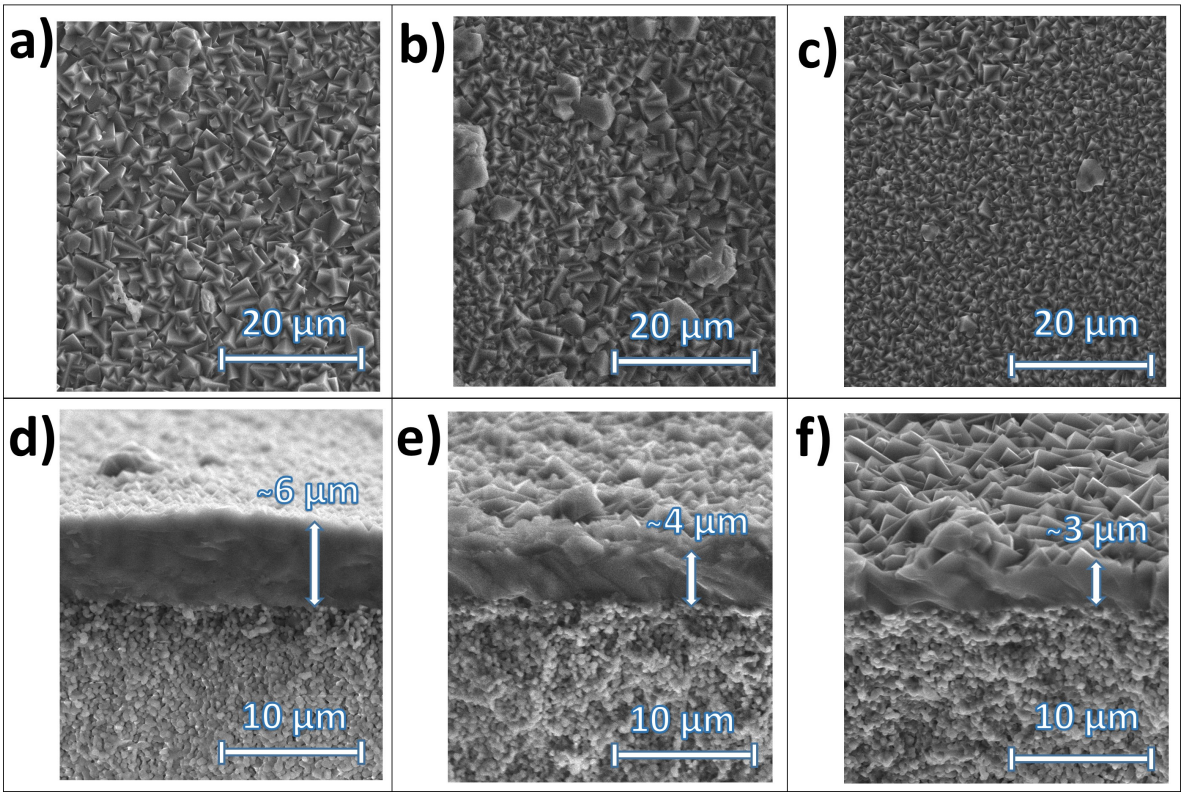

Figure II.26: SEM micrographs of the 5 cm long LTA membrane prepared with an increased amount of synthesis gel: (a) top view, bottom part of the membrane, (b) top view, middle part of the membrane, (c) top view, top part of the membrane, (d) side view, bottom part of the membrane, (e) side view, middle part of the membrane, (f) side view, top part of the membrane.

As observed on the SEM micrographs featured on Figure II.26, increasing the amount of synthesis gel has improved the density of the LTA deposit to the point that the surface of the support is no longer visible from the top views (Figure II.26a,b,c). Thus, the membrane synthesized through this method seems defect free. Nevertheless, the membrane exhibits irregular thickness, with a notably greater thickness evident at the lower portion (Figure II.26d) in contrast to the upper section of the membrane (Figure II.26f). The absence of mixing during synthesis is likely to allow a sedimentation of reactants towards the bottom of the vessel. Consequently, a concentration gradient is established along the membrane's length, resulting in disparate availability of reactants between the bottom and top of the hydrothermal vessel. This asymmetry in reactant distribution contributes to the heterogeneous growth of the zeolite membrane along its length.

II.2.3.1.b Study on reactant diffusivity within the synthesis gel

The membrane preparation method for this study follows the previous one where the hydrothermal vessel was completely filled with synthesis gel and the shorter Teflon holder was employed. To generate mixing in the synthesis gel, the hydrothermal vessel was put on a moving plate that moves in circles horizontally. The moving plate was set at 1750 rpm during the reaction. The whole contraption was then placed in oven for hydrothermal synthesis.

Figure II.27: Photograph of the setup employed for generating mixing inside the hydrothermal vessel. On this picture, the hydrothermal vessel is fixed between two plates which shakes the vessel horizontally.

Mixing of the synthesis gel lead to more uniform membrane thickness contained between 3 and 4 µm (Figure II.28d,e,f). Moreover, no defects can be spotted by observing the top views of the membrane (Figure II.28a,b,c). Thus, mixing of the synthesis gel prevents the sedimentation of reactants towards the bottom of the hydrothermal vessel and eliminates the presence of a concentration gradient along the membrane length. Although the membrane thickness exhibits greater uniformity because of mixing, it does not surpass that of the thinnest region observed in the membrane prepared without stirring (Figure II.26f). Consequently, the introduction of mixing in the synthesis gel does induce additional membrane growth. This observation suggests that the growth of the zeolite membrane is unlikely hindered by a lack of diffusion of reactants towards the membrane surface. It also indicates that the depletion of reactants, due to the sedimentation of zeolite nuclei to the bottom of the reaction vessel, is not a contributing factor.

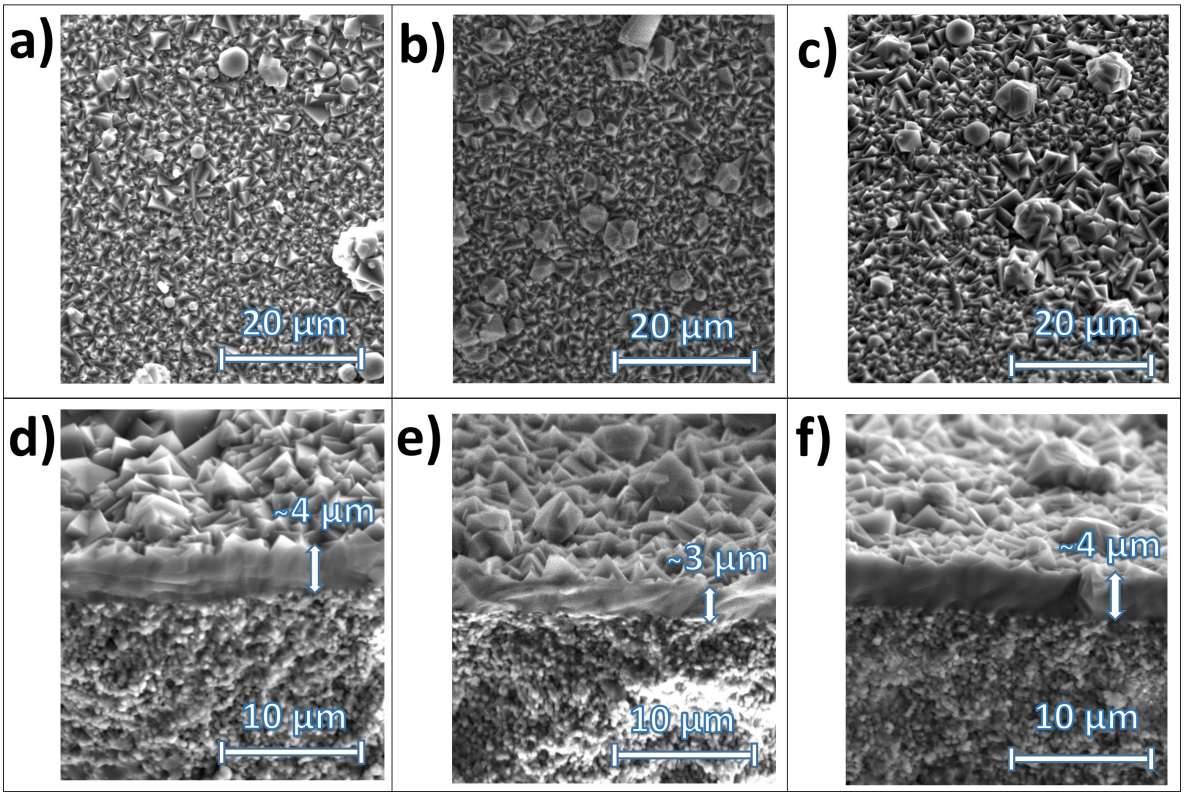

Figure II.28: SEM micrographs of the 5 cm long LTA membrane prepared with an increased amount of synthesis gel and mixed during the synthesis: (a) top view, bottom part of the membrane, (b) top view, middle part of the membrane, (c) top view, top part of the membrane, (d) side view, bottom part of the membrane, (e) side view, middle part of the membrane, (f) side view, top part of the membrane.

II.2.3.2 Long SOD membrane preparation

5 cm long SOD membrane were prepared with the knowledge acquired during the scale up of the LTA membrane's synthesis method. As such, the hydrothermal vessel was completely filled with synthesis gel and the shorter Teflon holder was employed (as described in Figure II.11b). No mixing of the synthesis gel was applied as the moving plate apparatus was unable to withstand the higher reaction temperatures required for SOD synthesis.

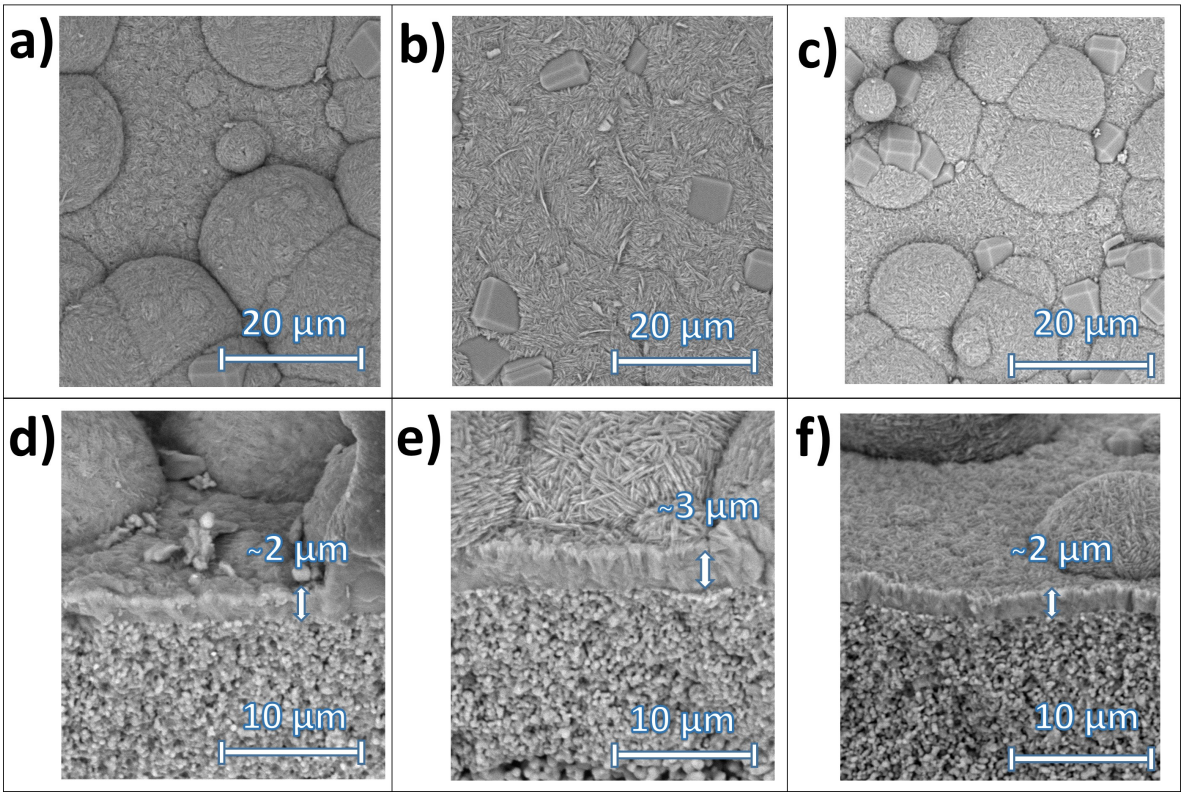

Figure II.29: SEM micrographs of the 5 cm long SOD membrane prepared with an increased amount of synthesis gel: (a) top view, bottom part of the membrane, (b) top view, middle part of the membrane, (c) top view, top part of the membrane, (d) side view, bottom part of the membrane, (e) side view, middle part of the membrane, (f) side view, top part of the membrane.

The SEM micrographs featured on Figure II.29 present a well intergrown SOD membrane with no defects visible from the surface. The membrane is acceptably 2-3 µm thick in its thinnest regions. These observations are in line with the ones made on the preparation of shorter 1 cm long SOD membrane. The improvement due to the increase in quantity of synthesis gel applies as well as in the synthesis of 5 cm long SOD membrane. Furthermore, no thickness gradient is visible from the micrographs.

II.2.3.3 Numerical investigation of diffusion limitations

To further investigate that the diffusion of reactants inside the synthesis gel of both long LTA and SOD membrane is the limiting factor of the growth of the membrane, a dimensionless number (analog to a Damköhler's number) comparing diffusion and growth rates was created (Eq. II.5).

$$Da = \frac{Diffusion\ rate}{Growth\ rate} = \frac{\frac{DC_m}{r_t}}{\frac{\Delta_m}{s\Delta_t}} \tag{II.5}$$

$$D = \frac{k_B T}{6\pi\eta r_{pz}} \tag{II.6}$$

The diffusion rate is calculated through a simplified Fick's law where the mass concentration of reactants is supposed to be equal to 0 at the membrane surface and C_m at the center of

the tubular support. Thus, the characteristic length in this calculation is the radius r_t of the support. The diffusion coefficient D is calculated by the Stokes-Einstein equation with various zeolite particle radius sizes r_{pz} of LTA seeds formed during the synthesis (equation II.6). The growth rate is calculated by weighing the support before and after hydrothermal synthesis Δm, taken from a synthesis with no mixing, in relation to the surface of the support S and the duration of the synthesis Δt. This analysis, using this dimensionless number, does not account for the potential depletion of reactants in the synthesis solution caused by the extent of the reaction or by the sedimentation of zeolite nuclei towards the bottom of the hydrothermal vessel.

Table II.7: Viscosity measurements of different composition of synthesis gel at various temperatures. (a) LTA synthesis gel: 1 Al_2O_3 : 5 SiO_2 : 50 Na_2O : 1000 H_2O, (b) SOD synthesis gel: 1 Al_2O_3 : 5 SiO_2 : 50 Na_2O : 500 H_2O.

Gel composition	**(a)**		**(b)**	
Temperature (°C)	21	60	21	90
Viscosity (Pa.s)	$4.06{\cdot}10^{-3}$	$1.88{\cdot}10^{-3}$	$1.45{\cdot}10^{-2}$	$2.66{\cdot}10^{-3}$

During the rheological studies of LTA and SOD synthesis gel, the viscosity of both gel at reaction temperature is around 10^{-3} Pa.s (Table II.7). According to the calculations of the Damköhler's number (Figure II.30), the diffusivity of small zeolite nuclei (<10-20 nm) is sufficient to allow these crystals to contribute to membrane growth, whereas larger zeolite nuclei cannot reach the support surface in time. This cutoff nuclei size is high enough to suggest that dissolved silica and alumina as well as small zeolite nuclei are able to participate in the reaction without requiring a mixing of the gel. This result is in line with what was observed experimentally as mixing of the synthesis gel displayed no improvement on the membrane synthesis.

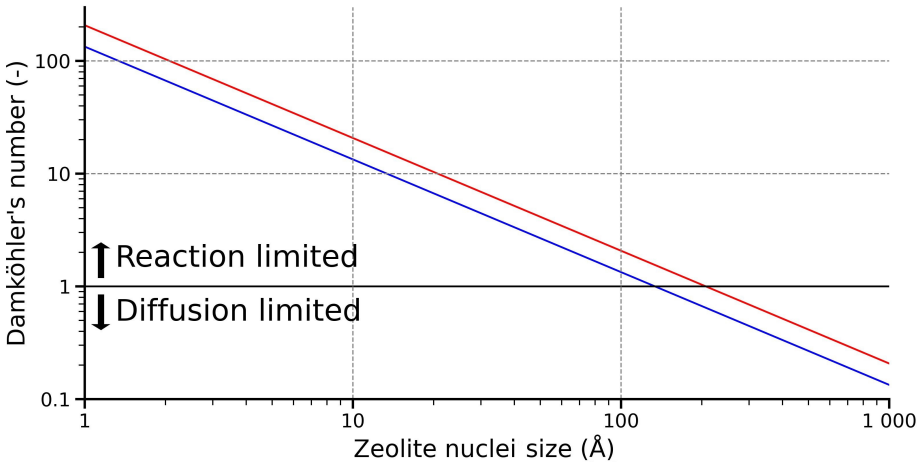

Figure II.30: Damköhler's number calculation for different size of zeolite nuclei. Blue line: LTA synthesis gel at 60°C, Red Line: SOD synthesis gel at 90°C.

Similarly, Huang *et al.* [27] reported that gravitational forces caused zeolite powders to settle at the bottom of the hydrothermal vessel, which hypothetically led to a depletion of reactants in their synthesis solutions. Similar to our observations, the mixing of the synthesis gel (achieved

through the use of a vacuum in their study) resulted in a decrease in the thickness gradient of the zeolite membrane. However, unlike our findings, they observed an enhancement in membrane growth. Additionally, Tiscareno *et al.* [66] noted that the application of centrifugal forces to direct reactants towards the support's surface improved the quality of the zeolite membrane. Nevertheless, their study employed substantially higher gel concentrations, likely resulting in increased viscosity and thus lower diffusivity in a static synthesis environment.

II.2.4 Conclusion

In this study, the optimal parameters of the hydrothermal synthesis of LTA membranes are found to be 60°C for 24 h. Exceeding these values leads to unwanted SOD and FAU phase formation. Moreover, an ageing of 20h of the synthesis gel increases the density of the zeolite membrane layer by generating more zeolite nuclei before synthesis. Support treatment is also a key element to prevent defects in LTA membranes. Although secondary growth protocols are more complex than primary growth methods, they are more reliable, allowing for precise control of crystal growth by decoupling the nucleation and growth steps. However, the synthesis of nanosized seeds and other additional steps will increase the cost of membrane preparation, particularly when scaling up from laboratory methods to an industrial level [72].

For the preparation of SOD membranes, the implementation of two successive hydrothermal syntheses results in the formation of a homogeneous SOD layer on the support. By increasing gel concentration, SOD membranes are selectively synthesized at lower temperatures. Nevertheless, findings in the present study indicate that SOD membranes exhibit lower thermal stability compared to LTA membranes, which contradicts previous reports in the literature.

Increasing the quantity of synthesis gel in the reaction vessel is critical for scaling up LTA and SOD synthesis methods on 5 cm membrane supports. However, mixing the synthesis gel during synthesis plays a negligible role in membrane growth, as the diffusion of reactants is fast enough not to impede on crystal growth.

II.3 Gas and vapor permeation studies

In this section, the separation performances of the membranes synthesized in Section II.2 are measured using a custom-made and designed membrane test bench. The objective is to provide extensive permeance data for all of the species present during methanol synthesis (H_2, CO_2, CO, H_2O and MeOH) at reaction condition (200°C to 280°C). These comprehensive permeation laws would then be utilized to accurately model membrane behavior at reaction conditions in membrane reactors models for realistic membrane-assisted process simulations.

This work was conducted at CEA Grenoble's LRP (*Laboratoire des Réacteurs et Procédés*) under the supervision of Dr. Albin CHAISE.

II.3.1 Materials and methods

II.3.1.1 Permeation experiments

II.3.1.1.a Experimental setup

The permeation performances of selected LTA and SOD membranes were determined in a custom-made membrane test-bench represented on Figure II.31.

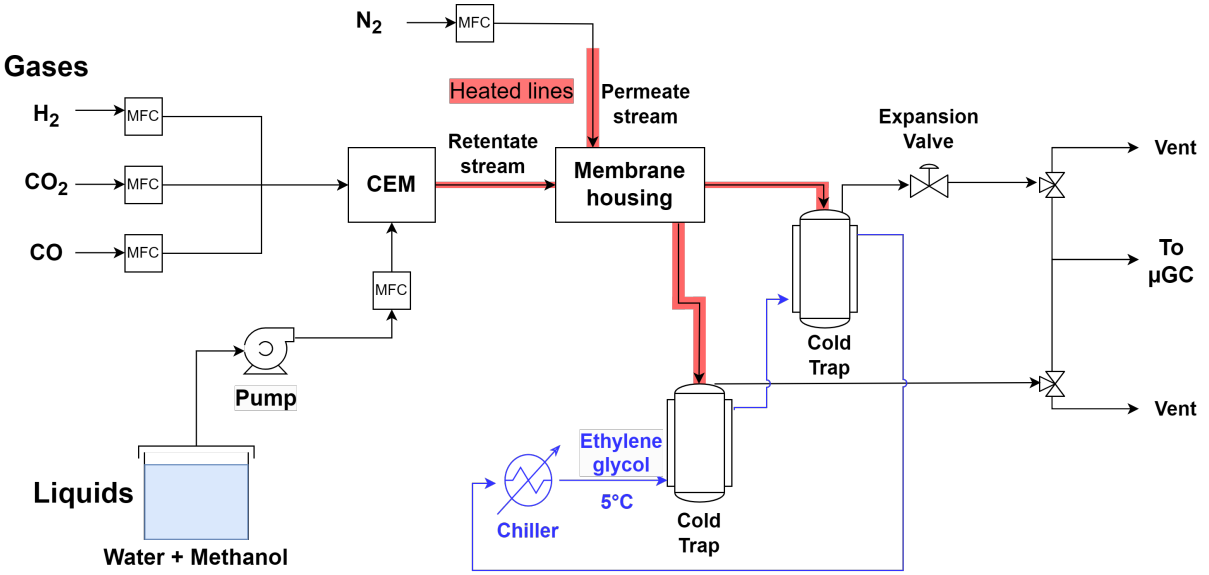

Figure II.31: Experimental setup for the permeation experiments.

Gases (H_2, CO_2 and CO) were fed from individual gas cylinder stacks to the test bench using Bronkhorst EL-FLOW Select mass flow controllers (MFCs). Liquids (H_2O and MeOH) were pumped from a reservoir containing an equimolar mixture of water and methanol and then fed using a Bronkhorst LIQUI-FLOW MFC. The flowrate of every gas and liquid were calculated to produce an equimolar $H_2/CO_2/CO/H_2O$/MeOH mixture. Thus, the flowrate for each individual gas was 0.5 NL/min and the corresponding liquid flowrate was 67 g/h. All gases and liquid were fed to the Controlled Evaporation Mixing (CEM) (Bronkhorst), set to 200°C to evaporate and mix water and methanol vapors to the gases. This equimolar mixture was then fed, using heated lines set to 200°C, to prevent condensation, to a custom-made membrane housing, set at the

desired temperature. After the membrane separation, this retentate stream was cooled down using a cold trap set at 5°C using a Julabo 1000F chiller. Afterward, gases exiting the cold trap were expanded to atmospheric pressure using an APTech expansion valve. Using the expansion valve, the pressure inside the apparatus was set to 10 barg during the permeation experiments. The resulting gases were either analyzed by the micro-gas chromatography (μGC) or vented.

The permeate stream (or sweep gas) was fed with N_2 to the test bench from an individual gas cylinder stack using an Alicat MC MFC at a flowrate of 50 sccm (standard conditions: 298 K, 1 atm). This stream was heated using a heating wire set to 130°C and fed to the membrane housing to the permeate side. The resulting permeate stream was then directed to a cold trap, cooled to 5°C using the Julabo 1000F chiller, via a heated line set to 130°C to prevent premature condensation. The gas stream exiting the cold trap was either analyzed by the μGC, vented or had its flowrate measured using an Agilent ADM Flowmeter. Since no expansion valve was fitted to the permeate stream, the stream was subjected to the atmospheric pressure whose value is approximated at 1.01325 bar for the following calculations.

For these permeation experiments, a custom-made membrane housing was employed. A helical line ran to the exterior of the housing, fed with heated oil, to heat the membrane at a specific temperature. The temperature of the membrane was measured by inserting a type K thermocouple, reaching to the middle part of the inner side of the membrane. The sealing between the permeate and retentate stream was performed using FFKM Kalrez 4079 O-rings (Techniparts) lubricated using a Teflon-based IKV Fluor MPA 0 H (IKV Tribology) grease. The sealing of this custom setup was tested externally by applying 15 barg of pressure to the retentate side of an entirely glazed-out membrane support and by measuring the flowrate at the permeate stream using the ADM flowmeter. No flow was measured using the ADM flowmeter ($< 0.1\,\mathrm{Ncm^3/min}$) validating the correct sealing of this setup.

II.3.1.1.b Analytical setup

Gases exiting the membrane test bench were analyzed using an Inficon Fusion μGC. The μGC includes two modules. The first one, fed with argon, is equipped with a Rt-Q-Bond (3 m) pre-column and a Molsieve 5A column (10 m x 0.25 mm) separated by a backflush for the analysis of H_2, N_2 and CO. For the analysis the column is set at a pressure of 30 psi and the temperature is first set at 60°C for 20 s, then heated to 92°C with a heating rate of 0.4°C/s and finally the target temperature is then held for 200 s. The second module, fed with helium, is equipped with a Rt-Q-Bond (12 m x 0.25 mm) column for the analysis of CO_2. This column is set for the analysis at a pressure of 25 psi and the temperature follows this program: 70°C held for 40 s, ramp to 100°C (heating rate: 1°C/s), ramp to 250°C (heating rate: 2.5°C/s), final target temperature of 250°C held for 70 s.

Liquid condensates (containing water and methanol) were analyzed using an Agilent 6890N gas chromatography (GC) equipped with a Restek Stabilwax column (30 m x 0.25 mm x 0.25 µm) fed with Helium. 0.2 µL of the liquid sample were injected in an injector set to 250°C with a 170:1 split ratio. The vapors were analyzed using a thermal conductivity detector (TCD) set to 150°C. The temperature for the column during the analysis was set as follows: the initial temperature of 40°C was held for 2 min then a ramp of 10°C/min was set to a target temperature of 100°C.

For the analysis of gases in the retentate, an external standardization was conducted on CO_2, H_2 and CO. Inversely, N_2 on the permeate side was used as an internal standard as no N_2 would back permeate through the membrane to the retentate side due to the pressure differences between the two compartments.

II.3.1.1.c Experimental methodology

The permeation experiments were performed as follows. First, the membrane was fitted to the membrane housing which was then mounted on the membrane test bench. Afterward, the membrane was heated to 200°C with a heating rate of 1°C/min. Until the membrane reached 100°C, only H_2, CO_2, CO was fed to the retentate side of the membrane with methanol and water being fed after this target temperature was reached. To ensure steady state, the membrane was left at 200°C with the equimolar $H_2/CO_2/CO/H_2O$/MeOH mixture being fed to the retentate side of the membrane overnight. The next day, the permeation test was performed for each studied temperature with a running time of approximately 1 h for each temperature condition. The steady state regime of the membrane was checked by taking multiple μGC measurement on each retentate and permeate side until the peak areas were stables. The permeation experiments were run over one day to prevent potential membrane instability from interfering with the results.

On Figure II.32 is represented the membrane test bench with the annotations of streams that will be re-used in the following paragraphs.

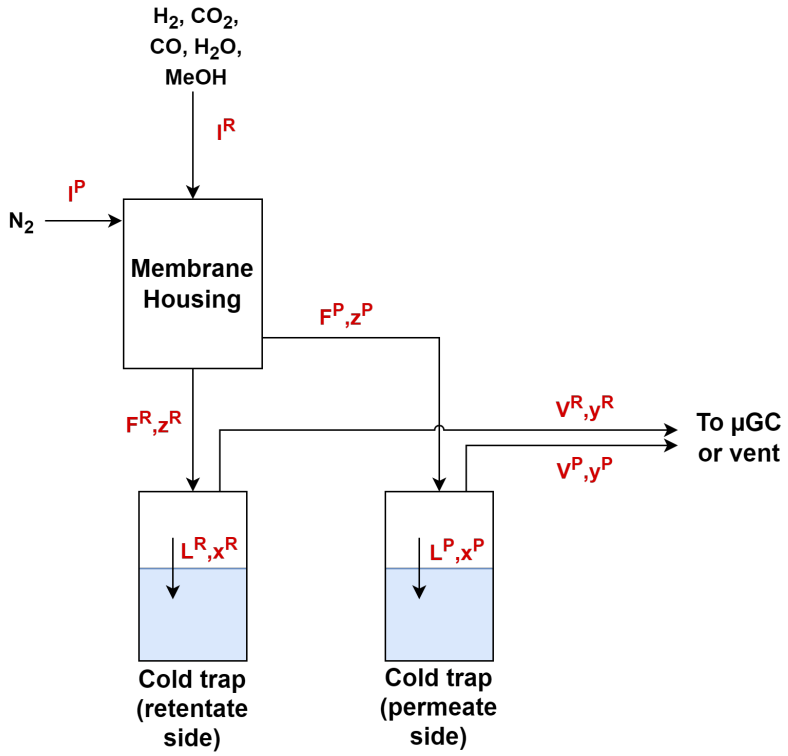

Figure II.32: Simplified diagram of the experimental setup for the permeation experiments.

The calculations of the streams on the permeate side were done independently of the retentate side. For the permeate side calculations, an ideal gas is considered for the gas phase calculations and the dissolution of gases in the liquid phase is neglected as all permeate side

streams are at atmospheric temperature. First, the flowrate of incondensable gases (H_2, CO_2, CO and N_2) are calculated using Eq. II.7. The amount of condensed water and methanol were calculated using the weight difference of the cold trap before and after an experiment and the molar fraction of the liquid determined by GC (Eq. II.8). The molar fraction of water and methanol in the vapor stream were determined according to an extended Raoult law for non-ideal solutions presented in Eq. II.9. In Eq. II.9, the activity coefficient are calculated using the non-random two-liquids (NRTL) thermodynamic model (Appendix A.2) while the Poynting factor and fugacity coefficients are neglected (due to the atmospheric pressure and the ideal gas assumption). The vapor pressure for water and methanol are calculated using correlations from the National Institute of Standards and Technology (NIST) [52, 53]. Then, the total vapor flowrate and the partial vapor flowrates of water and methanol on the permeate side were calculated using respectively Eqs. II.10 and II.11. Afterward, the partial flowrates exiting the membrane housing on the permeate side were calculated using Eqs. II.12 and II.13. The partial pressure on the permeate side of the membrane can finally be calculated using Eq. II.14.

$$F^{P,inc} = \frac{I^P_{N_2}}{y^{P,inc}_{N_2}} \tag{II.7}$$

$$L^P_i = \frac{\Delta m^P}{\Delta t} \frac{x^P_i}{x^P_{MeOH} M_{MeOH} + x^P_{H_2O} M_{H_2O}} \; ; \; i : MeOH, H_2O \tag{II.8}$$

$$y^P_i = \frac{x^P_i \gamma_i P^{sat}_i}{P^P} \; ; \; i : MeOH, H_2O \tag{II.9}$$

$$V^P = \frac{F^{P,inc}}{1 - y^P_{MeOH} - y^P_{H_2O}} \tag{II.10}$$

$$V^P_i = V^P y^P_i \; ; \; i : MeOH, H_2O \tag{II.11}$$

$$F^P_i = F^{P,inc} y^{P,inc}_i \; ; \; i : H_2, CO_2, CO, N_2 \tag{II.12}$$

$$F^P = L^P_i + V^P_i \; ; \; i : MeOH, H_2O \tag{II.13}$$

$$P^P_i = z^P_i P^P = \frac{F^P_i}{F^P} P^P \tag{II.14}$$

The flowrates in the retentate side streams were calculated dependently of the permeate side as no flowrate could have been measured during the experiments. Moreover, due to significant deviations between the desired flowrate, the amount of trapped water and methanol during the experiment, and the externally measured flowrate of liquid entering the CEM, no reliable data could be obtained on the actual flowrate of methanol and water fed to the membrane. Thus, unfortunately, the material balance had to be assumed to be fully closed and the amount of trapped water and methanol during the experiments were used to perform the following calculations.

To calculate the flowrates of every stream on the retentate side, the desired inlet flowrate of water and methanol set on the MFC was used as an initial estimation. Then, the flowrate exiting the membrane housing was calculated by subtracting the permeate-side flowrate to the retentate-side feed flowrate (Eq. II.15). Next, a vapor-liquid equilibrium (VLE) calculation using the predictive Soave-Redlich-Kwong (PSRK) equation of state (EoS) (described in Appendix A) was performed on the cold trap to calculate the liquid L^R and vapor V^R streams. The inlet methanol and water flowrates were then recalculated using scipy's 'least_squares' solver to match the amount of water and methanol collected in the cold trap (Eq. II.16). The outline of this algorithm is described in Figure II.33. Finally, the fugacity of the species on the retentate side of the membrane were calculated using Eq. II.17, with the fugacity coefficients being computed by the PSRK EoS (Appendix A.1).

$$F_i^R = I_i^R - F_i^P \tag{II.15}$$

$$\sum_{i:MeOH,H_2O} (L_i^{R^{Mod}} - L_i^{R^{Exp}})^2 = 0 \tag{II.16}$$

$$f_i^R = z_i^P \Phi_i^R P^R \tag{II.17}$$

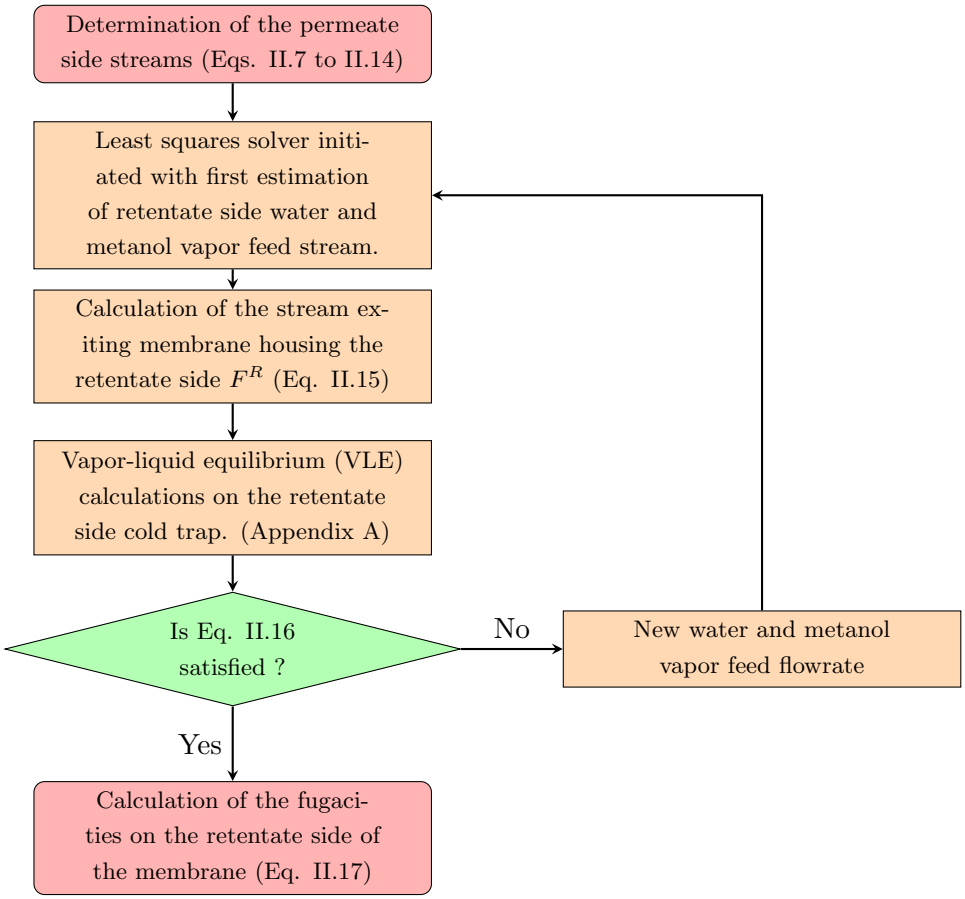

Figure II.33: Flow diagram of the algorithm used to determine the flowrates and fugacities inside the membrane test-bench.

The permeances of every species were calculated using Eq. II.18 and the permselectivity of the species were calculated using respectively Eq. II.2.

$$\Pi_i = \frac{F_i^P}{S(f_i^R - P_i^P)} \tag{II.18}$$

II.3.1.2 Defect assessment

Several LTA and SOD membranes were synthesized to investigate on the reproducibility of the synthesis methods. In this subsection, a fast method to qualitatively assess the presence of defects in the membrane is proposed. This method, inspired by Durand's PhD work [17], relies on the different transport mechanisms of species across the membrane. As transmembrane pressure differences rise, membranes with small pores where only Knudsen flow and configurational diffusion are governing the transport of species should display permeances independent of the transmembrane pressure difference (Figure II.34). However, considering a membrane with pores big enough for viscous flow to occur, the permeance of the membrane should increase at higher transmembrane pressure differences (Figure II.34). Moreover, by conducting this test at the same temperature for all pressure differences, a linear law should be observed of which coefficient is dependent partly on the mean radius of the pore (Figure II.34). As such, membrane samples with larger pore sizes should show higher slopes than those with smaller pore sizes.

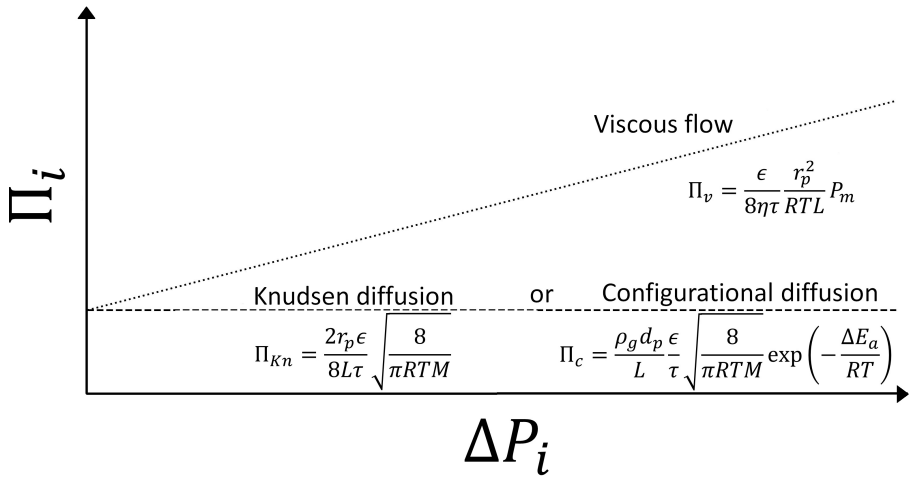

Figure II.34: Transport through the membrane relative to the pressure difference across the membrane. Figure reproduced from [17].

II.3.1.3 Experimental setup

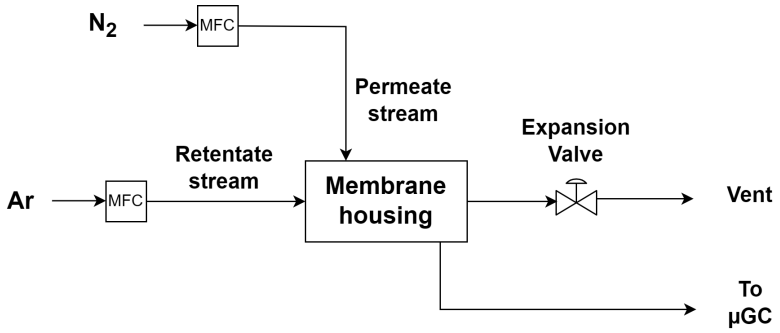

Figure II.35: Simplified diagram of the experimental setup for the defect assessment experiments.

Experiments relying on the permeation of dry argon through the membrane, were conducted at various transmembrane pressures on the test bench described in Section II.3.1.1 but simplified (represented on Figure II.35). For every membrane, argon was fed to the retentate side of the membrane using a Bronkhorst EL-FLOW Select MFC while N_2 was fed to the permeate side of the membrane using an Alicat MC MFC. The pressure inside the retentate side of the membrane ranged from 2 to 10 barg and was controlled using an APTech expansion valve. The gas exiting the permeate side of the membrane was analyzed using an Inficon Fusion μGC described in Section II.3.1.1. For these experiments, the custom-made membrane housing described in Section II.3.1.1 was re-employed without the heating with oil.

II.3.1.4 Experimental methodology

In this experiment, membranes were first stored in a desiccator to prevent moisture from affecting the results. The membranes were then mounted in the housing and placed on the test bench. Argon gas was introduced at a flow rate of 1 NL/min on the retentate side, with a transmembrane pressure difference set to 2 bar. Nitrogen (N_2) was supplied to the permeate side at a flow rate of 50 sccm (under standard conditions: 298 K, 1 atm). Four μGC analyses were performed on the gas exiting the permeate side before increasing the transmembrane pressure difference to 6 bar. The same set of four analyses was repeated at a transmembrane pressure difference of 10 bar, and finally again at 2 bar to check if the membrane's performance remained stable. The experiment was considered valid if the permeance at both 2 bar tests differed by less than 5%, ensuring that the membrane's performance was not affected by the drying of the zeolite crystals. These experiments were conducted at ambient temperature.

To determine N_2 concentration in the permeate side stream after exiting the membrane housing, the peak area of N_2 was compared to an analysis done with pure N_2 in the permeate side gas (Eq. II.19). Then, the argon flowrate exiting the membrane to the permeate side was measured using the μGC analysis along with the flow of N_2 at the inlet of the membrane housing (Eq. II.20). Finally, the argon permeance was calculated according to Eq. II.21.

$$z_{N_2}^{P} = \frac{A_{N_2}}{A_{N_2}^{pure}} \tag{II.19}$$

$$F_{Ar}^{P} = \frac{I_{N_2}^{P}}{z_{N_2}^{P}}(1 - z_{N_2}^{P}) \tag{II.20}$$

$$\Pi_{Ar} = \frac{F_{Ar}^{P}}{S(P^{R} - (1 - z_{N_2}^{P})P^{P})} \tag{II.21}$$

II.3.2 Results and discussion

II.3.2.1 Defects assessment

A total of 10 LTA membranes and 4 SOD membranes were synthesized for the permeation studies. Among the 10 LTA membranes, 6 underwent a single hydrothermal synthesis, 2 went through two successive syntheses, and the remaining 2 underwent three consecutive hydrothermal syntheses. The results of all the membrane are presented on Table II.8. Some membranes broke apart during the mounting stage due to irregularities in diameters of the membrane support, yielding critical stress on the alumina support while squishing the O-rings.

Table II.8: Evolution of argon permeance relative to the transmembrane pressure difference for LTA and SOD membrane materials.

Membrane type	**Membrane name**	$\Pi_{Ar}(\Delta P)$ **(mol.s^{-1}.m^{-2}.Pa^{-1})**			**Slope (mol.s^{-1}.m^{-2}.Pa^{-2})**	**r^2**
		$\Delta P = 2bar$	$\Delta P = 6bar$	$\Delta P = 10bar$		
LTA (1 synthesis)	LTA1a		Broken		N.D.	
	LTA1b	$5.2{\cdot}10^{-8}$	$9.1{\cdot}10^{-8}$	$1.3{\cdot}10^{-7}$	$1.3{\cdot}10^{-13}$	0.988
	LTA1c	$3.5{\cdot}10^{-7}$	$4.9{\cdot}10^{-7}$	$6.0{\cdot}10^{-7}$	$6.8{\cdot}10^{-13}$	0.94
	LTA1d	$4.0{\cdot}10^{-7}$	$6.1{\cdot}10^{-7}$	$7.6{\cdot}10^{-7}$	$8.6{\cdot}10^{-13}$	0.95
	LTA1e		Broken		N.D.	
	LTA1f		Broken		N.D.	
LTA (2 syntheses)	LTA2a	$1.1{\cdot}10^{-7}$	$2.1{\cdot}10^{-7}$	$2.7{\cdot}10^{-7}$	$2.9{\cdot}10^{-13}$	0.98
	LTA2b	$4.0{\cdot}10^{-8}$	$6.7{\cdot}10^{-8}$	$8.8{\cdot}10^{-8}$	$9.1{\cdot}10^{-14}$	0.98
LTA (3 syntheses)	LTA3a		Broken		N.D.	
	LTA3b	$1.4{\cdot}10^{-8}$	$3.4{\cdot}10^{-8}$	$4.8{\cdot}10^{-8}$	$4.7{\cdot}10^{-14}$	0.998
SOD	SODa	$1.2{\cdot}10^{-9}$	$2.7{\cdot}10^{-9}$	$3.4{\cdot}10^{-9}$	$3.4{\cdot}10^{-15}$	0.989
	SODb	$1.3{\cdot}10^{-7}$	$2.3{\cdot}10^{-7}$	$2.8{\cdot}10^{-7}$	$3.1{\cdot}10^{-13}$	0.97
	SODc	$2.4{\cdot}10^{-9}$	$4.5{\cdot}10^{-9}$	$6.2{\cdot}10^{-9}$	$6.0{\cdot}10^{-15}$	0.991
	SODd	$3.5{\cdot}10^{-8}$	$6.1{\cdot}10^{-8}$	$7.5{\cdot}10^{-8}$	$8.0{\cdot}10^{-14}$	0.97

Membranes with the highest permeances show the highest slopes, indicating the presence of larger defects in the membrane material. Therefore, viscous flow through the large defects increases the flow of argon through the membrane leading to higher overall permeances. For the LTA membranes, both permeance and slope decrease with the number of consecutive syntheses applied to the membrane material. Conducting several consecutive hydrothermal syntheses thus likely promotes additional crystal growth, covering previous macroporous defects present in the membrane layer. According to the results shown on Table II.8, SOD membranes have the lowest slopes, usually an order of magnitude below that of LTA membranes, indicating the

presence of fewer or smaller defects. This is also accompanied by argon permeance lower than that of LTA membranes, presumably due to less material transport occurring through viscous flow. However, all synthesized membranes showed a significant increase in permeance with rising pressure, suggesting the presence of macropore-sized defects in each sample, where viscous flow may be the main transmembrane transport mechanism. Finally, membrane samples synthesized through the same preparation method present significantly different results on this test, showing a poor reproducibility of the preparation methods.

II.3.2.2 Permeation experiments

In this subsection, three zeolite membranes were selected for permeation experiments at methanol synthesis temperature conditions: LTA1b, LTA3b and SODa.

On Figure II.36, LTA membranes presented higher water permeances than the SODa membrane. This observation is similar to what has been observed in the literature, where LTA membranes have larger micropores and thus have less steric hindrance for water molecules than SOD membranes [70]. Alternatively, based on the results in Section II.3.2.1, the SOD preparation method employed in this study, comprising two successive hydrothermal syntheses through primary growth, could have produced fewer defects than that of the LTA membranes, thereby reducing viscous flow through the membrane. Moreover, the water permeance for LTA membrane decreased with additional consecutive hydrothermal syntheses. A first hypothesis for this observation would be that with several consecutive hydrothermal syntheses, the increase in membrane thickness would cause a longer path for molecules to go through the zeolite layer leading to decreased flow. The other explanation would be that additional hydrothermal syntheses healed some of the intercristalline defects due to additional growth of the zeolite crystals thus reducing flow in macropores.

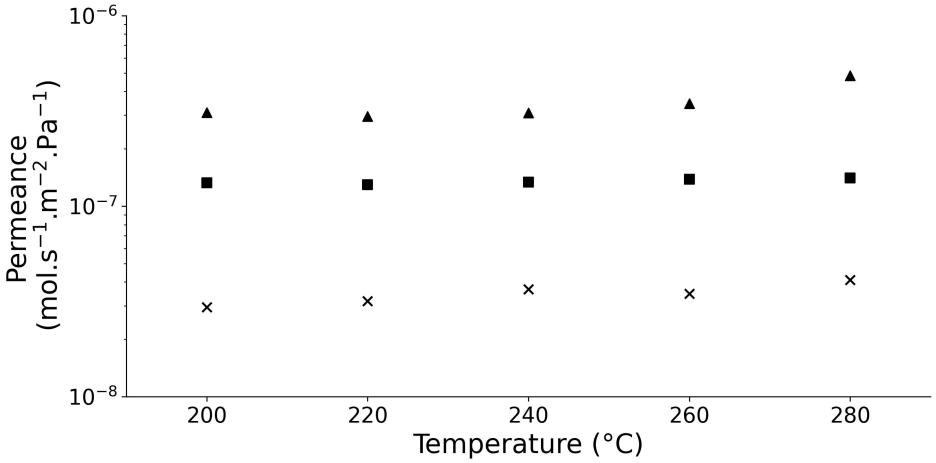

Figure II.36: H_2O permeances of: × SODa, ▲ LTA1b (1 synthesis), ■ LTA3b (3 syntheses) at methanol synthesis temperature conditions. Equimolar mixture of $H_2/CO_2/CO/H_2O$/MeOH. Transmembrane pressure difference of 10 bar.

According to the permeation results featured on Figure II.37, the permeance for every species and for every membrane increased with rising temperature. Since permeance through viscous flow and Knudsen diffusion decreases with rising temperatures, only configurational diffusion

of species through the zeolite crystal pores can explain this rise in permeance according to the temperature (Figure II.34). For most membranes tried here, the permeances of species generally ranked the following: H_2, H_2O, CO, MeOH, CO_2, which are classed according to their molecular mass. This observation points out to Knudsen type flow where permeance is inversely proportional to the square root of the molar mass of a given molecule (Figure II.34).

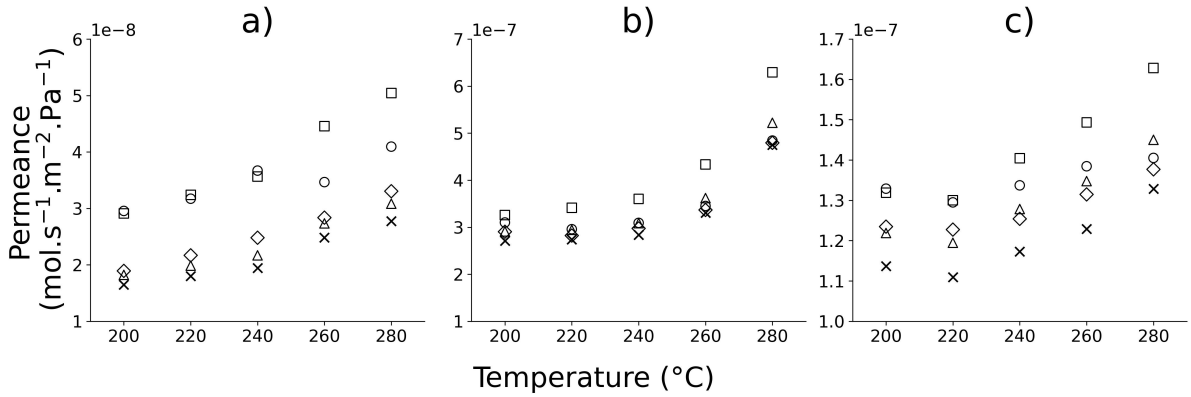

Figure II.37: Permeances of: □ H_2, ○ H_2O, ◊ MeOH, △ CO, × CO_2 at methanol synthesis temperature conditions. Equimolar mixture of $H_2/CO_2/CO/H_2O$/MeOH. Transmembrane pressure difference of 10 bar. a) SODa, b) LTA1b (1 synthesis), c) LTA3b (3 syntheses).

Permselectivities are higher for the SODa membranes than for LTA membrane which, according to the literature, could be due to the smaller micropore size of the zeolite (Figure II.38). However, the permselectivities displayed on Figure II.38 are far below than what has been described in the literature on similar membrane material (Table II.2) which points out to the presence of macropores where mostly non-selective flow would occur. Moreover, permselectivities presented in Figure II.38, follows a downward trend with temperatures rising, even markedly crossing the value of 1 for the H_2O/H_2 permselectivities (indicating the membrane is more selective towards hydrogen than water). This indicates the presence of Knudsen diffusion, in which hydrogen being lighter than water would permeate better through the intercristalline mesopores.

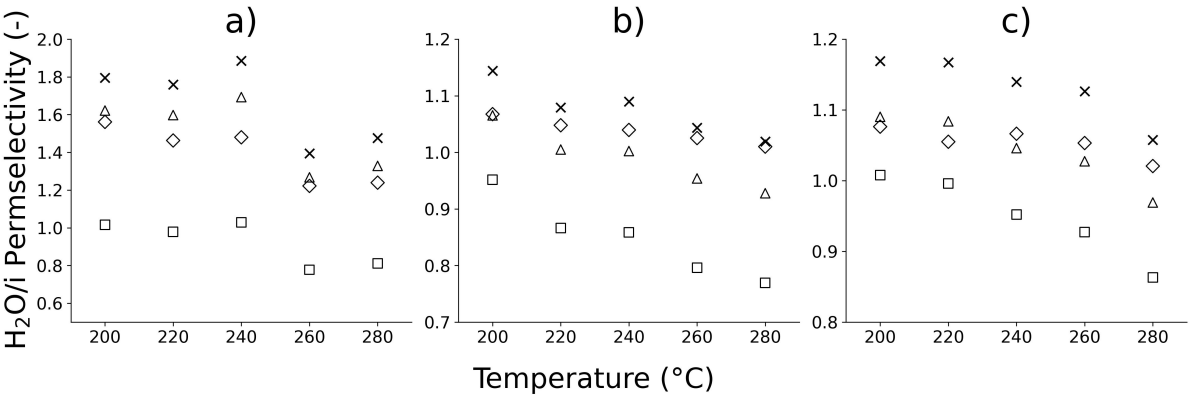

Figure II.38: Permselectivities of: × H_2O/CO_2, △ H_2O/CO, ◊ H_2O/MeOH, □ H_2O/H_2 at methanol synthesis temperature conditions. Equimolar mixture of $H_2/CO_2/CO/H_2O$/MeOH. Transmembrane pressure difference of 10 bar. a) SODa, b) LTA1b (1 synthesis), c) LTA3b (3 syntheses).

II.3.2.3 Data regression

In order to produce permeance correlations in the studied sample for every species, temperature-dependent regressions of the experimental data is proposed in this subsection.

The regressions are done on Python using the 'lm_fit' module. This module allows for fitting a model to data using the least squares method. To fit parameters to data, this module uses solvers from the scipy module. In this instance, the 'least_squares' solver from scipy has been utilized here.

A first approach using an exponential-based regression (Mod C) is proposed in Eq. II.22. This equation relies on the temperature dependence of the permeance of a species due to configurational diffusion. To study the presence of viscous flow or Knudsen diffusion, two additional models are proposed. The first one accounts for viscous flow and configurational diffusion transport through the membrane (Mod VC) (Eq. II.23), while the second one accounts for Knudsen and configurational diffusion (Mod KC) (Eq. II.24). Model parameters were fitted to a given species at a time.

$$Mod\ C\ :\ \Pi_i = a\sqrt{\frac{1}{T}}exp(-\frac{b}{T}) \tag{II.22}$$

$$Mod\ VC\ :\ \Pi_i = a\frac{1}{T} + b\sqrt{\frac{1}{T}}exp(-\frac{c}{T}) \tag{II.23}$$

$$Mod\ KC\ :\ \Pi_i = a\sqrt{\frac{1}{T}} + b\sqrt{\frac{1}{T}}exp(-\frac{c}{T}) \tag{II.24}$$

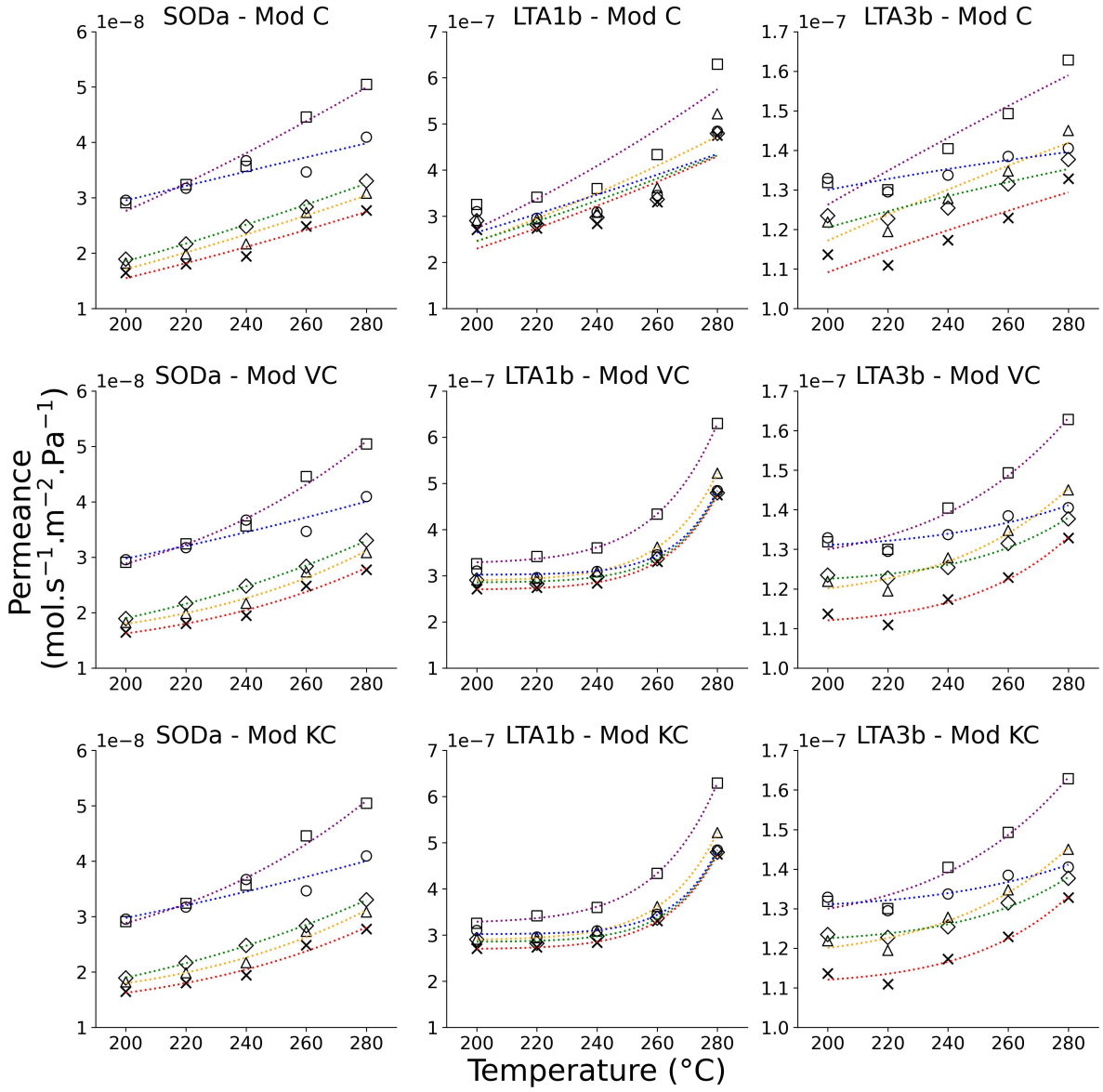

Figure II.39: Permeances predicted using Mod C, VC and KC on all studied membranes. □ H_2, ○ H_2O, ◇ MeOH, △ CO, × CO_2.

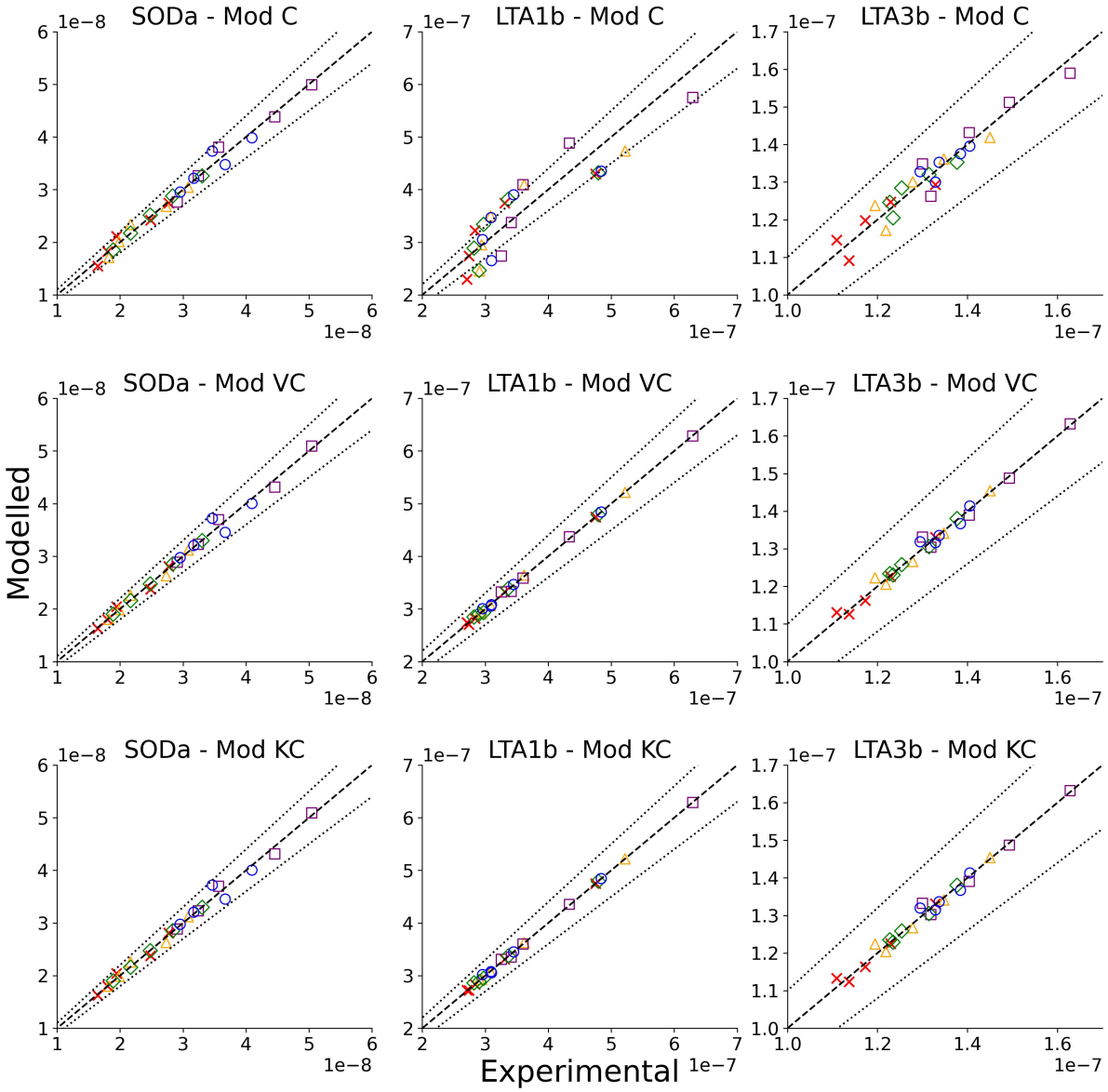

Figure II.40: Parity plots for Mod C, VC and KC on all studied membranes. □ H_2, ○ H_2O, ◊ MeOH, △ CO, × CO_2. Dotted line represents ±10% error.

Mod C fits well on the permeance data of the SODa membrane with less than 10% error on the prediction of experimental data (Figure II.40). However, this model does not fit properly on the permeance data of LTA membrane (Figure II.39 and II.40). One hypothesis linked with the poor selectivity of the synthesized LTA membranes is the presence of non-selective viscous flow or less selective Knudsen diffusion, with Mod VC and Mod KC proposed to study this hypothesis. Both models fit well the experimental data (Figure II.39 and II.40) as the permeance data the regression of these model is not sensitive enough so that no difference can be seen from fitting a law inversely dependent of the temperature (corresponding to viscous flow) or inversely dependent on the square root of the temperature (corresponding to Knudsen diffusion). This lack of distinction between these two transport regimes is further highlighted by the quasi-constant nature with rising temperatures of both of these terms as seen on Figure II.41.

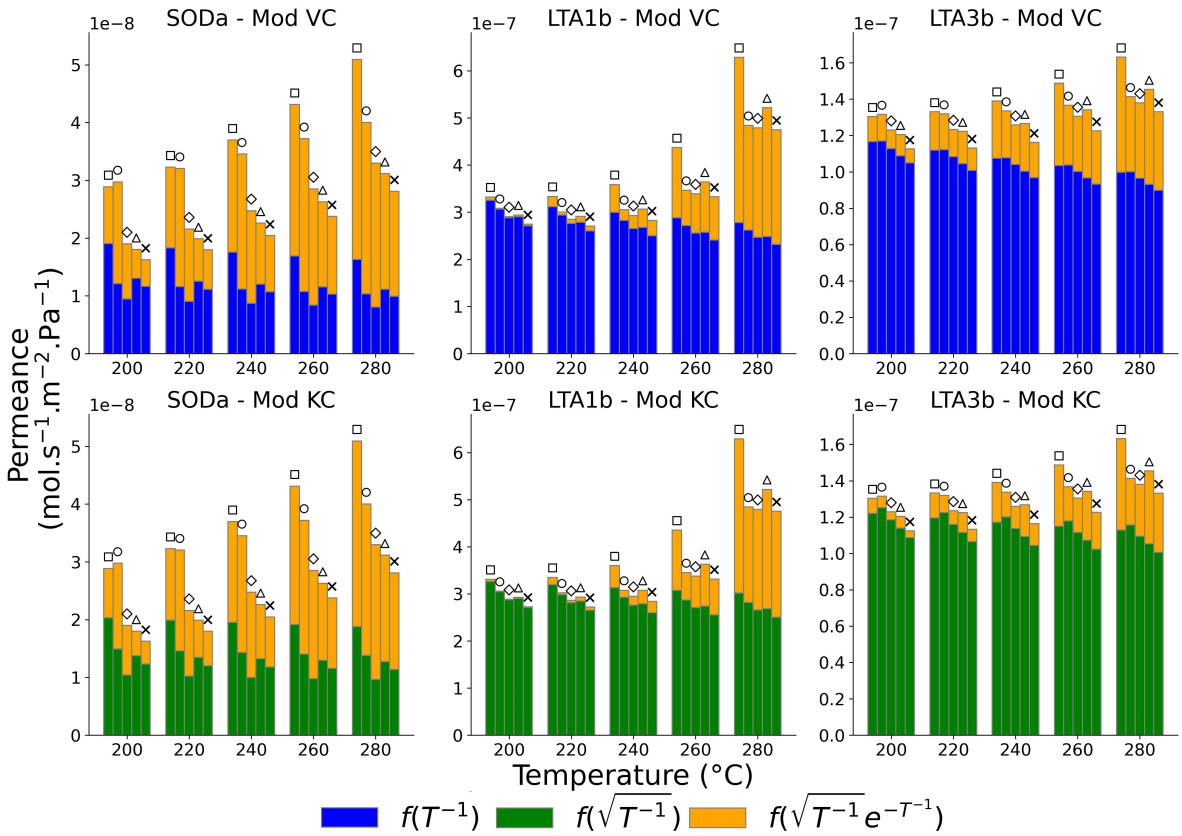

Figure II.41: Fractions of viscous flow (blue) and configurational diffusion (yellow) for Mod VC, or Knudsen diffusion (green) and configurational diffusion (yellow) for Mod KC. □ H_2, ○ H_2O, ◊ MeOH, △ CO, × CO_2.

In Figure II.41 are presented the predicted fraction of configurational diffusion, Knudsen diffusion and viscous flow in models VC and KC. According to these results, the main mode of flow at low temperature would be either viscous flow or Knudsen diffusion. At higher temperature, the increasing permeances can only be described using the configuration diffusion term and thus its fraction increases.

The configurational diffusion term of both Mod VC and KC have been isolated to produce the permeance laws featured on Figure II.42. However, the results present unrealistic membranes performances for LTA1b as the permeance ranges for four orders of magnitude on the range of studied conditions. Moreover, even after removing the terms either associated with viscous flow or Knudsen diffusion, the separation performances of each of the membranes are still well below of what have been described in the literature (Table II.2). Therefore, Model VC and KC are not able to accurately predict the fractions of transmembrane material transport happening through configurational diffusion or less selective viscous flow and Knudsen diffusion.

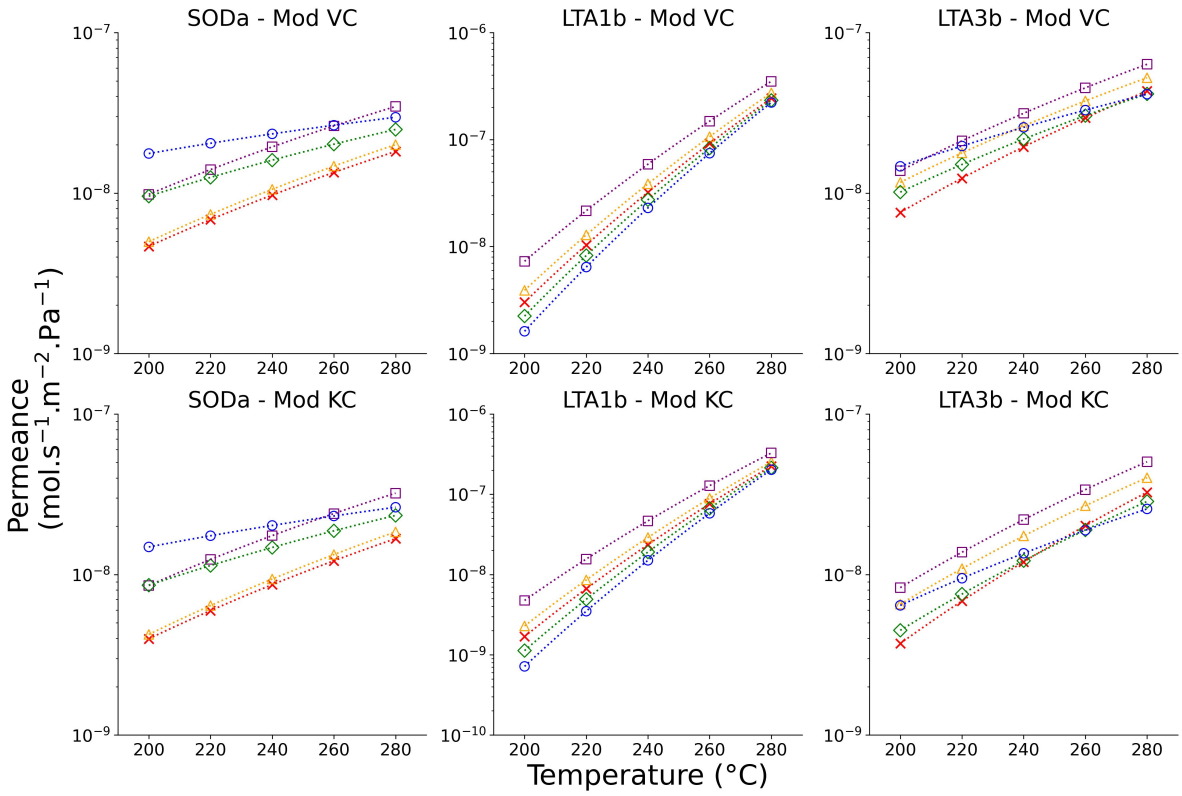

Figure II.42: Permeances calculated using only the configurational diffusion term of Mod VC and KC. □ H_2, ○ H_2O, ◊ MeOH, △ CO, × CO_2.

Due to the low temperature sensitivity of the viscous flow or Knudsen diffusion terms of both Mod VC and KC, a last simplified Mod CC model is proposed (Eq. II.25) featuring a constant and an exponential law and its results are featured on Figure II.43 and Table II.9.

$$Mod\ CC\ :\ \Pi_i = a + b \cdot exp(-\frac{c}{T}) \tag{II.25}$$

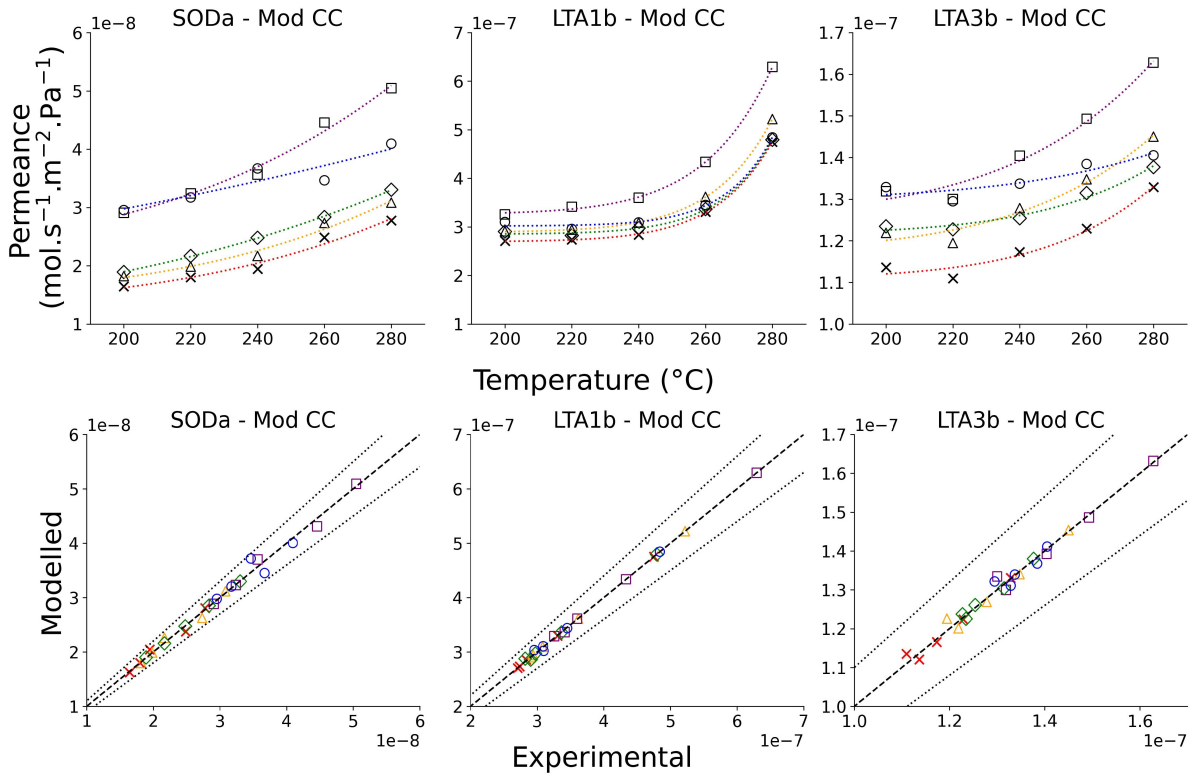

Figure II.43: Permeance predictions and parity plot for Mod CC on all studied membranes. □ H_2, ○ H_2O, ◊ MeOH, △ CO, × CO_2. Dotted line on parity plots represents ±10% error.

Table II.9: Fitted parameters of Mod CC for H_2, CO_2, CO, H_2O and MeOH for all the studied membranes.

SOD			
	a	**b**	**c**
H_2	$(1.29 \pm 0.44)\cdot10^{-8}$	$(1.22 \pm 5.86)\cdot10^{-4}$	$(4.97 \pm 2.8)\cdot10^{3}$
H_2O	$(1.45 \pm 0.40)\cdot10^{-8}$	$(1.69 \pm 7.04)\cdot10^{-4}$	$(5.1 \pm 2.41)\cdot10^{3}$
MeOH	$(2.15 \pm 0.69)\cdot10^{-8}$	$(1.11 \pm 3.76)\cdot10^{-4}$	$(4.56 \pm 1.98)\cdot10^{3}$
CO	$(1.14 \pm 0.13)\cdot10^{-8}$	$(1.02 \pm 0.50)\cdot10^{-5}$	$(3.41 \pm 0.32)\cdot10^{3}$
CO_2	$(1.78 \pm 5.52)\cdot10^{-8}$	$(8.79 \pm 90.0)\cdot10^{-7}$	$(2.03 \pm 6.80)\cdot10^{3}$
LTA1			
	a	**b**	**c**
H_2	$(2.70 \pm 0.01)\cdot10^{-7}$	$(3.37 \pm 3.00)\cdot10^{7}$	$(1.81 \pm 0.05)\cdot10^{4}$
H_2O	$(2.89 \pm 0.01)\cdot10^{-7}$	$(8.80 \pm 3.92)\cdot10^{6}$	$(1.73 \pm 0.02)\cdot10^{4}$
MeOH	$(3.26 \pm 0.04)\cdot10^{-7}$	$(3.00 \pm 3.93)\cdot10^{5}$	$(1.53 \pm 0.07)\cdot10^{4}$
CO	$(2.85 \pm 0.04)\cdot10^{-7}$	$(6.24 \pm 20.6)\cdot10^{8}$	$(1.98 \pm 0.18)\cdot10^{4}$
CO_2	$(3.02 \pm 0.06)\cdot10^{-7}$	$(1.87 \pm 11.4)\cdot10^{10}$	$(2.17 \pm 0.334)\cdot10^{4}$
LTA3			
	a	**b**	**c**
H_2	$(1.11 \pm 0.03)\cdot10^{-7}$	$(7.95 \pm 56.8)\cdot10^{-1}$	$(9.62 \pm 4.00)\cdot10^{3}$
H_2O	$(1.17 \pm 0.05)\cdot10^{-7}$	$(2.88 \pm 18.5)\cdot10^{-2}$	$(7.66 \pm 3.62)\cdot10^{3}$
MeOH	$(1.26 \pm 0.06)\cdot10^{-7}$	$(2.13 \pm 11.1)\cdot10^{-2}$	$(7.33 \pm 2.96)\cdot10^{3}$
CO	$(1.22 \pm 0.02)\cdot10^{-7}$	$(2.35 \pm 13.2)\cdot10^{-1}$	$(9.11 \pm 3.15)\cdot10^{3}$
CO_2	$(1.30 \pm 0.06)\cdot10^{-7}$	$(5.21 \pm 79.6)\cdot10^{-3}$	$(7.21 \pm 8.65)\cdot10^{3}$

The simplified Mod CC fits the experimental data well (Figure II.43). However, uncertainties featured on Table II.9, are often very high especially on the 'b' and 'c' parameters, which represent the exponential law corresponding to configurational diffusion. Therefore, the experimental data set is likely not precise or not comprehensive enough to fit a three-parameter model to it. Moreover, the 'c' term corresponds to an activation energy linked with the adsorption of a molecule on the zeolite. Thus, for a hydrophilic zeolite, the lowest value is expected to be found for water due to its affinity with the membrane material, which is unfortunately never the case (Table II.9). This further indicates the inaccuracy of this approach for rationalizing the different flow regimes through the membrane, despite correctly fitting the experimental data.

II.3.3 Post permeation SEM analysis

The membranes tested for gas permeation at temperatures ranging from 200 to 280°C were analyzed with a SEM to observe potential structural change and defect formation on the membrane due to the exposure of harsh hydrothermal conditions.

With regards to the SEM micrographs featured on Figure II.44, all LTA membranes feature changes after being exposed to harsh hydrothermal conditions. Notably, the LTA1b membrane exhibits significant defects, including large fractures and signs of delamination. However, this

membrane underwent more temperature cycles than the others due to repeated gas permeation experiments. The LTA3b membrane also shows structural alterations, with a surface layer that appears to result from zeolite de-alumination and recrystallization into another zeolite structure. In contrast, The SODa membrane appears to be the most unchanged with micrographs resembling those in Section II.2.2.2 showing no surface cracks despite similar temperature-induced fractures under dry conditions, as noted in Section II.2.2.3.

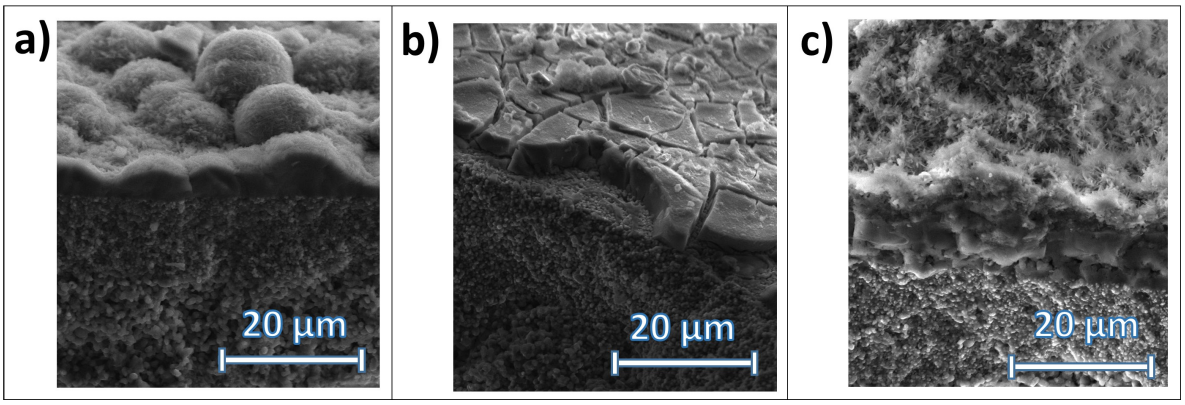

Figure II.44: SEM micrographs of: a) SOD, b) LTA1b and c) LTA3b membranes after the permeation studies.

Pinholes with diameter around 100 µm were observed on the glaze layer of the SODa membrane (Figure II.45). While it is not certain that these holes are able to pierce through the sealing glaze layer, these holes are large enough to warrant concerns on the sealing of the membrane in the membrane housing which would influence the results presented in this section.

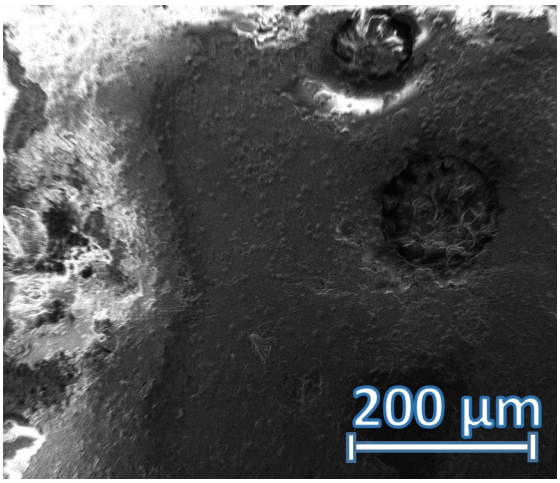

Figure II.45: SEM micrographs of SOD, LTA1b and LTA3b membranes after the permeation studies.

II.3.4 Conclusion

Separation performances of LTA and SOD membranes synthesized in-house were investigated through gas permeation of H_2, CO_2, CO, H_2O and MeOH using a custom membrane test bench.

First, a fast defect assessment method relying on the evolution of the permeance relative

to the transmembrane pressure difference was proposed. This highlighted the presence of viscous flow through the membrane due to the presence of macro-pores on the membrane surface. According to this test, SOD membranes present fewer defects than LTA membranes. Moreover, the significance of defects decreased on LTA membrane along the number of consecutive hydrothermal synthesis the membrane was subjected to.

During the gas permeation experiments, LTA membranes presented higher permeance towards water than the SOD membrane, which is commonly observed in the literature and attributed to the smaller pore size of SOD. However, this could also result from a higher defect density in LTA membranes due to differences in preparation methods. Moreover, the LTA membrane with 3 consecutive hydrothermal synthesis showed a decreased water permeance compared to the one subjected to only one synthesis, possibly indicating defect coverage by additional crystal growth. The permselectivities of both SOD and LTA membranes were significantly lower than those reported in the literature with values close to one. This observation is another clue towards the presence of defects where viscous flow or Knudsen diffusion hindering the separation performance of the membranes. Nonetheless, SOD membranes presented the highest permselectivities which is either due to the small size of the zeolite crystal acting as a molecular sieve between water and the other molecule or the reduced presence of defects (which is consistent with the defect assessment experiments).

Fitting an exponential type of law, representing the flow of compounds through configurational diffusion inside the zeolite pores, on the experimental permeance data proved to be inaccurate for the LTA membranes while good accuracy was reached for the SOD membrane. Incorporating viscous flow or Knudsen diffusion improved the fit to the experimental data, but neither approach accurately modeled the flow fractions occurring through the membrane. Given that there is evidence for every type of transmembrane flow in these permeation experiments, it is thus likely that a combination of viscous flow, Knudsen and configurational diffusion occurred in these permeation experiments.

II.4 Conclusion

In this chapter, preparation methods for the synthesis of LTA and SOD zeolite membranes have been proposed and implemented with key synthesis parameters being studied for an optimal synthesis of these materials. Secondary growth methods were seen as more effective in preventing the formation of defects as it allowed for more control in the nucleation and growth stages of the preparation of the zeolite membrane. A small scale-up of the preparation of these materials was also explored and the quantity of synthesis gel during synthesis has been identified as a significant factor to prevent defect formation in longer membranes.

While the SEM micrographs presented during the synthesis stages of zeolites membranes were promising with no defects visible from the surface of the membranes, the permeation studies identified major defects in every membrane sample synthesized. The proposed fast defect assessment test indicated the presence of viscous flow happening in macropores more so in LTA membranes than in SOD ones, potentially indicating a more robust SOD preparation method. Moreover, while the permselectivities of every membrane sample were much lower than expected compared to the literature, the SOD membranes displayed permselectivities higher

than of the other LTA membranes. Analysis of the membrane samples after the permeation studies revealed significant hydrothermal degradation of the LTA membranes. Additionally, pinholes were spotted on the sealing glaze layer of the support indicating that these permeation tests were potentially disrupted by viscous flow happening outside the membrane layer.

To fully assess the potential of membrane reactor technologies, extensive permeance data on state-of-the-art zeolite membrane materials at reaction conditions are still required to support accurate modeling and simulation efforts. Additionally, understanding the stability of these materials and their ability to endure temperature cycles, is crucial for conducting thorough environmental and techno-economic analyzes at the process level. Although this study did not succeed in producing state-of-the-art membrane materials, it did identify some limitations regarding their stability. Therefore, further research is needed to determine the operational boundaries of these materials.

Glossary (Chapter II)

Acronyms

μGC Micro-Gas Chromatography
APTES 3-aminopropyltriethoxysilane
CBU Composite Building Unit
CEM Controlled Evaporation Mixing (Bronkhorst)
CHA Chabazite
DFT Density Functional Theory
DME Dimethyl Ether
EoS Equation of State
FAU Faujasite
GC Gas Chromatography
IUPAC International Union of Pure and Applied Chemistry
IZA International Zeolite Association
LTA Linde Type A
MFC Mass Flow Controller
MFI Mobil Five
MOR Mordenite
N.D. Not Determined
NIST National Institute of Standards and Technology
NRTL Non-Random Two-Liquids
PBU Primary Building Unit
PSRK Predictive Soave-Redlich-Kwong
SBU Secondary Building Unit
SDA Structure Directing Agent
SEM Scanning Electron Microscope
SOD Sodalite
T Linde type T (IZA code: OFF)
TCD Thermal Conductivity Detector
TEOS Tetraethyl orthosilicate
VLE Vapor-Liquid Equilibrium
XRD X-Ray Diffraction
ZSM-5 Zeolite Socony Mobil-5

Roman letters

A_i Peak area of species i in the on the micro gas chromatographs (arb. unit.)
C_m Mass concentration of reactants in the synthesis gel (g/m^3)
Da Damköhler number (-)
D Diffusion coefficient (m^2/s)
F_i Partial molar flowrate of species i at the exit of the membrane housing (P: permeate side, R: retentate side, inc: incondensable gases (H_2, CO_2, CO and N_2)) (mol/s)

F Total molar flowrate at the exit of the membrane housing (P: permeate side, R: retentate side) (mol/s)

G_i Permeability of species i (mol.m^{-1}.Pa^{-1}.s^{-1})

I_i Partial molar flowrate of species i at the inlet (P: permeate side, R: retentate side) (mol/s)

L_i Partial molar flowrate of species i in the condensed liquid stream (P: permeate side, R: retentate side, Mod: calculated, Exp: experimental) (mol/s)

L Total molar flowrate of the liquid stream (P: permeate side, R: retentate side) (mol/s)

M_i Molar mass of species i (g/mol)

P_i^{sat} Vapor pressure of species i (Pa)

P_i Partial pressure of species i (P: permeate side, R: retentate side) (Pa)

P Total pressure (P: permeate side, R: retentate side) (Pa)

R Ideal gas constant ($R = 8.314\,462\,618\,153\,24\,\mathrm{J\,mol^{-1}\,K^{-1}}$)

S Membrane surface (m^2)

T Temperature (K)

V_i Partial molar flowrate of species i in the vapor stream (P: permeate side, R: retentate side) (mol/s)

V Total molar flowrate of the vapor stream (P: permeate side, R: retentate side) (mol/s)

a, b, c, d Parameters for the permeance models.

e Membrane thickness (m)

f_i Fugacity of species i (P: permeate side, R: retentate side) (Pa)

k_B Boltzmann constant ($1.380649{\cdot}10^{-23}$ J.K^{-1})

r_p Pore radius (m)

r_t Internal radius of the support (m)

r_{pz} Radius of a zeolite particle (m)

v^l Molar volume (liquid phase) (mol/m^3)

x_i Molar fraction of species i in the condensed liquid stream (P: permeate side, R: retentate side)

y_i Molar fraction of species i in the vapor stream (P: permeate side, R: retentate side, inc: incondensable gases (H_2, CO_2, CO and N_2))

z_i Molar fraction of species i in the membrane housing (P: permeate side, R: retentate side)

Greek letters

ΔP_i Partial pressure difference across the membrane (Pa)

Δm^P Weight of liquid condensate collected in the permeate side cold trap (g)

Δm Mass of zeolite gained on the support during the synthesis (g)

Δt Duration of the experiment (s)

Φ_i Fugacity coefficient of species i (P: permeate side, R: retentate side)

Π_i Permeance of species i across the membrane (mol.s^{-1}.m^{-2}.Pa^{-1})

α^*_{AB} Separation factor between species A and B

α_{AB} Permselectivity between species A and B

η Dynamic viscosity of the gel (Pa.s)

γ_i Activity coefficient of species i

σ_i Surface tension of species i (N/m)

References

[1] Catia Algieri and Enrico Drioli. "Zeolite membranes: Synthesis and applications". In: *Separation and Purification Technology* 278 (Dec. 2021), p. 119295. ISSN: 13835866. DOI: 10.1016/j.seppur.2021.119295.

[2] Devipriyanka Arepalli et al. "Optimal synthesis of nanosize seeds for secondary growth of high performance hydroxy-sodalite (H-SOD) zeolite membranes for small gas and water separations". In: *Microporous and Mesoporous Materials* 329 (Jan. 2022), p. 111451. ISSN: 13871811. DOI: 10.1016/j.micromeso.2021.111451.

[3] A. Ateka et al. "Kinetic modeling and reactor design of the direct synthesis of dimethyl ether for CO_2 valorization. A review". In: *Fuel* 327 (Nov. 2022), p. 125148. ISSN: 00162361. DOI: 10.1016/j.fuel.2022.125148.

[4] Mirza A. Baig et al. "In-situ aging microwave heating synthesis of LTA zeolite layer on mesoporous TiO_2 coated porous alumina support". In: *Journal of Crystal Growth* 432 (Dec. 2015), pp. 123–128. ISSN: 00220248. DOI: 10.1016/j.jcrysgro.2015.09.012.

[5] Thomas Bein. "Synthesis and Applications of Molecular Sieve Layers and Membranes". In: *Chemistry of Materials* 8.8 (Jan. 1, 1996). Publisher: American Chemical Society, pp. 1636–1653. ISSN: 0897-4756. DOI: 10.1021/cm960148a.

[6] Travis C. Bowen, Richard D. Noble, and John L. Falconer. "Fundamentals and applications of pervaporation through zeolite membranes". In: *Journal of Membrane Science* 245.1 (Dec. 2004), pp. 1–33. ISSN: 03767388. DOI: 10.1016/j.memsci.2004.06.059.

[7] Zishu Cao, Ninad D. Anjikar, and Shaowei Yang. "Small-Pore Zeolite Membranes: A Review of Gas Separation Applications and Membrane Preparation". In: *Separations* 9.2 (Feb. 9, 2022), p. 47. ISSN: 2297-8739. DOI: 10.3390/separations9020047.

[8] J Caro et al. "Zeolite membranes - state of their development and perspective". In: *Microporous and Mesoporous Materials* 38.1 (July 2000), pp. 3–24. ISSN: 13871811. DOI: 10.1016/S1387-1811(99)00295-4.

[9] Jürgen Caro, Manfred Noack, and Peter Kölsch. "Zeolite Membranes: From the Laboratory Scale to Technical Applications". In: *Adsorption* 11.3 (July 2005), pp. 215–227. ISSN: 0929-5607, 1572-8757. DOI: 10.1007/s10450-005-5394-9.

[10] Gangling Chen et al. "Novel preparation of low-cost support for NaA zeolite membrane by utilizing natural clay". In: *Applied Water Science* 11.10 (Oct. 2021), p. 160. ISSN: 2190-5487, 2190-5495. DOI: 10.1007/s13201-021-01492-4.

[11] Xiaoxia Chen et al. "High-performance zeolite T membrane for dehydration of organics by a new varying temperature hot-dip coating method". In: *AIChE Journal* 59.3 (2013). _eprint: https://onlinelibrary.wiley.com/doi/pdf/10.1002/aic.13851, pp. 936–947. ISSN: 1547-5905. DOI: 10.1002/aic.13851.

[12] Marlon T. Conato et al. "Framework stabilization of Si-rich LTA zeolite prepared in organic-free media". In: *Chemical Communications* 51.2 (2015), pp. 269–272. ISSN: 1359-7345, 1364-548X. DOI: 10.1039/C4CC07396G.

[13] Joaquín Coronas and Jesús Santamaría. "Separations Using Zeolite Membranes". In: *Separation and Purification Methods* 28.2 (Jan. 1999), pp. 127–177. ISSN: 0360-2540. DOI: 10.1080/03602549909351646.

[14] Domenico De Meis, M. Richetta, and E. Serra. "Microporous Inorganic Membranes for Gas Separation and Purification". In: *Interceram - International Ceramic Review* 67.4 (July 2018), pp. 16–21. ISSN: 0020-5214, 2523-8957. DOI: 10.1007/s42411-018-0023-2.

[15] Yuzhen Deng et al. "Low-cost and facile fabrication of defect-free water permeable membrane for CO_2 hydrogenation to methanol". In: *Chemical Engineering Journal* 435 (May 2022), p. 133554. ISSN: 13858947. DOI: 10.1016/j.cej.2021.133554.

[16] M.D. Dolan. "FUELS - HYDROGEN PRODUCTION — Gas Cleaning: Membrane Separators". In: *Encyclopedia of Electrochemical Power Sources*. Ed. by Jürgen Garche. Amsterdam: Elsevier, Jan. 1, 2009, pp. 319–334. ISBN: 978-0-444-52745-5. DOI: 10.1016/B978-044452745-5.00311-7.

[17] Véronique Durand. "Développement d'un nouveau procédé de synthèse de membranes inorganiques ou composites par voie CO_2 supercritique pour la séparation de gaz". PhD thesis. 2011.

[18] M.J. den Exter et al. "Zeolite-based membranes preparation, performance and prospects". In: *Studies in Surface Science and Catalysis*. Vol. 102. Elsevier, 1996, pp. 413–454. ISBN: 978-0-444-82499-8. DOI: 10.1016/S0167-2991(06)81409-6.

[19] Eric Favre. "Perméation gazeuse". In: (2023).

[20] D.A. Fedosov et al. "Methanol dehydration in NaA zeolite membrane reactor". In: *Journal of Membrane Science* 486 (July 2015), pp. 189–194. ISSN: 03767388. DOI: 10.1016/j.memsci.2015.03.047.

[21] Fausto Gallucci, Luca Paturzo, and Angelo Basile. "An experimental study of CO_2 hydrogenation into methanol involving a zeolite membrane reactor". In: *Chemical Engineering and Processing: Process Intensification* 43.8 (Aug. 2004). Number: 8, pp. 1029–1036. ISSN: 02552701. DOI: 10.1016/j.cep.2003.10.005.

[22] Xuechao Gao et al. "Fabrication of stainless steel hollow fiber supported NaA zeolite membrane by self-assembly of submicron seeds". In: *Separation and Purification Technology* 234 (Mar. 2020), p. 116121. ISSN: 13835866. DOI: 10.1016/j.seppur.2019.116121.

[23] J. Gorbe et al. "Preliminary study on the feasibility of using a zeolite A membrane in a membrane reactor for methanol production". In: *Separation and Purification Technology* 200 (July 2018), pp. 164–168. ISSN: 13835866. DOI: 10.1016/j.seppur.2018.02.036.

[24] N. E. Gordina et al. "Use of Combinations of Ultrasonic Treatment and Microwave Crystallization to Intensify the Synthesis of LTA Zeolite Membranes". In: *Petroleum Chemistry* 61.3 (Mar. 2021), pp. 292–298. ISSN: 0965-5441, 1555-6239. DOI: 10.1134/S09655441213021X.

[25] Tian Gui et al. "Scale-up of NaA zeolite membranes using reusable stainless steel tubes for dehydration in an industrial plant". In: *Journal of Membrane Science* 583 (Aug. 2019), pp. 180–189. ISSN: 03767388. DOI: 10.1016/j.memsci.2019.04.046.

[26] Na Hu et al. "Fluoride-mediated synthesis of high-flux chabazite membranes for pervaporation of ethanol using reusable macroporous stainless steel tubes". In: *Journal of Membrane Science* 510 (July 2016), pp. 91–100. ISSN: 03767388. DOI: 10.1016/j.memsci.2016.03.001.

[27] Aisheng Huang, Y.S. Lin, and Weishen Yang. "Synthesis and properties of A-type zeolite membranes by secondary growth method with vacuum seeding". In: *Journal of Membrane Science* 245.1 (Dec. 2004), pp. 41–51. ISSN: 03767388. DOI: 10.1016/j.memsci.2004.08.001.

[28] Aisheng Huang, Nanyi Wang, and Jürgen Caro. "Seeding-free synthesis of dense zeolite FAU membranes on 3-aminopropyltriethoxysilane-functionalized alumina supports". In: *Journal of Membrane Science* 389 (Feb. 2012), pp. 272–279. ISSN: 03767388. DOI: 10.1016/j.memsci.2011.10.036.

[29] Aisheng Huang et al. "Preparation and separation properties of LTA membranes by using 3-aminopropyltriethoxysilane as covalent linker". In: *Journal of Membrane Science* 350.1 (Mar. 15, 2010), pp. 5–9. ISSN: 03767388. DOI: 10.1016/j.memsci.2009.12.029.

[30] "Introduction of Microporous Membranes". In: *Microporous Materials for Separation Membranes*. Section: 1 _eprint: https://onlinelibrary.wiley.com/doi/pdf/10.1002/9783527343997.ch1. John Wiley & Sons, Ltd, 2019, pp. 1–52. ISBN: 978-3-527-34399-7. DOI: 10.1002/9783527343997.ch1.

[31] Anne Julbe and Martin Drobek. "Zeolite A Type". In: *Encyclopedia of Membranes*. Ed. by Enrico Drioli and Lidietta Giorno. Berlin, Heidelberg: Springer Berlin Heidelberg, 2016, pp. 2055–2056. ISBN: 978-3-662-44324-8. DOI: 10.1007/978-3-662-44324-8_604.

[32] Jasper van Kampen et al. "Steam separation enhanced reactions: Review and outlook". In: *Chemical Engineering Journal* 374 (Oct. 2019), pp. 1286–1303. ISSN: 13858947. DOI: 10.1016/j.cej.2019.06.031.

[33] Sheida Khajavi, Freek Kapteijn, and Jacobus C. Jansen. "Synthesis of thin defect-free hydroxy sodalite membranes: New candidate for activated water permeation". In: *Journal of Membrane Science* 299.1 (Aug. 2007), pp. 63–72. ISSN: 03767388. DOI: 10.1016/j.memsci.2007.04.027.

[34] Matthieu Lafleur et al. "Development of a water-selective zeolite composite membrane by a new pore-plugging technique". In: *Microporous and Mesoporous Materials* 237 (Jan. 2017), pp. 49–59. ISSN: 13871811. DOI: 10.1016/j.micromeso.2016.09.004.

[35] Sang Moon Lee et al. "Structure, stability and permeation properties of NaA zeolite membranes for H_2O/H_2 and CH_3OH/H_2 separations". In: *Journal of the European Ceramic Society* 38.1 (Jan. 2018), pp. 211–219. ISSN: 09552219. DOI: 10.1016/j.jeurceramsoc.2017.08.012.

[36] Huazheng Li et al. "Na^+-gated water-conducting nanochannels for boosting CO_2 conversion to liquid fuels". In: *Science* 367.6478 (Feb. 7, 2020), pp. 667–671. ISSN: 0036-8075, 1095-9203. DOI: 10.1126/science.aaz6053.

[37] Huazheng Li et al. “Synthesis of zeolite NaA membranes with high performance and high reproducibility on coarse macroporous supports”. In: *Journal of Membrane Science* 444 (Oct. 2013), pp. 513–522. ISSN: 03767388. DOI: 10.1016/j.memsci.2013.04.030.

[38] Yanshuo Li and Weishen Yang. “Microwave synthesis of zeolite membranes: A review”. In: *Journal of Membrane Science* 316.1 (May 2008), pp. 3–17. ISSN: 03767388. DOI: 10.1016/j.memsci.2007.08.054.

[39] Yanshuo Li et al. “Hydrothermal stability of LTA zeolite membranes in pervaporation”. In: *Journal of Membrane Science* 297.1 (July 5, 2007), pp. 10–15. ISSN: 03767388. DOI: 10.1016/j.memsci.2007.03.041.

[40] Yichuan Li et al. “Preparation, mechanism and applications of oriented MFI zeolite membranes: A review”. In: *Microporous and Mesoporous Materials* 312 (Jan. 2021), p. 110790. ISSN: 13871811. DOI: 10.1016/j.micromeso.2020.110790.

[41] Zhan Li et al. “High Temperature Water Permeable Membrane Reactors for CO_2 Utilization”. In: *Chemical Engineering Journal* 420 (Sept. 2021), p. 129834. ISSN: 13858947. DOI: 10.1016/j.cej.2021.129834.

[42] Bo Liu, Hidetoshi Kita, and Katsunori Yogo. “Preparation of Si-rich LTA zeolite membrane using organic template-free solution for methanol dehydration”. In: *Separation and Purification Technology* 239 (May 2020), p. 116533. ISSN: 13835866. DOI: 10.1016/j.seppur.2020.116533.

[43] *LTA: Framework Type*. Internation Zeolite Association. URL: https://europe.iza-structure.org/IZA-SC/framework.php?ID=138 (visited on 08/07/2024).

[44] Yohana Martinez Galeano, Ana M. Tarditi, and Laura M. Cornaglia. “NaA zeolite membranes on modified porous stainless steel supports: a comparative study of different SiO_2 sources”. In: *Brazilian Journal of Chemical Engineering* 37.2 (June 2020), pp. 383–397. ISSN: 0104-6632, 1678-4383. DOI: 10.1007/s43153-020-00024-y.

[45] Yohana Martínez Galeano, Laura Cornaglia, and Ana M. Tarditi. “NaA zeolite membranes synthesized on top of APTES-modified porous stainless steel substrates”. In: *Journal of Membrane Science* 512 (Aug. 2016), pp. 93–103. ISSN: 03767388. DOI: 10.1016/j.memsci.2016.04.005.

[46] L. Marcela Martínez T. et al. “Synthesis and Identification Methods for Zeolites and MOFs”. In: *Zeolites and Metal-Organic Frameworks*. Ed. by Vincent Blay, Luis F. Bobadilla, and Alejandro Cabrera García. Red. by Christian Ngô. Amsterdam University Press, 2018, pp. 25–52. ISBN: 978-94-6298-556-8. DOI: 10.2307/j.ctvcmxprm.5.

[47] Masahiko Matsukata and Eiichi Kikuchi. “Zeolitic Membranes: Synthesis, Properties, and Prospects”. In: *Bulletin of the Chemical Society of Japan* 70.10 (Oct. 1, 1997), pp. 2341–2356. ISSN: 0009-2673. DOI: 10.1246/bcsj.70.2341.

[48] T.J. Mays. “A new classification of pore sizes”. In: *Studies in Surface Science and Catalysis*. Ed. by P.L. Llewellyn et al. Vol. 160. Elsevier, Jan. 1, 2007, pp. 57–62. ISBN: 0167-2991. DOI: 10.1016/S0167-2991(07)80009-7.

[49] S. Mintova et al. *Verified Syntheses of Zeolitic Materials*. Synthesis Commission of the International Zeolite Association, 2016. ISBN: 978-0-692-68539-6.

[50] Mohau Moshoeshoe, Misael Silas Nadiye-Tabbiruka, and Veronica Obuseng. "A Review of the Chemistry, Structure, Properties and Applications of Zeolites". In: *American Journal of Materials Science* 7.5 (2017). Publisher: Scientific & Academic Publishing, pp. 196–221. ISSN: 2162-8424.

[51] Anelia van Niekerk et al. "Direct crystallisation of a hydroxy sodalite membrane without seeding using a conventional oven". In: *Journal of Membrane Science* 300.1 (Aug. 2007), pp. 156–164. ISSN: 03767388. DOI: 10.1016/j.memsci.2007.05.021.

[52] *Methyl Alcohol*. https://webbook.nist.gov/cgi/cbook.cgi?ID=67-56-1.

[53] *Water*. https://webbook.nist.gov/cgi/cbook.cgi?ID=C7732185.

[54] M. Noack et al. "Proof of the ISS-concept for LTA and FAU membranes and their characterization by extended gas permeation studies". In: *Microporous and Mesoporous Materials* 102.1 (May 4, 2007), pp. 1–20. ISSN: 1387-1811. DOI: 10.1016/j.micromeso.2006.12.024.

[55] R. Raso et al. "Zeolite membranes: Comparison in the separation of $H_2O/H_2/CO_2$ mixtures and test of a reactor for CO_2 hydrogenation to methanol". In: *Catalysis Today* (Mar. 2020), S0920586120301310. ISSN: 09205861. DOI: 10.1016/j.cattod.2020.03.014.

[56] M.P. Rohde et al. "Fischer-Tropsch synthesis with in situ H_2O removal, Directions of membrane development". In: *Microporous and Mesoporous Materials* 115.1 (Oct. 2008). Number: 1-2, pp. 123–136. ISSN: 13871811. DOI: 10.1016/j.micromeso.2007.10.052.

[57] Ali Said. "Synthèse de membranes minérales de nanofiltration par formation de films minces de zéolithes sur un support tubulaire en alumine : étude de l'évolution des propriétés de surface et des caractéristiques de filtration en milieu aqueux". PhD thesis. 2016.

[58] Ken-Ichi Sawamura et al. "Selective permeation and separation of steam from water-methanol-hydrogen gas mixtures through mordenite membrane". In: *Catalysis Today* 132.1 (Mar. 2008), pp. 182–187. ISSN: 09205861. DOI: 10.1016/j.cattod.2007.12.005.

[59] Masahiro Seshimo et al. "Membrane Reactor for Methanol Synthesis Using Si-Rich LTA Zeolite Membrane". In: *Membranes* 11.7 (June 30, 2021), p. 505. ISSN: 2077-0375. DOI: 10.3390/membranes11070505.

[60] *SOD: Framework Type*. Internation Zeolite Association. URL: https://europe.iza-structure.org/IZA-SC/framework.php?ID=221 (visited on 08/07/2024).

[61] Guoqiang Song et al. "Semi-hollow LTA zeolite membrane for water permeation in simulated CO_2 hydrogenation to methanol". In: *Journal of Membrane Science* 678 (July 15, 2023), p. 121666. ISSN: 0376-7388. DOI: 10.1016/j.memsci.2023.121666.

[62] R.P.W.J. Struis, S. Stucki, and M. Wiedorn. "A membrane reactor for methanol synthesis". In: *Journal of Membrane Science* 113.1 (May 1996). Number: 1, pp. 93–100. ISSN: 03767388. DOI: 10.1016/0376-7388(95)00222-7.

[63] Lian-Ming Sun and Jean-Yves Thonnelier. "Perméation gazeuse". In: (2004).

[64] Rosemarie Szostak. *Handbook of molecular sieves: structures*. Springer Science & Business Media, 1992.

[65] Adalgisa Tavolaro and Enrico Drioli. "Zeolite Membranes". In: *Advanced Materials* 11.12 (Aug. 1999), pp. 975–996. ISSN: 0935-9648, 1521-4095. DOI: 10.1002/(SICI)1521-4095(199908)11:12<975::AID-ADMA975>3.0.CO;2-0.

[66] F Tiscareño-Lechuga. "A novel device for preparing zeolite—A membranes under a centrifugal force field". In: *Journal of Membrane Science* 212.1 (Feb. 15, 2003), pp. 135–146. ISSN: 03767388. DOI: 10.1016/S0376-7388(02)00491-X.

[67] Leland M Vane. "Review: membrane materials for the removal of water from industrial solvents by pervaporation and vapor permeation: Removal of water from industrial solvents by pervaporation and vapor permeation". In: *Journal of Chemical Technology & Biotechnology* 94.2 (Feb. 2019), pp. 343–365. ISSN: 02682575. DOI: 10.1002/jctb.5839.

[68] Lei Wang et al. "Microwave synthesis of NaA zeolite membranes on coarse macroporous α-Al_2O_3 tubes for desalination". In: *Microporous and Mesoporous Materials* 306 (Oct. 2020), p. 110360. ISSN: 13871811. DOI: 10.1016/j.micromeso.2020.110360.

[69] Lei Wang et al. "Sustainable fabrication of large-scale tubular LTA zeolite membranes by a simple wet gel conversion". In: *Microporous and Mesoporous Materials* 329 (Jan. 2022), p. 111541. ISSN: 13871811. DOI: 10.1016/j.micromeso.2021.111541.

[70] N. Wang et al. "Hydrophilic SOD and LTA membranes for membrane-supported methanol, dimethylether and dimethylcarbonate synthesis". In: *Microporous and Mesoporous Materials* 207 (May 2015), pp. 33–38. ISSN: 13871811. DOI: 10.1016/j.micromeso.2014.12.028.

[71] N. Wang et al. "Supported SOD membrane with steam selectivity by a two-step repeated hydrothermal synthesis". In: *Microporous and Mesoporous Materials* 192 (July 2014), pp. 8–13. ISSN: 13871811. DOI: 10.1016/j.micromeso.2013.08.013.

[72] I. G. Wenten et al. "LTA zeolite membranes: current progress and challenges in pervaporation". In: *RSC Advances* 7.47 (2017), pp. 29520–29539. ISSN: 2046-2069. DOI: 10.1039/C7RA03341A.

[73] X. Xu et al. "Synthesis of a High-Permeance NaA Zeolite Membrane by Microwave Heating". In: *Advanced Materials* 12.3 (Feb. 2000), pp. 195–198. ISSN: 0935-9648, 1521-4095. DOI: 10.1002/(SICI)1521-4095(200002)12:3<195::AID-ADMA195>3.0.CO;2-E.

[74] Wenzhe Yue et al. "Highly Selective CO_2 Conversion to Methanol in a Bifunctional Zeolite Catalytic Membrane Reactor". In: *Angewandte Chemie International Edition* 60.33 (Aug. 9, 2021), pp. 18289–18294. ISSN: 1433-7851, 1521-3773. DOI: 10.1002/anie.202106277.

[75] Chen Zhou et al. "Efficient Synthesis of Dimethyl Ether from Methanol in a Bifunctional Zeolite Membrane Reactor". In: *Angewandte Chemie International Edition* 55.41 (Oct. 4, 2016), pp. 12678–12682. ISSN: 14337851. DOI: 10.1002/anie.201604753.

Chapter III

Catalytic systems for membrane-assisted CO_2 hydrogenation to methanol

In methanol synthesis, the most commonly used catalysts are heterogeneous catalysts composed of copper and zinc, supported on alumina (Al_2O_3), and are often referred to as CZA catalysts. Despite their widespread use, CZA catalysts face significant challenges: they exhibit optimal activity only at high temperatures (above 250°C), where current membrane technologies fail and thermodynamic equilibria become unfavorable. These constraints have spurred the search for novel catalysts that demonstrate higher activity at lower temperatures. First, this chapter reviews the functioning and limitations of existing catalysts used in methanol synthesis, while also exploring recent advancements in the development of innovative catalytic materials (Section III.1). Next, an experimental investigation is undertaken to evaluate potential catalyst candidates for low-temperature CO_2 hydrogenation to methanol, along with alternative synthesis pathways for direct catalyst deposition on the membrane (Section III.2).

III.1 Catalysts for CO_2 hydrogenation to methanol

Historically, methanol synthesis was carried out under very harsh operating conditions (300-400°C, 25-30 MPa) with ZnO-Cr_2O_3 catalysts [44, 67]. However, in the 1960s, Cu/ZnO/Al_2O_3 (CZA) catalysts emerged, enabling operation under much milder conditions (200-300°C, 5-10 MPa) [44, 67, 15]. Today, methanol synthesis processes still almost exclusively use CZA [44, 48]. However, CZA catalysts suffer from a limited lifespan [29, 49, 16]. In a conventional methanol process based on syngas, the bed has to be replaced every 2 to 4 years [48, 38]. This lifetime is shorter when the process is fed without CO, where large quantities of catalyst-deactivating water are generated [38]. New catalytic systems are currently being studied in order to outperform CZA catalysts in terms of stability, activity and selectivities. Details specific to the catalysis of CO_2 towards methanol are available in various reviews [67, 29, 16, 25, 58, 17, 8, 45]. In this section, a condensed summary of current and emerging catalysts for methanol synthesis will be given, followed by a discussion of the potential of these materials for application in membrane reactors.

III.1.1 Copper and zinc catalysts

III.1.1.1 Copper-Zinc-Alumina (CZA)

$Cu/ZnO/Al_2O_3$ (CZA) catalysts have been extensively studied on both laboratory and industrial scales for a century. Nevertheless, the reaction mechanisms involved in methanol synthesis, as well as the roles and effects of the various catalyst compounds, are still very active research topics [67, 29, 16]. Thus, despite decades of study, progress is still expected on these catalytic systems thanks to a better understanding of the reaction mechanisms involved [67].

In common commercial catalysts, copper is combined with zinc oxide as a promoter and alumina as a support. A typical CZA catalyst composition is around 60 wt.% Cu, 30 wt.% ZnO and 10 wt.% Al_2O_3 [67, 23].

Copper and zinc oxide alone are not very active in methanol synthesis (Figure III.1a) [8]. The activity of the copper-zinc catalyst therefore lies in the excellent synergy between these two metals. In this catalytic system, copper is in its metallic Cu^0 state after a reduction step [8]. On the other hand, zinc is mainly present in its oxidized Zn^{2+} state [8]. Additionally, ZnO helps to disperse copper particles, thereby increasing the available catalyst surface area [9]. The combination of these two components creates a very complex and dynamic system and is thought to host the most active sites of this catalyst (Figure III.1b) [40, 32, 10, 8, 45].

However, the active site(s) responsible for methanol formation are still under debate. CZA catalysts operate as a dynamic system during reduction and reaction, demonstrating morphological changes that depend on environmental factors such as pressure, temperature, and the species present in the reaction mixture [8, 45, 27, 26, 14]. Thus, due to the difficulty of their study, there is so far no consensus on its active sites and reaction mechanisms.

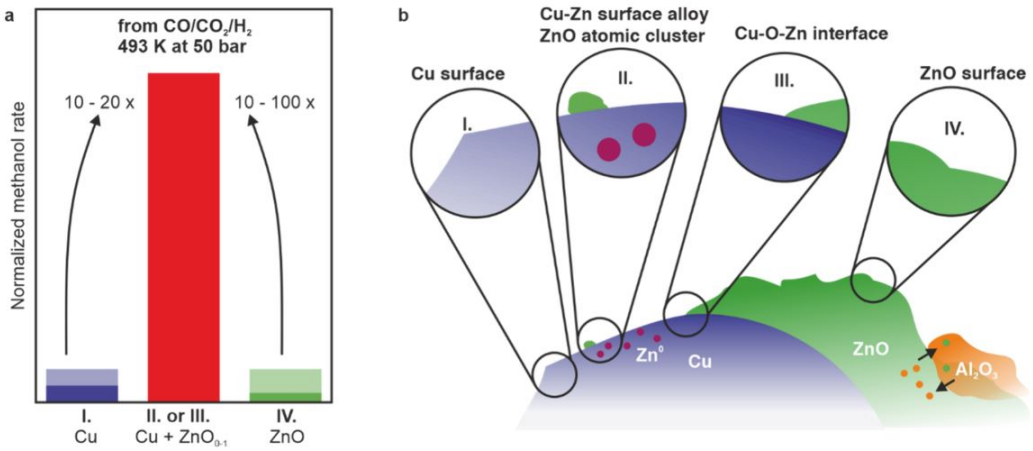

Figure III.1: (a) effect of the copper-zinc synergy on catalyst activity. (b) Complex nature of the copper-zinc interface. Figure from [8].

Alumina (Al_2O_3) is the support for the CZA catalyst. Its addition to the Cu-Zn couple results in a more stable and active catalyst. The major effect of alumina is to disperse the copper nanoparticles, thereby increasing the effective surface area of available catalytic sites [44, 67, 48]. In addition, alumina helps to thermally stabilize the copper-zinc catalyst [44]. However, alumina has certain shortcomings due to its inherent acidity. As such, this acidity enhances the

catalyst's affinity for water and hampers its desorption [5, 46]. This exacerbates the sintering of copper particles due to the presence of water and high temperatures [29, 57]. This effect is more pronounced for reaction mixtures rich in CO_2 where higher water contents are present inside the reactor [29, 57].

III.1.1.2 Promoters

The use of promoters on the Cu/ZnO pair is common practice in laboratory and industrial catalysts. The promoter is not a particularly active substance, but it improves catalytic performance by modifying certain characteristics of the catalyst. Promoters used for copper-based catalysts include alkali and alkaline earth metals, rare earths, transition metals as well as other metals from the main group [29].

Manufacturers have been using additional promoters such as Mg, Ca, Si, and Zr [48]. The use of alkali and alkaline-earth metals help to mitigate the acidity of alumina due to their basicity [29, 7].

The addition of noble metals such as Pt, Pd or Rh to CZA catalysts increased their catalytic activity [25]. This effect is attributed to better adsorption of H_2 on the copper atoms at lower temperatures, as well as improved hydrogen transfer between the metal particles [25]. However, performance gains are accompanied by an increase in the cost of these catalysts. Moreover, no recycling strategy for these promoters has been studied. These shortcomings make these promoters unlikely candidates to replace promoters already in use [25].

III.1.1.3 Supports

Rather than mitigating the harmful acid effects of alumina support on Cu-Zn catalysts, substituting it with other supports is an interesting approach. A good support also disperses the active metal particles, resulting in a larger active metal surface. Although, by definition, the support is supposed to be inert, the best supports help adsorb certain species leading to more active catalysts. Among the substitutes for alumina studied, ZrO_2, Ga_2O_3, CeO_2, SiO_2 are examples commonly cited in the literature [29, 25]. Other less conventional carriers such as carbon nanotubes, graphene oxide, MOFs or the encapsulation of copper particles in ZnO are emerging from the literature [29, 25]. The main role of the support is to provide resistance to operating conditions, such as reducing sintering phenomena.

Of the above-mentioned oxide supports, zirconia (ZrO_2) is considered the best substitute for alumina in the hydrogenation of CO_2 to methanol [25]. As mentioned in Section III.1.1.2, zirconia facilitates the adsorption of CO_2, thanks to its higher basicity than alumina [25]. Moreover, unlike alumina, zirconia is active and participates in several stages of the reaction mechanism for CO_2 [5, 3] (Figure III.2). Cerium oxide (CeO_2) is also being studied as a substitute for alumina. This support plays a major role in both CO_x and H_2 chemisorption and shows a much higher normalized activity on the catalyst surface ($mmol_{MeOH}.m^{-2}.h^{-1}$) far superior to alumina and zirconia [6]. However, cerium oxide is not very effective as a texturing agent, resulting in specific surface areas too low to compete with alumina and zirconia [6]. Thus, two comparative studies rank zirconia as the best support for Cu-Zn among Al_2O_3, CeO_2 in terms of activity [3, 6]. Gallium oxide (Ga_2O_3) has also been examined as a support for the Cu-Zn couple. In these

catalysts, gallium combines with Zn to form a $ZnGa_2O_4$ spinel structure [39]. This structure enhances the adsorption of certain reaction intermediates, improving catalyst activity [39].

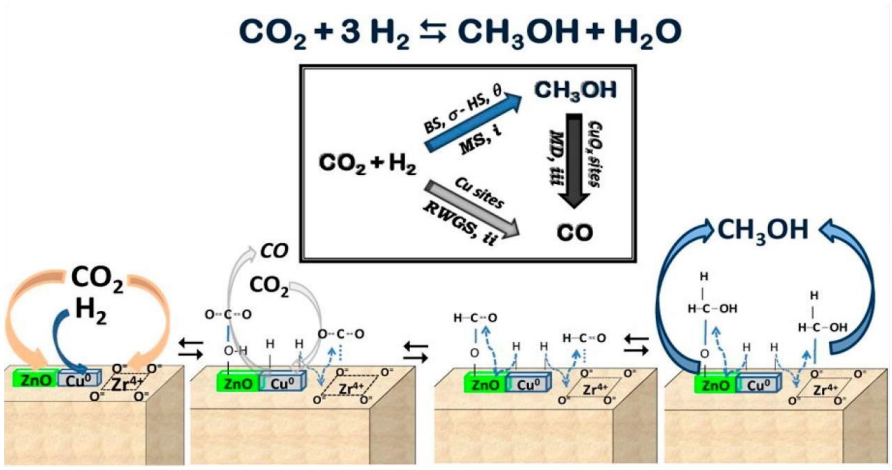

Figure III.2: Effect of zirconia as a support for the Cu-Zn couple [6].

Among the new supports emerging from the literature, graphene oxide (GO) in nanosheet form has also been studied for supporting copper-zinc-zirconia catalysts [56]. Graphene oxide helps transfer adsorbed reagents between the various metal particles [56]. This minimizes the amount of inactive metal particles due to the lack of neighboring particles with which to interact [56]. Catalyst activity is enhanced by optimal interactions between metal particles [56].

III.1.1.4 Reaction mechanism

Despite decades of research, major debates persist as to the reaction mechanism involved in methanol formation on copper-zinc catalysts. Two opposing mechanisms explain the hydrogenation of CO_2: (1) the formate pathway (HCOO*), where the acidic carbon of CO_2 reacts with a hydride, (2) the carboxyl pathway (COOH*), where the basic oxygen of CO_2 reacts with a proton [65]. Another hypothesis proposes a transformation of CO_2 into CO by reverse water-gas shift (RWGS) to be further hydrogenated into methanol (formyl pathway) [65].

Theoretical studies carried out on the hydrogenation of CO_2 to methanol on copper-zinc catalysts tend towards the formate route for carrying out the reaction [59, 30], although some studies indicate that the carboxyl route is preferable, as the formate species is only a spectator [32, 61, 66]. Others point out that both routes are viable [24]. The various mechanisms explored are detailed in Figure III.3. The addition of dopants can alter the preferential pathway for methanol formation. The addition of certain dopants, such as Pt, Pd, Rh and Ni, led to methanol formation preferentially by the formyl pathway [61]. The reaction mechanism is also strongly dependent on the structure of the metal particles [65, 30, 24]. Indeed, the presence of steps and defects on certain facets of copper particles would stabilize certain reaction intermediates and thus increase their activity [30, 24]. Operating conditions, such as temperature, can also change the preferred route for methanol synthesis [61].

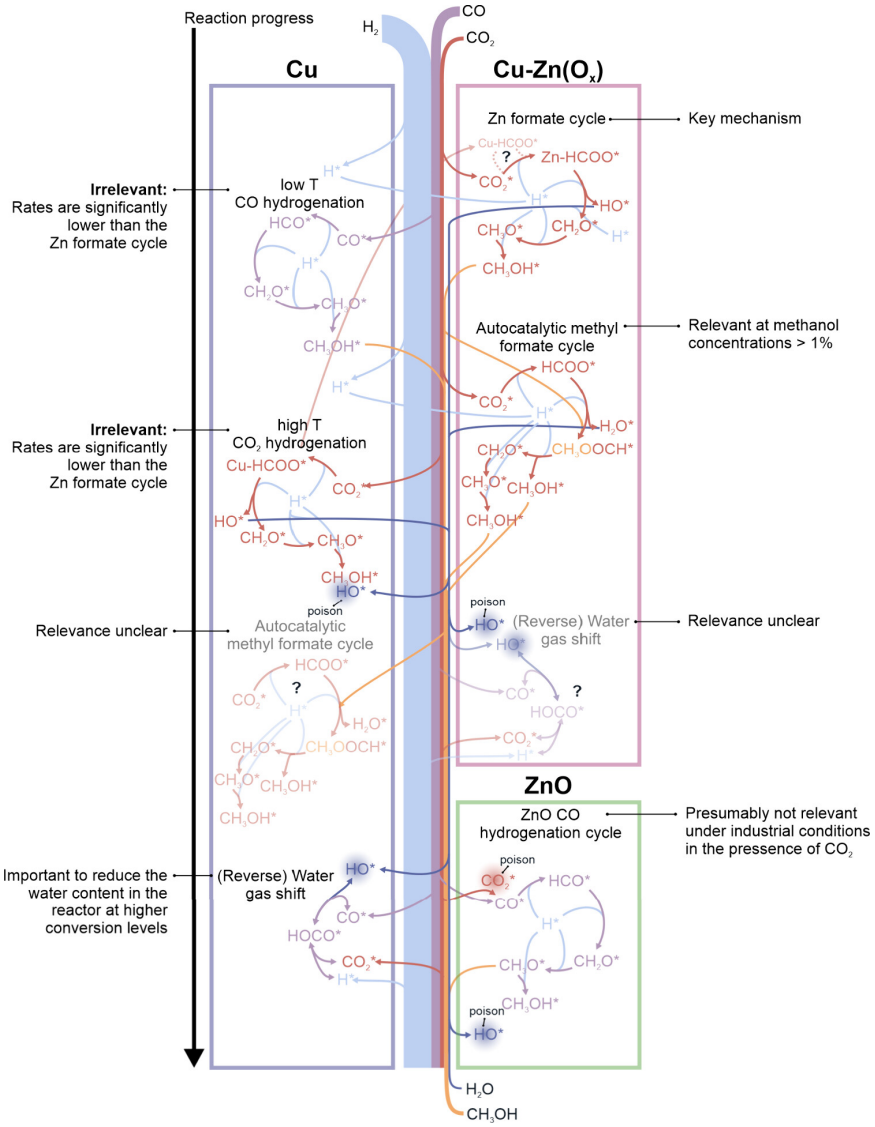

Figure III.3: Reaction mechanism for CO and CO_2 hydrogenation into methanol over CZA catalyst on different hypothetical active sites. Comments by Beck *et al.* [8] on pathway relevance on the left and right of the figure. Figure from [8].

The presence of water in the reaction medium is generally considered to be detrimental to catalyst operation. This water, generated at high temperature, is responsible for the degradation of Cu-ZnO particles during sintering [29, 57]. The oxidizing atmosphere associated with the presence of water also influences the morphology of copper-zinc catalysts [26, 14]. In these cases, "wetting" of the copper particles leads to their "spherification" on ZnO. In a more reducing atmosphere, the copper would tend to spread out on ZnO to form an interface and a larger specific surface area [26, 14]. However, some studies indicate that the presence of water is beneficial for the conversion of CO and CO_2 to methanol. Theoretical studies by Yang *et al.* [62] indicate that low activity was observed when the reaction mixture was completely devoid of water.

Interactions between catalytic elements and the influence of reaction conditions on the catalyst structure make the methanol formation mechanism difficult to clarify. The obstacles to understanding these mechanisms are not solely linked to a lack of mathematical and numeri-

cal tools. In particular, better *in-situ* characterizations are needed to better observe reaction phenomena in real time in order to support and guide modeling work [29].

III.1.1.5 Preparation methods for copper-zinc catalysts

The method used to synthesize a catalyst is a crucial step in obtaining an active catalyst. The most commonly used synthesis method for copper-zinc catalysts is co-precipitation. Co-precipitation methods involve firstly the dissolution of the metal salts to form a solution. Then, the addition of a basic agent in the right pH range, all the metallic species simultaneously co-precipitate, ensuring a good homogeneity in the precipitated solid. This solution can be aged to stabilize certain catalyst structures. Afterwards, the resulting precipitate is washed, dried and then calcined. Finally, the catalyst is reduced before being used for methanol synthesis in a catalytic reactor.

Nevertheless, the limited homogeneity of batch co-precipitated precursors can also have an impact on the quality of the synthesized catalyst. Indeed, during co-precipitation, the mixing of solutions is never truly ideal. Uncontrolled concentration gradients make it difficult to control the growth of metal crystals and can lead to the creation of poorly dispersed particles. Much effort has therefore been invested in improving the co-precipitation method, leading to a multitude of variations. For example, reverse precipitation [6] microfluidic precipitation [3, 36] and the use of ultrasound [6] have been studied to solve these problems. Other methodologies, such as precipitation under supercritical anti-solvents aim to stabilize certain types of catalyst precursors sought to lead to more active methanol catalysts [35, 34, 33].

Reverse precipitation involves adding the metal salt solution to the precipitating agent, rather than adding a precipitating agent to the metal salt solution. The advantage of this method is that it prevents the creation of single-phase particles with limited dispersion between them. These single-phase particles result from differences in precipitation kinetics between the metal cations [4]. Continuous microfluidic precipitation involves reproducing the co-precipitation method in a micro-reactor [3, 36]. By using much smaller volumes, linked to the fine diameters of the channels used, control of the various parameters is much easier. With well-controlled mixing and temperature, the catalysts synthesized by this method have enhanced dispersion and particle interactions compared with conventional batch co-precipitation [3, 36]. Moreover, thanks to the finer control of synthesis parameters, these methods are highly reproducible [3, 36].

III.1.2 Alternative catalysts for methanol synthesis

In order to surpass the activity, selectivity and stability of copper-zinc catalysts, alternative catalysts are now being studied. The catalysts presented here include indium oxide-based catalysts (In_2O_3), intermetallic compounds (Ni-Ga), noble metal-based catalysts (Pd, Pt, Rh, ...) and finally catalysts supported on MOFs.

III.1.2.1 Indium oxide catalysts (In_2O_3)

Indium oxide catalysts (In_2O_3) have recently emerged as serious candidates for replacing copper-based catalysts [54, 41]. Using an In_2O_3 catalyst supported on m-ZrO_2, Martin *et al.* [41] show

high yields, selectivities close to 100% in methanol stable at high temperatures. The catalyst also demonstrates excellent stability even at high temperatures in the presence of water, thanks to good resistance to sintering phenomena.

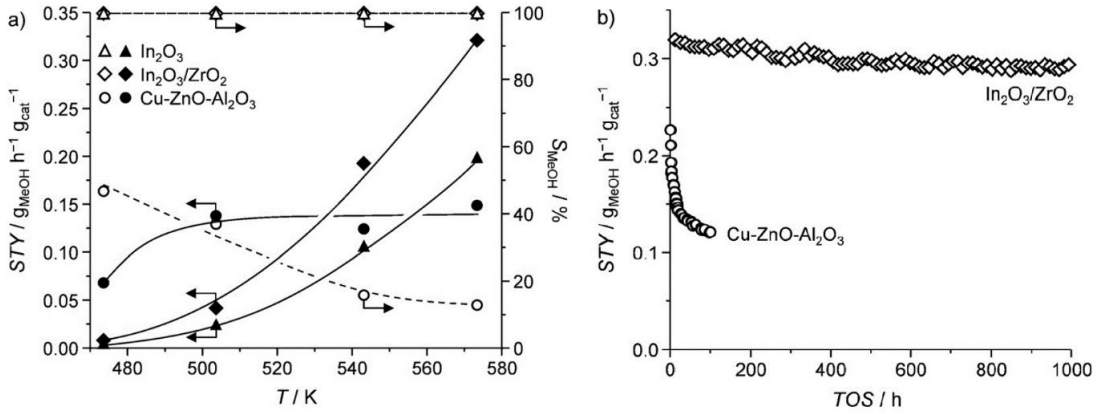

Figure III.4: Comparison of In_2O_3/ZrO_2 and CZA. a) Yields and selectivities (P=5.0 MPa, H_2/CO_2 =4:1, GHSV=16,000 h-1), b) stability (T=573 K, P=5.0 MPa, H_2/CO_2 =4, GHSV=16,000 h-1) [41].

However, high methanol yields can only be obtained at elevated temperatures (Figure III.4). Martin *et al.* [41] only achieve yields higher than those of a CZA catalyst at 250°C and above. Furthermore, the catalyst of Martin *et al.* [41] demonstrates up to twice the activity in the presence of CO, thanks to the generation of oxygen vacancies by CO.

In their review of indium oxide catalysts, Meng *et al.* [43] present the effect of each promoter and support on the activity of these catalysts. Among them, metal oxides provide support for active indium oxide particles. Frei *et al.* [22] identified monoclinic zirconia (m-ZrO_2) as the best support among t-ZrO_2, CeO_2, Al_2O_3 . Yang *et al.* [60] used Li to dope ZrO_2 by transforming it into m-ZrO_2. This method resulted in a more active catalyst than In_2O_3/t-ZrO_2. In addition, indium oxide has often been used to support noble metal catalysts. Among these noble metals, Pt, Pd, Au, Ag, Ir and Rh have been studied on In_2O_3. Unfortunately, the use of noble metals entails a very high cost, limiting large-scale applications. To come closer to industrial constraints, efforts have been made to combine indium oxide with transition metals such as Ni [28] or Cu [50, 51, 63].

III.1.2.2 Ni-Ga intermetallic compounds

An intermetallic compound (IMC) is a substance comprising two metallic elements. Unlike an alloy, IMCs retain a well-defined structure and stoichiometry between the two metals. Among this class of catalysts, Ni-Ga IMCs have been extensively studied for methanol synthesis. In the study by Studt *et al.* [53] the most active Ni-Ga IMC for methanol synthesis is Ni_5Ga_3. This catalyst exhibits better selectivity and extended activity over a wider temperature range compared with a conventional CZA (Figure III.5) [53].

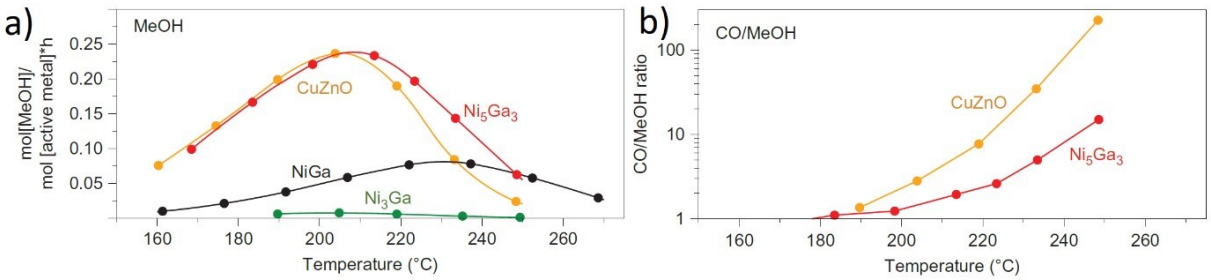

Figure III.5: Comparison of Ni-Ga catalysts with a CuZnO catalyst for methanol synthesis [53].

Duyar *et al.* [21] studied the addition of promoters to Ni-Ga catalysts. The turn-over frequencies (TOFs) (represent the number of conversions performed by an active site per unit time) observed are decreasing according to AuNiGa > CuNiGa > NiGa > CoNiGa. Despite AuNiGa's high TOF, CuNiGa has the highest methanol yield. The origins of these yields are hypothetically due to the formation of a phase between Cu and Ga [21]. Smitshuysen *et al.* [52] also used Fe to dope Ni-Ga. The activity of the NiFeGa catalyst at 200°C is comparable to that of a commercial CZA catalyst doped with MgO. Rasteiro *et al.* [47] studied the influence of ZrO_2, CeO_2 and SiO_2 supports on the Ni-Ga catalyst by DFT and DRIFTS in-situ. Here too, zirconia appears to be the best support for these catalysts, participating in the adsorption of CO_2. Among less conventional supports, Chen *et al.* [13] studied a $Ni_5Ga_3/SiO_2/Al_2O_3$ catalyst deposited on aluminum fibers to dissipate the heat of reaction. This catalyst shows higher yield and selectivity than Studt *et al.* [53]. This is attributed to the 1% SiO_2 proportion in the material, which enables the size of the Ni-Ga nanoparticles to be controlled.

III.1.2.3 Noble metal catalysts

Noble metals (Pd and Pt) have been studied as catalysts for methanol synthesis. In particular, palladium-based catalysts are the most extensively studied after copper-zinc catalysts [25]. Supported palladium-based catalysts can drive the reaction at low temperatures. For example, Matsumura *et al.* [42] observed on a Pd/CeO_2 catalyst a methanol yield at 170°C comparable to that obtained on a copper-zinc catalyst at 230°C. Other supports such as oxides (ZnO, Ga_2O_3, CeO_2, In_2O_3), mesoporous silicas (SBA-15, MCM-41), silicon carbide (SiC) or carbonaceous materials (nanotubes and nanofilms) have also been used to support palladium [67]. In the literature, the Pd-Zn, Pd-Ga and Pd-In pairs stand out as the most interesting. This strategy of combining palladium with a transition metal improves catalyst activity by facilitating the transfer of H_2 between metal particles. Moreover, mixing palladium with a less expensive metal can significantly reduce the cost of the catalyst [58].

III.1.2.4 Catalysts supported on MOFs

The use of MOFs for methanol catalysis is an emerging topic. These crystalline, microporous solids can be tuned for specific surface area and pore size. Their application to copper-zinc catalysts makes it possible to encapsulate catalyst nanoparticles and thus control their size and available surface area.

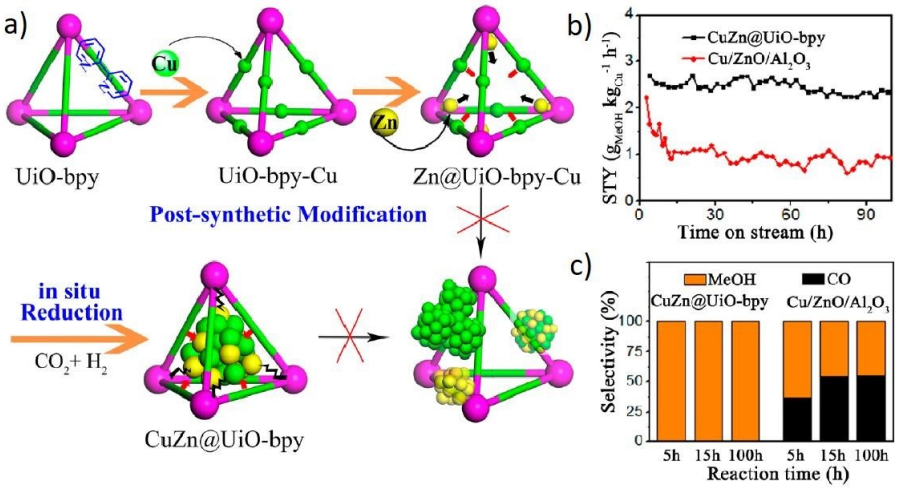

Figure III.6: Application of a MOF to the CuZn couple. a) Encapsulation method for CuZn nanoparticles, b) Stability of CuZn@MOF catalyst, c) Selectivity of CuZn@MOF catalyst (H_2/CO_2 =3, P=4MPa, T = 250 °C, GHSV=18000h-1) [1].

The study by An *et al.* [1] is presented here as an example (Figure III.6). By limiting the formation of monometallic sites in this way, the RWGS reaction is strongly limited and very high selectivities towards methanol are observed. Additionally, the CuZn nanoparticles are protected by the MOFs cages, eliminating the problem of particle sintering and increasing stability compared with a conventional CZA-supported catalyst. Although the activity relative to the amounts active metal have also been improved compared to a conventional CZA catalyst, the weight of the inert support results in methanol productivities ($mol_{MeOH}.g_{cat}^{-1}.h^{-1}$) productivities comparable to conventional CZA catalysts. MOFs have also been applied to noble metal or indium oxide catalysts, the precise data on these materials are compiled in the review by Din *et al.* [17].

III.1.3 Suitability of catalysts for membrane-assisted methanol synthesis

Temperature is a key factor for the membrane reactor applied to methanol synthesis. Above a certain temperature, membrane performance is no longer advantageous for separating water from the reaction mixture, and thermodynamic equilibria are no longer favorable. Observations in the literature show that above 250°C, zeolite membrane performance is severely degraded. For example, Gallucci *et al.* [23] show that above the critical methanol temperature (238°C), membrane reactor performance gains only decrease. In the context of Figure III.7 this temperature sensitivity forces us to select a catalyst located in the "blue zones" (>250°C) of the Figure III.7.

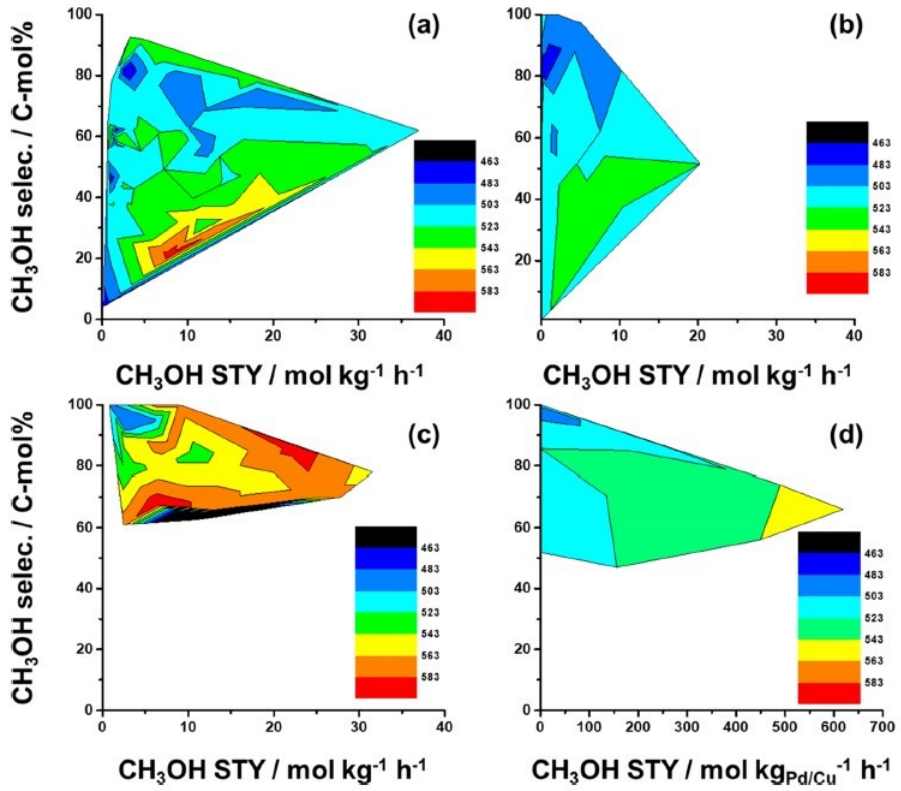

Figure III.7: a) Copper-based catalysts, b) Noble metal-based catalysts (Pd, Pt), c) Indium oxide and zinc oxide-based catalysts, d) Catalysts supported on MOFs. Data compiled and plotted by Jiang *et al.* [29].

In the light of these remarks, catalysts based on indium oxide (In_2O_3) and zinc (ZnO) are excluded for use in membrane reactors, due to their activity reached at high temperatures. Noble metals appear as good candidates, due to their high yields and selectivity at low temperatures. However, the cost of using these compounds in relation to their proven performance compared to cheaper and more abundant copper-zinc catalysts makes their industrialization unlikely. According to the criteria set out above, MOFs show potential for application in a membrane reactor, although certain obstacles to their application remain to be elucidated. For example, the hydrothermal sensitivity of MOFs as well as the unreliability and very difficult scale-up of synthesis methods are currently hampering the development of these catalysts [29]. Thus, to date, copper-based catalysts seem to be the best candidates based on several points: (1) good yields and selectivities observed at low temperatures, (2) better availability of these materials among the catalysts studied and (3) significant bibliographical hindsight on the synthesis and operation of these catalysts. However, most of the alternative catalysts presented here are still in early research development phases while copper-zinc catalysts have been used industrially for decades. Thus, future developments in this field of research could change the observations made here.

III.1.4 Catalyst deposition on membrane materials.

For methanol synthesis, the catalytic membrane reactor can incorporate a functional permselective membrane, featuring a catalyst layer synthesized on the zeolite membrane. Catalyst and

membrane are then in close proximity, with a high contact surface.

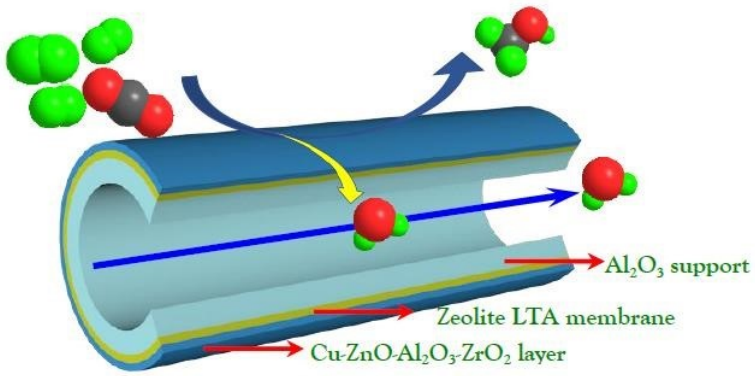

Figure III.8: Example of a catalytic membrane reactor set up by Yue *et al.* [64].

Yue *et al.* [64] have successfully synthesized a Cu-ZnO-Al_2O_3-ZrO_2 catalyst layer on a LTA membrane (Figure III.8). Their catalytic membrane reactor achieved 100% selectivity towards methanol and also increased catalyst lifetime. According to the authors, by effectively separating water from the reaction mixture, the formation of by-products as well as premature deactivation of the catalyst due to water can be avoided [64]. However, in these experiments, the catalyst was dip-coated onto the support from a slurry of catalyst powder in deionized water, resulting in a low loading on the membrane (0.13g of catalyst after 20 coats for a tubular membrane with the following dimensions: length of 7.5 cm and outside diameter of 1.2 cm) [64].

Possible leads to further increase the efficacy of the catalyst deposition would be to modify the synthesis method of the catalyst. In that regard, sol-gel methods have already been applied to synthesize catalyst on solid substrates [31]. Supercritical anti-solvent, whom have already been used to synthesize active methanol catalyst [35, 34, 33], can also be applied for film deposition onto a support [11, 20, 18, 19].

III.2 Development of catalysts for enhanced membrane reactor integration.

In order to optimize membrane reactor performances for methanol synthesis, the optimum temperature range for membrane selectivity (<250°C) and for catalytic activity (>250°C) must match. In this section, two Cu/ZnO-based catalysts, supported respectively on zirconia and indium oxide, are synthesized and compared against a CZA commercial catalyst to investigate possible low temperature performances.

Moreover, catalytic membrane reactors, where the catalyst is synthesized upon the membrane, have displayed, in the literature, synergistic effects between catalytic and separation performances due to the closeness of the two functions [64]. Thus, two alternative methods for catalyst preparation, potentially suitable for efficient deposition on a zeolite membrane, are also explored: the pseudo sol-gel method and the supercritical CO_2 route.

This experimental section was conducted at ICPEES in the ECED (*Energie et Carburants pour un Environnement Durable*) team under the supervision of Pr. Anne-Cécile ROGER.

III.2.1 Preparation methods

To study possible catalytic activity at low temperature (<250°C), two Cu/ZnO-based catalysts have been synthesized through CP: CZZ (CP) and CZI (CP). Furthermore, to study potential preparation method for catalyst deposition onto zeolite membrane, three catalysts were synthesized through two different route: CZZ (SG), CZZ (CO_2sc), CZYSZ (CO_2sc). A commercial CZA catalyst ($CuO/ZnO/Al_2O_3/MgO$, Alfa Aesar) is also studied for comparison purposes. All studied catalysts along their characteristics are featured on Table III.1.

Table III.1: List of prepared catalysts for this study.

Catalyst	Preparation method	Catalyst's support	Metal oxide loading (wt.%)			
			CuO	ZnO	Support	Other
CZZ (CP)	Co-precipitation	ZrO_2	44.8	27.5	27.7	(-)
CZZ (SG)	Pseudo sol-gel	ZrO_2	44.8	27.5	27.7	(-)
CZZ (CO_2sc)	Super-critical CO_2	ZrO_2	44.8	27.5	27.7	(-)
CZYSZ (CO_2sc)	Super-critical CO_2	YSZ	43.0	26.4	ZrO_2: 25.9 Y_2O_3: 4.7	(-)
CZI (CP)	Co-precipitation	In_2O_3	51.0	31.3	17.8	(-)
AA (Commercial)	Unknown	Al_2O_3	[60-68]	[22-26]	[9-15]	MgO: [1-3]

III.2.1.1 Co-precipitation

This co-precipitation method follows the ones from Angelo [2] and L'Hospital [37]. Metallic salts: copper nitrate ($Cu(NO_3)_2$,$5H_2O$), zinc nitrate ($Zn(NO_3)_2$,$6H_2O$), zirconium nitrate ($ZrO(NO_3)_2$,$6H_2O$) or indium nitrate ($In(NO_3)_3$,$5H_2O$) were dissolved in deionized water (homemade) to produce a 1.0 mol/L solution. The molar composition of this solution was 5.0 CuO : 3.0 ZnO : 2.0 ZrO_2 for the CZZ catalyst and 5.0 CuO : 3.0 ZnO : 0.5 In_2O_3 for the CZI catalyst.

The precipitating solution was made by dissolving sodium carbonate (Na_2CO_3) in deionized water at a concentration of 1.6 mol/L. The amount of solution produced was calculated to produce a molar carbonate/nitrate ratio of 1.1 after mixing the two solutions.

The two solutions were added dropwise in 100 mL deionized water at 60°C and pH of the resulting solution was monitored using a Hanna Instruments HI 11102 pH meter and adjusted to stay within a 6.0-6.5 range by adding sulfuric acid (H_2SO_4) dropwise. The resulting solution was then aged for 3 h at 60°C.

Afterward, the precipitate was washed and filtered with 3 L deionized water. Then, the precipitate was dried at 110°C overnight. Finally, the resulting solid was calcined at 400°C for 4 h with a heating rate of 2°C/min. The freshly produced catalyst was then sieved between 63-125 µm before characterization.

III.2.1.2 Pseudo sol-gel synthesis

The pseudo sol-gel method follows the one described by Angelo [2]. Metallic salts: copper acetate ($Cu(OOCCH_3)_2{,}1H_2O$), zinc acetate ($Zn(OOCCH_3)_2{,}2H_2O$) and zirconium pentadionate ($Zr(C_5H_7O_2)_4$) were dissolved separately in propionic acid ($C_3H_6O_2$) to make solutions with molar concentrations of respectively 0.12, 0.07, 0.12 mol/L. The dissolution of zinc acetate required heating the solution to boiling temperature (≈140°C).

Afterward, the solutions were mixed in a round bottom flask and heated to reflux for 24 h. The resulting solution was then distilled until a resin of mixed metallic propionates was obtained. This resin was then solidified with liquid nitrogen to facilitate its retrieval from the flask. Finally, the resin was calcined at 400°C for 4 h with a heating of 2°C/min to thermally decomposes the proprionates species and leave out the catalyst. The resulting catalyst was then sieved between 63-125 µm before characterization.

III.2.1.3 Supercritical CO_2 synthesis

The catalysts synthesized through the supercritical CO_2 route were prepared by Clément HOCINE and Loan AVEDIKIAN of CEA Marcoule's LPSD (*Laboratoire de Procédés Super-critiques et de Décontamination*) under the supervision of Dr. Audrey HERTZ.

Metal salts: copper nitrate ($Cu(NO_3)_2{,}5H_2O$), zinc nitrate ($Zn(NO_3)_2{,}6H_2O$), zirconium acetate hydroxide ($Zn(Ac)_x(OH)_y$, x+y=4) and yttrium acetate ($Y(OOCCH_3)_3{,}4H_2O$) were weighted to match the aimed compositions of the catalysts featured in Table III.1. The metal salts were dissolved simultaneously at a 0.57 mol/L concentration in an isopropanol solution containing 10vol.% of nitric acid (to help dissolution). The resulting solution was then aged at room temperature for 20 h.

Then, the solution was inserted in a stainless steel autoclave along with 1 cm long LTA and SOD membranes (synthesized according to the procedure described in Chapter II for Section II.2.3.1 and II.2.3.2) to deposit the catalyst directly onto the membrane during synthesis. CO_2 was inserted in the autoclave to reach a pressure of 60 bar. Then, the autoclave was heated to 350°C at which the pressure in the autoclave would reach between 260 and 280 bar. The reaction lasted 2 h at those conditions. Afterward, the autoclave was cooled down and depressurized at approximately 1 bar/s.

The side-produced powdered catalyst was retrieved from the bottom autoclave and sieved between 63-125 µm before characterization.

III.2.2 Catalyst characterization

III.2.2.1 Apparent density

The apparent density of the catalyst was measured with a glass tube of 2.2 mm of internal diameter filled with fresh and sieved catalyst (63-125 µm).

Table III.2: Apparent density of the studied catalyst.

Catalyst	Apparent density (g/cm^3)
CZZ (CP)	0.86
CZZ (SG)	2.63
CZZ (CO_2sc)	0.75
CZYSZ (CO_2sc)	0.30
CZI (CP)	0.48
AA (Commercial)	1.90

All catalysts (except for the one synthesized through the sol-gel route) display lower densities than the commercial catalysts. Substituting zirconia for indium oxide in co-precipitated catalysts and for yttriated zirconia in the catalysts synthesized through super-critical CO_2 led to a diminution of the apparent density.

III.2.2.2 Crystalline structure

The crystalline structure of the catalyst was measured through XRD using a Brüker D8 Advance, fitted with a LYNXEYE detector with a nickel filter to filter out copper Kα emissions. The XRD of the sample was measured with a 2Θ ranging from 10 to 80° with a step size of 0.021° held for 1 s per step. The co-precipitated catalysts required a smaller step size of 0.003° held for 1.6 s per step to reach a sufficient resolution.

$$D = \frac{K\lambda}{Bcos(\Theta)} \tag{III.1}$$

The size of crystals contained in the catalysts were estimated using Debye-Scherrer's equation (Eq. III.1). This estimation was performed on several rays and ranges for crystal sizes are presented on Table III.3.

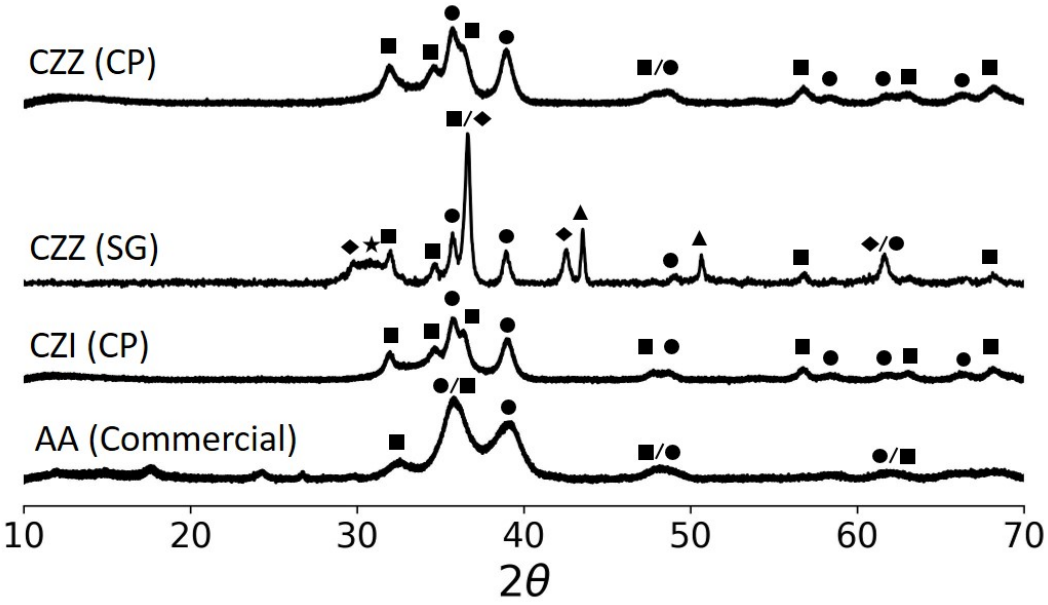

Figure III.9: X-ray diffractograms of the studied catalysts (CO_2sc excluded). •) CuO, ■) ZnO, ⋆) ZrO_2, ▲) Cu^0, ◆) Cu_2O.

Co-precipitated catalysts and the commercial catalyst display similar X-ray diffractograms with wide poorly defined rays (Figure III.9) as crystal size remains small (Table III.3). In these catalysts, no rays from the support can be seen, likely indicating its presence in amorphous state. These diffractograms contrast the one resulting from the catalyst prepared through the sol-gel route where sharper rays are featured, indicating the presence of larger crystals. Moreover, a wide ray at around 30.4° suggests the partial crystallization of the zirconia support. But most striking, after calcination at 400°C, copper is present in Cu^0 and Cu^+ states. These observations deviate from the one made by Angelo [2] using a similar synthesis method. In her work, all proponiates degraded at after a calcination temperature of 400°C and thus no other phases aside CuO were observed on the diffractograms. The presence of Cu^0 and Cu^+ phases thus indicates that the calcination temperature was likely too low.

Table III.3: Crystal sizes of the studied catalyst calculated with Scherrer's law. *CO_2sc: Cu^0, rest: CuO.

Catalyst	**Crystal size (nm)**		
	Copper*	**ZnO**	**Support**
CZZ (CP)	10-15	10-15	N.D.
CZZ (SG)	20-40	20	N.D.
CZZ (CO_2sc)	40-45	50-55	5-15
CZYSZ (CO_2sc)	65-70	75-85	5-15
CZI (CP)	3-4	10	N.D.
AA (Commercial)	5-10	N.D.	N.D.

From the diffractograms featured in Figure III.10, catalysts prepared through the supercritical CO_2 route only display metallic copper rays for the copper phase. However, after calcination,

these rays are substituted by CuO rays indicating the oxidation of Cu^0 to Cu^{2+} during calcination. Additionally, contrary to co-precipitated catalysts, the supports partially crystallize as wide rays attributed to zirconia are visible from the diffractograms. These diffractograms also feature very sharp rays belonging to copper as well as zinc oxide that point to the presence of larger crystal sizes than co-precipitated catalysts III.3. These results highly contrast those of Kondrat *et al.* [33] on their work about CZA catalyst synthesized through CO_2sc, where no rays were observed for the zinc oxide phase as it remained amorphous. Moreover, they observed poorly defined rays belonging to poorly crystallized copper oxide nanoparticles before calcination which is the exact opposite of our findings.

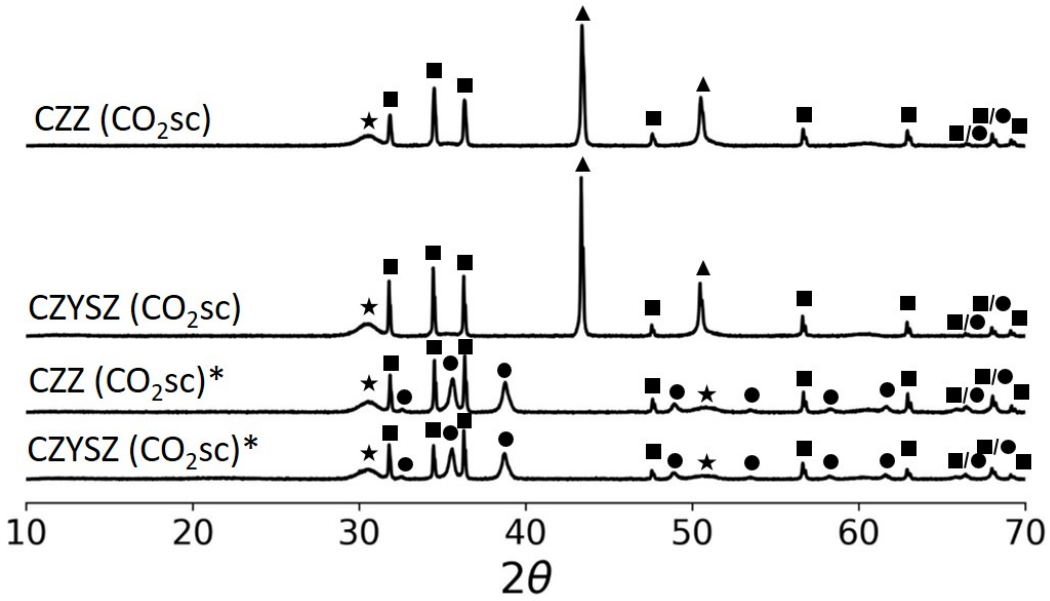

Figure III.10: X-ray diffractograms of catalysts synthesized through the supercritical CO_2 route. *XRD after catalyst calcination under air. •) CuO, ■) ZnO, ⋆) ZrO_2, ▲) Cu^0.

III.2.2.3 Porosity

The porosity of the catalyst was investigated by N_2 physisorption at 77 K through the Brunauer-Emmet-Teller (BET) method using a Micromeritics Tristar II Plus. On Table III.4, are featured for each catalyst its specific pore volume and surface as well as its porosity defined by the ratio between the specific pore volume of a catalyst and its bulk density. The catalyst's bulk density was calculated assuming a bed void fraction of 0.4. Figure III.11 presents the pore size distribution and isotherms for each studied catalyst. The pore size distribution was calculated on the desorption branch of using the Barrett, Joyner et Halenda (BJH) method.

Table III.4: Specific pore volume, porosity and specific surface of the studied catalysts.

Catalyst	Specific pore volume (cm^3/g)	Porosity (%)	Specific surface (m^2/g)
CZZ (CP)	0.30	21	74
CZZ (SG)	0.08	2	32
CZZ (CO_2sc)	0.13	11	38
CZYSZ (CO_2sc)	0.14	28	34
CZI (CP)	0.17	21	78
AA (Commercial)	0.17	5	80

The co-precipitated catalysts and the commercial one feature the highest pore volume and surface area. Due to their lower density, co-precipitated have higher porosity values than the commercial catalyst. Additionally, the zirconia-supported CZZ has significantly more pore volume than its indium oxide-supported CZI counterpart.

The sol-gel synthesized catalyst features the lowest porosity, pore volume and area. While the catalysts synthesized through the supercritical CO_2 route display more porosity and higher pore volume, the pore area is not significantly greater than the sol-gel catalyst. Anyway, none of these catalysts synthesized through alternative routes can match the specific pore volumes and surfaces of more conventional co-precipitated and commercial catalysts.

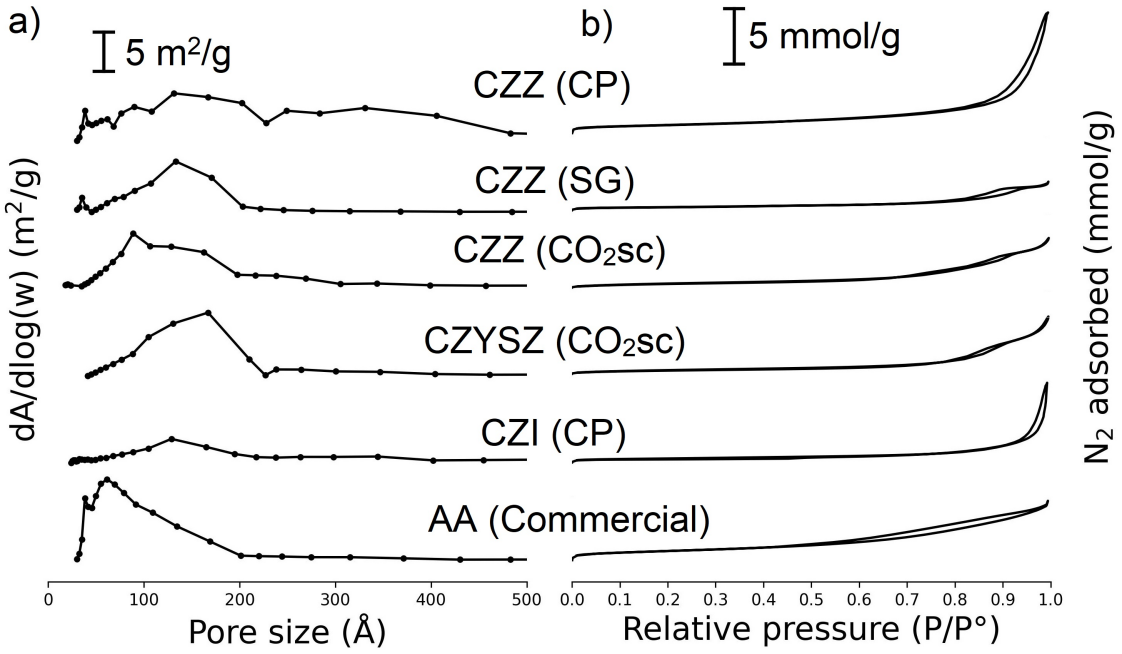

Figure III.11: Temperature-programmed reduction of the studied catalysts.

The adsorption isotherms of both commercial and co-precipitated catalysts match the type II isotherms, as classified by the IUPAC system [55]. Moreover, the commercial catalyst features a long hysteresis starting from a relative pressure of 0.5, indicating the presence of narrow slit-

shaped and small mesopores. Conversely, the hystereses of co-precipitated catalysts are thinner and taller, indicating the presence of larger pores [55]. These observations are corroborated on Figure III.11a, where the pore size distribution of the commercial catalyst is narrow with all its pore being smaller than 20 nm whereas the co-precipitated catalysts have more spread out pore size distribution with pore sizes extending beyond 20 nm.

The catalysts synthesized through alternative synthesis routes (SG and CO_2sc) feature, according to the IUPAC classification system, type VI adsorption isotherm with two steps. The first step possesses a hysteresis loop indicating the presence of particles with some mesoporosity [55]. However, the second step leads to think that once these pores are filled, these materials have no more porosity as nitrogen gets adsorbed in a subsequent layer on the particles.

III.2.2.4 Reducibility of the catalysts

The reducibility of the metallic oxides present in the catalysts was studied through temperature-programmed reduction (TPR) using a Micromeritics AutoChem II 2920. For the reduction, the catalyst was exposed to 50 mL/min of a gas containing 10% H_2 in Argon. The sample was heated to 900°C with a heating rate of 10°C/min.

The first peak of the reduction profile is attributed to the reduction of copper oxide (CuO) (Eq. III.2).

$$CuO + H_2 \rightleftharpoons Cu + H_2O \tag{III.2}$$

The fraction of copper oxide that has been reduced $\%_{CuO,reduced}$ is calculated using the theoretical weight fraction of copper present in the sample and the amount of H_2 consumed during the reduction step according to Eq. III.3.

$$\%_{CuO,reduced} = \frac{m_{CuO,reduced}}{m_{CuO,theoretical}} = \frac{n_{H_2,consumed}}{M_{CuO} \cdot m_{CuO,theoretical}} \tag{III.3}$$

Table III.5: Fraction of CuO that has been reduced during the reduction step for the studied catalysts.

Catalyst	$\%_{CuO,reduced}$
CZZ (CP)	106
CZZ (SG)	70
CZZ (CO_2sc)	<1
CZYSZ (CO_2sc)	<1
CZI (CP)	102

Both the co-precipitated catalyst features fraction of reduced copper oxide above 100%, which could signal either that the other components of the catalyst are getting partly reduced along with copper. Alternatively, parts of the zinc, zirconium or indium oxide nitrate may not have fully precipitated during synthesis. Additionally, the reduction peak of co-precipitated catalysts are not symmetric which either supports the idea that other species are getting reduced with

copper [12] or that different sizes of copper particles are present in the sample [5].

The fraction of reduced copper oxide does not reach 100% in the CZZ (SG) catalyst and is negligible in the CO_2sc synthesized catalyst. This is explained by the presence of Cu^0 and Cu^+ phases already identified in the XRD analysis of the CZZ (SG) catalyst (Section III.2.2.2). Moreover, the XRD analysis of the CO_2sc synthesized catalyst featured exclusively rays belonging to the metallic copper Cu^0 (Section III.2.2.2), which would not be measurable in this TPR experiment. A small peak is nevertheless measurable in the TPR profile of these catalysts (Figure III.12), likely belonging to the reduction of a passivation layer on the metallic copper particles.

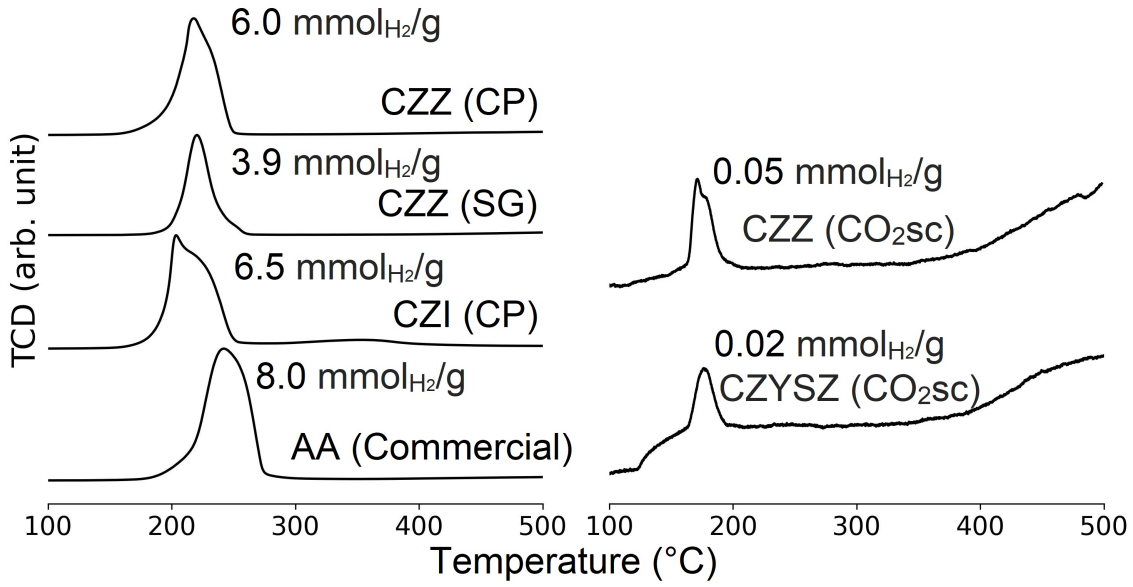

Figure III.12: Temperature-programmed reduction of the studied catalysts.

III.2.2.5 Thermogravimetric analysis (TGA)

The sample prepared through the supercritical CO_2 route showed no reducibility under H_2. To further study the oxidized state of copper in these fresh catalysts, a TGA was conducted using a TA instruments TGA Q5000 under air. For these experiments, samples were heated to 600°C at a 10°C/min rate.

$$\mathrm{Cu} + \frac{1}{2}\,\mathrm{O_2} \rightleftharpoons \mathrm{CuO} \tag{III.4}$$

Here, we hypothesize that the weight gained Δm during the TGA is due to the oxidation of metallic copper within the sample (Eq. III.4). Under this assumption, the weight fraction of metallic copper w_{Cu} contained in the sample can be calculated through Eq. III.5.

$$w_{Cu} = \frac{m_{Cu}}{m_{cat}} = \frac{n_{O,consumed} \cdot M_{Cu}}{m_{cat}} = \frac{\Delta m \cdot M_{Cu}}{M_O \cdot m_{cat}} \tag{III.5}$$

Table III.6: Comparison of copper fraction in the catalyst synthesized through the supercritical CO_2 route between TGA-based estimated and theoretical values.

Catalyst	w_{Cu} (%)	
	Theoretical	**Calculated**
CZZ (CO_2sc)	37.6	35.9
CZYSZ (CO_2sc)	37.6	34.3

The mass gained during the TGA loosely matches the theoretical values for the catalysts synthesized through the supercritical CO_2 route (Table III.6). This observation is another evidence of the presence of copper in its metallic Cu^0 oxidation state along with the XRD the TPR analyses. Additionally, the fact that 470samples gained mass during the TGA experiments indicates that no nitrates or acetates species were left in the catalyst after synthesis as no mass loss can be accounted for these compounds. This can be attributed to the high synthesis temperature of 350°C which should induce the thermal degradation of these species during synthesis.

III.2.2.6 Metallic surfaces

The metallic surface of the catalyst was measured by N_2O-RFC using a Micromeritics AutoChem II 2920. For this operation, the catalyst is first reduced under 50 mL/min of a 10% H_2 in Ar gas at 300°C for 3 h (heating rate: 10°C/min). The catalyst is then cooled down to 50°C under Ar. Finally, the reduced catalyst is exposed to 50 mL/min of an oxidant gas containing 2% N_2O in Ar for 20 min. The quantity of N_2 produced in the surface reaction is measured using a Pfeiffer Vaccum Omni Star mass spectrometer.

The low reduction temperature of 300°C implies that copper oxide is the main species that get reduced during this operation. Hence, only surface metallic copper is assumed to oxidize when the sample is exposed to N_2O (Eq. III.6).

$$2\,Cu^0 + N_2O \rightleftharpoons Cu_2O + N_2 \tag{III.6}$$

Table III.7: Specific metallic surfaces for the studied catalysts by N_2O-RFC.

Catalyst	**Metallic surface**	
	$\mathbf{m^2.g_{cat}^{-1}}$	$\mathbf{m^2.g_{Cu}^{-1}}$
CZZ (CP)	9.9	26.0
CZZ (SG)	N.D.	N.D.
CZZ (CO_2sc)	1.5	3.3
CZYSZ (CO_2sc)	1.4	3.1
CZI (CP)	11.4	27.6
AA (Commercial)	20.7	40.6

Copper surfaces are higher for co-precipitated catalysts than that of SG and CO_2sc-synthesized

catalysts but lower than that of the commercial catalyst. Regarding the catalyst synthesized through alternative routes (sol-gel and CO_2sc), their metallic surfaces were respectively non-measurable and very poor. For the sol-gel catalyst, no significant signal was measured using the mass spectrometer even after repeating the experiment twice. One hypothesis can be made by considering an insufficient calcination of the sample in which propionates species can possibly still be bound to the copper surface atoms making them unavailable for the N_2O reaction. The poor metallic surface of CO_2sc-synthesized catalysts is consistent with the presence of well crystallized and large copper particles as evidenced by the XRD analysis.

III.2.2.7 Catalytic activity

III.2.2.7.a Experimental setup

The catalytic activity of the catalysts for CO_2 hydrogenation to methanol were investigated in a custom-made test bench shown on Figure III.13. Gases (CO_2, H_2 and N_2) were fed through gas bottles. Reduction of the catalyst was done using a bottle containing pure H_2 while the reaction was performed with a bottle of composition 72vol.% H_2, 24vol.% CO_2 and 4vol.% N_2. In the bottle containing the reactants, N_2 was used as an internal standard for the micro-gas chromatography (μGC) analyses. Flowrates inside the test bench were controlled using Brooks mass flow controller (MFC) piloted by a Brooks 0254 controller. The gases exiting the MFCs were fed in a mixer filled with quartz wool. The pressure was measured at the exit of the gas mixer with a Keller Léo 2 pressure gauge (PI). Afterwards the gases entered a stainless steel reactor of internal diameter 3/8" heated using a Thermocoax heating wire coiled around the reactor. Inside the reactor, the catalyst was maintained between two pieces of quartz wool positioned directly on top of a type K thermocouple used to regulate and measure the temperature of the bed. After exiting the reactor, water and methanol were condensed in cold trap cooled with tap water running in the double jacket of the trap. The trap has an internal diameter of 1" and was filled with silica balls to reduce its volume and therefore the residence time of the gases. Pipes running between the reactor and the cold trap were heated using a Horst heating wire to prevent early condensation of water and methanol before the cold trap. After the cold trap, gases were expanded using a Brooks 5866 pressure controller (PC) before finally reaching an Inficon μGC to measure the concentrations of gases (CO_2, CO, H_2 and N_2).

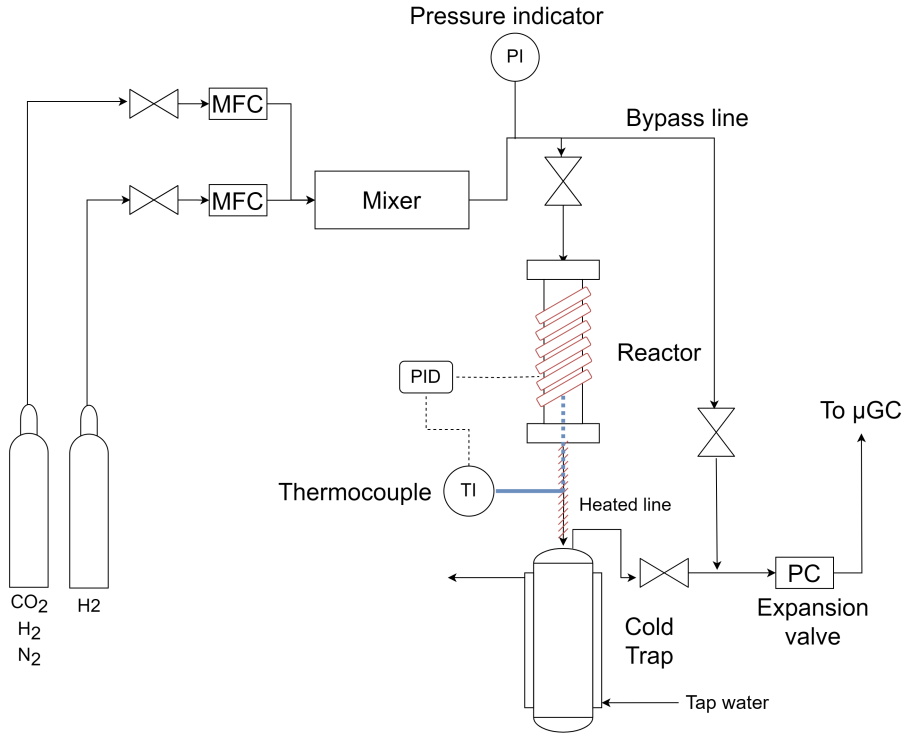

Figure III.13: Experimental setup for the catalytic activity measurements.

To make the catalyst bed, the catalyst was sometimes diluted in inert SiC in order to eliminate potential hotspots as well as to produce a long enough catalytic bed to prevent a bypass of reactants of the bed. Both the catalyst and the SiC were sieved to 63-125 µm. The bed dilution can lead to a maximum error below 10% on the conversion of reactants. This value is low enough to make fair comparisons between the catalysts featured in this study. Plug-flow conditions were met for all the catalyst bed studied. Full details are provided in Appendix B.1.

III.2.2.7.b Analytical setup

Exhaust gases were measured using an Inficon μGC equipped with two modules: (1) 'MS5A' module with backflush equipped with a Poraplot U pre-column (3 m x 320 µm x 30 µm) and a Molsieve 5A column (10 m x 320 µm x 30 µm) for the separation of H_2, N_2 and CO (carrier gas: Ar), (2) 'PPQ' module with two Poraplot Q column (pre-column: 1 m x 320 µm x 10 µm; column: 8 m x 320 µm x 10 µm) for the separation of CO_2 from light gases (H_2 N_2, CO) (carrier gas: He). Both modules were equipped with thermal conductivity detectors (TCDs). No other carbon-containing compounds (such as CH_4, dimethyl ether, etc...) were detected on both 'MS5A' and 'PPQ' modules during experiments. Molar concentrations and ratios of exhaust gases were calculated according to respectively Eqs. III.7 and III.8.

$$y_i = \frac{A_i / f_{i/N_2}}{\sum_j A_j / f_{j/N_2}} \tag{III.7}$$

$$i/j = \frac{F_i}{F_j} \cdot \frac{F}{F} = \frac{y_i}{y_j} \tag{III.8}$$

III.2.2.7.c Experimental method

All steps involving the measurement of the catalytic activity of a catalyst are described in this subsection.

Experiments were performed as follows:

1. The catalyst was reduced at a temperature of 300°C in pure H_2 at atmospheric pressure with a flow rate of 40 sccm.
2. After the reactor was cooled down to room temperature, the reaction mixture was introduced at the desired flow rate to match the aimed GHSV (Eq. III.9) and its flow rate was checked externally using an Agilent ADM Flowmeter.
3. The expansion valve was set to the operating pressure.
4. A first blank measurement of the unreacted gas mixture was analyzed in the μGC using the bypass line.
5. The reactor was set to its desired reaction temperature and exhaust gases were analyzed by μGC.
6. After reaction, the unreacted gas mixture was analyzed a second time through the bypass line.
7. The pressure was relieved from the reactor and the flow rate was checked a second time externally.

$$GHSV\ (h^{-1}) = \frac{Q_{Normo}\ (Nm^3/h)\ \rho_{cat}\ (kg/m^3)}{m_{cat}\ (kg)} \tag{III.9}$$

The experimental setup is represented in Figure III.14 and the numeration of streams are re-utilized in the equations of this section to explain how CO_2 conversion as well as reaction selectivities are calculated.

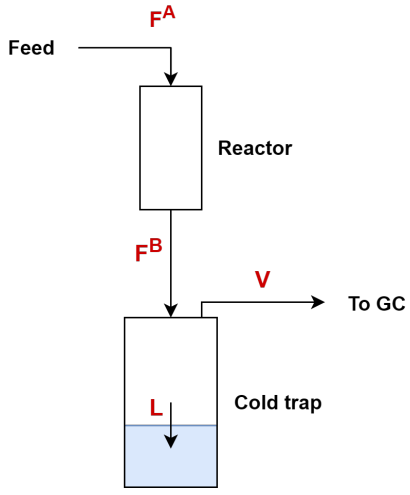

Figure III.14: Simplified diagram of the test bench with stream annotations.

The partial molar flowrates are determined by an average of measured flowrates before and after the reaction using Eq. III.10.

$$F_i^A = \frac{P_{Normo} Q_{Normo}}{RT_{Normo}} x_{i,bottle} \tag{III.10}$$

A first estimation of the conversion of CO_2 X_{CO_2} and the selectivities of both the hydrogenation of CO_2 to methanol reaction (S_{Hydro}) and the RWGS reaction (S_{RWGS}) were calculated using only the averaged data from the μGC with the following equations (Eq. III.11 and III.12):

$$X_{CO_2} = \frac{F_{CO_2}^A - F_{CO_2}^V}{F_{CO_2}^A} \cdot \frac{F_{N_2}}{F_{N_2}} = \frac{(CO_2/N_2)^{Blank} - (CO_2/N_2)^{Reaction}}{(CO_2/N_2)^{Blank}} \tag{III.11}$$

$$S_{RGWS} = \frac{F_{CO}^V}{F_{CO_2}^A X_{CO_2}} \cdot \frac{F_{N_2}}{F_{N_2}} = \frac{(CO/N_2)^{Reaction}}{(CO_2/N_2)^{Blank} X_{CO_2}}; S_{Hydro} = 1 - S_{RGWS} \tag{III.12}$$

The partial molar flowrates of stream B are calculated through the extent of the reaction described in Eqs. III.13 to III.18:

$$CO_2 : F_{CO_2}^B = F_{CO_2}^A (1 - X_{CO_2}) \tag{III.13}$$

$$H_2 : F_{H_2}^B = F_{H_2}^A - F_{CO_2}^A X_{CO_2} (3S_{Hydro} + S_{RWGS}) \tag{III.14}$$

$$CO : F_{CO}^B = F_{CO_2}^A X_{CO_2} S_{RWGS} \tag{III.15}$$

$$MeOH : F_{MeOH}^B = F_{CO_2}^A X_{CO_2} S_{Hydro} \tag{III.16}$$

$$H_2O : F_{H_2O}^B = F_{CO_2}^A X_{CO_2} \tag{III.17}$$

$$N_2 : F_{H_2O}^B = F_{N_2}^A \tag{III.18}$$

A vapor liquid equilibrium (VLE) calculation is then performed to compute the material balance on the cold trap. This calculation is explained in Appendix A. However, vapor molar fraction measured through μGC deviates from the exhaust of the reactor as it can only measure the concentration of incondensable gases (CO_2, CO, H_2 and N_2) at the exit of the experimental setup. Thus, due to the species lost in the cold trap (dissolved CO_2, CO, H_2 and N_2) as well as water and methanol vapors not detected on our μGC setup, the CO_2 conversion and the reaction selectivities calculated through the μGC are slightly erroneous. A better estimation can be obtained by solving the CO_2 conversion and reaction selectivities to match the composition of the exhaust gases analyzed by the μGC to the prediction of the VLE calculations at the exit of the cold trap. This is determined by implementing the above-mentioned method in scipy's 'least_squares' solver using Eq. III.20 as an objective function. The outline of this algorithm is summarized in Figure III.15.

$$y^{\mu GC}{}_{i,mod} = \frac{y_i}{1 - y_{H_2O} - y_{MeOH}} \tag{III.19}$$

$$\sum_{i:CO_2,CO,H_2,N_2} ({y^{\mu GC}}_{i,exp} - {y^{\mu GC}}_{i,mod})^2 = 0 \tag{III.20}$$

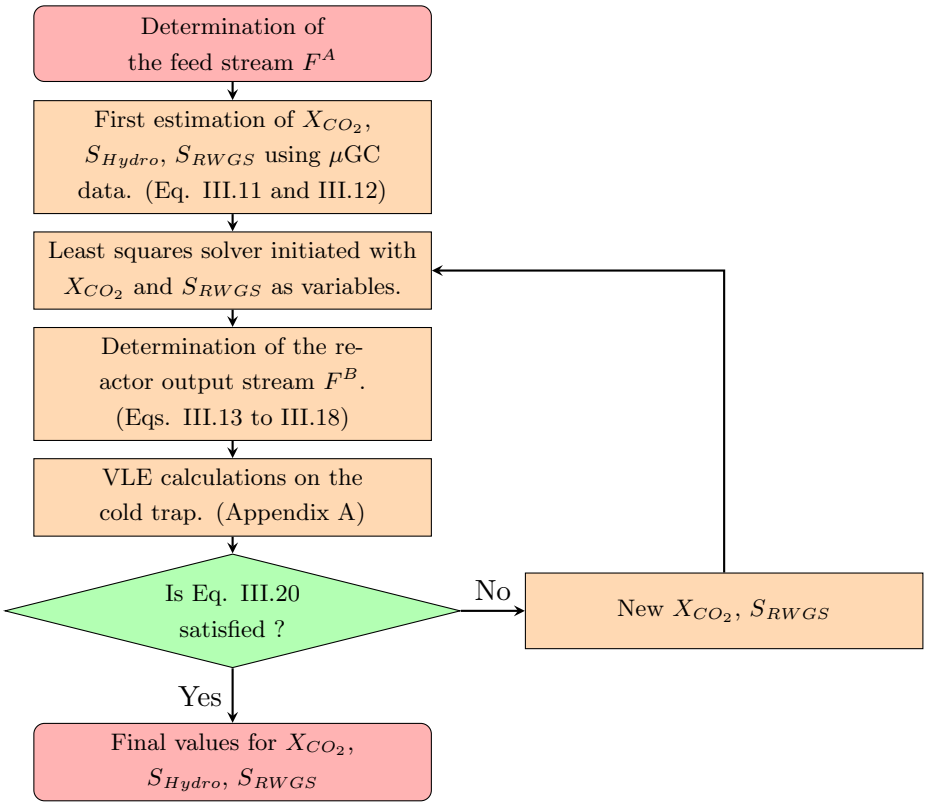

Figure III.15: Flow diagram of the algorithm used to determine the CO_2 conversion as well as reaction selectivities.

Nevertheless, due to the low activity of CZI (CP), CZZ (SG), CZZ (CO_2sc) and CZYSZ (CO_2sc), Eqs. III.11 and III.12 were used to determine the final values for CO_2 conversion and reaction selectivities as no liquid condensate was trapped during the experiments.

The productivity of the catalyst using Eqs. III.21 and III.22.

$$P_{MeOH} = \frac{F^A_{CO_2} * X_{CO_2} * S_{Hydro}}{m_{cat}} \tag{III.21}$$

$$Y = X_{CO_2} * S_{Hydro} \tag{III.22}$$

The material balance of the experimental setup was calculated twice in separate experiments using the AA commercial catalyst (Appendix B.2).

III.2.2.7.d Results and discussion

CZZ (CP) and AA (Commercial) were tested at 30 bar of pressure at a GHSV of 30,000 h^{-1} while the other catalysts were tested at 50 bar of pressure at a GHSV of 10,000 h^{-1} in order to get measurable activity on the μGC chromatographs. The H_2/CO_2 ratio value was 3 in every experiment. Table III.8 presents the results of the catalytic activity measurements on all studied

catalysts.

Table III.8: Catalytic performances of the studied performances for CO_2 hydrogenation into methanol.

Catalyst	GHSV (h^{-1})	Pressure (bar)	Temperature (°C)	X_{CO_2} (%)	S_{Hydro} (%)	Yield (%)	Productivity $g_{MeOH}.h^{-1}.kg_{cat}^{-1}$	Productivity $g_{MeOH}.h^{-1}.kg_{Cu}^{-1}$
CZZ (CP)	30 000	30	210	3.7	100*	3.7	527	1 384
			230	5.9	72.9	4.3	625	1 643
			250	9.8	50.3	5.0	718	1 886
			270	13.9	30.2	4.2	609	1 602
CZZ (SG)	10 000	50	250	2.9	54.0	1.5	22	50
			270	6.2	46.8	2.9	42	94
CZZ (CO_2sc)	10 000	50	250	0.6	100*	0.6	38	85
			300	4.7	70.0	3.3	205	458
CZYSZ (CO_2sc)	10 000	50	300	0.6	73.0	0.4	54	122
CZI (CP)	10 000	50	300	2.3	58.9	1.4	80	192
AA (Commercial)	30 000	30	210	5.0	73.6	3.7	237	465
			230	8.1	52.7	4.2	273	536
			250	13.8	34.7	4.8	307	604
			270	18.4	23.1	4.3	274	538

Between CZZ (CP), CZI (CP) and AA (Commercial), none of these catalysts present peak productivity below 250°C. However, the CZZ (CP) catalyst displays increased catalytic activity per mass of catalyst compared to the commercial AA catalyst. This observation is in line with what has been observed in the literature, where the higher basicity of zirconia facilitates the adsorption and activation of the acid carbon of CO_2 [5, 25]. While the CZI catalyst possess all the intrinsic characteristics of the other more active CZZ (CP) and AA catalysts, such as: low crystallinity with small crystal sizes (Section III.2.2.2), high surface area (Section III.2.2.3), some interaction with its support as evidenced by the shape of its TPR profile (Section III.2.2.4), as well as adequate metallic copper surface (Section III.2.2.6), the catalytic activity of the indium oxide-supported co-precipitated catalyst is much lower than its zirconia-supported CZZ and alumina-supported AA counterparts. It is unclear why the substitution of zirconia for indium oxide led to such a major drop in catalytic activity and further investigations into the interactions between indium oxide and the copper-zinc couple must be conducted to provide answers to these observations.

The catalysts synthesized via either the sol-gel method or the supercritical CO_2 route exhibit significantly lower catalytic activities compared to the commercial AA catalyst. In Angelo's PhD research on CZA catalysts [2], the sol-gel synthesized catalyst demonstrated poorer catalytic performance relative to its co-precipitated counterpart. Additionally, the sol-gel catalyst's higher density contributed to a productivity that, while similar in magnitude to the results obtained in this study, remained substantially lower than that of co-precipitated catalysts.

In their study on CZA catalysts, Kondrat *et al.* [35, 34, 33] demonstrated that stabilizing a specific precursor phase of zinc oxide using supercritical CO_2 resulted in a more active catalyst. Our results contrast their findings as our CO_2sc synthesized catalysts are much less active than our commercial CZA catalyst. However, as revealed through the XRD and TGA characteriza-

tions (Section III.2.2.2 to III.2.2.5), our syntheses produced a catalyst much different from that reported by Kondrat *et al.* [35, 34, 33]. It is thus likely that our sample contained well crystallized particles of isolated metallic copper, zinc oxide and zirconia, which is the exact opposite of what is aimed for an active methanol catalyst [33]. The differences in catalyst morphologies are likely due to the significantly harsher synthesis conditions we employed, at 350°C and 240 to 260 bar, compared to the milder conditions of 40°C and 110 bar used by Kondrat *et al.* [35, 34, 33]. The high synthesis temperature likely increased crystallization kinetics and favored individual metal or oxide phase formations.

III.2.2.8 Catalyst coating on LTA membrane

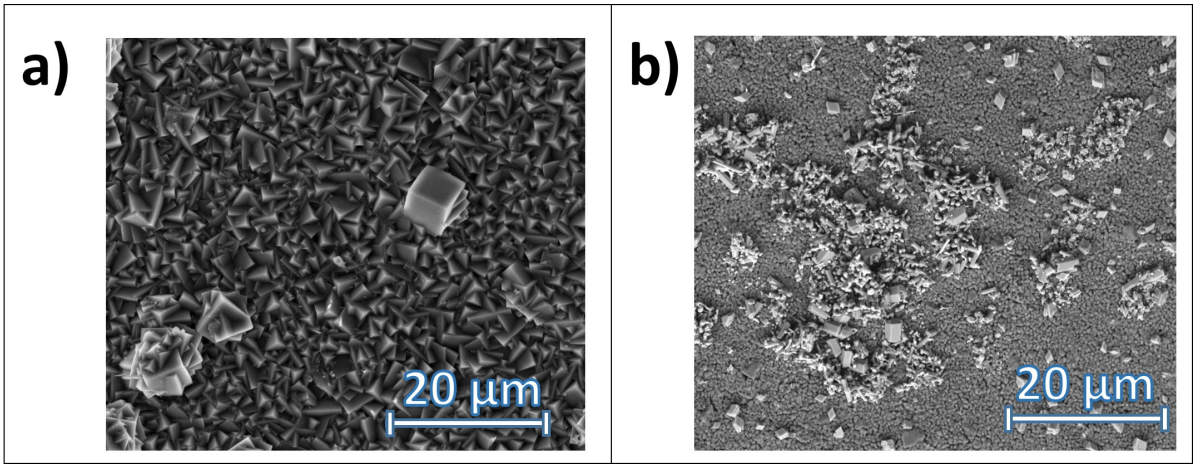

Figure III.16: SEM micrographs of a LTA membrane before and after the catalyst coating procedure through the CO_2sc route: a) before, b) after.

As shown in Figure III.16, coating the membrane with catalyst through the CO_2sc route led to its near complete destruction, with sparsely dispersed zeolite crystals present after the coating procedure. One explanation involves the harsh acidic conditions, employed to dissolve metal salts before synthesis, which would dissolve the zeolite membrane as well. If this assumption is to be correct, it would mean that coating the membrane with catalyst during the catalyst synthesis would require to carefully mitigate strongly acidic conditions to protect the membrane. As such, co-precipitation and sol-gel protocols, both utilizing acidic conditions to dissolve metal salts, would require modifications to make the synthesis possible. Another hypothesis involves the depressurization step at the end of the CO_2sc route. If supercritical CO_2 would be present in intercristalline pores, then depressurization of this gas could shatter the membrane as the gas expands.

III.3 Conclusion

In this chapter, recent advancements in the literature on both copper-zinc catalysts and emerging alternatives for methanol synthesis were reviewed. This short literature review highlighted that, to date, copper-zinc catalysts are the most viable candidates for low-temperature methanol synthesis. Nevertheless, copper-zinc catalysts benefit from decades of industrial applications.

Conversely, alternative catalytic systems are still in the early stages of research and development. However, future advancements could alter the conclusions drawn from this review.

Based on insights gained from the literature review, several copper-zinc catalysts were investigated for potential low temperature catalytic activity suited for membrane-assisted methanol synthesis from CO_2. Among the catalysts tested, only the CZZ (CP) catalyst exhibited greater activity, relative to its mass, compared to the commercial catalyst. Nonetheless, this catalyst did not demonstrate notable activity at low temperatures for methanol production. A copper-zinc catalyst supported on indium oxide was also studied. Despite promising characteristics observed in XRD, TPR, N_2O-RFC, and BET analyses, the catalyst surprisingly displayed low catalytic activity.

Additionally, alternative synthesis routes were explored to directly synthesize the catalyst on the membrane (ensuring close proximity between the catalytic and separation functions). Both the sol-gel and supercritical CO_2 methods failed to yield a copper-zinc catalyst with sufficient activity. While the underperformance of the sol-gel-synthesized catalyst aligns with existing literature, the poor results of the CO_2sc-synthesized catalysts contrast with findings by Kondrat *et al.* [35, 34, 33] on CO_2sc-synthesized CZA catalysts. However, unlike Kondrat *et al.* [35, 34, 33], the catalysts synthesized via the CO_2sc route in this study exhibited substantial properties differences from those typically associated with active methanol catalysts. Finally, this supercritical CO_2 method, as presented in this chapter, is inadequate for catalyst deposition on the membrane as it led to its complete destruction.

Besides this catalytic study, a new method was developed to solve the material balance of a catalytic test bench. Using an advanced thermodynamic model and rigorous VLE calculations, this approach accurately predicts liquid-phase composition down to the molar fraction percentages while relying solely on gas-phase data. This approach highlights that neglecting the dissolution of CO_2 in the liquid phase leads to non-negligible errors in the estimation of the CO_2 conversion and reaction selectivities.

Glossary (Chapter III)

Acronyms

μGC Micro-Gas Chromatography
AA Alfa Aesar (CZA commercial catalyst)
BET Brunauer-Emmet-Teller
BJH Barrett, Joyner et Halenda
CO_2sc Supercritical CO_2
CP Co-Precipitation
CZA Copper-Zinc-Alumina
CZI Copper-Zinc-India
CZYSZ Copper-Zinc-Yttria-Stabilized Zirconia
CZZ Copper-Zinc-Zirconia
DFT Density Functional Theory
DRIFTS Diffuse Reflectance Infrared Fourier Transform Spectroscopy
GC Gas Chromatography
GHSV Gas Hourly Space Velocity
IMC Intermetallic Compound
IUPAC International Union of Pure and Applied Chemistry
LTA Linde Type-A (zeolite crystal)
MFC Mass Flow Controller
MOF Metal Organic Framework
N_2O-RFC N_2O Reaction Frontal Chromatography
N.D. Not Determined
PC Pressure Controller
PI Pressure Indicator (gauge)
RWGS Reverse Water-Gas Shift
SEM Scanning Electron Microscope
SG Sol-Gel
SiC Silicon Carbide
SOD Sodalite (zeolite crystal)
TCD Thermal Conductivity Detector
TGA Thermogravimetric Analysis
TOF Turn-Over Frequency
TPR Temperature-Programmed Reduction
VLE Vapor Liquid Equilibrium
XRD X-Ray Diffraction

Roman letters

A_i Area of the peak of species i on the micro gas chromatographs (arbitrary unit)
B Ray width at half height (arbitrary unit)
D Crystal size (nm)
F_i^k Partial molar flowrate of species i in stream k (mol.s^{-1})

F^k Total molar flowrate of stream k ($mol.s^{-1}$)

K Scherrer constant ($K = 0.9$)

M_i Molar mass of compound i ($g.mol^{-1}$)

P_{MeOH} Productivity of the catalyst ($g_{MeOH}.h^{-1}.kg_{cat}^{-1}$ or $g_{MeOH}.h^{-1}.kg_{Cu}^{-1}$)

P_{Normo} Pressure at normal conditions ($P_{Normo} = 1.01325{\cdot}10^5$ Pa)

Q_{Normo} Normal volumetric flow rate in $Nm^3.s^{-1}$ (measured using the Agilent ADM flowmeter)

R Ideal gas constant ($R = 8.314\,J.mol^{-1}.K^{-1}$)

S_i Molar selectivity for reaction i (-)

T_{Normo} Temperature at normal conditions ($T_{Normo} = 273.15\,K$)

X_{CO_2} Molar conversion of CO_2 (-)

Y Reaction yield of the CO_2 hydrogenation to methanol (-)

$\%_{CuO,reduced}$ Percentage of copper oxide reduced (%)

$^i/_j$ Molar ratio between compound i and j (-)

f_{i/N_2} Response factor of compound i relative to N_2 (-)

$m_{CuO,reduced}$ Mass of reduced copper oxide measured experimentally with the TPR experiments (g)

$m_{CuO,theoretical}$ Theoretical mass of reduced copper oxide according to the preparation protocol (g)

m_{Cu} Copper mass in the catalyst sample (g)

m_{cat} Weight of the catalyst sample (g)

$n_{H_2,consumed}$ Amount of H_2 consumed by the reduction of the catalyst (mol)

$n_{O,consumed}$ Amount of oxygen consumed by the catalyst during the TGA (mol)

w_{Cu} Copper mass fraction in the catalyst (wt.%)

$x_{i,bottle}$ Molar fraction of species i in the reaction mixture bottle (measured using the blank measurement with the μGC) (mol.%)

$y_i^{\mu GC}$ Molar fraction of gas i in the exhaust stream measurable by the μGC (does not comprise MeOH and H_2O) (mod: calculated, exp: measured experimentally) (mol.%)

y_i Molar fraction of gas i in the exhaust stream (mol.%)

Greek letters

Δm Mass difference of the catalyst sample after the TGA experiment (g)

Θ Bragg angle of reflection (rad)

λ X-ray wavelength ($\lambda = 0.1541$ nm)

ρ_{cat} Apparent density of the catalyst sample ($g.cm^{-3}$)

References

[1] Bing An et al. "Confinement of Ultrasmall Cu/ZnO_x Nanoparticles in Metal-Organic Frameworks for Selective Methanol Synthesis from Catalytic Hydrogenation of CO_2". In: *Journal of the American Chemical Society* 139.10 (Mar. 15, 2017), pp. 3834–3840. ISSN: 0002-7863, 1520-5126. DOI: 10.1021/jacs.7b00058.

[2] Laetitia Angelo. "Développement de catalyseurs pour la synthèse de méthanol produit par hydrogénation du dioxyde de carbone". PhD thesis. 2014.

[3] Laetitia Angelo et al. "Study of CuZnMOx oxides (M=Al, Zr, Ce, CeZr) for the catalytic hydrogenation of CO_2 into methanol". In: *Comptes Rendus Chimie* 18.3 (Mar. 2015), pp. 250–260. ISSN: 16310748. DOI: 10.1016/j.crci.2015.01.001.

[4] F Arena et al. "Synthesis, characterization and activity pattern of Cu-ZnO/ZrO_2 catalysts in the hydrogenation of carbon dioxide to methanol". In: *Journal of Catalysis* 249.2 (July 25, 2007), pp. 185–194. ISSN: 00219517. DOI: 10.1016/j.jcat.2007.04.003.

[5] F. Arena et al. "Basic evidences for methanol-synthesis catalyst design". In: *Catalysis Today* 143.1 (May 15, 2009), pp. 80–85. ISSN: 09205861. DOI: 10.1016/j.cattod.2008.11.022.

[6] Francesco Arena et al. "Effects of oxide carriers on surface functionality and process performance of the Cu-ZnO system in the synthesis of methanol via CO_2 hydrogenation". In: *Journal of Catalysis* 300 (Apr. 2013), pp. 141–151. ISSN: 00219517. DOI: 10.1016/j.jcat.2012.12.019.

[7] Atul Bansode et al. "Impact of K and Ba promoters on CO_2 hydrogenation over Cu/Al_2O_3 catalysts at high pressure". In: *Catalysis Science & Technology* 3.3 (Feb. 12, 2013). Publisher: The Royal Society of Chemistry, pp. 767–778. ISSN: 2044-4761. DOI: 10.1039/C2CY20604H.

[8] Arik Beck et al. "The Enigma of Methanol Synthesis by Cu/ZnO/Al_2O_3-Based Catalysts". In: *Chemical Reviews* 124.8 (Apr. 24, 2024). Publisher: American Chemical Society, pp. 4543–4678. ISSN: 0009-2665. DOI: 10.1021/acs.chemrev.3c00148.

[9] Malte Behrens. "Meso- and nano-structuring of industrial Cu/ZnO/Al_2O_3 catalysts". In: *Journal of Catalysis* 267.1 (Oct. 2009), pp. 24–29. ISSN: 00219517. DOI: 10.1016/j.jcat.2009.07.009.

[10] Malte Behrens et al. "The Active Site of Methanol Synthesis over Cu/ZnO/Al_2O_3 Industrial Catalysts". In: *Science* 336.6083 (May 18, 2012). Publisher: American Association for the Advancement of Science, pp. 893–897. DOI: 10.1126/science.1219831.

[11] Jason M. Blackburn et al. "Deposition of Conformal Copper and Nickel Films from Supercritical Carbon Dioxide". In: *Science* 294.5540 (Oct. 5, 2001), pp. 141–145. ISSN: 0036-8075, 1095-9203. DOI: 10.1126/science.1064148.

[12] G. Bonura et al. "The changing nature of the active site of Cu-Zn-Zr catalysts for the CO_2 hydrogenation reaction to methanol". In: *Applied Catalysis B: Environmental* 152-153 (June 2014), pp. 152–161. ISSN: 09263373. DOI: 10.1016/j.apcatb.2014.01.035.

[13] Pengjing Chen et al. "Monolithic Ni_5Ga_3/SiO2/Al_2O_3/Al-fiber catalyst for CO_2 hydrogenation to methanol at ambient pressure". In: *Applied Catalysis A: General* 562 (July 2018), pp. 234–240. ISSN: 0926860X. DOI: 10.1016/j.apcata.2018.06.021.

[14] Bjerne S. Clausen et al. "Wetting/non-wetting phenomena during catalysis: Evidence from in situ on-line EXAFS studies of Cu-based catalysts". In: *Topics in Catalysis* 1.3 (Sept. 1, 1994), pp. 367–376. ISSN: 1572-9028. DOI: 10.1007/BF01492289.

[15] Francesco Dalena et al. "Advances in Methanol Production and Utilization, with Particular Emphasis toward Hydrogen Generation via Membrane Reactor Technology". In: *Membranes* 8.4 (Oct. 18, 2018). Number: 4, p. 98. ISSN: 2077-0375. DOI: 10.3390/membranes8040098.

[16] Shanshan Dang et al. "A review of research progress on heterogeneous catalysts for methanol synthesis from carbon dioxide hydrogenation". In: *Catalysis Today* 330 (June 2019), pp. 61–75. ISSN: 09205861. DOI: 10.1016/j.cattod.2018.04.021.

[17] Israf Ud Din et al. "Prospects for a green methanol thermo-catalytic process from CO_2 by using MOFs based materials: A mini-review". In: *Journal of CO_2 Utilization* 43 (Jan. 2021), p. 101361. ISSN: 22129820. DOI: 10.1016/j.jcou.2020.101361.

[18] Martin Drobek et al. "Evaluation of a new supercritical CO_2-assisted deposition method for preparing gas selective polymer/zeolite composite membranes". In: *Journal of Membrane Science* 429 (Feb. 2013), pp. 428–435. ISSN: 03767388. DOI: 10.1016/j.memsci.2012.11.058.

[19] Véronique Durand et al. "Evaluation of a new On-Stream Supercritical Fluid Deposition process for sol–gel preparation of silica-based membranes on tubular supports". In: *The Journal of Supercritical Fluids* 77 (May 2013), pp. 17–24. ISSN: 08968446. DOI: 10.1016/j.supflu.2013.02.016.

[20] Véronique Durand et al. "Potential of sub- and supercritical CO_2 reaction media for sol–gel deposition of silica-based molecular sieve membranes". In: *Separation and Purification Technology* 121 (Jan. 2014), pp. 30–37. ISSN: 13835866. DOI: 10.1016/j.seppur.2013.06.031.

[21] Melis S. Duyar et al. "Low-pressure methanol synthesis from CO_2 over metal-promoted Ni-Ga intermetallic catalysts". In: *Journal of CO_2 Utilization* 39 (July 2020), p. 101151. ISSN: 22129820. DOI: 10.1016/j.jcou.2020.03.001.

[22] Matthias S. Frei et al. "Role of Zirconia in Indium Oxide-Catalyzed CO_2 Hydrogenation to Methanol". In: *ACS Catalysis* 10.2 (Jan. 17, 2020), pp. 1133–1145. ISSN: 2155-5435, 2155-5435. DOI: 10.1021/acscatal.9b03305.

[23] Fausto Gallucci. "Inorganic Membrane Reactors for Methanol Synthesis". In: *Methanol*. Elsevier, 2018, pp. 493–518. ISBN: 978-0-444-63903-5. DOI: 10.1016/B978-0-444-63903-5.00018-2.

[24] L. C. Grabow and M. Mavrikakis. "Mechanism of Methanol Synthesis on Cu through CO_2 and CO Hydrogenation". In: *ACS Catalysis* 1.4 (Apr. 1, 2011), pp. 365–384. ISSN: 2155-5435, 2155-5435. DOI: 10.1021/cs200055d.

[25] R. Guil-López et al. "Methanol Synthesis from CO_2: A Review of the Latest Developments in Heterogeneous Catalysis". In: *Materials* 12.23 (Nov. 26, 2019), p. 3902. ISSN: 1996-1944. DOI: 10.3390/ma12233902.

[26] Poul L. Hansen et al. "Atom-Resolved Imaging of Dynamic Shape Changes in Supported Copper Nanocrystals". In: *Science* 295.5562 (Mar. 15, 2002). Publisher: American Association for the Advancement of Science, pp. 2053–2055. DOI: 10.1126/science.1069325.

[27] Xing Huang et al. "Visualizing Structural and Chemical Transformations of an Industrial $Cu/ZnO/Al_2O_3$ Pre-catalyst during Activation and CO_2 Reduction". In: *ChemCatChem* 14.24 (2022). _eprint: https://onlinelibrary.wiley.com/doi/pdf/10.1002/cctc.202201280, e202201280. ISSN: 1867-3899. DOI: 10.1002/cctc.202201280.

[28] Xinyu Jia et al. "Selective hydrogenation of CO_2 to methanol over Ni/In_2O_3 catalyst". In: *Journal of Energy Chemistry* 50 (Nov. 2020), pp. 409–415. ISSN: 20954956. DOI: 10.1016/j.jechem.2020.03.083.

[29] Xiao Jiang et al. "Recent Advances in Carbon Dioxide Hydrogenation to Methanol via Heterogeneous Catalysis". In: *Chemical Reviews* 120.15 (Aug. 12, 2020), pp. 7984–8034. ISSN: 0009-2665, 1520-6890. DOI: 10.1021/acs.chemrev.9b00723.

[30] Deok Yeon Jo et al. "Role of the Zn atomic arrangements in enhancing the activity and stability of the kinked Cu(211) site in CH_3OH production by CO_2 hydrogenation and dissociation: First-principles microkinetic modeling study". In: *Journal of Catalysis* 373 (May 2019), pp. 336–350. ISSN: 00219517. DOI: 10.1016/j.jcat.2019.04.009.

[31] Lole Jurado et al. "Enhancing the catalytic performance of Ni based catalysts in toluene reforming at low temperature by structuring on SiC extrudates". In: *Sustainable Energy & Fuels* 7.17 (2023), pp. 4273–4287. ISSN: 2398-4902. DOI: 10.1039/D3SE00705G.

[32] Shyam Kattel et al. "Active sites for CO_2 hydrogenation to methanol on Cu/ZnO catalysts". In: *Science* 355.6331 (Mar. 24, 2017), pp. 1296–1299. ISSN: 0036-8075, 1095-9203. DOI: 10.1126/science.aal3573.

[33] Simon A. Kondrat et al. "Preparation of a highly active ternary Cu-Zn-Al oxide methanol synthesis catalyst by supercritical CO_2 anti-solvent precipitation". In: *Catalysis Today* 317 (Nov. 2018), pp. 12–20. ISSN: 09205861. DOI: 10.1016/j.cattod.2018.03.046.

[34] Simon A. Kondrat et al. "Stable amorphous georgeite as a precursor to a high-activity catalyst". In: *Nature* 531.7592 (Mar. 2016), pp. 83–87. ISSN: 0028-0836, 1476-4687. DOI: 10.1038/nature16935.

[35] Simon A. Kondrat et al. "The effect of sodium species on methanol synthesis and water-gas shift Cu/ZnO catalysts: utilising high purity zincian georgeite". In: *Faraday Discussions* 197 (2017), pp. 287–307. ISSN: 1359-6640, 1364-5498. DOI: 10.1039/C6FD00202A.

[36] Valentin L'hospital et al. "Optimization of the continuous coprecipitation in a microfluidic reactor: Cu-based catalysts for CO_2 hydrogenation into methanol". In: *Fuel* 319 (July 2022), p. 123689. ISSN: 00162361. DOI: 10.1016/j.fuel.2022.123689.

[37] Valentin L'Hospital. "Développement et optimisation de catalyseurs à base de cuivre pour la synthèse de méthanol et de diméthyléther à partir de CO_2". PhD thesis. 2018.

[38] Avishai Lerner et al. "Life cycle analysis (LCA) of low emission methanol and di-methyl ether (DME) derived from natural gas". In: *Fuel* 220 (May 2018), pp. 871–878. ISSN: 00162361. DOI: 10.1016/j.fuel.2018.02.066.

[39] Molly Meng-Jung Li et al. "Enhanced CO_2 hydrogenation to methanol over CuZn nanoalloy in Ga modified Cu/ZnO catalysts". In: *Journal of Catalysis* 343 (Nov. 2016), pp. 157–167. ISSN: 00219517. DOI: 10.1016/j.jcat.2016.03.020.

[40] Thomas Lunkenbein et al. "Formation of a ZnO Overlayer in Industrial $Cu/ZnO/Al_2O_3$ Catalysts Induced by Strong Metal-Support Interactions". In: *Angewandte Chemie* 127.15 (Apr. 7, 2015), pp. 4627–4631. ISSN: 00448249. DOI: 10.1002/ange.201411581.

[41] Oliver Martin et al. "Indium Oxide as a Superior Catalyst for Methanol Synthesis by CO_2 Hydrogenation". In: *Angewandte Chemie International Edition* 55.21 (May 17, 2016), pp. 6261–6265. ISSN: 14337851. DOI: 10.1002/anie.201600943.

[42] Yasuyuki Matsumura et al. "Low-Temperature Methanol Synthesis Catalyzed over Ultrafine Palladium Particles Supported on Cerium Oxide". In: *Journal of Catalysis* 197.2 (Jan. 2001), pp. 267–272. ISSN: 00219517. DOI: 10.1006/jcat.2000.3094.

[43] Xin-Yu Meng et al. "Recent progress and understanding on In_2O_3-based composite catalysts for boosting CO_2 hydrogenation". In: *Journal of CO_2 Utilization* 55 (Jan. 2022), p. 101844. ISSN: 22129820. DOI: 10.1016/j.jcou.2021.101844.

[44] Jörg Ott et al. "Methanol". In: *Ullmann's Encyclopedia of Industrial Chemistry*. Ed. by Wiley-VCH Verlag GmbH & Co. KGaA. Weinheim, Germany: Wiley-VCH Verlag GmbH & Co. KGaA, Oct. 15, 2012, a16_465.pub3. ISBN: 978-3-527-30673-2. DOI: 10.1002/14356007.a16_465.pub3.

[45] Gianfranco Pacchioni. "From CO_2 to Methanol on $Cu/ZnO/Al_2O_3$ Industrial Catalyst. What Do We Know about the Active Phase and the Reaction Mechanism?" In: *ACS Catalysis* 14.4 (Feb. 16, 2024). Publisher: American Chemical Society, pp. 2730–2745. DOI: 10.1021/acscatal.3c05669.

[46] Thanaree Phongamwong et al. "CO_2 hydrogenation to methanol over CuO-ZnO-ZrO_2-SiO_2 catalysts: Effects of SiO_2 contents". In: *Chemical Engineering Journal* 316 (May 2017), pp. 692–703. ISSN: 13858947. DOI: 10.1016/j.cej.2017.02.010.

[47] Letícia F. Rasteiro et al. "Insights into the alloy-support synergistic effects for the CO_2 hydrogenation towards methanol on oxide-supported Ni_5Ga_3 catalysts: An experimental and DFT study". In: *Applied Catalysis B: Environmental* 302 (Mar. 2022), p. 120842. ISSN: 09263373. DOI: 10.1016/j.apcatb.2021.120842.

[48] Jens Sehested. "Industrial and scientific directions of methanol catalyst development". In: *Journal of Catalysis* 371 (Mar. 2019), pp. 368–375. ISSN: 00219517. DOI: 10.1016/j.jcat.2019.02.002.

[49] Poonam Sharma et al. "Recent advances in hydrogenation of CO_2 into hydrocarbons via methanol intermediate over heterogeneous catalysts". In: *Catalysis Science & Technology* 11.5 (Mar. 15, 2021). Publisher: The Royal Society of Chemistry, pp. 1665–1697. ISSN: 2044-4761. DOI: 10.1039/D0CY01913E.

[50] Zhisheng Shi, Qingqing Tan, and Dongfang Wu. "A novel Core-Shell structured CuIn@SiO_2 catalyst for CO_2 hydrogenation to methanol". In: *AIChE Journal* 65.3 (Mar. 2019), pp. 1047–1058. ISSN: 0001-1541, 1547-5905. DOI: 10.1002/aic.16490.

[51] Zhisheng Shi et al. "CO_2 hydrogenation to methanol over Cu-In intermetallic catalysts: Effect of reduction temperature". In: *Journal of Catalysis* 379 (Nov. 2019), pp. 78–89. ISSN: 00219517. DOI: 10.1016/j.jcat.2019.09.024.

[52] Thomas E. L. Smitshuysen et al. "Optimizing Ni-Fe-Ga alloys into Ni_2FeGa for the Hydrogenation of CO_2 into Methanol". In: *ChemCatChem* 12.12 (June 18, 2020), pp. 3265–3273. ISSN: 1867-3880, 1867-3899. DOI: 10.1002/cctc.202000174.

[53] Felix Studt et al. "Discovery of a Ni-Ga catalyst for carbon dioxide reduction to methanol". In: *Nature Chemistry* 6.4 (Apr. 2014). Number: 4, pp. 320–324. ISSN: 1755-4330, 1755-4349. DOI: 10.1038/nchem.1873.

[54] Kaihang Sun et al. "Hydrogenation of CO_2 to methanol over In_2O_3 catalyst". In: *Journal of CO_2 Utilization* 12 (Dec. 2015), pp. 1–6. ISSN: 22129820. DOI: 10.1016/j.jcou.2015.09.002.

[55] Lian-Ming Sun et al. "Adsorption - Aspects théoriques". In: (2016).

[56] Thongthai Witoon et al. "Enhanced activity, selectivity and stability of a CuO-ZnO-ZrO_2 catalyst by adding graphene oxide for CO_2 hydrogenation to methanol". In: *Chemical Engineering Journal* 334 (Feb. 2018), pp. 1781–1791. ISSN: 13858947. DOI: 10.1016/j.cej.2017.11.117.

[57] Jingang Wu et al. "The stability of Cu/ZnO-based catalysts in methanol synthesis from a CO_2-rich feed and from a CO-rich feed". In: *Applied Catalysis A: General* 218.1 (Sept. 2001), pp. 235–240. ISSN: 0926860X. DOI: 10.1016/S0926-860X(01)00650-0.

[58] Qian Wu et al. "Current advances in bimetallic catalysts for carbon dioxide hydrogenation to methanol". In: *Fuel* 313 (Apr. 2022), p. 122963. ISSN: 00162361. DOI: 10.1016/j.fuel.2021.122963.

[59] Xiao-Kuan Wu et al. "Unraveling the catalytically active phase of carbon dioxide hydrogenation to methanol on Zn/Cu alloy: Single atom versus small cluster". In: *Journal of Energy Chemistry* 61 (Oct. 2021), pp. 582–593. ISSN: 20954956. DOI: 10.1016/j.jechem.2021.02.016.

[60] Chengsheng Yang et al. "Strong Electronic Oxide-Support Interaction over In_2O_3/ZrO_2 for Highly Selective CO_2 Hydrogenation to Methanol". In: *Journal of the American Chemical Society* 142.46 (Nov. 18, 2020), pp. 19523–19531. ISSN: 0002-7863, 1520-5126. DOI: 10.1021/jacs.0c07195.

[61] Yixiong Yang, Michael G. White, and Ping Liu. "Theoretical Study of Methanol Synthesis from CO_2 Hydrogenation on Metal-Doped Cu(111) Surfaces". In: *The Journal of Physical Chemistry C* 116.1 (Jan. 12, 2012), pp. 248–256. ISSN: 1932-7447, 1932-7455. DOI: 10.1021/jp208448c.

[62] Yixiong Yang et al. “Fundamental studies of methanol synthesis from CO_2 hydrogenation on Cu(111), Cu clusters, and Cu/ZnO(0001)”. In: *Physical Chemistry Chemical Physics* 12.33 (2010), p. 9909. ISSN: 1463-9076, 1463-9084. DOI: 10.1039/c001484b.

[63] Libo Yao et al. “Synergy between active sites of Cu-In-Zr-O catalyst in CO_2 hydrogenation to methanol”. In: *Journal of Catalysis* 372 (Apr. 2019), pp. 74–85. ISSN: 00219517. DOI: 10.1016/j.jcat.2019.02.021.

[64] Wenzhe Yue et al. “Highly Selective CO_2 Conversion to Methanol in a Bifunctional Zeolite Catalytic Membrane Reactor”. In: *Angewandte Chemie International Edition* 60.33 (Aug. 9, 2021), pp. 18289–18294. ISSN: 1433-7851, 1521-3773. DOI: 10.1002/anie.202106277.

[65] Xue Zhang et al. “Optimum Cu nanoparticle catalysts for CO_2 hydrogenation towards methanol”. In: *Nano Energy* 43 (Jan. 2018), pp. 200–209. ISSN: 22112855. DOI: 10.1016/j.nanoen.2017.11.021.

[66] Ya-Fan Zhao et al. “Insight into methanol synthesis from CO_2 hydrogenation on Cu(111): Complex reaction network and the effects of H_2O”. In: *Journal of Catalysis* 281.2 (July 2011), pp. 199–211. ISSN: 00219517. DOI: 10.1016/j.jcat.2011.04.012.

[67] Jiawei Zhong et al. “State of the art and perspectives in heterogeneous catalysis of CO_2 hydrogenation to methanol”. In: *Chemical Society Reviews* 49.5 (2020). Number: 5, pp. 1385–1413. ISSN: 0306-0012, 1460-4744. DOI: 10.1039/C9CS00614A.

Chapter IV

Investigation of potential biases in the comparison of membrane and conventional reactors in CO_2 to methanol processes using process optimization

Abstract

Membrane reactors applied to methanol synthesis from CO_2 aim to alleviate low reaction conversions by shifting the thermodynamic equilibrium through *in-situ* water removal. The comparison between membrane reactors and conventional fixed-bed reactors has been previously studied in the literature at the process level. In fact, in the literature, membrane and conventional fixed-bed reactors have been so far compared under identical operating conditions at the process scale. However, studies at the reactor scale have identified that these types of reactors might have different optimal operating conditions. Therefore, potential biases in previous process simulation studies are investigated in the present article through process optimization using an energy cost criterion. This study uses design-free pseudo-homogeneous isothermal and isobaric plug-flow reactor models allowing the use of simplified and broad optimization variables. As a result, the optimal operating conditions for the membrane reactor process were found to depend significantly on the reactor's GHSV and the membrane's selectivity, and these conditions can differ greatly from those of a conventional fixed-bed reactor process. As such, comparing the two reactor types under the same operating conditions at the process level can lead to a bias favoring one reactor type depending on the chosen conditions. This study also explores the advantages of using compressed sweep gas and compares the performance of the two reactor types when varying levels of energy penalties are applied to high recycle ratios through the purge rate.

IV.1 Introduction

The growing concern over climate change caused by our societies' dependency on fossil hydrocarbons is driving scientists and engineers to seek out more sustainable and cleaner alternatives. Among these solutions, methanol synthesis stands out as a promising pathway due to its versatility as a renewable energy carrier and chemical feedstock. Traditionally, methanol production has relied on fossil fuel-based processes. In these processes, the fossil feedstock is transformed into syngas containing a significant amount of CO. Inside a conventional fixed-bed reactor, this CO within the reaction mixture reacts with water using the water-gas shift (WGS) reaction to

produce additional CO_2 and H_2 for further methanol production (Eqs. IV.1 and IV.2) [4, 11].

In order to develop more efficient and environmentally friendly alternative processes, much research is put into switching to more sustainable CO_2 rich feedstocks (obtained either from carbon capture or biomass conversion) combined with hydrogen generated through sustainable water electrolysis. However, as fewer CO is available in these feed gases, a greater amount of water is generated and accumulates in the reactor, which hinders CO_2 conversion and prematurely deactivates common copper-zinc-alumina catalysts [4]. Membrane technology inside membrane reactors aims to alleviate these issues by separating water molecules *in-situ*, thus increasing the conversion of CO_2 (through the Le Chapelier's principle) and protecting the catalyst.

While this study will focus on methanol synthesis from CO_2, studies on membrane-assisted processes for direct dimethyl ether (DME) synthesis are also discussed here as they represent a major body of work in the literature for their suitability with membrane reactors. Direct DME synthesis from CO_2 involves methanol dehydration (Eq. IV.3) along CO_2 hydrogenation within the same reactor. The benefits of this strategy involve the conversion of methanol inside the reactor which, on top of water removed from the reaction by the membrane, induces further conversion of reactants per pass through shifting of the thermodynamic equilibrium [1].

$$CO_2\ Hydrogenation:\ CO_2 + 3\,H_2 \rightleftharpoons CH_3OH + H_2O \qquad \Delta_r H_{298K} = -49.8\,kJ \cdot mol^{-1} \tag{IV.1}$$

$$RWGS:\ CO_2 + H_2 \rightleftharpoons CO + H_2O \qquad \Delta_r H_{298K} = 41{,}0\,kJ \cdot mol^{-1} \tag{IV.2}$$

$$Methanol\ dehydration:\ 2\,CH_3OH \rightleftharpoons H_3COCH_3 + H_2O \qquad \Delta_r H_{298K} = -23{,}4\,kJ \cdot mol^{-1} \tag{IV.3}$$

To date, no known industrial methanol or direct DME synthesis process uses a membrane reactor. However, academic works on process simulations of hypothetical membrane-assisted methanol or direct DME synthesis processes have studied their viability in terms of energy efficiency [2, 9, 8, 7] and economic performances [7, 15] compared to conventional processes using fixed-bed reactors.

In the literature, membrane reactor processes for methanol and DME synthesis are considered to be more energy-efficient than a process using a conventional fixed-bed reactor [9, 8, 7]. These effects were measured by Hamedi *et al.* [9] for an ideal membrane, with a 32% reduction in power requirement and 21% exergy production in the best case. Conversely, Atsonios *et al.* [2] did not measure any significant energy efficiency benefits of the membrane reactor process for a membrane permeable only to water and methanol. Nevertheless, the authors do note potential economic gains through a reduction in reactor volume and a significant drop in flow rate within the recirculation loop [2].

However, real gas permeation membranes are not ideal and lead to losses of reactants through the membrane [9, 10]. Consequently, Hamedi et al. [9] calculated a minimum H_2O/H_2 separation factor of 970, which is on the high end of what has been achieved in the literature on microporous membrane material, to start achieving energy savings compared with the conventional fixed-bed

reactor process. Nevertheless, according to the study of Dieterich et al. [7], the energy efficiency of a membrane-assisted process equipped with a poorly selective membrane can be improved by compressing a reactant-laden sweep gas to prevent loss of reactants through the membrane (also known as co-feeding strategy).

For the direct synthesis of DME, Hamedi and Brinkman [8] show in their study that the energy consumption of the membrane reactor process is 1.5% lower than that of the conventional fixed-bed reactor process. This reduction in energy consumption was accompanied by a 44.5% and 69.4% reduction respectively in the use of hot and cold utilities.

The study of techno-economics of membrane-assisted CO_2 to methanol or DME processes is a very recent research topic. So far, conflicting results have been presented on the economic viability of membrane-assisted processes for methanol or DME synthesis. In their study on methanol synthesis, Dieterich *et al.* [7] have calculated membrane prices much lower than what is currently offered along with permeation performances yet unheard of in the literature. Conversely, Poto *et al.* [15] on the membrane-assisted direct synthesis of DME from CO_2 predict significant economic gains over conventional fixed-bed reactor processes. In this latter study, the main economic gain was made on purchase of the catalyst due to the smaller catalytic bed of the membrane reactor required for similar performances compared to the conventional reactor one.

Studies on membrane-assisted methanol or DME synthesis from CO_2 at the process scale have yielded conflicting results regarding their viability. A potential issue is that these studies often compare membrane reactors and conventional reactors using identical operating parameters (such as temperature and pressure). However, studies at the reactor scale have shown that membrane reactors and conventional reactors may have different optimal operating parameters [14, 10]. Thus, comparing them under the same set of parameters can introduce bias, potentially favoring one technology over the other based on the chosen conditions. To investigate whether such bias exists in previous studies, this work compares the energy efficiency of both membrane-assisted and conventional fixed-bed reactor processes using process optimization specific to each technology.

IV.2 Materials and methods

IV.2.1 Reactor models

To simplify the optimization problem, 1D pseudo-homogeneous isothermal and isobaric plug-flow reactor models are used for both membrane reactors and conventional fixed-bed reactors. These types of models are used here as they do not require a specific reactor design, which greatly simplifies the optimization problem. Such models have been used previously in the literature to model lab-scale experimental membrane reactors [17] or conduct studies at the reactor scale [6].

All of the reactors described in this section are written in python language and communicate with the process simulation software ProSimPlus3 via a local COM server. Material balance equations were solved using scipy's 'solve_ivp' function with the 'BDF' solver. To reach sufficient accuracy on the resolution of differential equations, the maximum step size of the solver was set to 0.5% of the value of the desired modified residence time τ_0. Furthermore, to reduce computational costs, reaction kinetics and the Soave-Redlich-Kwong (SRK) equation of state were written in C++ language.

IV.2.1.1 Conventional fixed-bed reactor

Eq. IV.4 describes the material balance of a catalytic plug-flow reactor under steady-state conventionally integrated along the mass of catalyst inside the reactor.

$$\frac{d\dot{n}_i}{dw_{Bed}} = \sum_j^{N_r} r_j \nu_{ij} \tag{IV.4}$$

Expressing τ (m^3_{Bed}.s.Nm^{-3}), representing a modified residence time described in Eq. IV.6, the material balance within the conventional reactor leads to Eq. IV.5, which is the equation used to solve the material balance in the present simulations.

$$\frac{d\dot{n}_i}{d\tau} = \Big(\sum_j^{N_r} r_j \nu_{ij} \Big) \dot{Q}_0 \rho_{Bed} \tag{IV.5}$$

$$\tau_0 = \frac{w_{Bed}}{\dot{Q}_0 \rho_{Bed}} = \frac{1}{GHSV_0} \tag{IV.6}$$

The amount of heat transferred to the hypothetical shell of the reactor is calculated using the amount of heat generated during the reaction (Eq. IV.7). The reaction enthalpy for both the CO_2 hydrogenation reaction and RWGS is calculated using Eqs. IV.8 and IV.9.

$$Q_{Shell} = \dot{Q}_0 \rho_{Bed} \int_0^{\tau_0} \Big(\sum_j^{N_r} r_j \Delta r H_j \Big) \, d\tau \tag{IV.7}$$

$$\Delta r H_j(T) = \Delta r H_j(T_{ref}) + \int_{T_{ref}}^{T} \Delta C_{p_i} \, dT \tag{IV.8}$$

$$\Delta C_{p_i} = \sum_i^{N_c} \nu_{ij} C_{p_i} \tag{IV.9}$$

IV.2.1.2 Membrane reactor

The material balance inside the membrane reactor is solved using Eq. IV.10 for the retentate stream and Eq. IV.11 for the permeate stream. While counter-current flow is best suited for membrane reactors, the proposed model in this study implies a co-current flow regime to save on computational costs. To neglect heat transfer between the retentate and permeate sides of the membrane reactor, both streams are set at the same temperature, which is assumed to remain constant.

$$\frac{d\dot{n}_i^R}{d\tau} = \Big(\sum_j^{N_r} r_j \nu_{ij}\Big)\dot{Q}_0 \rho_{Bed} - J_i S_\tau \tag{IV.10}$$

$$\frac{d\dot{n}_i^P}{d\tau} = J_i S_\tau \tag{IV.11}$$

$$S_\tau = S\frac{\dot{Q}_0 \rho_{Bed}}{w_{Bed}} = \frac{S}{\tau_0} \tag{IV.12}$$

The transmembrane flowrate per modified residence time is calculated by multiplying a transmembrane molar flowrate per membrane surface area J_i (expressed in $\text{mol.s}^{-1}\text{.m}^{-2}$) with a membrane surface area per modified residence time S_τ (expressed in $\text{m}^2\text{.m}_{Bed}^{-3}\text{.s}^{-1}\text{.Nm}^3$). For water, the J_{H_2O} term includes the permeance of water through a zeolite membrane (Eq. IV.13). For other compounds (CO_2, CO, H_2, MeOH), the J_i terms are calculated using permselectivities as described in Eq. IV.14. For simplicity, the membrane performances featured in this study, being the water permeance and the permselectivities, are assumed to be independent of temperature conditions and its values are loosely inspired from the Linde Type A (LTA) membrane featured in the study of Raso *et al.* [16] (Table IV.1). Noteworthy, the study of Raso *et al.* [16] involves the permeation of a gas mixture and, thus, the permselectivities derived from it, featured in our study, do not represent ideal permselectivities (which are evaluated in separate gas permeation experiments of single gases). An artificial GSF is introduced and can be set to different values to study the sensitivity of the process optimum regarding the selectivity of the membrane (Eq. IV.14). A GSF value of 1 represents the base membrane selectivities described in Table IV.1, while higher values increase the membrane selectivity towards water and, as such, decrease the permeation of other compounds through the membrane.

$$J_{H_2O} = \Pi_{H_2O}(f_{H_2O}^R - f_{H_2O}^P) \tag{IV.13}$$

$$J_i = \frac{\Pi_{H_2O}}{\alpha_{H_2O/i} GSF}(f_i^R - f_i^P) \tag{IV.14}$$

Table IV.1: Membrane performances utilized in the membrane reactor.

Parameter	Value
Π_{H_2O}	$1 \cdot 10^{-7}\ mol.s^{-1}.m^{-2}.Pa^{-1}$
α_{H_2O/CO_2}	100
$\alpha_{H_2O/CO}$	25
α_{H_2O/H_2}	25
$\alpha_{H_2O/MeOH}$	50

The heat collected in the hypothetical shell side of the reactor is calculated by subtracting the heat transferred to the permeate side due to species exiting the catalytic bed (corresponding to the ΔH^P term) to the heat generated by the reaction (Eq. IV.15). This ΔH^P term is calculated by the difference in enthalpy between the inlet and the outlet of the permeate side of the membrane reactor using ProSimPlus3.

$$Q_{Shell} = \dot{Q}_0 \rho_{Bed} \Big(\int_0^{\tau_0} \big(\sum_j^{N_r} r_j \Delta r H_j \big)\, d\tau \Big) - \Delta H^P \tag{IV.15}$$

IV.2.1.3 Reaction kinetics

Reaction kinetics were taken from Slotboom *et al.* [18] (Eqs. IV.16 to IV.18) as their model covers a wide range of operating conditions. This model was built using a commercial copper-zinc-alumina methanol catalyst. In this kinetic model, the formation of side products, such as CH_4 and DME, is neglected.

$$r_{CO_2} = k_{CO_2} f_{CO_2} f_{H_2}^2 \Big(1 - \frac{1}{Kp^{\circ}_{CO_2}(T)} \frac{f_{CH_3OH} f_{H_2O}}{f_{H_2}^3 f_{CO_2}} \Big) \Theta^{*^2} \tag{IV.16}$$

$$r_{RWGS} = k_{RWGS} f_{CO_2} f_{H_2}^{\frac{1}{2}} \Big(1 - \frac{1}{Kp^{\circ}_{RWGS}(T)} \frac{f_{CO} f_{H_2O}}{f_{H_2} f_{CO_2}} \Big) \Theta^{*} \tag{IV.17}$$

$$\Theta^* = \big(f_{H_2}^{\frac{1}{2}} k_{H_2} + f_{H_2O} k_{H_2O/9} + f_{CH_3OH} \big)^{-1} \tag{IV.18}$$

Table IV.2: Parameters for the Slotboom *et al.* kinetic model [18].

Parameter	Value or equation
k_{CO_2}	$7.414 \cdot 10^{14} exp\big(-\frac{166{,}000}{RT} \big)$
k_{RWGS}	$1.111 \cdot 10^{19} exp\big(-\frac{203{,}700}{RT} \big)$
$k_{H_2O/9}$	126.4
k_{H_2}	1.099
$log_{10}(Kp^{\circ}_{CO_2}(T))$	$\frac{3066}{T} - 10.592$
$log_{10}(Kp^{\circ}_{RWGS}(T))$	$\frac{-2073}{T} + 2.029$

To reproduce Slotboom *et al.* [18] kinetic results, the thermodynamic model utilized in their

study has been reutilized for the calculations of the fugacity coefficients. This thermodynamic model, from Bennekom *et al.* [3], is a modified SRK equation of state with a modified alpha function now dependent of a polarity factor of the molecules present in the gas (Appendix C.1).

IV.2.2 Process configurations

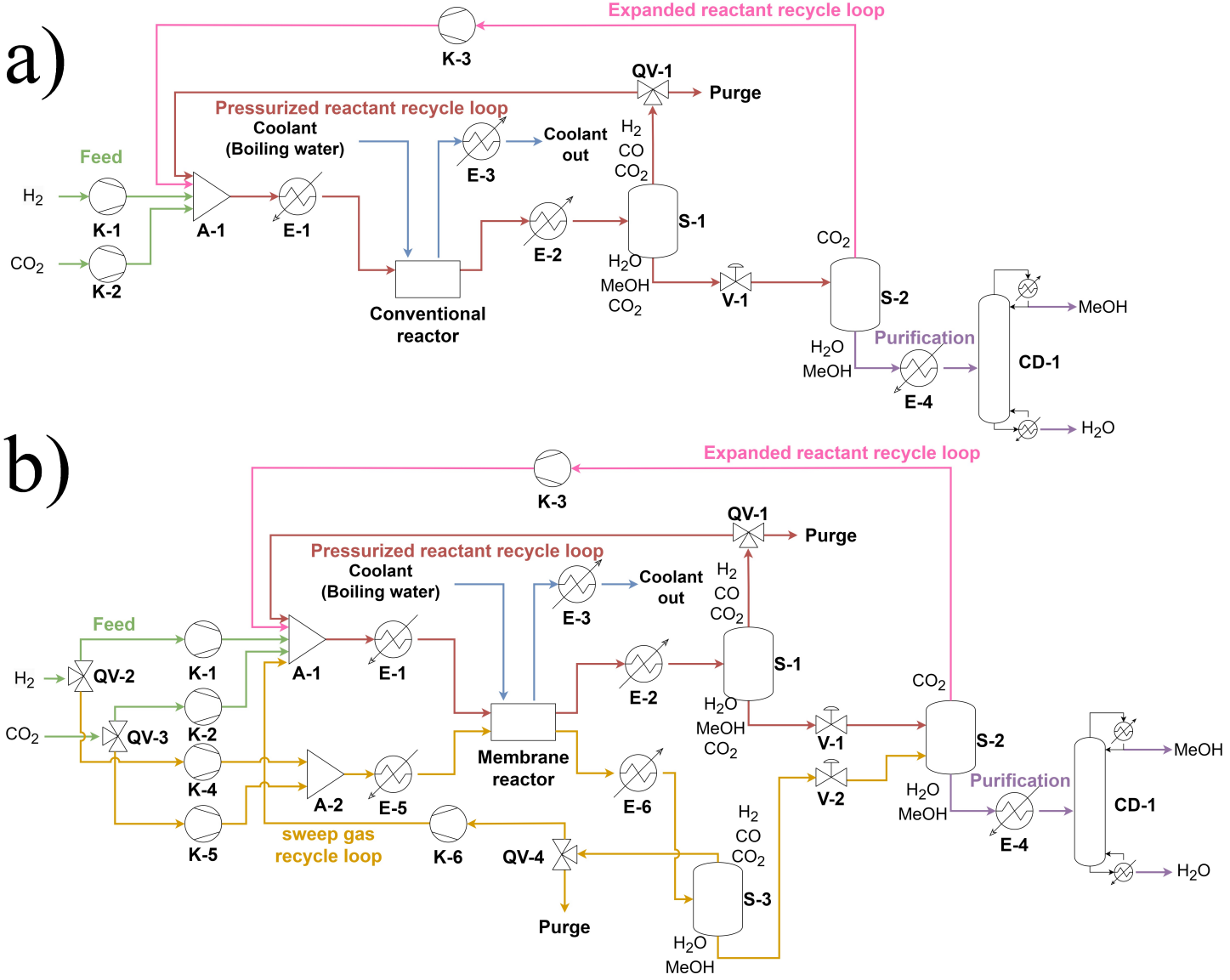

Figure IV.1: Process flowsheets for: a) CRP, b) MRP.

On Figure IV.1 are presented both conventional reactor process (CRP) and membrane reactor process (MRP). These processes were conceptualized to be adaptable to a wide range of operating conditions to identify broad tendencies about parameters values.

Feed streams

For both processes, pure CO_2 is fed at a flowrate of 1 t/h while pure H_2 is fed at a flowrate calculated to have a stoichiometry number S_t ratio of 2.05 (Eq. IV.19) at the inlet of the reactive side of the reactor, which correspond to a slight excess of hydrogen inside the reactor [12]. Both feed streams are at ambient conditions (25°C and 1 atm).

$$S_t = \frac{x_{H_2} - x_{CO_2}}{x_{CO_2} + x_{CO}} \tag{IV.19}$$

The feed for the MRP is split using the QV-2 and QV-3 valves to either direct reactants towards the catalytic bed or towards the sweep gas of the reactor.

Recycles

The CRP contains two recycles: a pressurized reactant recycle loop for gases exiting the S-1 separator and an expanded reactant recycle loop at atmospheric pressure for the gases exiting the S-2 separator. On top of these two recycles, the MRP possesses another recycle loop for the sweep gas exiting the S-3 separator. Additionally, the liquid phase exiting the S-3 separator is mixed with the one exiting the S-1 separator. This design choice is implemented so as not to lose the methanol that permeated through the membrane.

Compression

For both processes, feed H_2 and CO_2 are compressed separately in the respectively 5-stages K-1 and 4-stages K-2 compressors. As no pressure drop is assumed inside the reactor, no compressor is present on the pressurized reactants recycle loop. However, the gases stripped in the S-2 separator have been expanded to atmospheric pressure and thus are recompressed in the 4-stages K-3 compressor.

In the MRP, the sweep gas can be compressed using the 5-stages K-4 and 4-stages K-5 compressors for respectively H_2 and CO_2. The gases exiting the reactor via the permeate stream are re-compressed in the 4-stages K-6 compressor before being recycled to match the retentate-side pressure. Thus, using this setup, the pressure in the sweep gas cannot exceed the one in the retentate-side pressure.

The isentropic efficiency of every compressor is assumed to be 65% and, in between compression stages of every compressor, gases are cooled to 50°C.

Reactors

Reactors are assumed to be cooled with pressurized boiling water. The energy released by the reaction and collected in the hypothetical shell of the reactor is gathered back using the E-4 condenser. Moreover, gases exiting the reactors are cooled to 20°C using the E-2 and E-6 coolers before entering the S-1 and S-3 separators.

Distillation

In the purification step of both processes, methanol is separated from water using the CD-1 distillation column modelled by a shortcut module in ProSimPlus3. Methanol is the light key of this column with a recovery rate of 99.9% and water is the heavy key with a recovery rate calculated to correspond to 99.85% methanol purity (grade AA) at the condensate stream.

Purges

In both processes, a purge valve (referred to as QV-1) is located in the pressurized reactant recycle loop. Although this purge is not necessary for the calculations, since pure CO_2 and H_2 are assumed to enter the process and no inert by-products are formed in the reactor, it is used to analyze the sensitivity of the process's optimal conditions with respect to the purge rate.

In the membrane reactor process, an additional purge valve (referred to as QV-4) is located on the sweep gas recycle loop to prevent hypothetical impurities building up in this recycle loop. The purge rate is defined as the volume fraction of the valve feed stream flow rate being deviated to be purged.

IV.2.3 Optimization

Process optimization was performed using the external solver option of ProSimPlus3. This option allows to use an external solver in python for process optimization. As such, scipy's 'minimize' function was utilized using the 'Nelder-Mead' solver. Noteworthy, the 'Nelder-Mead' solver is built to search a local minimum with regard to the set initial parameters. A local search of the objective function has been chosen here because of insufficient computational resources for global optimization algorithms. Although multiple starting points were tested to find the global minimum, there is no guarantee that the optimal solutions presented in this study actually reached it.

IV.2.3.1 Objective function

Processes are optimized by minimizing a function representing the energy cost per quantity of methanol produced. The energy cost includes utilities, compression and hydrogen consumption (Eq. IV.20).

$$F_{Objective} = \frac{W_{CU} + W_{HU} + W_C + W_{H_2}}{\dot{w}_{MeOH}} \tag{IV.20}$$

W_{CU} represents the power consumption of the cold utilities (Eq. IV.21). The minimum energy requirement (MER) for the cold utilities is calculated using the pinch analysis module of ProSimPlus3. A coefficient of performance (CoP) of 4.5 is assumed to calculate the amount of power consumption for cooling.

$$W_{CU} = \frac{MER_{CU}}{CoP_{Cu}} \tag{IV.21}$$

W_{HU} represents the power consumption of the hot utilities (Eq. IV.22). It is calculated using the MER for the hot utilities given by the pinch analysis module. Then the power consumption

of the hot utilities is calculated by using a CoP of 0.9.

$$W_{HU} = \frac{MER_{HU}}{CoP_{HU}} \tag{IV.22}$$

W_C represents the power consumption of every compressor in the process (Eq. IV.23).

$$W_C = \sum W_{C_i} \tag{IV.23}$$

Finally, W_{H_2} represents the power consumption of hydrogen production (Eq. IV.24). A value of 48 kWh/kg of hydrogen produced is taken to represent hydrogen produced using water electrolysis with an alkaline electrolyser [19].

$$W_{H_2} = \dot{w}_{H_2}^{Process\ \ feed} E_{Alk_{H_2}} \tag{IV.24}$$

IV.2.3.2 Optimization parameters

For the CRP, two optimization parameters are chosen: the operating temperature and pressure. On top of these two parameters, the MRP has three more optimization parameters due to the presence of the membrane: the membrane surface area per modified residence time (S_τ), the fraction of process feed deviated to feed the sweep gas (α^P), operating pressure of the permeate stream (P^P) defined as a fraction of the retentate side pressure. In the next section, the optimum of these parameters will be studied with regard to the GHSV of the reactor, the general selectivity factor (GSF) of the membrane and the purge rate in the process. The operating pressure of the permeate stream is only featured as an optimization variable for the Section IV.3.1 to simplify the optimization problem in the other sections. In most scenarios, the purge rate will be kept at 1% to give enough energy penalty to high recycle ratios and make the objective function sensitive enough to the optimization variables as to not stall the optimizer in an otherwise mostly flat objective function.

Table IV.3: Optimization variables and process conditions featured in this study.

Section	**Scenario**	**Optimization variables**	**Conditions**			
			GHSV (h^{-1})	**Purge rate**	**GSF**	P^P
IV.3.1	CRP	T, P	1000	1%	-	-
	MRP - Atm (GSF = 1)	T, P^R, α^P, S_τ	1000	1%	1	1 atm
	MRP - Comp (GSF = 1)	T, P^R, α^P, S_τ, P^P	1000	1%	1	Varied
	MRP - Comp (GSF = 10)	T, P^R, α^P, S_τ, P^P	1000	1%	10	Varied
IV.3.2	CRP	T, P	1000	Varied	-	-
	MRP	T, P^R, α^P, S_τ	1000	Varied	1	1 atm
IV.3.3	CRP	T, P	1000	1%	-	-
	MRP	T, P^R, α^P, S_τ	1000	1%	Varied	1 atm
IV.3.4	CRP	T, P	Varied	1%	-	-
	MRP	T, P^R, α^P, S_τ	Varied	1%	10	1 atm

Bounds for the optimization variables are presented on Table IV.4. Operating temperature and pressure bounds are set according to the condition ranges in which the kinetic model was

derived.

Table IV.4: Optimization variables and their bounds.

Variable	**Lower bound**	**Upper Bound**
T (°C)	200	270
P^R (bar)	20	70
α^P (%)	0.1	99.9
S_τ ($m^2.m_{Bed}^{-3}.s^{-1}.Nm^3$)	10^{-3}	10^{+10}
P^P	1 atm	P^R

IV.2.4 Performance assessments

To investigate the difference in performances of CRPs and MRPs, the following performances indicators were evaluated. For the MRP, the CO_2 conversion and the recycle ratio comprise both retentate and permeate side (Eqs. IV.25 and IV.26). The fraction of water removed in the membrane reactor is calculated by dividing the quantity of water that permeated through the membrane relative to the amount of water generated inside the reactor (Eq. IV.27).

$$\begin{cases} CRP : X_{CO_2} = 1 - \frac{\dot{n}_{CO_2}^{Out}}{\dot{n}_{CO_2}^{In}} \\ MRP : X_{CO_2} = 1 - \frac{\dot{n}_{CO_2}^{R^{Out}} + \dot{n}_{CO_2}^{P^{Out}}}{\dot{n}_{CO_2}^{R^{In}} + \dot{n}_{CO_2}^{P^{In}}} \end{cases} \tag{IV.25}$$

$$\begin{cases} CRP : Recycle\ ratio = \frac{\dot{w}^{Reactor\ inlet}}{\dot{w}^{Process\ feed}} - 1 \\ MRP : Recycle\ ratio = \frac{\dot{w}^{Retentate\ inlet} + \dot{w}^{Permeate\ inlet}}{\dot{w}^{Process\ feed}} - 1 \end{cases} \tag{IV.26}$$

$$Water\ removed = \frac{\dot{n}_{H_2O}^{P^{Out}} - \dot{n}_{H_2O}^{P^{In}}}{\dot{n}_{H_2O}^{P^{Out}} - \dot{n}_{H_2O}^{P^{In}} + \dot{n}_{H_2O}^{R^{Out}} - \dot{n}_{H_2O}^{R^{In}}} \tag{IV.27}$$

IV.3 Results and discussion

IV.3.1 Sweep gas loop under pressure

Some authors in the literature have argued the benefits of compressing a reactant-laden sweep gas, especially when the membrane selectivity is low [7, 10, 13]. Their arguments involve lowering transmembrane partial pressure difference of reactants to reduce their permeation through the membrane. Moreover, reactants transported to a compressed permeate stream will require less additional compression for recycling this gas and thus reduce the penalties for poorly selective membrane.

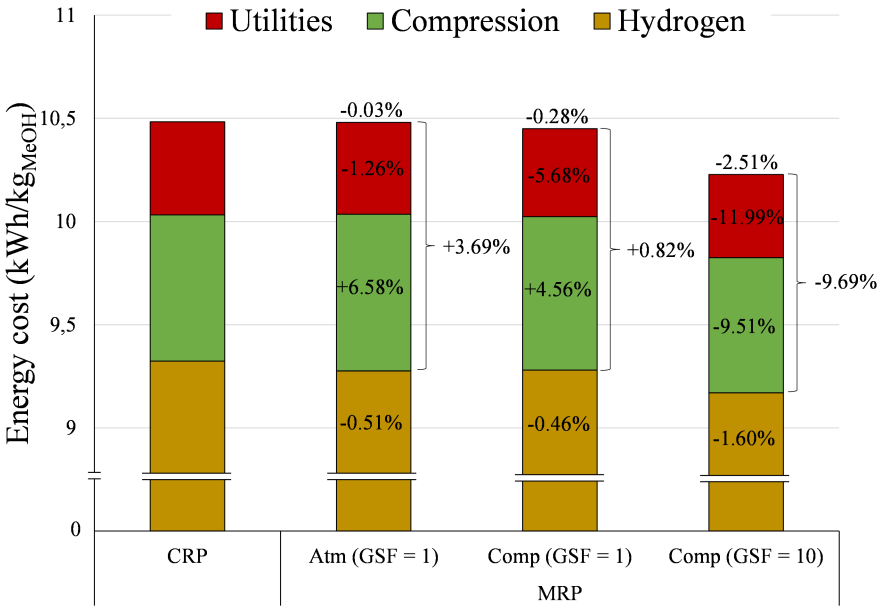

Figure IV.2: Minimum energy cost for the investigation of the compressed sweep gas. Conditions featured on Table IV.1.

In the case of the MRP with the base membrane selectivities (GSF = 1), using a sweep gas feed above atmospheric pressure leads to a reduction in overall compression costs (Figure IV.2). This is due to a reduction in the energy cost of re-compressing the reactants that permeated through the membrane to match the operating pressure of the reaction side for their recycling. This results in a lower overall compression cost compared to using sweep gas at atmospheric pressure. Additionally, compression enables the reactor to accommodate more membrane surface area, enhancing water separation by reducing and lessening the penalties of reactant permeation (Table IV.5). However, the optimal performance occurs at high transmembrane pressure differences (Table IV.5). Lower transmembrane pressure differences would require higher sweep gas flow rates to maintain low water partial pressure on the permeate side of the membrane. This increase in gas flow rate would then increase the utility demands for heating and cooling the larger sweep gas flow.

Table IV.5: Optimization results for the investigation of the compressed sweep gas. Conditions featured on Table IV.3. *Upper bound.

	CRP	**MRP**		
		Atm (GSF = 1)	**Comp (GSF = 1)**	**Comp (GSF = 10)**
Temperature (°C)	244	245	243	228
P^R (bar)	70*	70*	69	52
P^P (bar)	-	1	8	1
α^P (%)	-	1 %	46 %	23 %
Membrane surface (m^2)	-	$8.84 \cdot 10^1$	$2.44 \cdot 10^2$	$2.80 \cdot 10^3$
Recycle ratio (-)	2.6	2.1	2.1	2.0
Water removed (%)	0 %	43 %	70 %	97 %

Additionally, when increasing the membrane selectivity, the optimum lies in a sweep gas at atmospheric pressure, since lowering transmembrane pressure differences for reactants is now no longer required to limit reactants escaping from the reaction mixture through the membrane (Table IV.5), which matches the observations described in the literature on the subject [7, 10, 13].

IV.3.2 Influence of purge rate

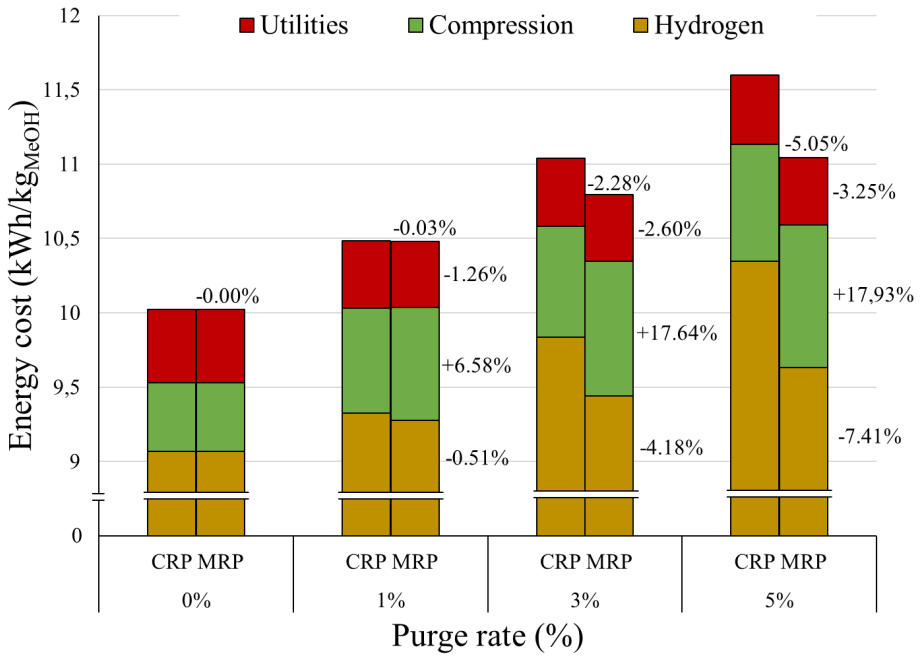

Figure IV.3: Minimum energy cost for the CRP and MRP at various purge rate. Conditions featured on Table IV.3.

By removing the purge, the optimum of a MRP converges towards the CRP as the optimizer opts to remove the membranes from the reactor (Figure IV.3). Since no pressure drop is modeled within the reactor, the primary penalty in a purge-free system arises from the energy required to heat and cool the recycled stream for the separation in the S-1 flash separator. This is highlighted by the optimizer selecting a reaction pressure of 20 bar (Table IV.6), which reduces compression costs, as achieving a high reactant conversion per pass is no longer the main factor driving energy consumption. In that scenario, the energy required to recompress reactants that have permeated through the membrane exceeds the benefits of increased conversion offered by the membrane reactor. However, when a purge is introduced, high recycle ratios are heavily penalized due to the loss of energy-intensive hydrogen in the purge stream. Thus, at identical purge rate, MRPs are more energy-efficient than CRPs (Figure IV.3) because they achieve higher reactant conversions and lower recycle rates by shifting the thermodynamic equilibrium through water removal (Table IV.6). This advantage is maintained despite significant increases in compression costs, primarily driven by the K-6 compressor, which handles the recycling of reactants that permeate through the membrane (Table IV.6). In contrast, the conventional reactor is limited by thermodynamic constraints, preventing significant improvements in conversion.

Table IV.6: Optimization results for the investigation of the influence of the purge rate on optimum operating parameters. Conditions featured on Table IV.3. *Upper bound. **Lower Bound.

Purge rate (%)	**0%**		**1%**		**3%**		**5%**	
Process type	**CRP**	**MRP**	**CRP**	**MRP**	**CRP**	**MRP**	**CRP**	**MRP**
Temperature (°C)	227	227	244	245	244	241	244	238
Pressure (bar)	20**	20**	70*	70*	70*	70*	70*	70*
α^P (%)	-	0.1 %	-	0.7 %	-	0.1 %	-	0.1 %
Membrane surface (m^2)	-	$3.60{\cdot}10^{-3}$	-	$8.84{\cdot}10^{1}$	-	$3.23{\cdot}10^{2}$	-	$3.84{\cdot}10^{2}$
X_{CO_2} (%)	12 %	12 %	29 %	34 %	29 %	50 %	29 %	53 %
Recycle ratio (-)	8.6	8.6	2.6	2.1	2.4	1.1	2.2	1.0

Comparing the two processes at a purge rate other than 0% favors the MRP over the CRP. However, at the 1% purge rate fixed throughout this article, very low benefits are achievable with only a 0.03% gain on energy costs is achievable compared to the CRP (Figure IV.3), marginally favoring the MRP over the CRP. Nevertheless, in real-world practice, the purge rate would be adjusted in each individual process based on various factors, mainly dependent on the level of impurities in the process feed streams, and thus it would be unlikely that both processes would operate at the same purge rate.

IV.3.3 Influence of membrane selectivity

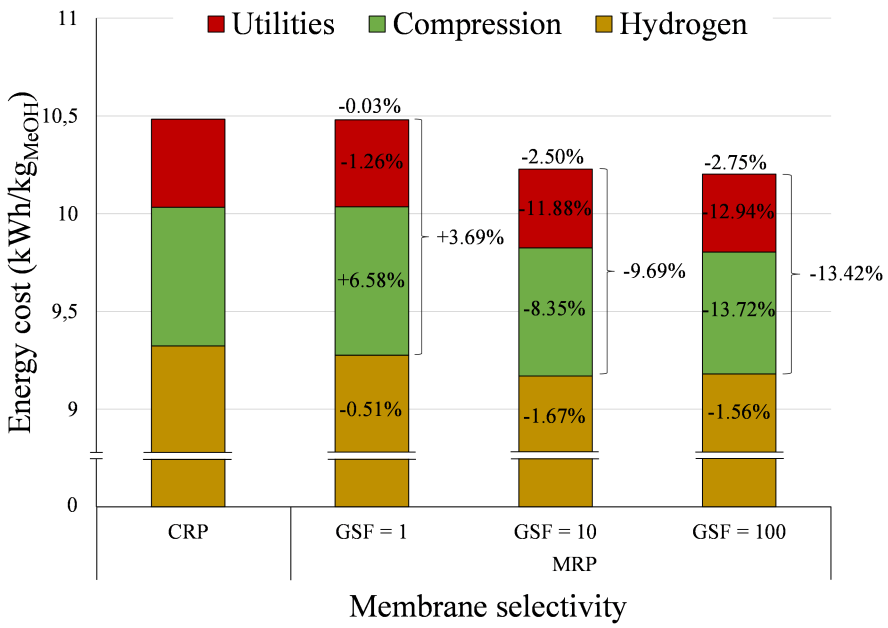

Figure IV.4: Minimum energy cost for the CRP and MRP at various membrane selectivity. Conditions featured on Table IV.3.

Increasing the membrane selectivity allows for further energy savings over the CRP (Figure IV.4). On top of additional savings on utilities and hydrogen, MRPs with increased membrane selectivities now features lower compression cost compared to the CRP (Figure IV.4). When looking at the optimum temperature and pressure conditions, using membranes with higher selectivity allows maintaining high reactor performances with high conversions at less harsh conditions, explaining the lower compression and utilities costs (Table IV.7). With higher reactant conversions, the recycle ratio decreases, which reduces the gas flowrate and, in turn, the amount of catalyst needed to maintain the same GHSV. While significant gains have been made by increasing the membrane selectivity from the base case (GSF = 1) with a factor of 10 (GSF = 10) (Figure IV.4), a plateau seems to appear when increasing the membrane selectivity a 100-fold (GSF = 100) as the membrane reactor is close to full water separation (Table IV.7). With methanol still remaining in the retentate feed due to the high selectivity of the membrane, the membrane reactor is unable to reach full conversion per pass and still requires a recycle loop. The fact that methanol is now the limiting factor hindering further reactant conversions suggest that further energy savings could have been made by converting methanol into other compounds (such as DME) inside the reactor.

Table IV.7: Optimization results for the comparisons between CRP and MRP at different GSFs for the membrane. Conditions featured on Table IV.3. *Upper bound.

	CRP	**MRP**		
		GSF = 1	**GSF = 10**	**GSF = 100**
Temperature (°C)	244	245	228	223
Pressure (bar)	70*	70*	52	47
α^P (%)	-	1 %	20 %	28 %
Membrane surface (m^2)	-	$8.84{\cdot}10^1$	$2.80{\cdot}10^3$	$3.70{\cdot}10^4$
Catalyst mass (kg)	$6.10{\cdot}10^3$	$5.26{\cdot}10^3$	$3.06{\cdot}10^3$	$3.11{\cdot}10^3$
X_{CO_2} (%)	29 %	34 %	54 %	53 %
Recycle ratio	2.6	2.1	1.0	1.1
Water removed (%)	0 %	43 %	97 %	98 %

While more selective membranes have the potential to significantly reduce compression and utility energy costs (Figure I.4), increasing membrane selectivity also greatly increases the required membrane surface area. As a result, the optimal membrane surface expands much faster than the decrease in energy costs, which seems to plateau at around a 3% gain (hydrogen included) (Figure IV.4). Given the current high cost of membranes, estimated to be around 2,000$ per square meter [7], it is unclear whether the small energy savings would justify the much higher operational costs. Moreover, the separation performance of very highly selective membranes in these conditions has yet to be reported in the literature, adding further uncertainty to their viability in this scenario.

IV.3.4 Influence of GHSV on the process optimum

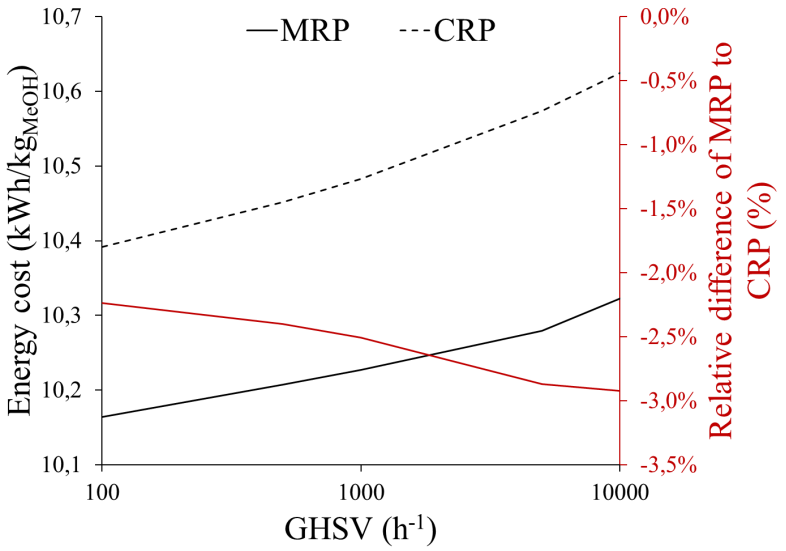

Figure IV.5: Influence of the GHSV on the minimum energy cost for the CRP and MRP. Conditions featured on Table IV.3.

In the literature, membrane reactors are described to operate more efficiently at lower space velocities as higher residence times allow for greater thermodynamic equilibrium shifting through water removal [14, 5]. Despite this information, it can be seen from Figure IV.5 that the differences in energy efficiency between the MRPs and the CRPs are larger at higher GHSVs than at lower ones. This effect is largely a consequence of the CRPs reaching the upper bounds of temperature and pressure conditions (Table IV.8). Without these bounds, the variations of the differences in energy efficiency between the two processes due to the GHSVs are expected to be minimal.

Table IV.8: Optimization results for the comparisons between the CRP and MRP at various GHSVs. Conditions featured on Table IV.3. *Upper bound.

GHSV (h^{-1})	**100**		**500**		**1 000**		**5 000**		**10 000**	
Process type	**CRP**	**MRP**	**CRP**	**MRP**	**CRP**	**MRP**	**CRP**	**MRP**	**CRP**	**MRP**
Temperature (°C)	222	205	238	220	244	228	261	245	270*	253
Pressure (bar)	66	36	70*	45	70*	52	70*	67	70*	70*
α^P (%)	-	29%	-	27%	-	20%	-	15%	-	17%
Membrane surface (m^2)	-	$4.26{\cdot}10^3$	-	$3.70{\cdot}10^3$	-	$2.80{\cdot}10^3$	-	$2.34{\cdot}10^3$	-	$2.37{\cdot}10^3$
X_{CO_2} (%)	34%	49%	31%	52%	29%	54%	25%	61%	23%	59%
Recycle ratio (-)	2.0	1.1	2.3	1.1	2.6	1.0	3.2	0.9	3.6	1.0
Water removed (%)	0 %	97 %	0 %	97 %	0 %	97 %	0 %	97 %	0 %	98 %

The lack of influence of the GHSV on the performance differences between the CRP and MRP at optimum conditions can be attributed to the optimizer adjusting the operating conditions to each reactor type. This ensures that no reactor is severely limited by either kinetics or thermodynamics, which would otherwise favor the conventional reactor in the first case and the membrane reactor in the latter.

The optimal temperature and pressure conditions differ significantly between the two processes at lower space velocities (Table IV.8). The MRP operates under less severe conditions than the CRP due to the presence of the highly selective membrane able to reach high reactor performances at milder reaction conditions. However, at higher space velocities, the reduced contact time between the reaction mixture and the catalytic bed requires the MRP to operate under harsher conditions, closer to those of the CRP, to reach the thermodynamic equilibrium in order to shift it (Table IV.8). As a result, comparing the two processes at identical space velocities, especially at low space velocities, and under the same temperature and pressure conditions may introduce bias toward one reactor type, depending on the chosen conditions, therefore confirming the initial assumptions of this study.

IV.4 Conclusion

Using a simple isothermal, pseudo-homogeneous plug flow reactor model, it is possible to study membrane reactor processes with the presence of the sweep gas without requiring a defined reactor design. This enables pre-sizing of a membrane-assisted process and its equipment, as well as process optimization for membrane reactor processes, which can be applied to reactions beyond methanol synthesis.

Several process parameters were studied to compare both CRP and MRP at the optimum operating conditions. Pressurizing the permeate side of the membrane reactor helped reduce energy costs by minimizing the energy penalty associated with the re-compression of the reactants permeating through the membrane in view to their recycling. Nevertheless, the optimal sweep gas pressure remained low to avoid reducing the transmembrane pressure difference, which would otherwise require a high sweep gas flow rate for effective water removal. This effect is only observable with poorly selective membranes as highly selective membranes do not benefit from this effect due to limited permeation of reactants through the membrane.

Additionally, MRPs are more efficient when a high energy penalty is applied to high recycle ratios, such as a high purge rate, due to the membrane ability to shift the thermodynamic equilibrium and reach reactor performances unavailable without membranes.

Optimum conditions for CRPs and MRPs can vary greatly depending on the membrane selectivity and the GHSV. Thus, comparing these two processes with the same operating conditions, as has been done so far in the literature, may introduce a bias towards either type of process depending on the selected conditions.

While the results of this study present negligible energy savings with the MRP using current zeolite membrane materials, significant energy savings can be made on compression and utility costs using more selective membranes as they allow the reactor to reach high conversion performances at milder conditions (at the price of significantly raising the overall membrane surface required).

In this study, further potential energy savings on the MRP have been identified. For example, tweaking the process configuration or by applying membrane reactors to more water-limited reactions such as direct DME synthesis could achieve better results for the MRP in some conditions. Finally, studying these two types of reactors at the process scale should involve different optimization criteria, such as economic or environmental factors, to better assess the viability of MRPs. This would help determine how membrane reactors affect the optimal values of other parameters like the GHSV, and identify key targets for membrane costs, durability, sustainability, and permeation performance.

Glossary (Chapter IV)

Acronyms

CoP Coefficient of Performance (subscripts: CU (Cold utilities), HU (Hot utilities))

CRP Conventional Reactor Process

DME Dimethyl Ether

GHSV Gas Hourly Space Velocity ($Nm^3.h^{-1}.m^3_{Bed}$)

GSF General selectivity factor (GSF) (-)

LTA Linde Type A

MER Minimum Energy Requirement (W) (subscripts: CU (Cold utilities), HU (Hot utilities))

MRP Membrane Reactor Process

RWGS Reverse Water-Gas Shift reaction

SRK Soave-Redlich-Kwong equation of state

WGS Water-Gas Shift reaction

Roman letters

C_{p_i} Heat capacity for species i ($J.K^{-1}.mol^{-1}$)

$E_{Alk_{H_2}}$ Energy required to produce 1 kg of hydrogen from water electrolysis using an alkaline electrolyser ($E_{Alk_{H_2}} = 48$ $kWh.kg^{-1}_{H_2}$) [19]

$F_{Objective}$ Objective function minimized by the optimizer ($kWh.kg^{-1}_{MeOH}$)

J_i Transmembrane partial molar flowrate per meter squared of membrane for species i ($mol.s^{-1}.m^{-2}$)

Kp° Equilibrium constants (-).

N_c Number of constituents (-)

N_r Number of reactions (-)

P Operating pressure (bar) (superscripts: R (retentate), P (permeate))

Q_{Shell} Heat transferred to the hypothetical shell of the reactor (W)

R Ideal gas constant (R = 8.314 $J.mol^{-1}.K^{-1}$)

S_t Stoichiometric ratio for methanol synthesis (defined in Eq. IV.19)

S_τ Membrane surface per modified residence time ($m^2.m^{-3}_{Bed}.s^{-1}.Nm^3$)

S Overall membrane surface (m^2)

T Temperature (K)

W Power consumption of a group of equipment (W) (subscripts: CU (Cold utilities), HU (Hot utilities), C (Compressors), H_2 (Hydrogen production))

X_{CO_2} CO_2 conversion at the outlet of the reactor (-)

$\dot{Q}_0$ Total volumetric flowrate at the inlet the reactive side of the reactor ($Nm^3.s^{-1}$)

$\dot{n}_i$ Partial molar flowrate for species i ($mol.s^{-1}$) (superscripts: R (retentate), P (permeate))

$\dot{w}_i$ Mass flowrate of species i ($kg.s^{-1}$)

f_i Fugacity of species i (Pa) (superscripts: R (retentate), P (permeate))

k Kinetic constant (-).

r_i Reaction rate for reaction i ($mol.s^{-1}.kg^{-1}_{Bed}$)

w_{Bed} Total mass of the catalytic bed (kg_{Bed})

x_i Molar fraction of species i (-)

Greek letters

ΔC_{p_i} Variation of heat capacity for reaction i ($J.K^{-1}.mol^{-1}$)

ΔH^P Difference in enthalpy between the inlet and outlet of the permeate stream of the membrane reactor (J)

$\Delta r H_i$ Reaction enthalpy of reaction i ($J.mol^{-1}$)

Π_i Permeance of species i ($mol.s^{-1}.m^{-2}.Pa^{-1}$)

Θ^* Fugacity dependent free surface coverage Eqs. IV.16 and IV.17 (bar^{-1})

α^P Fraction of process feed stream deviated to feed the sweep gas (-)

$\alpha_{H_2O/i}$ Permselectivity of H_2O relative to species i (-)

ν_{ij} Stoichiometric coefficient for species i in reaction j (-)

ρ_{Bed} Density of the catalytic bed ($kg_{Bed}.m^{-3}_{Bed}$)

τ Modified residence time ($m^3_{Bed}.s.Nm^{-3}$)

References

[1] A. Ateka et al. "A Review on the Valorization of CO_2. Focusing on the Thermodynamics and Catalyst Design Studies of the Direct Synthesis of Dimethyl Ether". In: *Fuel Processing Technology* 233 (Aug. 2022), p. 107310. ISSN: 03783820. DOI: 10.1016/j.fuproc.2022.107310.

[2] Konstantinos Atsonios, Kyriakos D. Panopoulos, and Emmanuel Kakaras. "Thermocatalytic CO_2 Hydrogenation for Methanol and Ethanol Production: Process Improvements". In: *International Journal of Hydrogen Energy* 41.2 (Jan. 2016), pp. 792–806. ISSN: 03603199. DOI: 10.1016/j.ijhydene.2015.12.001.

[3] Joost G. van Bennekom et al. "Modeling and Experimental Studies on Phase and Chemical Equilibria in High-Pressure Methanol Synthesis". In: *Industrial & Engineering Chemistry Research* 51.38 (Sept. 26, 2012), pp. 12233–12243. ISSN: 0888-5885, 1520-5045. DOI: 10.1021/ie3017362.

[4] Filippo Bisotti et al. "Century of Technology Trends in Methanol Synthesis: Any Need for Kinetics Refitting?" In: *Industrial & Engineering Chemistry Research* 60.44 (Nov. 10, 2021), pp. 16032–16053. ISSN: 0888-5885, 1520-5045. DOI: 10.1021/acs.iecr.1c02877.

[5] Marcello De Falco, Mauro Capocelli, and Angelo Basile. "Selective Membrane Application for the Industrial One-Step DME Production Process Fed by CO_2 Rich Streams: Modeling and Simulation". In: *International Journal of Hydrogen Energy* 42.10 (10 Mar. 2017), pp. 6771–6786. ISSN: 03603199. DOI: 10.1016/j.ijhydene.2017.02.047.

[6] Nazely Diban et al. "Influence of the Membrane Properties on the Catalytic Production of Dimethyl Ether with in Situ Water Removal for the Successful Capture of CO_2". In: *Chemical Engineering Journal* 234 (Dec. 2013), pp. 140–148. ISSN: 13858947. DOI: 10.1016/j.cej.2013.08.062.

[7] Vincent Dieterich et al. "Performance Requirements of Membrane Reactors for the Application in Renewable Methanol Synthesis: A Techno-Economic Assessment". In: *Advanced Sustainable Systems* 6.12 (Dec. 2022), p. 2200254. ISSN: 2366-7486, 2366-7486. DOI: 10.1002/adsu.202200254.

[8] Homa Hamedi and Torsten Brinkmann. "Valorization of CO_2 to DME Using a Membrane Reactor: A Theoretical Comparative Assessment from the Equipment to Flowsheet Level". In: *Chemical Engineering Journal Advances* 10 (May 2022), p. 100249. ISSN: 26668211. DOI: 10.1016/j.ceja.2022.100249.

[9] Homa Hamedi, Torsten Brinkmann, and Sergey Shishatskiy. "Membrane-Assisted Methanol Synthesis Processes and the Required Permselectivity". In: *Membranes* 11.8 (Aug. 2021), p. 596. ISSN: 2077-0375. DOI: 10.3390/membranes11080596.

[10] Igor G.I. Iwakiri, Carlos V. Miguel, and Luis M. Madeira. "Modeling and Simulation of a Steam-Selective Membrane Reactor for Power-to-Methanol". In: *Computers & Chemical Engineering* 156 (Jan. 2022), p. 107555. ISSN: 00981354. DOI: 10.1016/j.compchemeng.2021.107555.

[11] Florian Nestler et al. “Methanol Synthesis - Industrial Challenges within a Changing Raw Material Landscape”. In: *Chemie Ingenieur Technik* 90.10 (Oct. 2018), pp. 1409–1418. ISSN: 0009286X. DOI: 10.1002/cite.201800026.

[12] Jörg Ott et al. “Methanol”. In: *Ullmann’s Encyclopedia of Industrial Chemistry*. Ed. by Wiley-VCH Verlag GmbH & Co. KGaA. Weinheim, Germany: Wiley-VCH Verlag GmbH & Co. KGaA, Oct. 15, 2012, a16_465.pub3. ISBN: 978-3-527-30673-2. DOI: 10.1002/14356007.a16_465.pub3.

[13] Serena Poto, Fausto Gallucci, and M. Fernanda Neira d’Angelo. “Direct Conversion of CO_2 to Dimethyl Ether in a Fixed Bed Membrane Reactor: Influence of Membrane Properties and Process Conditions”. In: *Fuel* 302 (Oct. 2021), p. 121080. ISSN: 00162361. DOI: 10.1016/j.fuel.2021.121080.

[14] Serena Poto et al. “Experimental Investigation of a Packed Bed Membrane Reactor for the Direct Conversion of CO_2 to Dimethyl Ether”. In: *Journal of CO2 Utilization* 72 (June 2023), p. 102513. ISSN: 22129820. DOI: 10.1016/j.jcou.2023.102513.

[15] Serena Poto et al. “Techno-Economic Assessment of the One-Step CO_2 Conversion to Dimethyl Ether in a Membrane-Assisted Process”. In: *Journal of CO2 Utilization* 69 (Mar. 2023), p. 102419. ISSN: 22129820. DOI: 10.1016/j.jcou.2023.102419.

[16] R. Raso et al. “Zeolite Membranes: Comparison in the Separation of $H_2O/H_2/CO_2$ Mixtures and Test of a Reactor for CO_2 Hydrogenation to Methanol”. In: *Catalysis Today* (Mar. 2020), S0920586120301310. ISSN: 09205861. DOI: 10.1016/j.cattod.2020.03.014.

[17] Martin P. Rohde, Dominik Unruh, and Georg Schaub. “Membrane Application in Fischer-Tropsch Synthesis to Enhance CO_2 Hydrogenation”. In: *Industrial & Engineering Chemistry Research* 44.25 (25 Dec. 2005), pp. 9653–9658. ISSN: 0888-5885, 1520-5045. DOI: 10.1021/ie050289z.

[18] Y. Slotboom et al. “Critical Assessment of Steady-State Kinetic Models for the Synthesis of Methanol over an Industrial $Cu/ZnO/Al_2O_3$ Catalyst”. In: *Chemical Engineering Journal* 389 (June 2020), p. 124181. ISSN: 13858947. DOI: 10.1016/j.cej.2020.124181.

[19] *Strategic Research and Innovation Agenda*. Hydrogen Europe, Oct. 2020.

Chapter V

Conclusions and outlook

This comprehensive PhD work examined membrane reactors from a material science perspective, including the synthesis and testing of microporous zeolite membranes and novel preparation methods for catalysis, up to the process scale, where the viability of membrane reactors was investigated. Through the collection of experimental data in material science, the objective is to describe more accurately the material performances at reaction conditions, thereby enhancing the realism of membrane reactor models used in process simulations. Through this approach, critical development pathways and key bottlenecks were identified, which must be addressed to advance membrane reactor technologies for CO_2 conversion into methanol.

V.1 Conclusions

The aim of **Chapter II** was to explore membrane materials and preparation methods able to selectively remove water from a $CO_2/CO/H_2/MeOH$ gas mixture at high temperatures (> 250°C). Then, selected materials were extensively tried to provide comprehensive permeation laws at reaction conditions for every compound present in methanol synthesis.

As such, a literature review identified microporous zeolite membranes as the most suitable candidates for selectively removing water from the reaction mixture under the harsh temperature (200-300°C) and pressure (20-50 bar) conditions required for methanol synthesis. As such, various methods for the preparation of high-quality, defect-free Linde Type A (LTA) and Sodalite (SOD) zeolite membranes were investigated. These membranes were coated via hydrothermal synthesis on porous alumina supports to provide the necessary mechanical strength.

The study's findings indicated that secondary growth protocols, while more complex to implement than primary growth methods, were more effective in producing defect-free LTA membranes. Secondary growth decouples the nucleation and growth stages by seeding the support allowing for more control of the membrane growth. This resulted in denser membranes with well-intergrown crystals compared to those produced by primary growth. However, secondary growth methods require the synthesis of nano-scale zeolite seeds, which could increase the economic and environmental costs of membrane production.

For SOD membranes, primary growth methods required multiple rounds of hydrothermal synthesis to achieve sufficient surface coverage of zeolite crystals on the support. Additionally, using a more concentrated synthesis gel allowed for selective SOD crystal formation under milder conditions.

During the small scale-up of these methods to synthesize 5 cm long membranes for gas permeation tests, the quantity of the synthesis gel was identified as a crucial factor for defect-free membrane production, while reactant diffusion limitations within the hydrothermal vessels were estimated to be negligible.

Although scanning electron microscope (SEM) micrographs of the prepared LTA and SOD membranes showed them to be defect-free, gas permeation experiments revealed significant defects, as non-selective viscous flow negatively affecting membrane separation performance was identified. Analysis of the permeance evolution with increasing temperature also provided evidence for the presence of Knudsen diffusion, and configurational diffusion through the zeolitic pores. However, attempts to quantify each flow regime were unsuccessful as the experimental data was not comprehensive enough, making it difficult to rigorously differentiate between these regimes based on their temperature dependence and identify the size of the membrane's defects. Post gas permeation SEM analysis of the zeolite membranes exposed to methanol synthesis conditions revealed several transformations, likely due to the harsh hydrothermal environment. These findings raise concerns about the long-term stability of these materials and highlight the need for further research on their operational boundaries under reaction conditions.

The optimal operating windows for membrane separation (< 250°C) and catalytic performance (> 250°C) in methanol synthesis currently do not match. To address this, in **Chapter III**, alternative catalyst formulations were investigated with the goal of enhancing catalytic activity at lower temperatures. Furthermore, in an attempt to explore potential synergies between the catalyst and the membrane by directly depositing the catalyst onto the membrane, alternative synthesis routes for the preparation of copper-zinc-zirconia catalysts were explored using a sol-gel and a supercritical CO_2 method.

Following a literature review of catalytic systems suitable for membrane reactors due to their potential for low-temperature activity, copper-zinc catalysts emerged as the most befitting candidates. However, these types of catalyst have been studied for over a century and advances on emerging catalytic materials could potentially change this observation in the years to come.

Several formulas of copper-zinc catalyst were synthesized by a co-precipitation method to study potential low temperature activity and compared to a commercial copper-zinc-alumina catalyst. Among these, the copper-zinc-zirconia catalyst exhibited superior catalytic performance per mass of catalyst but did not demonstrate distinct activity at lower temperatures. An alternative indium oxide-supported copper-zinc catalyst was prepared with promising intrinsic characteristics but displayed unexpectedly low activity towards methanol formation.

The studied alternative preparation methods produced catalysts with significantly lower activity than the co-precipitated ones. Characterization revealed the presence of large, isolated metal oxide crystals, which is undesirable for active methanol catalysts. Additionally, attempts to deposit the catalyst onto an LTA membrane using the supercritical CO_2 method resulted in membrane destruction, likely due to the high-temperature and harsh acidic conditions of the catalyst preparation process.

A novel approach for solving material balance using a complex equation of state was introduced, demonstrating its effectiveness in accurately predicting the composition of the liquid condensate down to the mole percent. This method revealed that CO_2 dissolution in the liquid

phase can significantly impact CO_2 conversion and must be accounted for when calculating the performances of highly active catalysts.

The initial objective in **Chapter IV** was to use the permeance laws obtained in Chapter II to evaluate the viability of membrane reactors at the process scale, using more realistic membrane behaviors inside revised reactor models. However, due to the insufficient separation performances of the prepared membranes, the objective shifted towards the comparison of membrane and conventional fixed-bed reactors using process optimization. In fact, membrane and conventional fixed-bed reactors in the literature have been so far compared under identical operating conditions at the process scale. However, studies at the reactor scale have identified that these types of reactors might have different optimal operating conditions. Therefore, a pseudo-homogeneous, plug-flow isothermal membrane reactor model, adapted from early membrane reactor studies, was developed. This design-independent model allowed for process optimization using simplified and broad optimization variables, addressing potential biases in previous process simulation studies.

Several authors suggest that compressing a reactant-laden sweep gas in membrane reactors can reduce reactant loss when using membranes with low selectivity. However, this approach has limitations, as it requires high sweep gas flow rates to keep water partial pressure low within the reactor, which significantly raises utility costs. Thus, the optimization results revealed some advantages to compress the sweep gas, but the optimal solution involved operating a high transmembrane pressure difference to maintain a strong driving force for water removal. Additionally, as membrane selectivity improves, the optimal configuration shifts to maintaining sweep gas at atmospheric pressure, eliminating the need to manage reactant loss through sweep gas compression.

Membrane reactor processes (MRPs) demonstrated superior performances in scenarios where there is a high energy penalty associated with high recycle ratios, such as an elevated purge rate. This is because membrane reactors can achieve performance levels unattainable by conventional reactors by shifting the thermodynamic equilibrium through water removal. However, when the energy cost of high recycle ratios is not penalized enough, the conventional reactor process (CRP) configuration is more efficient, because high conversions become unnecessary and managing a sweep gas too costly.

The optimal conditions of MRPs are highly dependent on the reactor gas hourly space velocity (GHSV) and on the membrane selectivity and can differ substantially from those of CRPs under similar process parameters. Therefore, comparing the two reactor types under the same operating conditions may introduce bias in favor of one reactor type, depending on the specific conditions chosen.

With membrane separation performance representative of current literature, the potential energy savings of MRPs compared to CRPs are minimal. However, further savings are achievable by increasing the membrane selectivity, although this requires a greater amount of membrane material within the reactor.

Lastly, while only modest energy savings are achievable using MRPs over CRPs for CO_2 hydrogenation to methanol, additional savings might be achievable by testing different process configurations or by applying membrane reactors to reactions more suited to their capabilities,

such as direct dimethyl ether (DME) synthesis.

V.2 Outlooks

Throughout this PhD work, development pathways in every field studied have been identified and are further discussed here.

While many publications on the preparation of membrane materials for gas permeation are available, very few focus on generating permeation data under actual reaction conditions and for all compounds involved in the reaction. Such experimental data are essential for accurately modeling membrane behavior across different operating conditions, enabling rigorous assessments of membrane reactors at both the reactor and process scales. Furthermore, discussions on the stability and operational limits of these materials are rare, yet this information is critical for conducting environmental and economic evaluations of membrane-assisted processes. The absence of this data impedes simulation studies, thereby limiting the ability to assess the viability of these technologies. Such assessments are critical steps to entice financial investments essential for scaling these technologies to higher technology readiness levels (TRLs).

Moreover, while zeolite membranes were selected in this PhD works due to their extensive literature background, many upcoming membrane materials (such as carbon membranes or new types of polymeric membranes) may offer superior separation performances and stability in the future, making them potentially more suitable for this application. Additionally, most microporous membranes currently rely on macroporous supports for their mechanical strength, which constitute the majority of both economic [1] and environmental [2] costs associated with membrane materials. Thus, investigating alternative supports that are cheaper to manufacture or operate could help the democratization of membrane reactors.

While the development of membrane materials capable of maintaining high separation performances at elevated temperatures remains essential, the introduction of new catalytic systems active at lower temperatures could broaden the operating windows for both membranes and catalysts. This research area extends beyond membrane reactors, as lower-temperature catalysts could also enhance the efficiency of conventional reactor processes.

Some synergetic effects have been reported in the literature when an active catalytic layer is deposited directly on the membrane. However, these studies often operate at very low reactant conversions due to the limited amount of catalyst deposited on the membrane surface. To further investigate these potential synergetic effects, alternative synthesis methods that enable the deposition of larger quantities of catalyst on the membrane are needed. These methods must operate under mild conditions to avoid damaging the zeolite membrane during catalyst preparation.

Additionally, membrane reactors are often described as having the potential to improve the long-term stability of water-sensitive industrial copper-zinc-alumina catalysts. However, to the best of our knowledge, this assumption has not been tested experimentally or numerically in the available literature. Research in this area would involve rigorously quantifying the effects of both temperature and water content in the reaction mixture on the aging of both the industrial catalyst and the membrane material. Such studies could uncover another significant advantage

of using membrane reactors.

Recent trends in the literature have focused on developing increasingly complex membrane reactor models to accurately describe material and heat transfer within reactors of specific geometries. However, simpler and more flexible tools, such as the simplified reactor model proposed in **Chapter IV**, should be first used at the process scale to broadly assess optimal process design configurations and parameters before proposing a specific reactor design. While the presented process-scale study for methanol synthesis yielded mixed results, the tools and methods developed in this research are applicable to other water-limited CO_2 conversion pathways. These include direct DME synthesis, CO_2 conversion to olefins, the reverse water-gas shift (RWGS) reaction, methanation, and Fischer-Tropsch synthesis, among others. The distinct characteristics of these reactions could reveal significant advantages for membrane reactors over conventional ones. Furthermore, applying these tools to alternative reaction pathways could help identify performance targets that will guide the development of new membrane materials, driving further advancements in membrane reactor technology.

Glossary (Chapter V)

Acronyms

CRP Conventional Reactor Process
DME Dimethyl Ether
GHSV Gas Hourly Space Velocity
LTA Linde Type A
MRP Membrane Reactor Process
RWGS Reverse Water-Gas Shift reaction
SEM Scanning Electron Microscope
SOD Sodalite
TRL Technology Readiness Level

References

[1] Jürgen Caro, Manfred Noack, and Peter Kölsch. "Zeolite Membranes: From the Laboratory Scale to Technical Applications". In: *Adsorption* 11.3-4 (July 2005), pp. 215–227. ISSN: 0929-5607, 1572-8757. DOI: 10.1007/s10450-005-5394-9.

[2] Alberto Navajas et al. "Environmental Evaluation of the Improvements for Industrial Scaling of Zeolite Membrane Manufacturing by Life Cycle Assessment". In: *ACS Sustainable Chemistry & Engineering* 6.11 (Nov. 5, 2018), pp. 15773–15780. ISSN: 2168-0485, 2168-0485. DOI: 10.1021/acssuschemeng.8b04336.

Appendix

Appendix A

Vapor-liquid equilibrium (VLE) calculations

The calculations of vapor-liquid equilibria inside a cold trap are essential to the material balance. However, cold traps for methanol synthesis features frequently gases and vapors under high pressure at low temperature in which some polar molecules prone to form hydrogen bonds are condensing. This environment leads to strongly non-ideal gas and liquid phases. Thus, rigorous and complex models are required to calculate the fugacity of each component in each phase.

For the following VLE calculations, these assumptions are made:

- Homogeneous temperature and pressure inside the cold trap.
- Steady state in which every species is at its vapor-liquid equilibrium.
- Ideal mixing in each phase.

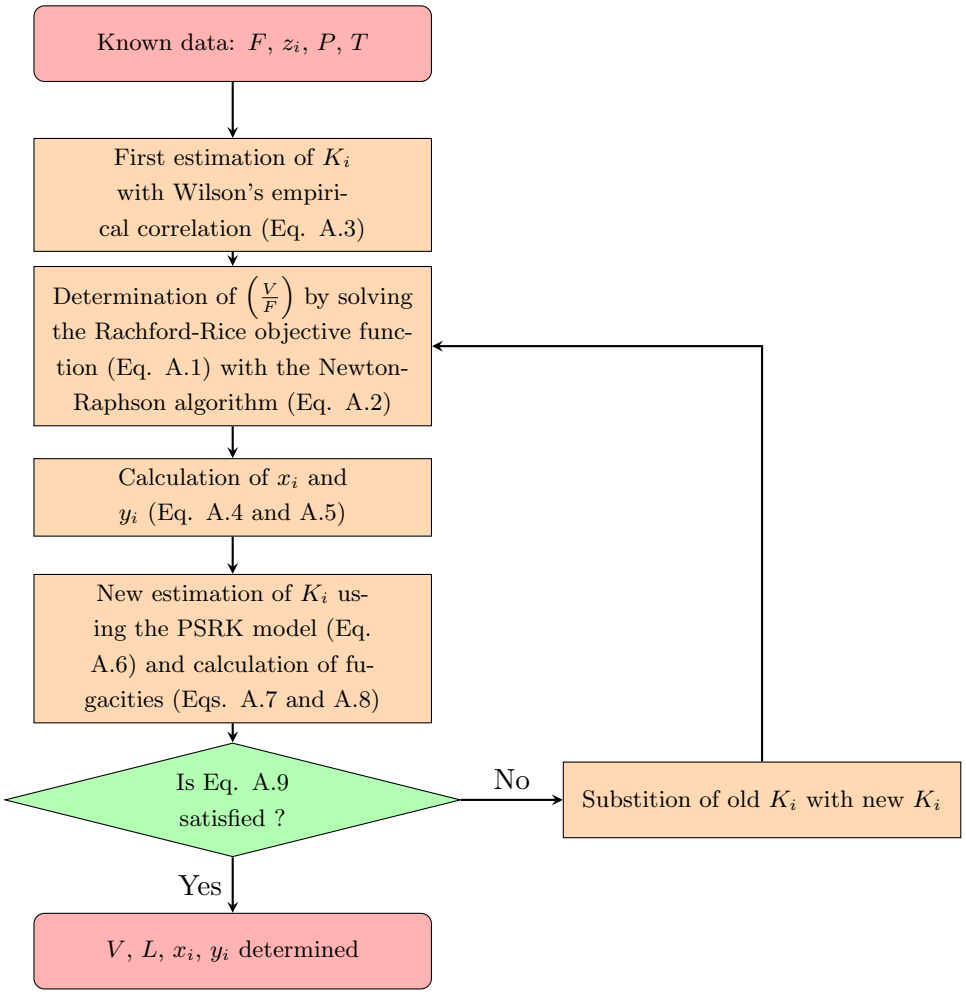

Figure A.1: Flow diagram of the algorithm used for VLE calculations.

To solve the VLE problem, the method described by Chabab et Al. [4] is followed. In this problem, the feed composition and flowrate as well as the temperature and pressure are known. The objective is thus to predict the composition and flowrates of both liquid and vapor streams. The equilibria were computed by solving the Rachford-Rice objective function (Eq. A.1) using a Newton-Raphson method (Eq. A.2). Initial values for the equilibrium ratios K_i were estimated using Wilson's empirical correlation (Eq. A.3). Compositions for the liquid and vapor phases were then calculated using respectively Eq. A.4 and A.5. Then, better estimations of equilibrium ratios were made using coefficient fugacities calculated by the predictive Soave-Redlich-Kwong (PSRK) model (Eq. A.6). This successive substitution method was repeated until the condition described in Eq. A.9 was met (where fugacities are calculated using fugacity coefficients (Eq. A.7 and A.8)). This condition describes the equality of fugacities for each compound in each phase, meaning the system is at equilibrium. This algorithm is summarized in Figure A.1.

$$f\left(\frac{V}{F}\right) = \sum_{i}^{N} \frac{z_i(K_i - 1)}{1 + \frac{V}{F}(K_i - 1)} = 0 \tag{A.1}$$

$$\left(\frac{V}{F}\right)^{new} = \left(\frac{V}{F}\right)^{old} + \frac{f((\frac{V}{F})^{old})}{f'((\frac{V}{F})^{old})} = \left(\frac{V}{F}\right)^{old} = \left(\frac{V}{F}\right)^{old} - \frac{\sum_i^N \frac{z_i(K_i-1)}{1+(\frac{V}{F})^{old}(K_i-1)}}{\sum_i^N \frac{z_i(K_i-1)^2}{(1+(\frac{V}{F})^{old}(K_i-1))^2}} \tag{A.2}$$

$$K_i = \frac{1}{P_{r_i}} exp\Big(5.37(1+\omega_i)(1-\frac{1}{T_{r_i}})\Big) \tag{A.3}$$

$$x_i = \frac{z_i}{1+\frac{V}{F}(K_i-1)} \tag{A.4}$$

$$y_i = K_i x_i \tag{A.5}$$

$$K_i = \frac{x_i}{y_i} = \frac{\phi_i^V(y_i,P,T)}{\phi_i^L(x_i,P,T)} \tag{A.6}$$

$$f_i^L = x_i \phi_i^L P \tag{A.7}$$

$$f_i^V = y_i \phi_i^V P \tag{A.8}$$

$$\sum_i^N (\frac{f_i^L}{f_i^V} - 1)^2 < 1 \times 10^{-14} \tag{A.9}$$

A.1 Predictive Soave-Redlich-Kwong (PSRK)

The PSRK model, originally developed by Holderbaum and Gmehling [7], was reproduced in python and used to calculate the fugacity coefficients for the VLE calculations. This model offers good accuracy without requiring binary interaction parameters that must be determined experimentally [7] (or commercially acquired). This model is based around the SRK equation (Eq. A.10 to A.12) of state but using a Mathias-Copeman alpha function (Eq. A.13) as well as original mixing rules for the calculations of the a parameter (Eq. A.14) [7].

$$P = \frac{RT}{v-b} - \frac{a}{v(v+b)} \tag{A.10}$$

$$a = 0.42748 \frac{R^2 {T_{c_i}}^2}{P_{c_i}} \alpha_i(T) \tag{A.11}$$

$$b = 0.08664 \frac{RT_{c_i}}{P_{c_i}} \tag{A.12}$$

$$\begin{gathered} \alpha_i(T) = (1 + C_1(1-{T_{r_i}}^{0.5}) + C_2(1-{T_{r_i}}^{0.5})^2 + C_3(1-{T_{r_i}}^{0.5})^3)^2 \qquad T_{r_i} < 1 \\ \alpha_i(T) = (1 + C_1(1-{T_{r_i}}^{0.5}))^2 \qquad T_{r_i} > 1 \end{gathered} \tag{A.13}$$

$$a = b\Big(\frac{G^E}{-0.64663} + \sum_i^N x_{s,i}\frac{a}{b} + \frac{RT}{-0.64663}\sum_i^N \ln(\frac{b}{b})\Big) \tag{A.14}$$

$$b = \sum_i^N x_{s,i} b \tag{A.15}$$

The perk of this model lies in the utilization of UNIFAC for its mixing rules to determine the excess Gibb's free energy G^E of the system (Eq. A.14 and A.16). The UNIFAC model, developed by Fredenslund *et al.* [5], is used for the calculation of activity coefficients (Eq. A.17 to A.22). This model avoids requiring binary interaction parameters by relying on a group contribution architecture in which molecules are decomposed in small subgroups [6]. Parameters for each subgroup were extracted from the ProSimPlus3 software.

$$G^E = RT\sum_i^N x_{s,i}\ln\gamma_i \tag{A.16}$$

$$\ln\gamma_i = \ln\gamma_i^C + \ln\gamma_i^R \tag{A.17}$$

Combinatorial term:

$$\ln\gamma_i^C = \ln\frac{\Phi_i}{x_{s,i}} + \frac{z}{2}\ln\frac{\theta_i}{\Phi_i} + l_i - \frac{\Phi_i}{x_{s,i}}\sum_j^N x_{s,j} l_j \tag{A.18}$$

With:

$$l_i = \frac{z}{2}(r_i - q_i) - (r_i - 1) \qquad \begin{array}{ll} r_i = \sum_k^{NG} \nu_k^{(i)} R_k & q_i = \sum_k^{NG} \nu_k^{(i)} Q_k \\ \Phi_i = \frac{x_{s,i} r_i}{\sum_j^N x_{s,j} r_j} & \theta_i = \frac{x_{s,i} q_i}{\sum_j^N x_{s,j} q_j} \end{array} \tag{A.19}$$

Residual term:

$$\ln\gamma_i^R = \sum_k^{NG} \nu_k^{(i)}(\ln\Gamma_k - \ln\Gamma_k^{(i)}) \tag{A.20}$$

$$\ln\Gamma_k = Q_k\Big(1 - \ln(\sum_m^{NG}\Theta_m\tau_{m,k}) - \sum_m^{NG}\frac{\Theta_m\tau_{k,m}}{\sum_n^{NG}\Theta_n\tau_{n,m}}\Big) \tag{A.21}$$

$$\tau_{n,m} = exp\Big(-\frac{a1_{n,m} + a2_{n,m}T + a3_{n,m}T^2}{T}\Big) \quad \Theta_m = \frac{Q_m X_m}{\sum_n^{NG} Q_n X_n} \quad X_m = \frac{\sum_j^N \nu_m^{(j)} x_{s,j}}{\sum_j^N x_{s,j}(\sum_n^{NG}\nu_n^{(j)})} \tag{A.22}$$

Eqs. A.22 are also used for the calculation of $\Gamma_k^{(i)}$ except Θ_k is now the fraction of group k in pure compound i.

Roots for the cubic SRK equation are first solved in python using numpy's 'roots' function. The largest root is taken to compute the molar volume of the vapor phase while the smaller root which satisfies $v > b$ is taken to compute the molar volume of the liquid phase [7]. Finally, fugacity coefficients can be calculated using Eqs. A.23 and A.24.

$$\ln \phi_i = \frac{b}{b}(\frac{Pv}{RT} - 1) - \ln \frac{P(v-b)}{RT} - \overline{\beta_i} \ln(\frac{v+b}{v}) \tag{A.23}$$

$$\overline{\beta_i} = \frac{1}{-0.64663}(\ln \gamma_i + \ln \frac{b}{b} + \frac{b}{b} - 1 + \beta_i) \qquad \beta_i = \frac{a}{bRT} \tag{A.24}$$

The correct implementation of this VLE calculations in python was checked by comparing its results with the ProSimPlus3 commercial software.

A.2 Non-Random Two Liquids (NRTL)

The non-random two-liquids (NRTL) model, developed by Renon and Prausnitz [9], was used to calculate activity coefficient in Section II.3.1.1. In the following equation, the number 1 represents water and the number 2 represents methanol. Here, $\alpha_{12}^{NRTL} = \alpha_{21}^{NRTL} = 0.2994$, $\Delta g_{12} = 845.206\, cal$, $\Delta g_{21} = -253.88\, cal$.

$$\begin{cases} \ln \gamma_1 = x_2^2 \left(\tau_{21} \left(\frac{G_{21}}{x_1 + x_2 G_{21}} \right)^2 + \frac{\tau_{12} G_{12}}{(x_2 + x_1 G_{12})^2} \right) \\ \ln \gamma_2 = x_1^2 \left(\tau_{12} \left(\frac{G_{12}}{x_2 + x_1 G_{12}} \right)^2 + \frac{\tau_{21} G_{21}}{(x_1 + x_2 G_{21})^2} \right) \end{cases} \tag{A.25}$$

$$\begin{cases} \ln G_{12} = -\alpha_{12}^{NRTL} \tau_{12} \\ \ln G_{21} = -\alpha_{21}^{NRTL} \tau_{21} \end{cases} \tag{A.26}$$

$$\begin{cases} \ln \tau_{12} = \frac{\Delta g_{12}}{RT} \\ \ln \tau_{21} = \frac{\Delta g_{21}}{RT} \end{cases} \tag{A.27}$$

Appendix B

Catalytic activity measurements

B.1 Bed uniformity

To assume plug-flow inside a catalytic bed, the following conditions must be met:

$$\frac{d_t}{d_p} > 10 \tag{B.1}$$

$$\frac{L_B}{d_p} > 50 \tag{B.2}$$

Where d_t is the internal reactor tube diameter, d_p is the diameter of a particle of catalyst of inert material (here a mean value of 94 µm is assumed for the 63-125 µm range of sieved particle diameter) and L_B is the length of the bed. Eq B.1 describes a condition in which wall effects causing radial velocity profiles of reactants can be neglected [11] while Eq. B.2 is a simplified Mears [8] condition to neglect the effect of axial dispersion on the residence time distribution.

$$\Delta = \frac{x_{inert}}{1 - x_{inert}} \frac{d_p}{L_B} \frac{n}{2} \tag{B.3}$$

The error in CO_2 conversion due to bed dilution was estimated using Berger *et al.* [3, 2] method where Δ is the error on the conversion, b is volumetric fraction of inert material in the bed and n the order of the reaction. For the calculations, a worst-case value of 4 for the reaction order was assumed (corresponding to CO_2 hydrogenation to methanol with no surface coverage of species on the catalyst) (Eq. B.3).

Table B.1: Bed uniformity calculation results.

Catalyst	$\frac{d_p}{L_B}$ **(-)**	$\frac{d_t}{d_p}$ **(-)**	$\frac{L_B}{d_p}$ **(-)**	x_{inert} **(vol.%)**	Δ **(%)**
CZZ (CP)	1.0	101	102	78	7.1
CZZ (SG)	0.7	101	68	0	(-)
CZZ (CO_2sc)	0.6	101	59	0	(-)
CZYSZ (CO_2sc)	0.6	101	64	0	(-)
CZI (CP)	1.0	101	101	79	7.3
AA (Commercial)	1.1	101	108	82	8.5

B.2 Material balance

The material balance of the test bench was measured twice with the AA commercial catalyst using the method featured in Section III.2.2.7.c.

Furthermore, in order to verify the material balance, the trapped water and methanol were collected, weighted and its concentration was analyzed using a Shimadzu gas chromatography (GC). This GC was equipped with a Poraplot Q (15m x 250µm x 8µm) leading to a TCD for analysis (carrier gas: Ar). The temperature of both the injector and the detector was 150°C. During a sample analysis, the temperature of the column was initially set at 60°C for 1min and then ramped up to 120°C at a rate of 20°C/min. Pressure of the column was set to 141,8 kPa and a split ratio of 5 was employed. For analysis, 1µL of the sample were injected with a syringe and the concentration of water and methanol were determined using an external calibration on the ratio of the peak areas of methanol and water.

B.2.1 Averaged material balance

To establish the average material balance, only one operating temperature and pressure was set and the activity of the catalyst was averaged along the total duration of the experiments. In this experiment, the reaction temperature and the operating pressure were respectively set to 280°C and 50 Bar. A SRA R3000 μGC was used with similar internals as the Inficon μGC described in Section III.2.2.7.c. However, due to malfunctioning of the TCD on the 'MS5A' module, the response factor of CO_2 relative to N_2 was recalculated before the experiment to match the molar ratio of CO_2 over N_2 in the reaction mixture bottle to the blank measurements.

The same methodology to calculate the CO_2 conversion and the reaction selectivities featured in Section III.2.2.7.c still using only the gas phase data from the μGC was used here.

The amount of condensed water and methanol can be estimated using Eq. B.4.

$$n_i = Lx\Delta t \tag{B.4}$$

Table B.2: Calculated activity of the AA catalyst and atomic balance errors for the averaged material balance experiment.

X_{CO_2}	**Selectivity**		**Atomic balance**		
	S_{Hydro}	S_{RWGS}	**Carbon**	**Hydrogen**	**Oxygen**
25.8%	49.9%	50.1%	2.2%	2.8%	3.1%

Table B.3: Comparisons between experimental analysis of the condensed liquid methanol and water to numerical estimations for the averaged material balance experiment.

	Liquid fraction		**Weight (g)**	
	x_{MeOH}	x_{H_2O}	**MeOH**	**H_2O**
Estimated	32.8%	67.2%	4.5	5.1
Measured	32.3%	67.7%	3.7	4.3
Relative error	-0.8%	1.5%	15.7%	17.7%

The method presented here to solve the material balance using only the gas-phase data shows that all atomic balances errors are below 5% (Table B.2). Moreover, the VLE calculations using the PSRK model are very good at predicting the composition of the liquid phase (Table B.3). This approach also allows accounting for the CO_2 lost in its dissolution in the liquid, which is commonly overlooked in the literature. In this case, the PSRK model predicts a 2% molar fraction of CO_2 present in the liquid phase. From the calculations results, neglecting the dissolution of CO_2 in the liquid phase would have led to significant absolute errors of 2.8% and 7.3% on respectively CO_2 conversion and CO_2 hydrogenation selectivity (corresponding to relative overestimations of respectively 10.7% and 14.6% on their final values). However, this material balance overestimates the amount of methanol and water being condensed by significant amounts. Additionally, It is unsure whether this missing liquid phase is due to experimental factors or modeling inaccuracies (Table B.3).

B.2.2 Integrated material balance

In the previous material balances, averaging the overall catalytic activity led to a good prediction of the composition of the while the amount of condensed water and methanol was overestimated. For this new material balance, the amount of condensed products was calculated by integrating the catalytic activity throughout the duration of the experiments. To match the experimental conditions of Section III.2.2.7.c, the temperature in the reaction varied during this test. The malfunctioning SRA R3000 μGC used in Section B.2.1 was swapped to the Inficon μGC used for the catalytic experiments of Section III.2.2.7.c.

For each individual μGC analysis, the method described in Section III.2.2.7.c was applied to calculate the CO_2 conversion as well as the reaction selectivities. Then, instantaneous partial molar flowrates can be calculated in each individual streams of the test bench. Quantities of each individual species trapped in the liquid phase or escaping in the gas phase were calculated by integrating instantaneous partial flowrates using Eq. B.5. Integrals were solved using the trapezoidal rule described in Eq. B.5.

$$n_i = \int_{t_{start}}^{t_{end}} F_i dt \approx \sum_{k=1}^{N_{mes}} \frac{F_i^{k-1} - F_i^k}{2} \Delta t_k \tag{B.5}$$

Table B.4: Calculated activity of the AA catalyst and atomic balance errors for the integrated material balance experiment.

Temperature (°C)	X_{CO_2}	**Selectivity**		**Overall atomic balance**		
		S_{Hydro}	S_{RWGS}	**Carbon**	**Hydrogen**	**Oxygen**
210	9,8%	71,9%	28,1%			
230	15,2%	61,9%	38,1%			
250	21,1%	59,7%	40,3%	0.6%	0.9%	1.1%
270	24,0%	55,1%	44,9%			
280	24,0%	47,9%	52,1%			

Table B.5: Comparisons between experimental analysis of the condensed liquid methanol and water to numerical estimations for the integrated material balance experiment.

	Liquid fraction		**Weight (g)**	
	x_{MeOH}	x_{H_2O}	**MeOH**	**H_2O**
Estimated	34.1%	65.9%	7.9	8.5
Measured	34.6%	65.4%	7.5	7.9
Relative error	-0.7%	1.3%	5.2%	6.9%

In this experiment, the material balance accuracy increased to the point that the error in the atomic balance is around 1%. The composition of the liquid phase is just as accurate as in Section B.2.1 and the overestimation of the quantity of product is more contained. However, the μGC was shut down right after the heating of the reactor was turned off, leading to no analysis of the gas that reacted before the shut-down which did not have time to reach the μGC due to high residence time inside the cold trap. Therefore, the error in material balance should be closer to what was observed in Section B.2.1.

After two experiments to validate the material balance of the experimental setup solely on gas phase data, we can conclude that this methodology is very accurate in its prediction of the composition of the liquid phase and thus its analysis becomes unnecessary. Moreover, the error in the material balance and the values for conversion and selectivity are comparable showing the reproducibility of the experimental setup. While some liquid products are missing leading to an uncertainty on the final value of the conversion, the reproducibility is high enough to allow a fair comparison of each individual catalyst evaluated in this experimental setup.

Appendix C

Process simulations

C.1 Thermodynamic model description

The SRK model, with modifications to the alpha function by Bennekom *et al.* [1] as utilized by Slotboom *et al.* [10] to fit their kinetic model, was used to calculate fugacity coefficients for every compound in the reactor. The model is described through Eqs. C.1 to C.10.

$$Z^3 - Z^2 + (-B^2 - B + A)Z - AB = 0 \tag{C.1}$$

$$Z = \frac{Pv}{RT} \tag{C.2}$$

$$a_i = 0.42748 \frac{R^2 T_{c_i}^2}{P_{c_i}} \alpha_{m_i}(T) \tag{C.3}$$

$$b_i = 0.08664 \frac{RT_{c_i}}{P_{c_i}} \tag{C.4}$$

$$\alpha_{m_i}(T) = \left(1 + m(1 - T_{r_i}^{0.5}) - p(1 - T_{r_i}^{0.5})(0.7 - T_{r_i})\right) \tag{C.5}$$

$$m = 0.480 + 1.574\omega_i - 0.176\omega_i^2 \tag{C.6}$$

$$a = \sum_i^N \sum_j^N x_i x_j \sqrt{a_i a_j}(1 - k_{i,j}) \tag{C.7}$$

$$b = \sum_i^N x_i b_i \tag{C.8}$$

$$A = \frac{aP}{R^2 T^2} \tag{C.9}$$

$$B = \frac{bP}{RT} \tag{C.10}$$

The binary coefficient parameters and critical properties were extracted from the article of

Bennekom *et al.* [1] (Tables C.1 and C.2).

Table C.1: Binary coefficient parameters used for the SRK model.

	CO_2	**CO**	**H_2**	**MeOH**	**H_2O**
CO_2	0	0.1164	0.1164	0.1	0.3
CO	0.1164	0	-0.0007	-0.37	-0.474
H_2	0.1164	-0.0007	0	-0.125	-0.745
MeOH	0.1	-0.37	-0.125	0	-0.075
H_2O	0.3	-0.474	-0.745	-0.075	0

Table C.2: Critical properties used for the SRK model.

	CO_2	**CO**	**H_2**	**MeOH**	**H_2O**
P_{c_i} (MPa)	3.494	7.374	8.097	1.293	22.064
T_{c_i} (K)	132.85	304.12	512.64	32.98	647.14
ω_i (-)	0.045	0.225	0.565	-0.217	0.344
p (-)	0	0	0.2359	0	0.1277

To solve the root of the cubic SRK equation of state, Cardano's method was employed, which applied to the SRK equation gives Eqs. C.11 to C.13.

$$r = \left(\frac{q}{3}\right)^3 + \left(\frac{s}{2}\right)^2 \tag{C.11}$$

$$q = (-B^2 - B + A) - \frac{1}{3} \tag{C.12}$$

$$s = -AB + \frac{(-B^2 - B + A)}{3} - \frac{2}{27} \tag{C.13}$$

For gaseous only mixtures, $r > 0$ and $q < 0$ and therefore the compressibility factors can be calculated using Eq. C.14.

$$Z = \sqrt[3]{\frac{-q}{2} + \sqrt{r}} + \sqrt[3]{\frac{-q}{2} - \sqrt{r}} + \frac{1}{3} \tag{C.14}$$

Finally, the fugacity coefficients are calculated using Eq. C.15.

$$\ln(\phi_i) = -\frac{A}{B}\left(\delta_i - \frac{B_i}{B}\right)\ln\left(\frac{Z+B}{Z}\right) + \frac{B_i}{B}(Z-1) - \ln(Z-B) \tag{C.15}$$

C.2 Kinetic model validation

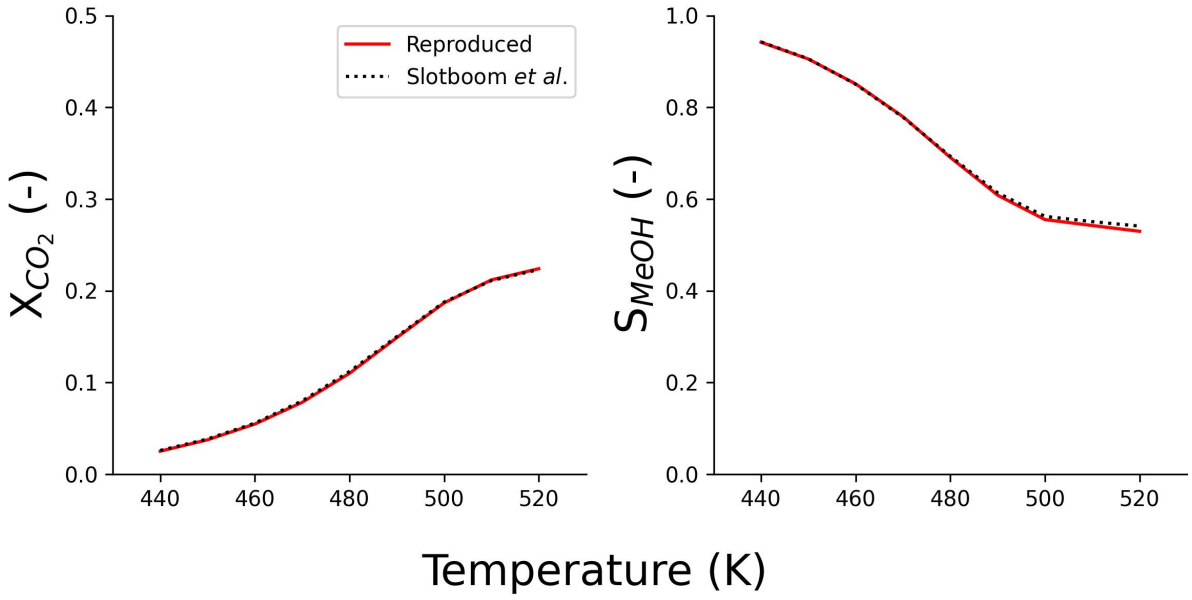

Figure C.1: Validation of the correct implementation of the Slotboom *et al.* [10] kinetic model.

Glossary (Appendix)

Acronyms

NRTL Non-Random Two-Liquids

PSRK Predictive Soave-Redlich-Kwong

SRK Soave-Redlich-Kwong equation of state

UNIFAC UNIQUAC **F**unctional-group **A**ctivity **C**oefficients

UNIQUAC Universal **Qua**si**c**hemical

VLE Vapor Liquid Equilibrium

Roman letters

A Adimensional mixture 'a' parameter (J/mol)

B_i Adimensional 'b' parameter for species i (-)

B Adimensional mixture 'b' parameter (-)

C_n Parameters for the Mathias-Copeman alpha function (-)

F Molar flowrate of the feed stream (mol/s)

G^E Excess Gibbs' free energy of the system (J/mol)

G_{ij} Coefficient defined in Eq. A.26

K_i Equilibrium ratio between the liquid and vapor phase of species i (-)

L_B Length of the catalytic bed (m)

L Molar flowrate of the liquid stream (mol/s)

NG Number of groups

N_{mes} Number of μGC analysis in the experiment

N Number of species in the system

P_{c_i} Critical pressure of species i (Pa)

P_{r_i} Reduced pressure of species i (Pa)

P Pressure (Pa)

Q_k Group k area parameter (-)

R_k Group k volume parameter (-)

R Ideal gas constant ($R = 8.314\,\mathrm{J\,mol^{-1}\,K^{-1}}$)

T_{c_i} Critical temperature of species i (K)

T_{r_i} Reduced temperature of species i (K)

T Temperature (K)

V Molar flowrate of the vapor stream (mol/s)

X_m Group fraction in the system (-)

Z Compressibility factor (-)

$\alpha_{i,j}^{NRTL}$ Non-randomness constant for binary i,j interaction for the NRTL model

α_{m_i} Modified alpha function by Bennekom *et al.* [1]

$\frac{V}{F}$ Ratio between the flowrates of the feed and vapor streams of the cold trap (-)

a_i 'a' Parameter for species i (J/mol)

$a_{i_{n,m}}$ UNIFAC parameter number i between group n and m (-)

a Mixture 'a' parameter (J/mol)

b_i 'b' parameter for species i (m^3/mol)

b Mixture 'b' parameter (m^3/mol)
d_p Particle diameter of the catalyst (m)
d_t Internal tube diameter of the reactor (m)
$f_i^{V,L}$ Fugacity of species i in phase: V (vapor phase), L (liquid phase)
$k_{i,j}$ Binary interaction parameter for the SRK model between species i and j.
l_i species parameter (-)
m Parameter dependent of the acentric factor defined in Eq. C.6.
n_i Amount of condensed water and methanol in the cold trap (mol)
n Overall reaction order (-)
p Polarity factor introduced by Bennekom *et al* [1].
q_i Area parameter for species i (-)
q Defined in Eq. C.12.
r_i Volume parameter for species i (-)
r Discriminant for the resolution of the cubic SRK equation of state.
s Defined in Eq. C.13.
v Molar volume (m^3/mol)
x_i Molar fraction in the liquid stream of the cold trap (-)
x_{inert} Volumetric fraction of inert material inside the catalytic bed (-)
$x_{s,i}$ Molar fraction of a compound for a given system s (-)
y_i Molar fraction in the vapor stream of the cold trap (-)
z_i Molar fraction in the feed stream of the cold trap (-)
z Lattice coordination number ($z = 10$)

Greek letters

Δg Interaction energy parameter for the NRTL model (Calories)
Δt_k Elapsed time between two μGC analysis (s)
Δt Duration of the experiment (s)
Δ Relative error on the CO_2 conversion value (-)
$\Gamma_k^{(i)}$ Activity coefficient of group k in pure component i (-)
Γ_k Activity coefficient of group k (-)
Φ_i Area fraction of species i (-)
Θ_k Area fraction of group k (-)
α_i Mathias-Copeman alpha function for species i (-)
γ_i^C Activity coefficient of species i (combinatorial component) (-)
γ_i^R Activity coefficient of species i (residual component) (-)
γ_i Activity coefficient of species i (-)
$\nu_k^{(i)}$ Number of group of kind k in a species i (-)
ω_i Acentric factors of species i (-)
$\phi_i^{V,L}$ Fugacity coefficient of species i (superscripts: V (vapor phase), L (liquid phase))
$\tau_{n,m}$ Temperature dependent parameter between group or molecule n and m (-)
θ_i Segment fraction for species i (-)

References

[1] Joost G. van Bennekom et al. "Modeling and Experimental Studies on Phase and Chemical Equilibria in High-Pressure Methanol Synthesis". In: *Industrial & Engineering Chemistry Research* 51.38 (Sept. 26, 2012), pp. 12233–12243. ISSN: 0888-5885, 1520-5045. DOI: 10.1021/ie3017362.

[2] R J Berger et al. "Catalyst performance testing radial and axial dispersion related to dilution in fixed-bed laboratory reactors". In: (2002).

[3] R.J. Berger et al. "Catalyst performance testing: the influence of catalyst bed dilution on the conversion observed". In: *Chemical Engineering Journal* 90.1 (Nov. 2002), pp. 173–183. ISSN: 13858947. DOI: 10.1016/S1385-8947(02)00078-5.

[4] Salaheddine Chabab, Patrice Paricaud, and Christophe Coquelet. "Détermination des propriétés thermodynamiques des fluides - Mélanges". In: *Physique énergétique* (Sept. 2020). DOI: 10.51257/a-v2-be8031.

[5] Aage Fredenslund, Russell L. Jones, and John M. Prausnitz. "Group-contribution estimation of activity coefficients in nonideal liquid mixtures". In: *AIChE Journal* 21.6 (1975). _eprint: https://onlinelibrary.wiley.com/doi/pdf/10.1002/aic.690210607, pp. 1086–1099. ISSN: 1547-5905. DOI: 10.1002/aic.690210607.

[6] Aage Fredenslund et al. "Computerized Design of Multicomponent Distillation Columns Using the UNIFAC Group Contribution Method for Calculation of Activity Coefficients". In: *Industrial & Engineering Chemistry Process Design and Development* 16.4 (Oct. 1977), pp. 450–462. ISSN: 0196-4305, 1541-5716. DOI: 10.1021/i260064a004.

[7] T Holderbaum and J Gmehling. "PSRK: A Group Contribution Equation of State Based on UNIFAC". In: ().

[8] David E. Mears. "The role of axial dispersion in trickle-flow laboratory reactors". In: *Chemical Engineering Science* 26.9 (Sept. 1971), pp. 1361–1366. ISSN: 00092509. DOI: 10.1016/0009-2509(71)80056-8.

[9] Henri Renon and J. M. Prausnitz. "Local Compositions in Thermodynamic Excess Functions for Liquid Mixtures". In: *AIChE Journal* 14.1 (Jan. 1968), pp. 135–144. ISSN: 0001-1541, 1547-5905. DOI: 10.1002/aic.690140124.

[10] Y. Slotboom et al. "Critical Assessment of Steady-State Kinetic Models for the Synthesis of Methanol over an Industrial $Cu/ZnO/Al_2O_3$ Catalyst". In: *Chemical Engineering Journal* 389 (June 2020), p. 124181. ISSN: 13858947. DOI: 10.1016/j.cej.2020.124181.

[11] Gregory Yablonsky, Rebecca Fushimi, and Guy B. Marin. "Kinetic Measurements in Heterogeneous Catalysis". In: *Kirk-Othmer Encyclopedia of Chemical Technology*. Ed. by Kirk-Othmer. 1st ed. Wiley, Mar. 26, 2021, pp. 1–44. ISBN: 978-0-471-48494-3 978-0-471-23896-6. DOI: 10.1002/0471238961.1109140513010704.a01.pub3.

Résumé en français

Introduction

La réaction d'hydrogénation du CO_2 en méthanol, en utilisant de l'hydrogène produit par électrolyse de l'eau alimentée par une énergie à faible teneur en carbone, vise à fournir des substituts aux hydrocarbures. Les objectifs associés à la production de méthanol à faible teneur en carbone sont, d'une part, de fournir des matières premières renouvelables pour une industrie chimique durable et, d'autre part, de produire des carburants synthétiques neutres en carbone pour les transports non électrifiables, qui ne peuvent donc pas se passer d'hydrocarbures liquides (aviation, transport maritime, etc.).

Actuellement, le méthanol est obtenu à partir de matières premières fossiles (gaz naturel, pétrole, charbon, etc.). Cette matière première est ensuite transformée en gaz de synthèse (mélange de CO_2, CO, H_2) avant d'être convertie en méthanol [9]. La proportion de CO_2 entrant dans le réacteur est faible afin d'obtenir des rendements de production optimaux. Les procédés industriels actuels de synthèse du méthanol ne fonctionnent pas avec du CO_2 pur en entrée, comme l'envisage le concept de Capture du Carbone, Utilisations et Stockage (CCUS). En effet, dans ce cas, de grandes quantités d'eau sont générées dans le réacteur (produit de la réaction d'hydrogénation du CO_2), ce qui limite les rendements de production et dégrade prématurément le catalyseur [3]. Pour remédier à ce problème, de nombreuses études ont démontré l'efficacité de réacteurs catalytiques intégrant des membranes capables de séparer sélectivement l'eau [14].

Pour mettre en évidence les avantages des réacteurs à membrane (RM) par rapport aux réacteurs conventionnels à lit fixe (RC) pour la synthèse du méthanol, une approche liant le développement de matériaux, la conception de catalyseurs et l'analyse à l'échelle du procédé est proposée. En synthétisant et en testant des matériaux membranaires avancés, combinés au développement de catalyseurs adaptés aux conditions uniques des RM, cette étude vise à générer des données de performance cruciales afin d'évaluer la viabilité des systèmes membranaires à l'échelle du procédé pour la synthèse du méthanol, et à identifier des axes d'amélioration pour leur conception.

Résultats et discussions

Membranes pour la séparation de vapeur d'eau d'un mélange $H_2/CO_2/CO/MeOH$ à haute température

Parmi les matériaux passés en revue pour la séparation de l'eau dans un réacteur à membrane pour la synthèse de méthanol, les membranes zéolitiques microporeuses semblent être les plus

adaptées. En effet, les performances de ces matériaux en termes de sélectivité dans des conditions de réaction (¿200°C) dépassent de loin celles des membranes en polymère dense et d'autres matériaux microporeux [12, 2]. Pour cette étude, deux types de zéolithes ont été sélectionnés : LTA (Linde Type A) et SOD (Sodalite) (Figure 1). Ces structures se caractérisent par leur faible rapport Si/Al, qui est responsable de leur hydrophilie.

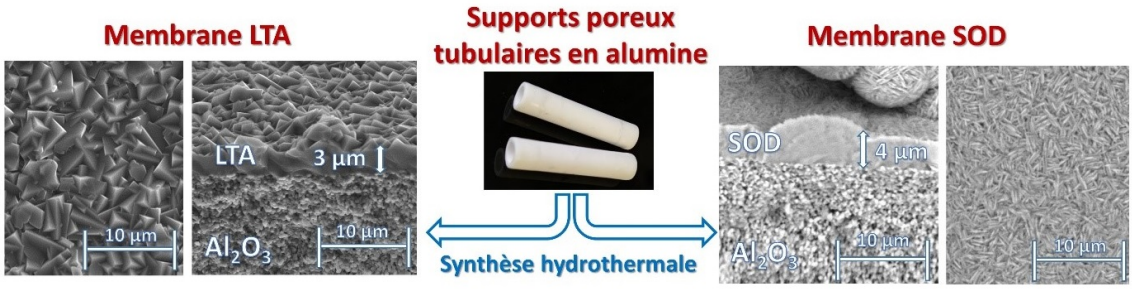

Figure 1: Micrographies MEB des membranes LTA et SOD déposées sur la face interne de supports tubulaires en alumine.

Dans cette étude, les paramètres optimaux de dépôt par voie hydrothermale des membranes LTA, sur des supports tubulaires poreux en alumine de 1 cm, sont de 60°C pendant 24 h. Le dépassement de ces valeurs entraîne la formation indésirable de phases SOD et FAU (Faujasite). De plus, un vieillissement de 20 h du gel de synthèse augmente la densité de la couche de membrane zéolitique en générant plus de germes de cristaux de zéolithes avant la synthèse. Le traitement du support est également un élément clé pour prévenir les défauts dans les membranes LTA. Bien que les protocoles de croissance secondaire soient plus complexes que les méthodes de croissance primaire, ils sont plus fiables, car ils permettent un contrôle précis de la croissance des cristaux en découplant les étapes de nucléation et de croissance.

Par ailleurs, la mise en œuvre de deux dépôts successifs par voie hydrothermale aboutit à la formation d'une couche homogène de SOD sur le support tubulaire en alumine. En augmentant la concentration de gel, il est possible de synthétiser sélectivement des membranes de SOD à des températures plus basses. Néanmoins, les résultats obtenus indiquent que les membranes SOD présentent une stabilité thermique inférieure à celle des membranes LTA, ce qui contredit les rapports précédents dans la littérature [13].

L'augmentation de la quantité de gel de synthèse dans la cuve de réaction est essentielle pour la mise à l'échelle des méthodes de synthèse de LTA et de SOD sur des supports membranaires de 5 cm. Cependant, le mélange du gel de synthèse pendant la synthèse joue un rôle négligeable dans la croissance des membranes, car la diffusion des réactifs est suffisamment rapide pour ne pas entraver la croissance des cristaux.

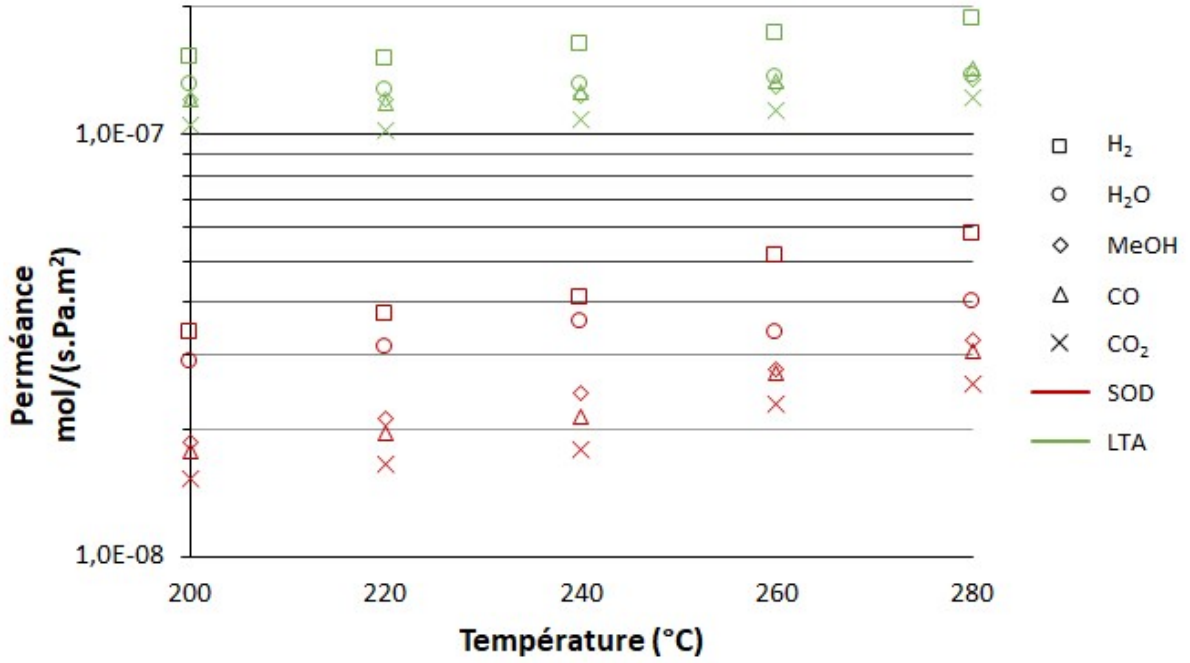

Figure 2: Perméances des molécules $H_2/H_2O/CO_2/CO/MeOH$ à travers des membranes LTA et SOD. Différence de pression transmembranaire de 10 bar. Mélange $H_2/H_2O/CO_2/CO/MeOH$ équimolaire.

Malgré les faibles sélectivités démontrées lors des tests des membranes en perméation gazeuse (Figure 2), certaines observations de la littérature ont été corroborés sur l'influence de la structure de la zéolithe sur les performances de la membrane. Les membranes SOD, grâce à leurs pores plus petits sont plus sélectives que les zéolithes à pores plus grands (telles que les zéolithes LTA). Cependant, les pores très fins des zéolithes SOD s'accompagnent d'un compromis de perméance plus faible que pour les zéolithes LTA.

Catalyseurs pour la synthèse de méthanol adaptés aux contraintes des réacteurs membranaires

Après avoir passé en revue les progrès récents de la littérature sur les catalyseurs cuivre-zinc et les alternatives émergentes pour la synthèse du méthanol, les catalyseurs cuivre-zinc semblent être les candidats les plus adaptés pour la synthèse du méthanol à basse température. Ces observations sont néanmoins à nuancer en considérant que les catalyseurs cuivre-zinc bénéficient de décennies d'applications industrielles alors qu'à l'inverse, les systèmes catalytiques alternatifs en sont encore aux premiers stades de la recherche et du développement. Toutefois, des progrès futurs pourraient modifier les conclusions tirées de cette étude.

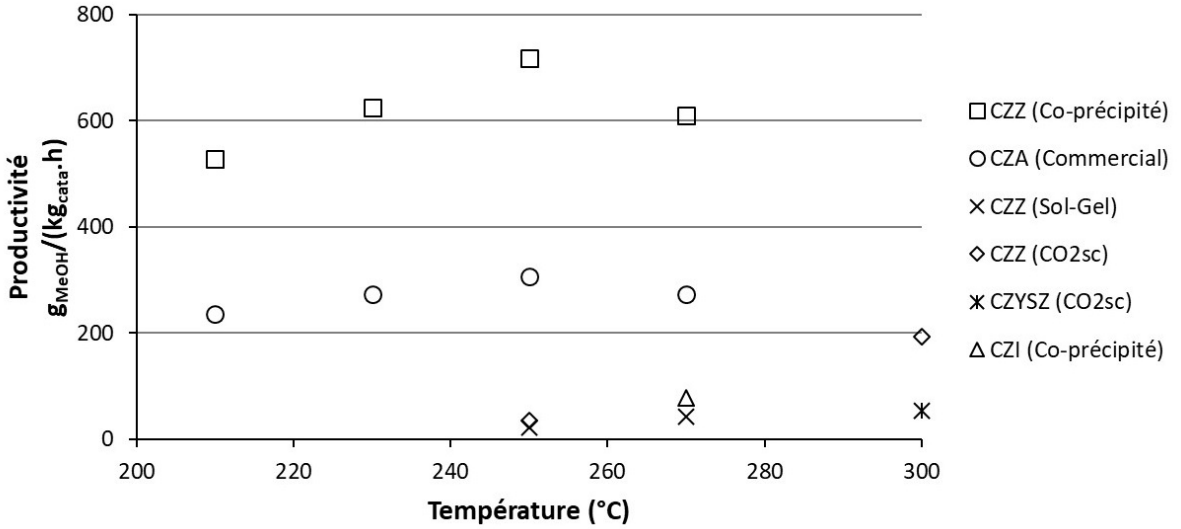

Figure 3: Productivité des catalyseurs étudiés pour réaliser la synthèse de méthanol au sein d'un réacteur membranaire. Conditions expérimentales : CZA (Commercial), CZZ (co-précipité) = 30 bar, GHSV 30 000 h^{-1}; reste = 50 bar, GHSV 10 000 h^{-1}.

Sur la base de l'analyse de la littérature, deux catalyseurs à base de Cu/ZnO ont été synthétisés par co-précipitation et caractérisés afin d'étudier les performances possibles à basse température (adaptée aux conditions de synthèse du méthanol à partir du CO_2 dans un RM). Ces catalyseurs, supportés respectivement sur de la zircone (CZZ) et de l'oxyde d'indium (CZI), ont été comparés à un catalyseur commercial supporté sur de l'alumine (CZA). Parmi ces catalyseurs, seul le catalyseur CZZ co-précipité a présenté une activité supérieure, par rapport à sa masse, à celle du catalyseur commercial (Figure 3). Néanmoins, ce catalyseur n'a pas démontré une activité notable à basse température pour la production de méthanol. Un catalyseur cuivre-zinc supporté sur oxyde d'indium a également été étudié. Malgré des caractéristiques prometteuses observées dans les analyses de diffraction des rayons X (DRX), de réduction programmée en température (TPR), de chromatographie frontale réactive par N_2O (N_2O-RFC) et physisorption de N_2 (BET), le catalyseur a étonnamment montré une faible activité catalytique.

En parallèle, des voies de synthèse alternatives ont été explorées pour synthétiser directement le catalyseur sur la membrane (assurant une proximité étroite entre les fonctions catalytiques et de séparation). Les méthodes sol-gel et CO_2 supercritique (essais exploratoires) n'ont pas permis d'obtenir un catalyseur cuivre-zinc ayant une activité suffisante (Figure 3). Alors que les performances insuffisantes du catalyseur synthétisé par voie sol-gel se rapproche à la littérature existante [1], les faible activités catalytiques des catalyseurs synthétisés par CO_2sc contrastent avec les conclusions de Kondrat et al. [6, 7, 8] sur des catalyseurs CZA synthétisés par CO_2sc. Cependant, contrairement à Kondrat et al. [6, 7, 8], les catalyseurs synthétisés par la voie CO_2sc dans cette étude présentent des différences de propriétés substantielles par rapport à celles généralement associées aux catalyseurs actifs au méthanol. Enfin, cette méthode du CO_2 supercritique, telle qu'exécutée, est inadéquate pour le dépôt de catalyseurs sur la membrane car elle conduit à sa destruction complète.

En plus de cette étude catalytique, une nouvelle méthode a été développée pour résoudre le bilan matière d'un banc d'essai catalytique. En utilisant un modèle thermodynamique avancé et

des calculs d'équilibre liquide-vapeur rigoureux, cette approche prédit avec précision la composition de la phase liquide jusqu'aux pourcentages de fraction molaire tout en se basant uniquement sur les données de la phase gazeuse. Cette approche met en évidence le fait que négliger la dissolution du CO_2 dans la phase liquide conduit à des erreurs non négligeables dans l'estimation de la conversion du CO_2 et des sélectivités de réaction.

Viabilité des technologies membranaires à l'échelle du procédé

La comparaison à l'échelle du procédé entre réacteurs conventionnels à lit fixe (RC) et les réacteurs membranaires (RM) pour la synthèse de méthanol a été étudiée dans la littérature sous l'angle de l'efficacité énergétique ainsi que de la performance économique [5, 4, 10]. Cependant, toutes les études présentées à ce jour sont des études de cas avec des paramètres identiques entre les deux types de procédés introduisant potentiellement un biais selon la valeur des paramètres fixée à travers les deux technologies.

Cette problématique est étudiée ici sous l'angle de l'optimisation de procédés. Afin de simplifier ce problème d'optimisation, un modèle de réacteur piston, isotherme et sans géométrie est proposé dans ces travaux. Grâce à ce modèle, il est possible de réaliser un pré-dimensionnement du réacteur membranaire en faisant apparaître la quantité de surface de membrane dans le problème d'optimisation tout en s'affranchissant de la définition d'une géométrie de réacteur.

Un procédé type, conçu pour être flexible sur une large plage de paramètres d'optimisation, est aussi proposé afin de réaliser une comparaison rigoureuse entre RM et RC. Dans cette étude, le critère d'optimisation est décrit comme un minimum d'énergie requise par quantité de méthanol produite. Ce critère comprend les coûts énergétiques de production d'hydrogène, de compression des gaz ainsi que de la chauffe et refroidissement des utilités (déterminés par la méthode de pincement). Les paramètres d'optimisation sont la température et la pression opératoire pour le procédé à RC, et pour le procédé à RM s'ajoutent la surface totale de membranes dans le réacteur ainsi que la quantité de gaz de balayage envoyée dans le réacteur.

Table 1: Effet de la vélocité spatiale (GHSV) sur l'optimum opératoire d'un procédé à RC et à RM selon un critère énergétique. Permsélectivité : H_2O/H_2, H_2O/CO_2, H_2O/CO, H_2O/MeOH = 250, 1000, 250, 500. *Borne haute de l'optimiseur.

GHSV (h^{-1})	**Economie énergétique du RM par rapport au RC**	**RC**		**RM**		
		T (°C)	**P (bar)**	**T (°C)**	**P (bar)**	**Surface de membrane (m^2)**
100	2,24%	222	66	205	36	$4.26 \cdot 10^3$
500	2,40%	238	70*	220	45	$3.70 \cdot 10^3$
1 000	2,50%	244	70*	228	52	$2.80 \cdot 10^3$
5 000	2,89%	261	70*	245	67	$2.34 \cdot 10^3$
10 000	3,16%	270*	70*	253	70*	$2.37 \cdot 10^3$

Sur la plage de vélocité spatiale (GHSV) étudiée, les procédés à RM montrent un gain énergétique croissant selon le GHSV par rapport aux procédés à RC (Tableau 1). Cependant, l'optimum du RC est souvent sur les bornes hautes des variables d'optimisation et, sans celles-ci, les gains du RM face au RC sont attendus comme constants. En effet pour chaque réacteur, l'optimiseur ajuste les paramètres opératoires pour qu'aucun d'entre ne se retrouve soit gravement limité par la cinétique ou par la thermodynamique. Toutefois, la vélocité spatiale influe

sur les paramètres opératoires optimaux et de plus, à même GHSV, le RC et le RM ont des paramètres opératoires différents. En effet, là où le RM peut déplacer l'équilibre grâce à la membrane, le RC va atteindre des conversions similaires en opérant à des conditions opératoires plus rudes en température et en pression. Ainsi, comparer ces deux procédés selon les mêmes paramètres opératoires peut mener à un biais selon l'un ou l'autre type de réacteur, selon les conditions opératoires choisies.

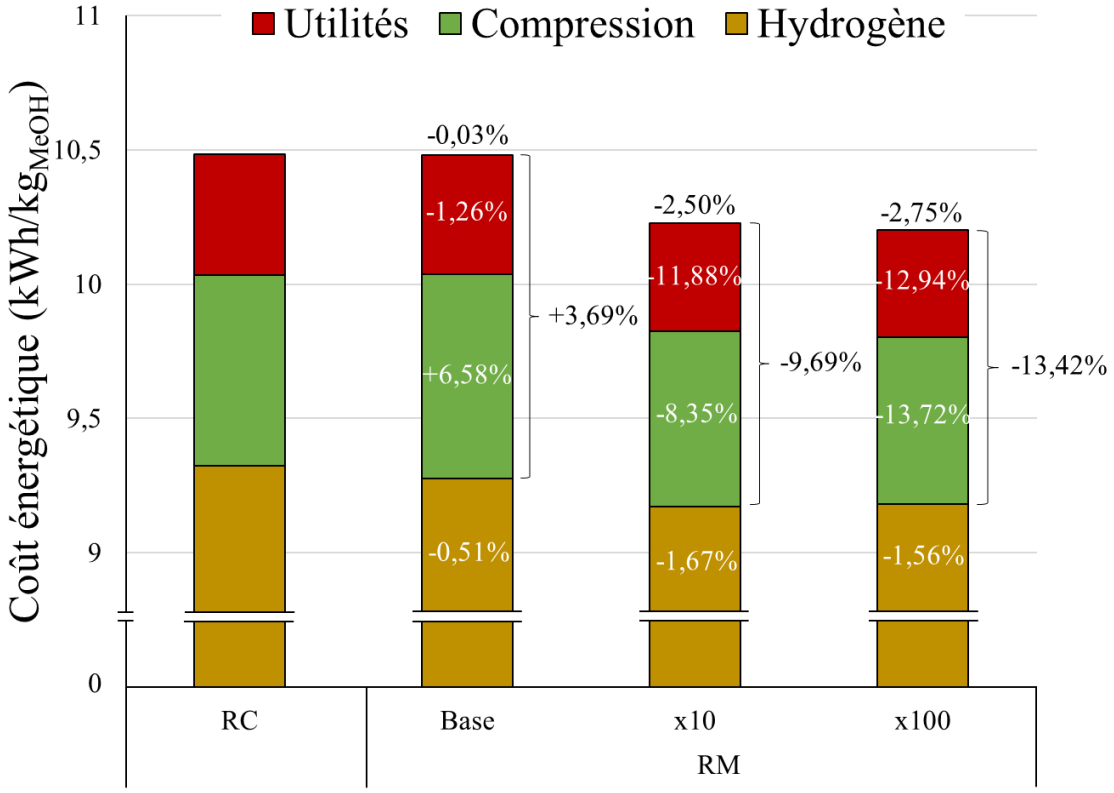

Figure 4: Effet de la sélectivité de la membrane sur le coût énergétique du procédé. Permsélectivité de base : H_2O/H_2, H_2O/CO_2, H_2O/CO, $H_2O/MeOH$ = 25, 100, 25, 50. GHSV = 1 000 $Nm^3.h^{-1}.m_{cat}^{-3}$.

Selon les résultats présentés sur la Figure 4, un gain de performance énergétique négligeable est réalisable selon les permsélectivité sélectionnées inspirées de la littérature [11]. Cependant, avec des membranes plus sélectives, les réacteurs membranaires sont moins énergivores grâce à leur capacité à obtenir des performances de réacteur élevées (hautes conversions) tout en opérant à des conditions opératoires plus douces. Ainsi, en plus d'entrainer une baisse des coûts d'utilités et de compression, grâce aux conditions opératoires plus douces, des économies supplémentaires sont réalisées grâce à une diminution des taux de recycles (grâce à leurs taux de conversions supérieurs) .

Conclusions

Ce travail réalise une étude complète de l'échelle matériau jusqu'à la simulation de procédés sur l'application des réacteurs membranaires pour l'hydrogénation du CO_2 en méthanol. Lors de ces travaux, des méthodes de synthèse de membrane LTA et SOD ont été développées afin de tester ces matériaux en conditions de réaction. Malgré des performances de séparation en deçà de ce qui est décrit dans la littérature, des données de perméance exhaustives sur l'ensemble des composés présents lors de la synthèse de méthanol à différentes températures ont pu être relevées.

Après une revue de la littérature sur les catalyseurs de synthèse de méthanol, les catalyseurs basés sur le couple cuivre-zinc émergent comme les plus adaptés aux contraintes des réacteurs membranaires. Lors de l'étude de ces systèmes catalytiques, un catalyseur cuivre-zinc-zircone a démontré des performances supérieure (par masse de catalyseur) à un catalyseur commercial. D'autres méthodes de synthèses alternatives pouvant permettre le dépôt du catalyseur sur la membrane n'ont pas permis de concurrencer les catalyseurs synthétisés par co-précipitation. Néanmoins, des pistes de progressions ont été identifiés pour améliorer l'activité catalytique des catalyseurs préparés par ces méthodes.

A ce jour, la comparaison des procédés à RC à ceux à RM dans la littérature a été réalisée en comparant les deux technologies avec les mêmes paramètres opératoires. Afin d'investiguer les possibles biais de cette méthode, une étude reposant sur l'optimisation énergétique de ces deux types de technologie a été réalisée. Les résultats révèlent que les paramètres opératoires optimaux sont différents entre les deux types de procédés, illustrant un biais couramment réalisé dans la littérature. De plus, les performances membranaires requises pour dépasser les procédés à RC sont aujourd'hui hors de portée pour la majorité des technologies membranaires reportées dans la littérature à ces conditions opératoires.

References

[1] Laetitia Angelo. "Développement de Catalyseurs Pour La Synthèse de Méthanol Produit Par Hydrogénation Du Dioxyde de Carbone". 2014.

[2] A. Ateka et al. "Kinetic Modeling and Reactor Design of the Direct Synthesis of Dimethyl Ether for CO_2 Valorization. A Review". In: *Fuel* 327 (Nov. 2022), p. 125148. ISSN: 00162361. DOI: 10.1016/j.fuel.2022.125148.

[3] Filippo Bisotti et al. "Century of Technology Trends in Methanol Synthesis: Any Need for Kinetics Refitting?" In: *Industrial & Engineering Chemistry Research* 60.44 (Nov. 10, 2021), pp. 16032–16053. ISSN: 0888-5885, 1520-5045. DOI: 10.1021/acs.iecr.1c02877.

[4] Vincent Dieterich et al. "Performance Requirements of Membrane Reactors for the Application in Renewable Methanol Synthesis: A Techno-Economic Assessment". In: *Advanced Sustainable Systems* 6.12 (Dec. 2022), p. 2200254. ISSN: 2366-7486, 2366-7486. DOI: 10.1002/adsu.202200254.

[5] Homa Hamedi, Torsten Brinkmann, and Sergey Shishatskiy. "Membrane-Assisted Methanol Synthesis Processes and the Required Permselectivity". In: *Membranes* 11.8 (Aug. 2021), p. 596. ISSN: 2077-0375. DOI: 10.3390/membranes11080596.

[6] Simon A. Kondrat et al. "Preparation of a Highly Active Ternary Cu-Zn-Al Oxide Methanol Synthesis Catalyst by Supercritical CO2 Anti-Solvent Precipitation". In: *Catalysis Today* 317 (Nov. 2018), pp. 12–20. ISSN: 09205861. DOI: 10.1016/j.cattod.2018.03.046.

[7] Simon A. Kondrat et al. "Stable Amorphous Georgeite as a Precursor to a High-Activity Catalyst". In: *Nature* 531.7592 (Mar. 2016), pp. 83–87. ISSN: 0028-0836, 1476-4687. DOI: 10.1038/nature16935.

[8] Simon A. Kondrat et al. "The Effect of Sodium Species on Methanol Synthesis and Water-Gas Shift Cu/ZnO Catalysts: Utilising High Purity Zincian Georgeite". In: *Faraday Discussions* 197 (2017), pp. 287–307. ISSN: 1359-6640, 1364-5498. DOI: 10.1039/C6FD00202A.

[9] Jörg Ott et al. "Methanol". In: *Ullmann's Encyclopedia of Industrial Chemistry*. Ed. by Wiley-VCH Verlag GmbH & Co. KGaA. Weinheim, Germany: Wiley-VCH Verlag GmbH & Co. KGaA, Oct. 15, 2012, a16_465.pub3. ISBN: 978-3-527-30673-2. DOI: 10.1002/14356007.a16_465.pub3.

[10] Serena Poto et al. "Techno-Economic Assessment of the One-Step CO_2 Conversion to Dimethyl Ether in a Membrane-Assisted Process". In: *Journal of CO2 Utilization* 69 (Mar. 2023), p. 102419. ISSN: 22129820. DOI: 10.1016/j.jcou.2023.102419.

[11] R. Raso et al. "Zeolite Membranes: Comparison in the Separation of $H_2O/H_2/CO_2$ Mixtures and Test of a Reactor for CO_2 Hydrogenation to Methanol". In: *Catalysis Today* (Mar. 2020), S0920586120301310. ISSN: 09205861. DOI: 10.1016/j.cattod.2020.03.014.

[12] M.P. Rohde et al. "Fischer-Tropsch Synthesis with in Situ H_2O Removal, Directions of Membrane Development". In: *Microporous and Mesoporous Materials* 115.1-2 (1-2 Oct. 2008), pp. 123–136. ISSN: 13871811. DOI: 10.1016/j.micromeso.2007.10.052.

[13] N. Wang et al. “Hydrophilic SOD and LTA Membranes for Membrane-Supported Methanol, Dimethylether and Dimethylcarbonate Synthesis”. In: *Microporous and Mesoporous Materials* 207 (May 2015), pp. 33–38. ISSN: 13871811. DOI: 10.1016/j.micromeso.2014.12.028.

[14] I. G. Wenten et al. “Zeolite Membrane Reactors: From Preparation to Application in Heterogeneous Catalytic Reactions”. In: *Reaction Chemistry & Engineering* 6.3 (2021), pp. 401–417. ISSN: 2058-9883. DOI: 10.1039/D0RE00388C.

Vincent GAUTIER

Membrane reactors for methanol synthesis: from material science to process simulations

Résumé

L'hydrogénation catalytique du CO_2 en méthanol, avec de l'hydrogène issu de sources d'énergie bas carbone, propose une alternative durable aux hydrocarbures fossiles. Cependant, dans les réacteurs traditionnels à lit fixe, de grandes quantités d'eau se forment, limitant les rendements. Pour y remédier, des réacteurs catalytiques intégrant des membranes, capables de séparer sélectivement l'eau, ont montré leur efficacité. Afin de comparer les réacteurs membranaires aux réacteurs conventionnels pour la synthèse du méthanol, une approche combinant développement de matériaux membranaires, conception de catalyseurs et simulation de procédé est proposée. En testant des matériaux membranaires avancés et des catalyseurs adaptés, cette étude vise à générer des données clés pour évaluer la viabilité des réacteurs membranaires et identifier des axes d'amélioration pour leur conception.

Mots-clés :

CO_2, H_2, méthanol, CCUS, réacteur, membranaire, zéolithe, matériaux, catalyse, procédé.

Résumé en anglais

Catalytic hydrogenation of CO_2 to methanol, using hydrogen derived from low-carbon energy sources, offers a sustainable alternative to fossil hydrocarbons. However, in traditional fixed-bed reactors, large quantities of water are produced, limiting yields. To address this, catalytic reactors incorporating membranes that can selectively separate water have demonstrated their effectiveness. To compare membrane reactors with conventional reactors for methanol synthesis, an approach combining membrane material development, catalyst design, and process simulations is proposed. By testing advanced membrane materials and suitable catalysts, this study aims to generate key data to evaluate the viability of membrane reactors and identify areas for improvement in their design.

Keywords:

CO_2, H_2, methanol, CCUS, reactor, membrane, zeolite, material science, catalysis, process.